



Wang, Tongguang (1999) *Unsteady aerodynamic modelling of horizontal axis wind turbine performance*.

PhD thesis

<http://theses.gla.ac.uk/4039/>

Copyright and moral rights for this thesis are retained by the author

A copy can be downloaded for personal non-commercial research or study, without prior permission or charge

This thesis cannot be reproduced or quoted extensively from without first obtaining permission in writing from the Author

The content must not be changed in any way or sold commercially in any format or medium without the formal permission of the Author

When referring to this work, full bibliographic details including the author, title, awarding institution and date of the thesis must be given

Unsteady Aerodynamic Modelling of Horizontal Axis Wind Turbine Performance

Tongguang Wang, B.Eng., M.Eng.

Dissertation submitted to the Faculty of Engineering,
University of Glasgow,
for the degree of Doctor of Philosophy

November 1999

©T. Wang, 1999

DECLARATION

The author hereby declares that this dissertation is a record of work carried out in the Department of Aerospace Engineering at the University of Glasgow during the period from November 1996 to October 1999. The dissertation is original in content except where otherwise indicated.

November 1999



Tongguang Wang

ACKNOWLEDGEMENTS

I avail myself of this opportunity to express my heartfelt gratitude to my supervisor, Dr. Frank N. Coton, for his excellent advice and encouragement during the course of this work.

I am also grateful to Prof. Roderick A. McD. Galbraith for the provision of the research student position in the Department of Aerospace Engineering and for his help during this study.

I gratefully acknowledge the financial support from the Committee of Vice-Chancellors and Principals (CVCP) of the Universities of the United Kingdom through the Overseas Research Students (ORS) Awards Scheme and from the University of Glasgow through the University of Glasgow Postgraduate Scholarship.

It is also my pleasure to express my thanks to Mr. X. Munduate, Miss A. Ferrechia, Mrs. E. Garman and Mrs. L. Floyd in the Department for their help.

Finally, I would like to express many thanks to my wife, Liqun, and daughter, Qianru, without whose allowance and support I could not be away from them for a few years and do this work abroad. Much support from my parents and parents-in-law is also gratefully acknowledged.

ABSTRACT

The present work presents a study of unsteady aerodynamic modelling of horizontal axis wind turbine performance. The unsteady aspects addressed in this work include effects of variations in turbine inflow velocity due to operation in yawed flow, in the atmospheric boundary layer, in a wind tunnel, and due to the tower wake. In each case, the basis for the analysis is a prescribed wake vortex model, the development and enhancement of which has been the main focus of the work.

In the prescribed wake model, the turbine blade is modelled as a series of bound vortex blade elements, from which vortex filaments are trailed. In unsteady cases, shed vorticity is introduced into the wake to account for the temporal changes in bound circulation. The turbine wake is divided into a near wake and far wake. The latter represents the far field equilibrium condition of the flow and is modelled as a semi-infinite cylinder. The geometry of the near wake is prescribed by simple prescription functions of induced velocity at the blade, which have been developed using vortex theory. An unsteady aerofoil model is coupled into the prescribed wake model to provide the unsteady aerodynamic and dynamic stall loads on the blades in yawed and shear flows. This method also gives low azimuthal resolution tower shadow effects if a velocity deficit is included to represent the tower wake effect on the onset flow.

A semi-empirical stall delay model, which is based on the analysis of laminar boundary layers on rotating blades, is amalgamated with the unsteady prescribed

wake method to account for 3-D rotational effects. The basis for the 3-D correction is the delay in the forward movement of the separation point due to the centrifugal pumping and Coriolis force. This delay modifies the blade normal force and, together with consideration of the likely chordwise loading distribution, provides the basis for corrections to the blade tangential force and pitching moment. The inclusion of the 3-D effects substantially improves the performance prediction.

A high resolution model has been developed to meet the requirement for adequate representation of the tower shadow effects. A near wake dynamic model has been enhanced with appropriate modifications and integrated into the prescribed wake scheme to produce a hybrid method capable of predicting the detailed high resolution unsteady response in the tower shadow region. The azimuthal interval used within the shadow region can be reduced to 0.5° whilst the computational cost introduced by the high resolution near wake model is almost negligible.

A low order source panel method and the prescribed wake model have been combined into a coupled scheme capable of assessing the basic effect of wind tunnel walls on wind turbine flow and performance. The wind tunnel walls are discretised into a series of panels on which source singularities are placed. The source strengths are related to the turbine bound and wake vorticities via their induced velocities. The geometry of the turbine wake is obtained by superposition of the contribution of the disturbance velocities due to the source panels upon the prescribed wake. This new wake structure modifies the wind turbine aerodynamic performance in turn.

The models developed in this study are discussed in detail and are shown to compare well with experiment across a wide range of cases.

Contents

DECLARATION	i
ACKNOWLEDGEMENTS	ii
ABSTRACT	iii
1 Introduction	1
1.1 Brief Introduction to Wind Energy	1
1.1.1 Status and Prospects for Wind Energy	1
1.1.2 Wind Turbine Technology	13
1.2 Aerodynamics of Wind Turbines	20
1.2.1 Theories and Models	20
1.2.2 Blade Element/Momentum Theory and Definitions	28
1.2.3 Vortex Wake Theory	35
1.2.4 Prescribed Wake Model	39
1.2.5 Unsteady and Three-Dimensional Aerodynamics	40
1.2.6 Experimental Studies	48
1.3 Scope of the Study	53
1.4 Outline of the Dissertation	56
2 Modelling of HAWT Aerodynamic Performance in Uniform Axial Flow	58
2.1 Introduction	58
2.2 The Prescribed Wake Model	60

2.2.1	Assumptions and Coordinate Systems	60
2.2.2	Blade Model	61
2.2.3	Wake Model	63
2.2.4	Wake Geometry Prescription	66
2.3	Performance Calculation	71
2.3.1	Discretisation	71
2.3.2	Blade Loading and Rotor Performance	73
2.3.3	Induced Velocity	78
2.3.4	Procedure of Calculation	83
2.4	Results and Discussion	89
2.5	Conclusions	110
3	Unsteady Prescribed Wake Model	112
3.1	Introduction	112
3.2	Prescribed Wake Model in Yawed and Shear Flow	114
3.2.1	Coordinate Systems and Wind Input	114
3.2.2	Wake Prescription	118
3.2.3	Induced Velocities	121
3.3	The Unsteady Aerofoil Model	124
3.3.1	Introduction	124
3.3.2	Attached Flow Behaviour	126
3.3.3	Leading Edge Separation	132
3.3.4	Trailing Edge Separation	133
3.3.5	Modelling of Dynamic Stall	136
3.3.6	Unsteady Aerodynamic Loads	138
3.4	Model Coupling	139
3.5	Results and Discussion	142
3.6	Conclusions	163
4	Unsteady HAWT Performance with Three-Dimensional Effects	165
4.1	Introduction	165

4.2	The Stall Delay Model	169
4.2.1	Solution of the Boundary Layer Equations	169
4.2.2	3-D Correction to 2-D Aerofoil Data	171
4.3	Correction for Unsteady 3-D Effects	173
4.3.1	Normal Force	173
4.3.2	Chordwise Force	175
4.3.3	Pitching Moment	176
4.4	Results and Discussion	177
4.5	Conclusions	192
5	Tower Shadow Problem	194
5.1	Introduction	194
5.2	Velocity Profile in the Tower Wake	196
5.3	Low Resolution Tower Shadow Effects	199
5.3.1	Wake Prescription with Tower Shadow Effects	199
5.3.2	Results and Discussion	200
5.4	High Resolution for Tower Shadow Effects	206
5.4.1	Introduction	206
5.4.2	The Near Wake Dynamic Model	209
5.4.3	Enhancement of the Near Wake Model	212
5.4.4	Application of the Near Wake Model to the Tower Shadow Problem	214
5.4.5	Results and Discussion	218
5.5	Conclusions	227
6	A Preliminary Study of the Numerical Simulation of HAWTs Operating in a Wind Tunnel	229
6.1	Introduction	229
6.2	Panel Method	231
6.2.1	Introduction	231

6.2.2	Integral Equation for a Source Distribution on the Body Surface	233
6.2.3	Numerical Source Panel Method	234
6.3	Numerical Model of Wind Tunnel	236
6.4	Combination of the Prescribed Wake Model and Panel Method	238
6.4.1	The Wind Tunnel Wall Boundary Condition	239
6.4.2	Wind Tunnel Wall Effects on the Turbine Wake	240
6.4.3	Numerical Procedure	242
6.5	Results and Discussion	246
6.6	Conclusions	257
7	Conclusions and Recommendations	258
7.1	The Prescribed Wake Model	258
7.2	Three-Dimensional Rotational Effects	260
7.3	Tower Shadow Effects	262
7.4	Wind Tunnel Wall Interference	263
A	Velocity Induced by a Straight-line Vortex	265
B	Description of NREL Wind Turbine	268
C	Nomenclature	272
	Bibliography	281

List of Figures

1.1	Comparison of electricity prices	7
1.2	Schematic of typical vertical axis wind turbines	15
1.3	Schematic of horizontal axis wind turbine configurations	16
1.4	Rankine–Froude one-dimensional flow	28
1.5	Streamtube model for wind turbine	30
1.6	Inflow velocity and aerodynamic forces on blade element	31
1.7	Coordinate system	36
1.8	Comparison of predicted and measured CER power	40
1.9	Measured normal force coefficients of CER blade aerofoil	41
1.10	Events of dynamic stall on NACA 0012 aerofoil	44
1.11	Comparison of N–S equations computation with experiment	54
2.1	Representative blade element distribution	62
2.2	Vortex model of blade and rotor wake	64
2.3	Imaginary grid behind a turbine blade in two dimensions	67
2.4	Flow chart for the steady prescribed wake model	84
2.5	Comparison of generated power for MOD–OA turbine	89
2.6	Calculated angle of attack for MOD–OA turbine	91
2.7	Comparison of far wake velocity parameter	91
2.8	Comparison of rotor power coefficient for NREL UAE Phase IV turbine	92
2.9	Calculated wake structure for MOD–OA turbine at $V_0 = 5$ m/s . . .	93
2.10	Calculated wake structure for MOD–OA turbine at $V_0 = 10$ m/s . .	94
2.11	Induced velocity factor for MOD–OA turbine	95

2.12	Bound circulation distribution along the MOD–OA turbine blade	96
2.13	Influence of vortex core size on power coefficient	97
2.14	Comparison of blade loading at $V_0 = 12.5$ m/s and $\gamma = 0.4^\circ$	99
2.15	Comparison of blade loading at $V_0 = 12.3$ m/s and $\gamma = -0.2^\circ$	100
2.16	Comparison of blade loading at $V_0 = 10.5$ m/s and $\gamma = 1.3^\circ$	101
2.17	Comparison of blade loading at $V_0 = 19.2$ m/s and $\gamma = 1.6^\circ$	102
2.18	Comparison of blade loading at $V_0 = 7.1$ m/s and $\gamma = 0.4^\circ$	103
2.19	Comparison of blade loading at $V_0 = 10.4$ m/s and $\gamma = -1.5^\circ$	104
2.20	Comparison of blade loading at $V_0 = 15.9$ m/s and $\gamma = 0.3^\circ$	105
2.21	Comparison of blade loading at $V_0 = 19.3$ m/s and $\gamma = 1.0^\circ$	106
2.22	Angle of attack on the NREL UAE Phase II blade in unyawed flow .	108
2.23	Angle of attack on the NREL UAE Phase IV blade in unyawed flow	109
3.1	Illustration of coordinate systems in yawed flow	115
3.2	Geometry of yawed inflow	117
3.3	Sketch of vortex system	120
3.4	Kirchhoff flow model for separated flow past a flat plate	134
3.5	Flow chart for the unsteady prescribed wake model	140
3.6	Comparison of power coefficient for the WG500 turbine in yaw	143
3.7	Comparison of power coefficients with and without wind shear	144
3.8	Comparison of predicted C_n with and without wind shear	145
3.9	Comparison of predicted C_n in condition of wind shear with field data	145
3.10	Comparison of blade loading at $V_0 = 12.5$ m/s and $\gamma = -19.7^\circ$	148
3.11	Comparison of blade loading at $V_0 = 12.3$ m/s and $\gamma = 9.9^\circ$	149
3.12	Comparison of blade loading at $V_0 = 15.9$ m/s and $\gamma = -17.2^\circ$	150
3.13	Comparison of blade loading at $V_0 = 15.9$ m/s and $\gamma = -30.1^\circ$	151
3.14	Comparison of blade loading at $V_0 = 6.1$ m/s and $\gamma = -35.4^\circ$	152
3.15	Comparison of blade loading at $V_0 = 7.8$ m/s and $\gamma = 21.4^\circ$	153
3.16	Comparison of blade loading at $V_0 = 6.7$ m/s and $\gamma = -38.2^\circ$	154
3.17	Comparison of blade loading at $V_0 = 6.8$ m/s and $\gamma = -18.7^\circ$	155

3.18 Comparison of blade loading at $V_0 = 9.9$ m/s and $\gamma = 21.9^\circ$	156
3.19 Comparison of blade loading at $V_0 = 10.3$ m/s and $\gamma = 41.4^\circ$	157
3.20 Comparison of blade loading at $V_0 = 12.5$ m/s and $\gamma = -21.2^\circ$	158
3.21 Angle of attack for UAE Phase II at $V_0 = 15.9$ m/s & $\gamma = -30.1^\circ$.	161
3.22 Comparison of the Kirchhoff flow model with wind tunnel data	162
3.23 Angle of attack for UAE Phase IV at $V_0 = 12.5$ m/s & $\gamma = -21.2^\circ$.	162
4.1 Coordinate system attached to rotating blade	169
4.2 Illustration of assumed change in pressure due to 3-D effects	176
4.3 Comparison of power coefficient for NREL UAE Phase IV turbine .	178
4.4 Comparison of generated power for MOD-OA turbine	178
4.5 Comparison of 3-D blade loading at $V_0 = 6.7$ m/s and $\gamma = -38.2^\circ$.	181
4.6 Comparison of 3-D blade loading at $V_0 = 12.5$ m/s and $\gamma = 0.4^\circ$.	182
4.7 Comparison of 3-D blade loading at $V_0 = 15.9$ m/s and $\gamma = -17.2^\circ$	183
4.8 Comparison of 3-D blade loading at $V_0 = 12.3$ m/s and $\gamma = -0.2^\circ$.	184
4.9 Comparison of 3-D blade loading at $V_0 = 10.5$ m/s and $\gamma = 1.3^\circ$.	185
4.10 Comparison of 3-D blade loading at $V_0 = 19.2$ m/s and $\gamma = 1.6^\circ$.	185
4.11 Comparison of 3-D blade loading at $V_0 = 12.5$ m/s and $\gamma = -19.7^\circ$	186
4.12 Comparison of 3-D blade loading at $V_0 = 12.3$ m/s and $\gamma = 9.9^\circ$.	186
4.13 Comparison of 3-D blade loading at $V_0 = 15.9$ m/s and $\gamma = -30.1^\circ$	187
4.14 Comparison of 3-D blade loading at $V_0 = 9.9$ m/s and $\gamma = 21.9^\circ$.	187
4.15 Comparison of 3-D blade loading at $V_0 = 10.3$ m/s and $\gamma = 41.4^\circ$.	188
4.16 Comparison of 3-D blade loading at $V_0 = 12.5$ m/s and $\gamma = -21.2^\circ$	188
4.17 Calculated separation point at $V_0 = 15.9$ m/s and $\gamma = -17.2^\circ$. . .	191
5.1 Definitions of tower shadow and its parameters	197
5.2 Drag coefficient for circular cylinders	198
5.3 Power coefficients with and without tower shadow effects	200
5.4 Calculated wake at $\lambda = 5$ and $\gamma = 30^\circ$	201
5.5 Low resolution tower shadow effect at $V_0 = 12.5$ m/s and $\gamma = 0.4^\circ$.	202
5.6 Low resolution tower shadow effect at $V_0 = 10.5$ m/s and $\gamma = 1.3^\circ$.	203

5.7	Low resolution shadow effect at $V_0 = 15.9$ m/s and $\gamma = -17.2^\circ$	204
5.8	Low resolution shadow effect at $V_0 = 12.5$ m/s and $\gamma = -19.7^\circ$	204
5.9	Low resolution shadow effect at $V_0 = 12.3$ m/s and $\gamma = 9.9^\circ$	205
5.10	Low resolution shadow effect at $V_0 = 15.9$ m/s and $\gamma = -30.1^\circ$	205
5.11	Circular arc line vortex of near wake	210
5.12	Comparison of Beddoes' original model with its modified version	212
5.13	Application of the near wake model to tower shadow problem	215
5.14	Numerical flow chart with tower shadow effects	217
5.15	Contour of C_n at $V_0 = 12.5$ m/s and $\gamma = 0.4^\circ$	219
5.16	High resolution tower shadow effect at $V_0 = 12.5$ m/s and $\gamma = 0.4^\circ$	220
5.17	High resolution shadow effect at $V_0 = 15.9$ m/s and $\gamma = -17.2^\circ$	221
5.18	High resolution shadow effect at $V_0 = 12.5$ m/s and $\gamma = -19.7^\circ$	221
5.19	High resolution shadow effect at $V_0 = 12.3$ m/s and $\gamma = 9.9^\circ$	222
5.20	High resolution shadow effect at $V_0 = 15.9$ m/s and $\gamma = -30.1^\circ$	222
5.21	Angle of attack around shadow at $V_0 = 12.3$ m/s and $\gamma = 9.9^\circ$	223
5.22	Comparison between high and low resolution calculations	223
5.23	Effects of tower shadow velocity deficit	225
5.24	Effects of tower shadow width	226
5.25	High resolution shadow effect with $B_t = 5D$	226
6.1	Approximation of the body surface by panel elements	232
6.2	Illustration of the Glasgow University wind tunnel	236
6.3	Panel discretisation of the wind tunnel	237
6.4	Numerical procedure for the wall interference calculation	243
6.5	Downstream convection of turbine wake at $\lambda = 4$ in head-on flow	246
6.6	Downstream convection of turbine wake at $\lambda = 5$ in head-on flow	247
6.7	Radial expansion of wind turbine wake at $\lambda = 4$ in head-on flow	247
6.8	Radial expansion of wind turbine wake at $\lambda = 5$ in head-on flow	248
6.9	Downstream convection of wind turbine wake at $\lambda = 5$ and $\gamma = 20^\circ$	249
6.10	Radial expansion of wind turbine wake at $\lambda = 5$ and $\gamma = 20^\circ$	250

6.11 Calculated mass flows in the modelled wind tunnel	251
6.12 Velocity normal to the modelled wind tunnel wall	253
A.1 Illustration of velocity induced by a straight-line vortex	266
B.1 Phases III and IV blade twist	269
B.2 NREL S809 aerofoil aerodynamic data	271

Chapter 1

Introduction

1.1 Brief Introduction to Wind Energy

1.1.1 Status and Prospects for Wind Energy

Wind Energy Resource

Wind energy is a sustainable and inexhaustible source of energy. It is ultimately a solar resource, created primarily by temperature differences, resulting from solar radiation, among the sea, land, and air, and by the overall temperature gradient that exists from the equator to the poles. About 0.25 percent of total solar radiation reaching the lower atmosphere is transformed into wind energy, which is then dissipated at a rate of about 30 times human energy consumption.

Only a small fraction of wind resource can be exploited in practice because of technical and social constraints. Limits imposed by technology include cut-in and cut-off at certain wind speeds, conversion efficiency of wind turbines, their height, and the interference between turbines in wind farms, a phenomenon known as array loss. Therefore, the amount of wind energy available for capture by wind turbines is determined by a number of factors and it is difficult to estimate accurately the potential of wind energy in the world. Nevertheless, the wind resource is vast even approximately estimated in its simple form.

According to a systematic and conservative approach (Grubb and Meyer 1993), the world wind energy utilisable for electricity generation is approximately 50,000 TWh/annum. In this method, the first order exclusions, which reflect indisputable constraints from cities, forests, unreachable mountain areas, and the like, are subtracted, and the second order exclusions, which come from social, environmental, and land-use constraints, are also considered. If any land which has a mean wind speed greater than 5.1 m/s is potentially exploitable and only 4 % of that land could be used as a result of practical and social constraints, in a more conservative approach (van Wijk and Coelingh 1993), the world wind energy available for electricity generation is approximately 20,000 TWh/annum (Table 1.1). Both of these figures exclude the offshore potential and are well in excess of 12,500 TWh/annum, the world consumption of electricity in 1994 (European Commission Directorate-General for Energy 1998).

Table 1.1: Wind Energy Potential

Region	TWh/annum (Grubb and Meyer 1993)	TWh/annum (van Wijk and Coelingh 1993)
Africa	10,600	-
Australia	3,000	1,638
North America	14,000	3,762
Latin America	5,400	-
Western Europe	480	520
Eastern Europe and CIS	10,600	-
Rest of Asia	4,900	-
Total OECD	-	6,351
Approximate world total	50,000	20,000

Wind Energy Status

Wind energy has been utilised for several thousands of years. Probably the oldest preserved documentation of such a deployment is a 5,000 year old drawing of a Nile river boat equipped with a sail to produce translational motion (Aspliden *et al.* 1981). The first wind energy conversion devices appeared in ancient Persia as early as 300 to 200 B.C. for grinding grain (Eldridge 1980). Wind turbines have since then been used in variety of aspects, such as water pumping to irrigate fields and to drain shallow lakes for the purpose of claiming land, and power providing for mills, etc.

Modern use of wind energy began in the late 1970s as part of response to the oil crises in 1973 and 1979, which drew the world's attention to the importance of exploiting renewable energy sources. Many research and development programmes were launched with governmental support. As a result of progress in wind technology, the wind power market began to thrive. Wind energy, as a renewable and sustainable source of energy, is now the fastest growing energy technology worldwide.

Between 1990 and 1997, according to Flavin and Dunn (1998) of the Worldwatch Institute, wind energy was by far the fastest growing energy source at a rate of more than 25% (see Table 1.2), leading to a total installed capacity of almost 8,000 MW in 1997 (Gipe 1998, Swisher 1998).

The key factor in this growth has been attributed to European policy. Of the world's 1,292 wind turbine installations recorded in 1996, more than 80% were supplied from European manufacturers. The demand side of the wind energy market is also dominated by European countries; in 1996, 75% of the world's installations were in Europe and, in 1997, 84% of the world's new wind capacity was installed in Europe (Bourillon 1999, Swisher 1998). In the space of fifteen years, European wind technology has evolved from an industry making small, simple wind machines

Table 1.2: Global Trends in Energy Use, 1990–1997

Energy Source	Annual Rate of Growth
Wind Power	25.7%
Solar Power	16.8%
Geothermal Power	3.0%
Natural Gas	2.1%
Hydroelectric Power	1.6%
Oil	1.4%
Coal	1.2%
Nuclear Power	0.6%

into a technology which can compete with the well established forms of power generation. The boom in wind energy markets is continuing in Germany, Denmark, the Netherlands, the United Kingdom, and Spain, etc.

German developers installed more than a billion DM of new wind turbines in 1997, pushing total installed capacity in Germany to more than 2,000 MW, nearly 25% more than currently still operating in California and thus displacing the U.S.A. as the world's largest installed capacity. In the first six months of 1998, Germany added another 300 MW and projected 770 new MW for the entire year.

The performance of the Danish market surprised even optimistic analysts. In 1997 Denmark installed more than 300 MW of new wind capacity, bringing total installed capacity to about 1,100 MW. By mid 1998, the total installed capacity in Denmark had increased to more than 1,300 MW. Wind turbines in Denmark generated about 1.1 TWh in 1997 which is equivalent to 5.6% of total Danish electricity generation. With the turbines added in 1997, Denmark will satisfy about 7.5% of its electricity consumption with wind energy.

In California, where the first significant commercial wind market of the world appeared, 400 MW of new capacity was installed in 1985. The California wind farming experience greatly helped the international wind energy industry to develop. In 1991 the cumulative wind capacity in California reached its peak, 1,700 MW (Gipe 1995). Since then, the capacity has declined 11%, and the total number of turbines in service has fallen 21% (Gipe 1998), mainly due to the expiry of the federal energy tax credits and the 10% federal investment tax credit at the end of 1985. Small amounts of yearly added capacity, for instance, 11 MW in 1997, and small repowerings (replacement of older wind turbines by new machines on the same wind site) were unable to reverse the trend. However, the US wind market will increase markedly in 1998/99, when anticipated growth is as much as 800 MW/year of new and repowered capacity (Swisher 1998). More than US\$500 million of new projects are scheduled for installation in the USA by mid-1999, not including a spate of potential repowerings in California (Gipe 1998).

China and India take the lead in wind application in Asia. With the introduction of a package of incentives to renewables including wind power generation by the Government, the growth of wind energy installations in India has been fairly rapid since 1992. A wind capacity of 230 MW was installed in 1994–95, 382 MW in 1995–96 and 170 MW in 1996–97 (Kumar 1999). Although the rate of growth has been slowed down due to the customary instability of the Cabinet, the total wind capacity reached 930 MW in 1997, an absolute leading position in Asia.

China is the largest small wind turbine generator manufacturer in the world. By the end of 1997, more than 147,000 wind-driven battery-chargers had been installed throughout the country's remote areas. The country's first grid-connected wind farm was built in 1986 (Han 1999). However, the development of wind farms in China was slow until the mid-1990s when the speed-up was stimulated by strongly supported governmental programmes, *i.e.* *Program on New and Renewable Energy Development in China from 1996 to 2010* and *China's Agenda 21*. By the end of 1997, the total installed capacity amounted to 166 MW, 109 MW of which was

installed in 1997 (Han 1999, Li and Zhu 1999). These figures do not include the contribution from small-sized wind turbine generators distributed in countryside areas.

Economics of Wind Energy

With the development of wind technology, the cost of wind energy plant has fallen substantially during the last fifteen years, and this trend is continuing. Wind energy prices have fallen even faster due to lower wind turbine prices, higher efficiency, and lower operation and maintenance costs. Wind turbine prices fell by a factor of at least three from 1981 to 1991, and the energy prices have halved in the last 9–10 years (Bourillon 1999). Wind power is already cost competitive with conventional sources of electricity generation under some conditions.

The unit cost of the wind energy produced by grid-connected wind farms depends on a number of parameters, such as installed cost (ex-factory cost of wind turbines, project preparation costs, and cost of the infrastructure, etc.), annual operation and maintenance cost, technical lifetime, annual net energy output (annual average wind speed at the wind farm), and fixed charge rate (cost of taxes, insurance, interest on debt, and rate of return on equity). Results from field operation in Denmark and California (Cavallo *et al.* 1993) have demonstrated that, in areas with good wind resources (450 W/m^2 wind power density at hub height), wind turbines generated electricity at a cost of US\$0.053 per kWh (6 percent interest, all taxes neglected). With mature wind turbine technology, the cost is expected to decline to US\$0.029 per kWh, rendering wind-generated electricity fully competitive with electricity from coal-fired generating stations. Sesto (1999) calculated the current cost of wind energy in Western Europe to be between 5 and 10 cECU/kWh, depending on the choice of the amortisation period and the real interest rate. Gipe (1995) shows a falling trend for the cost of wind energy, indicating that the cost of energy from California wind plants fell from nearly US\$0.45 per kWh in the early 1980s to less than US\$0.10 per kWh in the early 1990s, and was expected to

reach US\$0.05 per kWh in 1996. Price comparison of wind energy with the other conventional energy within European Union is shown in Fig. 1.1 (European Commission Directorate-General for Energy 1998), where the electricity energy prices have been derived using a 5% discount rate – to correspond with one set of wind price estimates. From this figure, the price of wind energy is already lower than that of nuclear energy, while still somewhat higher than the electricity prices for coal and gas in terms of the average value.

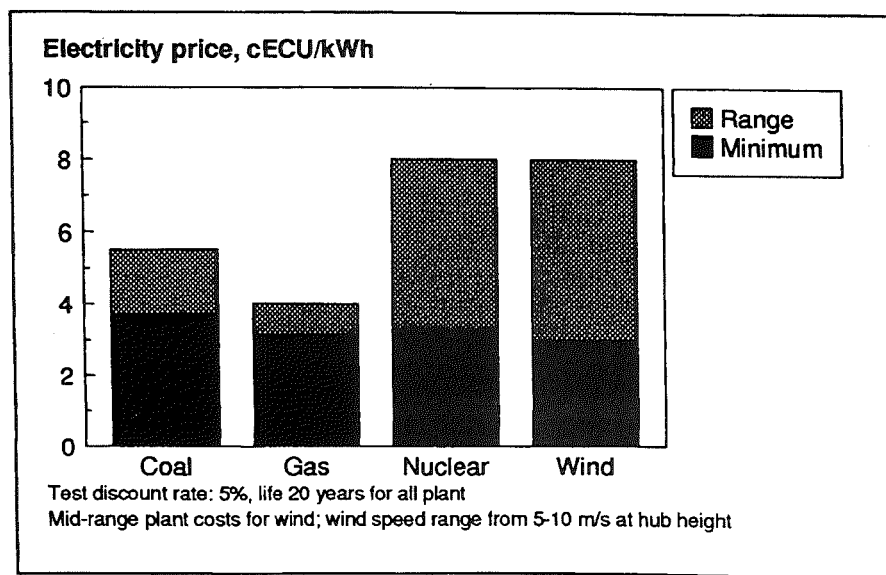


Figure 1.1: Comparison of electricity prices

Public Attitudes towards Wind Power

Wind energy as a renewable energy source has more credibility with the public than non-renewables such as fossil fuels and nuclear power (Breglio 1995). In a British analysis (Simon 1996) the typical arguments for wind power are summarised as follows:

- renewable energy is very much an alternative to other energy sources
- the climate change must be taken seriously

- wind energy is limitless unlike fossil fuels
- wind energy is non-polluting
- wind energy is safe

People with a high degree of knowledge about energy generation and renewables tend to be more positive about wind power than those with little knowledge. Surveys conducted in other countries (Krohn and Damborg 1999, Simon 1996, Omnibus Report 1995, Gipe 1995) obtained the same result that about 80% of the population were in favour of wind energy while only very small portion has opposite opinions.

One of the critiques is that development of wind energy precludes use of the land for other purposes. To the contrary, wind turbines are compatible with most land uses. The structures of a wind power plant actually take up only about 1% of all land concerned; therefore, 99% of the land in question can be left in agricultural use or remain a natural habitat (Sesto 1999). In a study intended specifically to address wind energy's land-use impact (Fulton *et al.* 1984), landscape architects at California note that "it is important to emphasise that WECS (wind energy conversion systems) do not constitute a singular use of the land, as most other energy generation sources do. Grazing, recreation and numerous other activities can occur in and around wind farms." In fact, they recommend deliberately choosing sites that offer the possibility of multiple uses in preference to using sites where only wind energy is suitable. Grasslands, for example, allow both wind turbines and grazing, and locations of dispersed ORV (off-road vehicle) use and hiking are also good choices.

The most frequently mentioned objection to the use of wind energy is the perceived aesthetic impact that wind turbines have on the rural vista. While some people have in mind that wind turbines spoil the scenery, others believe that wind farms can symbolise the hope for a better visual environment. The trend

appears that modern wind turbines are gradually becoming an accepted part of the cultural landscape (Krohn and Damborg 1999, Hammarlund 1997, Gipe 1995).

Next to aesthetic impact, no aspect of wind energy creates more alarm or more debate than noise. Absolutely, wind turbines are not silent. Researchers and manufacturers have made efforts to reduce the levels of aerodynamic noise by the design of new aerofoils, reducing tip speeds, and treating trailing and tip edges, etc. and of mechanical noise by redesigning the gearbox and adding resilient couplings in the drivetrain to isolate vibrations, etc. Public surveys in Denmark, the Netherlands, and Germany show, interestingly, that the annoyance caused by wind turbine noise affects few people and the level of annoyance is hardly related to the actual sound level of specific turbines. Instead, people living close to wind turbines do not consider noise to be a significant problem. As a matter of fact, people living closer to the nearest wind turbine than 500 metres tend to be more positive about wind turbines than people sited further away from the turbines (Krohn and Damborg 1999).

Wind turbines have little or no impact on most plants and animals, but they have killed some birds. No single environmental issue has caused more consternation among wind energy advocates and environmentalists alike than the existing or potential effects that wind turbines have on birds. The bird problem has attracted many researchers, see Musters *et al.* (1996) and Tucker (1996). U.S. DOE's biologists revealed that even on nights of high migration of birds, a single turbine would not be lethal to a significant number of birds, but they did observe a number of birds changing course to avoid the turbine. David *et al.* (1997) investigated bird collisions with turbines on a semi-offshore wind farm, where 5,000 birds daily moved, and concluded that the rate of collisions with the wind turbines in their 5 years of operation had been 1.2/turbine/year. In a recent assessment (Percival 1999), the ecologist concludes that "there are now numerous examples where it has been shown that wind farms have not had any adverse effect on bird

populations". That some wind turbines kill birds some of the time should come as no surprise. Most tall structures kill birds to some degree, as do most sources of energy. Nevertheless, this issue must be treated extensively.

Perspective

Wind energy as a clean and inexhaustible source of energy has been drawing more and more attention from the public and governments due to the growing concern about environmental problems and greenhouse effects, not to mention the fear that the fossil fuels will possibly be used up soon due to increasing exploitation of their limited reserves in the coming decades. Provided that future policies evidence a more caring attitude towards the environment, prospects of more widespread development in wind energy appear promising, although extensive production of significant amounts of electricity by wind farms is conditioned by a number of social, environmental, and technical factors.

Under some conditions and with good wind sources, as mentioned above, wind power is already cost competitive with conventional sources of electricity generation. In fact, not all costs of conventional power generation are reflected in the price of electricity. Environmental impacts from conventional sources, such as air pollution from fossil-fuelled plants and radiation from nuclear plants, impose costs on society at large. Even though the pollutant emissions meet society's accepted limits, they still extort a social or environmental cost, for example through additional sickness and death. At the same time that these costs are not reflected in the price of conventional sources of generation, the air quality benefits of wind-generated electricity are not incorporated into its purchase price.

Wind energy offers one of the cheapest renewable energy options for reducing CO₂ emissions from electricity generation. For instance, the US electricity industry remains the largest single industrial source of pollution in the US, accounting for 35% of CO₂, 66% of SO₂, 30% of NO_x, and 21% of mercury (Swisher 1998).

Therefore, replacement of a small part of the electricity generated from fuels could result in a sizeable amount of pollutant reduction.

According to Bourillon (1999), wind energy already avoids over 6,300,000 tons of CO₂, 21,000 tons of SO₂, and 17,500 tons of NO_x emissions per year in the EU alone. Wind energy has the capacity to avoid over 28,000,000 tons of CO₂, 94,000 tons of SO₂, and 78,000 tons of NO_x emissions per year outside the EU by 2005, and could reduce EU power sector CO₂ emissions by over 11% by 2040. Furthermore, wind energy does not create any dangerous waste by-products.

The generation of electricity from wind is and will be a rapidly growing industry. Additions of significant capacity and subsequent growth first occurred in California in 1980s, then in western Europe and now in Asia. There are definite signs that the next nucleating areas will be in eastern Europe and the southern region of South America (Twidell 1998). If the political will to address the environmental aspects of energy production continues to grow, the prospects for the wind energy industry are good. Worldwide wind capacity could increase from 7,200 MW in 1997 up to 60,000 MW by 2010 with a good percentage (20%) offshore 12,000 MW (Gaudiosi 1999).

Europe will continue the wind energy development lead. As long ago as 1991 the European Wind Energy Association (EWEA) calculated that the development of wind energy on a European basis at a responsible rate would yield 4,000 MW by the year 2000. Given that by the end of 1997 over 4,000 MW had been installed, EWEA has had to revise its target, doubling its earlier goal to 8,000 MW by the year 2000 (see Table 1.3). Thus, wind energy could supply about 10% of the electricity requirement in Europe by 2020. North European countries such as Denmark, the Netherlands, and the United Kingdom as well have already begun looking closely at their offshore wind resources. 8,000 MW of large sized turbines has been set as an offshore objective for 2010 by the European Commission (Gaudiosi 1999).

Table 1.3: EWEA Targets

Year	Old Targets (MW)	New Targets (MW)
2000	4,000	8,000
2005	11,500	-
2010	25,000	40,000
2020	-	100,000
2030	100,000	-

Source: European Commission Directorate-General for Energy (1998)

The US wind market, which was once the largest in the world and has been stagnant in recent years, is expecting an upturn; 5,000 MW of new growth is projected in the US over the next decade (Swisher 1998). Meanwhile, repowering of California's ageing wind plants may finally be getting underway. The AWEA released its white paper (AWEA 1997) just prior to the announcement of the UN Kyoto Protocol and emphasised that, with strong policy support, the wind industry is capable of achieving 30,000 MW of capacity in the US by 2010.

Asian countries have set up their ambitious targets in development of wind energy. China has mapped out a target of 1,000 MW for grid-connected wind power development by 2000 and 3,000 MW by 2010 respectively. In order to achieve these goals the Chinese Government encourages international investment in wind farm development. For example, the World Bank and Chinese Government have reached an agreement to develop 190 MW of wind farms in China by the year 1999 (Han 1999). The future of the wind energy sector in India looks very bright. It is envisaged to generate about 2,000 MW of power through wind by early 2002 with a new capacity of 400 MW per year in the next few years (Kumar 1999). With this, India would become one of the largest producers of wind power in the world.

Although the worldwide market for small wind turbines has not received as much attention, there is growing recognition that the market for small wind turbines is becoming increasingly attractive. A market projection by Jamieson (1998) shows a five-fold increase in the small turbine market by 2005.

Wind energy has become one of the most economically practical as well as the most technically and environmentally promising renewable energy options. The increasing reliability of wind turbines and growing penetration of worldwide markets mean that the future for the wind technology is bright.

1.1.2 Wind Turbine Technology

Experience with modern wind turbine technology commenced in the 1970s. In almost all aspects, wind turbine technology started as an application technology borrowed from other fields of technology. Now wind turbine technology has developed to a stage where it is considered to be an authentic, highly multi-disciplinary technology based on modern mechanics, material science, and sensoric techniques with widespread use of microcomputers as well as integration of new simulation and production techniques (Martinez and Prats 1999, van Kuik 1997). Modern wind turbine technology shows maturity of behaviour, offering the fulfilment of the following general characteristics:

- *simplicity*, in the sense of offering a product of reduced complexity and hence increasing reliability
- *reliability*, for performing long-term operation without intervention
- *efficiency*, for improving energy production
- *robustness*, to demonstrate survival in extreme external conditions
- *quietness*, to be used near other uses without impact

- *safety*, to have full confidence in the internal behaviour of the system
- *durability*, to provide the required profitability without future expenses
- *compatibility*, as a reduction of secondary effects of the turbine

Great progress has been made in wind turbine design and analysis. Specific engineering for wind turbines has been established. With the development of wind turbine technology, it may be possible to make significant improvements to the wind energy industry.

Wind Turbine Configurations

Wind turbines can be classified in several ways, for example, the way in which the wind energy is extracted, namely lift or drag type devices. But most commonly, wind turbines are categorised in terms of their axis of rotation relative to the wind stream, being labelled as:

1. *Horizontal Axis Wind Turbine* – HAWT

- This device has its axis of rotation parallel to the direction of the wind stream.

2. *Vertical Axis Wind Turbine* – VAWT

- For this device the axis of rotation is perpendicular to both the earth and the wind stream.

3. *Cross-wind Axis Wind Turbine* – CAWT

- This device has its axis of rotation parallel to the earth surface and perpendicular to the wind stream.

CAWTs have not been widely used due to the technical difficulty of turning the device into the wind as the wind direction changes. Some examples of this class can be found in de Vries (1979a) and Eldridge (1980).

VAWTs offer advantages over their counterparts, HAWTs, in some respects. For example, they do not need yaw control due to their vertical configuration. On the other hand, VAWTs do not usually self-start, and due to the 360 degree rotation of the blades with respect to the wind direction in operation, experience reversing aerodynamic loads (Touryan *et al.* 1987, Sutton-Vane 1988). VAWTs include Savonius, Darrieus, straight-bladed, and V-type turbines (Fig. 1.2).

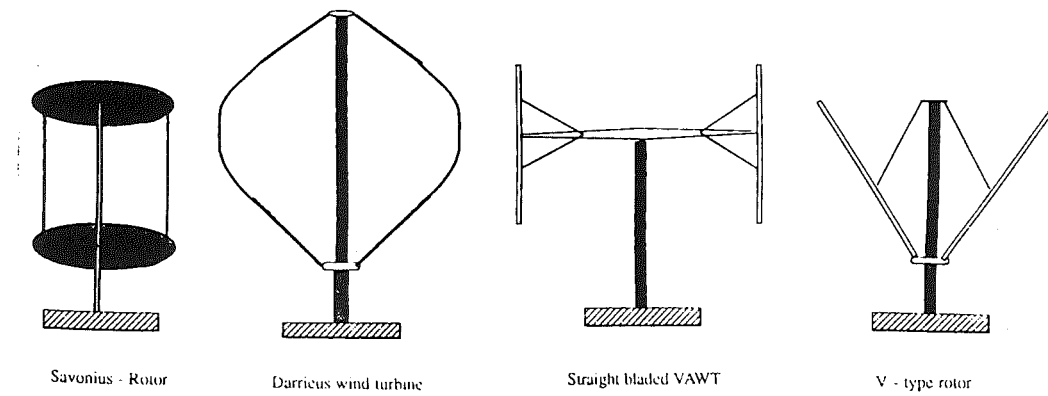


Figure 1.2: Schematic of typical vertical axis wind turbines

HAWTs can further be classified according to the placement of rotor, *i.e.* upwind or downwind of the tower (Fig. 1.3). Rotors for HAWTs have been built with various numbers of blades ranging from one (Stork and Solmi 1991) to more than twenty. A large number of blades results in a high solidity which provides a high starting torque. This is particularly useful for water pumping purposes, where turbines have typically about 24 blades (Aspliden *et al.* 1981). HAWTs for electricity generation are usually of low solidity mostly with two or three blades.

The upwind HAWT requires an active yaw control system to achieve orientation into the wind while free yaw, or passive orientation with the wind direction, is possible with the downwind type. The downwind configuration also allows blades to deflect away from the tower as rotor thrust loading increases. Coning can be eas-

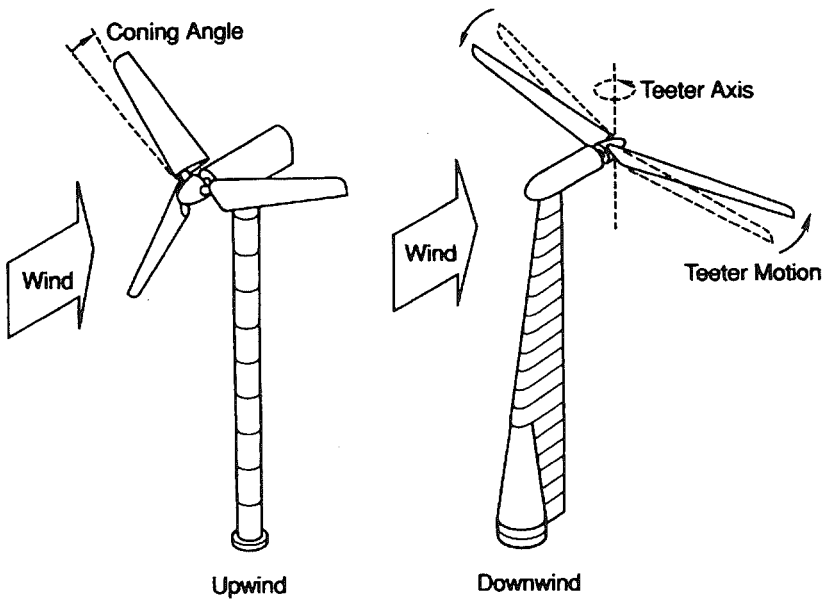


Figure 1.3: Schematic of horizontal axis wind turbine configurations

ily introduced to decrease mean blade loads by balancing aerodynamic loads with centrifugal loads for downwind turbines. Some early downwind turbine designs developed a distinction for generating noise as the blades passed through the tower shadow. Most downwind turbines operating today have greater tower clearances and lower tip speeds which result in negligible infrasound emissions (Kelley and McKenna 1985). Nevertheless, for the downwind HAWT, the blade and rotor experience additional dynamic loads when the blade passes through the tower wake. This kind of tower shadow effect is minimal for upwind HAWTs.

Wind Turbine Trends

Reviewing the development during the last few years, it is easy to detect a trend towards a horizontal axis machine with three blades and a cylindrical tower (Martinez and Prats 1999).

HAWTs have been more widely used than VAWTs. For example, only 3% of the turbines installed in California are VAWTs (Hansen and Butterfield 1993).

Wind turbines are becoming larger. During 1980s, when about 15,000 wind turbines were installed in California, the size of the average wind turbine generator (WTG) increased from 55 kW to 100 kW. The *standard Danish design*, which consisted of a three-bladed, upwind, stall-regulated rotor, was optimised and scaled up to 250 kW, thus making turbines more cost effective. The increase in available rated capacity by about a factor of 3 from 500 or 600 kW to 1.5 MW is striking and has been a very rapid development (Bourillon 1999). Exploitation of offshore wind energy requires the development of megawatt scale turbines.

In the USA downwind turbines were favoured initially, but the trend has been toward greater use of upwind rotors with current proportions of 55% upwind and 45% downwind configurations.

Aerofoil Design and Blade Construction

Early wind turbine blade aerofoils were taken from general aviation handbooks, e.g. *Theory of Wing Sections* (Abbott and von Doenhoff 1959). Among them the NACA 44xx and NACA 230xx families were popular turbine aerofoils owing to their high maximum lift coefficients ($C_{l\max}$) and low drag coefficients ($C_{d\min}$). Wind turbine designers felt that minor differences in aerofoil characteristics were far less important than optimising blade twist and taper (Hansen and Butterfield 1993). For this reason little attention was paid to the aerofoil selection.

However, there are differences in requirements regarding aerofoil characteristics between wind turbine designs and aircraft designs. While aerofoils for pitch-controlled rotors should have high $C_{l\max}$ to maintain high power efficiencies over a wide range of wind velocities, stall-controlled blades require aerofoils with restrained $C_{l\max}$ in their tip region to limit the peak power output in order to reduce generator damage or electrical breaker activation. Moreover, when the blades accumulate smog, dirt, and insects along the leading edge, power output

can drop to 40% of its clean value, resulting in a significant loss of energy (Clark and Davis 1991, Eggleston 1991, Yekutieli and Clark 1987). Therefore, The aerofoil LS(1) MOD (McGhee *et al.* 1979) and the NACA 63₂-xx have been chosen for wind turbine blades for their insensitivity to leading edge roughness. Specific aerofoil design techniques have been developed and new aerofoils have been designed for wind turbines (Tangler and Somers 1995, Dini *et al.* 1991, Eppler 1990). It has been verified in field tests that annual energy improvements from the NREL aerofoil families are 23% to 35% for stall-regulated turbines and the annual energy improvements with the NREL aerofoils are projected to be 8% to 20% for variable-pitch turbines and 8% to 10% for variable-rpm turbines, respectively (Tangler and Somers 1995).

Construction of a reliable blade with a long lifetime appeared to be very difficult for the first generation turbines; many designs failed. In particular, fatigue damage was under-estimated. A wind turbine experiences a considerably high number of fatigue cycles up to the order of 10^9 , while for aircraft designs the number of fatigue cycles has the order of 10^6 (van Kuik 1997). Therefore, significant modifications to the blade designs were necessary (Scherer 1999). Glass fibre with reinforced polyester and foam has now become a common construction material for wind turbine blades.

Design and Analysis

Since modern use of wind energy began in 1970s, research workers have played a vital role in the development of mathematical models which can represent the behaviour of wind turbines. This work has involved extensive measurement and model validation activities.

Aerofoils and Rotor Aerodynamics

There has been extensive research in this area. Special aerofoils for wind turbines have been designed not only for structural and construction requirements but also to improve rotor performance.

Great progress has been made in the analysis of wind turbine performance and characteristics through theoretical research and experimental investigation. However, the general understanding of the development of aerodynamic stall on a rotating wind turbine remains poor and the modelling of stall is considered to be the most significant inadequacy of current design and calculation methods. The requirement to understand details of the flow around the turbine requires further development in computational fluid dynamics (CFD) tools.

Aspects of wind turbine aerodynamics will be discussed in detail in Section 1.2.

Dynamics and Structural Analysis The dynamic structural loads experienced by a wind turbine play the major role in determining the lifetime of the turbine. Estimation of dynamic loads is the most difficult, though the most important, task facing the user of wind turbine aerodynamic models. The stochastic nature of the wind, flexibility of the wind turbine structure, a need to minimise the weight of the structure, and the unsteady, three-dimensional character of the flow all combine to make accurate determination of the structural response impossible (Hansen and Butterfield 1993). Recent progress in wind turbine dynamic and structural analysis can be found from Veers and Winterstein (1998), Henderson and Petel (1998), Quarton (1997) and Chaviaropoulos (1996). Further research efforts will be required in this context in order that the design tools can be used to undertake reliable calculations of the coupled modal properties, aeroelastic stability and loading of wind turbines with flexible components exhibiting large deflections.

Aeroacoustics Another very important topic is the acoustic noise produced by the wind turbine. Research on wind turbine aeroacoustics has been both theoretical and experimental (Fuglsang and Madsen 1998, Lowson 1994, Dawn 1994, Lowson 1992, van der Borg and Stam 1989). Better insulation of the nacelle and reduction of the aerodynamic noise have been achieved. The effects of the aerofoil shape and thickness on the emission of turbulent inflow noise have been

investigated. The study of the noise caused by different acoustic tip shapes has also contributed to noise reduction (Gipe 1995). All these, plus other measures, resulted in a significant noise reduction of about 10 dB(A) from 1989 to 1995 (van Kuik 1997).

1.2 Aerodynamics of Wind Turbines

The development of ancient windmills was based on empiricism and engineering skills. The study of the aerodynamics of windmills, wind turbines in modern usage, was begun after World War I by Betz (1926) and Glauert (1935) and spurred on by the modern use of wind turbines. Due to the similarities in their flowfields, many analysis and design methods for wind turbines were transformed with appropriate modifications from helicopter and propeller research. Nowadays, wind turbine aerodynamics is a worldwide field of research and greatly helps the development of the wind industry at large.

This section only discusses the aerodynamics of HAWTs, but many aspects of HAWT aerodynamics are applicable to VAWTs as well. Details of VAWT aerodynamics can be found in many articles, for example, de Vries (1979a), Basuno (1992), and Marini *et al.* (1992).

1.2.1 Theories and Models

The flow past a wind turbine is particularly complicated for several reasons. *First*, wind turbines operate in extremely unsteady circumstances. Both wind speed and wind direction can change frequently and very rapidly. Also, wind turbines always experience high turbulence and wind shear. *Second*, unlike the case of flow over a fixed wing, which can often be analysed by linear aerodynamics, the flow past a wind turbine is *never* what aerodynamicists consider to be “linear”. This presents significant problems in modelling since numerical simulations need to be iterative

in character and experimental observations of highly nonlinear phenomena are often difficult to interpret because of their complexity. *Third*, wind turbines may suffer more severe interactions. For a downwind turbine, the tower produces a dynamic wake which the rotor blade passes through every revolution. A wind turbine in a wind farm operates in complex wakes produced by other turbines. *Fourth*, blade angle of attack may be very high, especially for stall-regulated wind turbines. In addition to dynamic inflow, a wind turbine encounters both deep static stall and dynamic stall much more frequently than a fixed wing. *Finally*, there exist difficulties in experiment. For field tests, the extremely unsteady operational environment not only requires the data acquisition system to have an appropriate dynamic response but also makes the collected data difficult to resolve appropriately into individual aspects. For wind tunnel experiments, the wind tunnel wall interference remains a major difficulty in obtaining reliable data, which will be discussed further in Section 1.2.6.

Blade Element/Momentum Theory

The most simplified theory for wind turbine performance analysis is the so-called blade element/momentum (BEM) method. BEM methods were and still are popular for wind turbine designers owing to two factors. First, the methods have been proven accurate in gross performance analysis for a wide variety of turbines and flow conditions. Second, they are simple to learn and use and are readily implemented on virtually any desktop computer.

Analysis of the fluid mechanics of the wind turbine began by drawing an analogy with the study of propellers and helicopter rotors in climb or descent. The difference between them is that a wind turbine *extracts* energy from the flow whereas a propeller or helicopter rotor *imparts* energy into the flow.

Rankine (1865) developed a simple model of a propeller flowfield by applying linear momentum theory derived from the basic relationships of Newtonian mech-

anics. The representation of a propeller by a disc at which there is a sudden change in pressure without any discontinuity of velocity was introduced by Froude (1889) and is generally known as Froude's actuator disc. Glauert (1935) extended this one-dimensional Rankine–Froude flow to two-dimensional flow including rotational motion and applied the momentum theory – blade element theory combination to analyse the flows around propellers, helicopter airscrews, windmills and fans.

Significant progress was made in use of BEM methods for wind turbines by Wilson and Lissaman (1974). Their FORTRAN computer code PROP soon became so popular that almost every wind turbine designer knew of the program name although the method broke down at high speed ratios and the iteration in the program could be divergent for turbines of high solidity. The basic method assumes that the blade can be analysed as a number of independent elements or strips. The induced velocities at each element are found by mass conservation and by performing a momentum balance for an annular control volume containing the blade element in question. The aerodynamic forces on the element are calculated using two-dimensional lift and drag coefficients at the angle of attack of the blade element relative to the local flow velocity.

Since the work of Wilson and Lissaman, BEM theory has been widely used not only in wind turbine designs (Stewart 1976, Griffiths and Woppard 1978, Larrabee and French 1983, Vick *et al.* 1988, Rijs *et al.* 1992) and performance calculations (Griffiths 1977, Viterna and Janetzke 1982, Tangler 1983, Hansen *et al.* 1990, Nathan and Yin 1990, Neogi 1995) but also in the determination of the dynamic loads on wind turbines (Powles and Anderson 1984, Hansen *et al.* 1990, Hartin 1990, Riziotis *et al.* 1996). Meanwhile, BEM methods have been improved by many researchers (Beans 1983, Jones 1983, Manwell *et al.* 1991, Ackerman 1992, Wilson and Harman 1995).

The basic formulation of the BEM method can be found in Section 1.2.2.

Vortex Wake Theory

The BEM method offers the advantage of ease of understanding and use as well as minimal computation requirements, and, with modification, often predicts the gross performance of wind turbines with acceptable accuracy (Tangler 1982). However, there are a number of situations where it is not reasonable to expect the BEM method to offer the greatest accuracy due to the assumptions and oversimplifications made in it. For example, BEM theory is not adequate to describe the airload variations in the case of a rotor passing through the wake of the tower (Miller 1985). Therefore, vortex wake theory, which has been widely used for performance and loads analysis by helicopter designers, is an alternative for wind turbine performance analysis, especially for detailed aerodynamic calculations.

In modelling the rotor wake by system of vortices, three approaches have generally been used:

- rigid wake models
- prescribed wake models
- free wake models

In the rigid wake model (Miller *et al.* 1978, Rawlinson-Smith and Hales 1990, Kotb and AbdelHaq 1992), the vortex system position is specified as a function of speed ratio and thrust. The difficulty with the rigid wake model is that expansion of the wake is not taken into account and thus the blade load calculations might not be accurate enough.

To remedy this weakness, the prescribed wake model uses experimental data or other numerical results to locate the wake position. The wake geometry is defined as a continuous set of helix filaments which carry trailed and/or shed vorticities. This method is very efficient computationally compared to the free wake method. Hernandez and Crespo (1987) assume a form and position of the trailing vorticity

wake which is in accordance with experimental observations and theoretical considerations. The vortex is supposed to move initially, near the disc, with the fluid velocity and then, at a certain distance downstream, is supposed to roll into root and tip vortices. The radial displacement of the tip vortex is determined by using the global equation of mass conservation. Kocurek (1987) developed an application of lifting surface theory to the calculation of HAWT aerodynamic characteristics and performance. The wake model is extended from a hovering rotor experimental generalisation by including the effect of the windmill brake state on the radial and axial displacement rates of the trailing vortex system. Koh and Wood (1991a) proposed a prescribed wake model for HAWTs with novel features based on the calculation of the average velocities in the far wake. At high tip speed ratios, however, the method eventually fails to converge altogether (Koh and Wood 1991b). A progress report on the development of nonlinear lifting line and lifting surface models is given by Gould and Fiddes (1992). They use constant-pitch, expanding and non-expanding wakes convected with the onset wind speed for the first 2–4 turns, and a far wake expression beyond this point. Lain *et al.* (1995) report a lifting surface-2D panel method with a prescribed cylindrical wake which is nonlinearly convected downstream. Robison *et al.* (1995) developed a novel hybrid prescribed/free wake scheme to determine the HAWT wake geometry. This method expands the potential of the prescribed wake models since other numerical results may be used for prescription of the wake structure when experimental data of wake geometry are unavailable. Also, universal wake prescription functions for wind turbines may be found if a wide variety of HAWTs are investigated through this hybrid method.

In a free wake calculation, the vortex motion is calculated directly from the effects of all the other components of the wake vortex system and the effects of the blades. In this method, the wake is allowed to develop in time. Free wake analyses are fundamentally better suited to the complex flowfields generated by wind turbines and avoid the difficulty of prescribing a wake geometry but, in so doing,

introduce more computational expense. Nevertheless, the free wake calculation has become more affordable with the development of faster computers and more efficient computational techniques. Gohard (1978) presents a full free wake model for HAWTs, in which the unconstrained wake is permitted to move freely with the local velocities that exist in the wake. Full free wake methods are used for analysis of wind turbine aerodynamics also by Sipcic and Morino (1985), Crouse and Leishman (1993), Arsuffi *et al.* (1993), and Johnson (1995). These methods require large amounts of computer time, making them somewhat impractical as a design tool. To remedy the problem, Rosen *et al.* (1990) divide the wake into two regions, near and far wakes. The calculations associated with the far wake are speeded up by extension of the approximations made by Rand and Rosen (1984), Graber and Rosen (1987) and Chiu and Peters (1988). More significant simplifications to free wake models for HAWTs are attributed to Miller (1983a, 1983b, 1984, 1985) and Afjeh and Keith (1986a, 1986b, 1989). Simoes and Graham (1992) demonstrate a simplified free vortex wake model for both attached and separate flows over the HAWT rotor. The model combines a vortex lattice representation of the flow over the blade with a free vortex near wake which is iteratively relaxed into the local flow direction. Beyond this region the near wake is joined to a simplified axisymmetric far wake. Separated flow over the blades is represented by an extension of the source wake model of Parkinson and Jandali (1970), in which the separation pressure must be specified.

The methodology associated with the application of vortex wake theory will be discussed further in Section 1.2.3.

Eulerian Descriptions of the Wake

There are two means of determining the structure of a given flow field, Lagrangian and Eulerian descriptions. In a *Lagrangian description*, individual fluid particles are advanced in time and a specified formula for the velocity field is usually taken as the starting point. In wind turbine aerodynamics, this method corresponds to

the vortex wake method.

In an *Eulerian description*, solution of the velocity field is obtained at a number of specified field points. Thus, an Eulerian description involves a grid system which is not required in a Lagrangian description. The Eulerian descriptions correspond to the *full potential methods* as well as *Navier–Stokes and Euler Methods*. In wind turbine aerodynamics, these methods usually focus on the near wake of the turbine blade which is often patched to a model for the far wake that may be a prescribed or free wake. Even so, these methods, especially in the form of Navier–Stokes (N–S) computations, are too computationally demanding and not accurate enough to be used extensively in design, not to mention difficulties associated with numerical diffusion (Conlisk 1997) and turbulence modelling (Ekaterinaris and Platzer 1997) and a number of the other numerical problems encountered in the calculations. For instance, a complete unsteady N–S solver with efficient calculation of the flow near the blade, as reported by Ahmad and Duque (1996), takes a total of 45 hours of CPU time on a Cray C-90 supercomputer. On the other hand, since the N–S equations are probably the most pivotal equations in all of theoretical fluid dynamics, this type of calculation is expected to provide the most detailed and comprehensive aerodynamic information about wind turbine flowfield. In contrast to vortex formulations, the N–S equations contain the physics for vorticity generation at a surface and subsequent convection into the wake. Moreover, the viscous drag on the blade can also be determined for use in computing the turbine performance. With the development of the speed and memory of computational hardware and with the advances in computational fluid dynamics (CFD) techniques, the N–S solver is becoming a promising and powerful tool for analysis of wind turbine aerodynamics.

Wind turbine aerodynamic researchers have not generally given their attention to full potential methods, which have been widely used in helicopter aerodynamic research (Egolf and Sparks 1986, Strawn and Caradonna 1987, Steinhoff

and Ramachandran 1990, Ramachandran *et al.* 1993). The reason for this is not entirely clear. Possibly because, if an inadequate grid size is used, the methods suffer from the fact that vorticity diffuses at a much faster rate than that suggested by the influence of viscosity. This leads to errors in the calculation of blade aerodynamic characteristics (Conlisk 1997, Steinhoff and Ramachandran 1990).

A numerical procedure based on the full N–S equations was applied to the flow near a wind turbine rotor by Schetz and Figard (1982). The rotor was modelled as an actuator disk and the flow was assumed axisymmetric. Despite the inability of the actuator disc concept to treat blade-shed vortices and the necessity of time-averaging the effects of the rotor on the flow, Sorensen and Myken (1992) also used the actuator disc to represent the rotor in an unsteady model consisting of a finite-difference solution of the axisymmetric Euler equations (inviscid form of the N–S equations) in a vorticity-streamfunction formulation. In order to reduce the high cost of the computation, Giannakidis and Graham (1997) used a two-dimensional N–S algorithm only on one of the blades of the rotor, the others being modelled using the equivalent vortex lattice circulation. Similarly, in the hybrid N–S/potential flow approach of Xu and Sanka (1999), the costly viscous N–S equations were solved only in a small viscous flow region surrounding the rotor. The rest of the flowfield was modelled using potential flow methodology and the tip vortices were modelled using a free wake approach. More recent progress in N–S simulations can be viewed from Duque *et al.* (1999). Their method made extensive use of overset grids to model the wind turbine. Both an isolated rotor and a complete configuration that included the rotor, hub, nacelle and tower have been modelled. The isolated rotor computations show a strong dependence on turbulence modelling and on accurate definition of trailing edge geometry. The complete rotor-tower-nacelle computations demonstrate significant ability to simulate the flowfield and aerodynamics of HAWTs although there exist some deficiencies such as the adverse effect of grid density mismatches on the blade/tower interaction.

1.2.2 Blade Element/Momentum Theory and Definitions

The Rankine–Froude Theory

Simple axial momentum theory is based on the Rankine–Froude one-dimensional flow (Fig. 1.4).

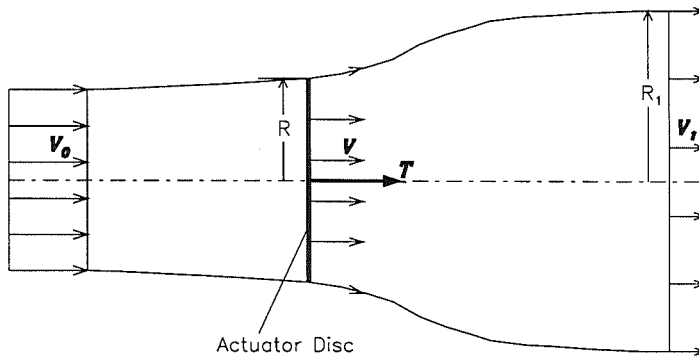


Figure 1.4: Rankine–Froude one-dimensional flow

Consider a wind turbine rotor of radius R operating in a uniform wind of velocity V_0 along its axis of rotation. The rotor is replaced by an actuator disc of area πR^2 . Let V be the flow velocity through the disc and V_1 denote the axial velocity in the ultimate wake whose radius is R_1 . The thrust T acting on the disc is equal to the decrease of axial momentum in unit time due to the rotor extracting energy:

$$T = \varrho \pi R_1^2 V_1 (V_0 - V_1) \quad (1.1)$$

where ϱ is the density of the air.

The pressure drop across the disc due to energy extraction by the rotor is obtained

$$\Delta p = \frac{1}{2} \varrho (V_0^2 - V_1^2)$$

by application of Bernoulli's equation to the flow region before and behind the disc, respectively, and noting that the pressure in the far wake downstream reaches

equilibrium with the undisturbed wind. This pressure drop determines the rotor thrust

$$T = \frac{1}{2} \varrho (V_0^2 - V_1^2) \pi R^2 \quad (1.2)$$

By equating Eq. 1.1 and Eq. 1.2 and from the condition of continuity of flow

$$R_1^2 V_1 = R^2 V$$

we can obtain

$$V = \frac{V_0 + V_1}{2} \quad (1.3)$$

showing that the axial velocity at the rotor is the arithmetic mean of the wind velocity and axial velocity of the wake far downstream.

For some purposes it is convenient to define the *axial interference factor* by

$$a = 1 - \frac{V}{V_0} \quad (1.4)$$

This is often called the *axial induced velocity factor* in vortex theory. Then

$$V_1 = (1 - 2a)V_0 \quad (1.5)$$

Thus, the rotor *thrust coefficient* is

$$C_T = \frac{T}{\frac{1}{2} \varrho V_0^2 \pi R^2} = 4a(1 - a) \quad (1.6)$$

The power output of the rotor, P , is the work done by the thrust in unit time. Therefore, the *rotor power coefficient* is

$$C_P = \frac{P}{\frac{1}{2} \varrho V_0^3 \pi R^2} = 4a(1 - a)^2 \quad (1.7)$$

Eq. 1.7 shows that, when $a = 1/3$, the maximum power coefficient is obtained and

$$C_{P_{\max}} = \frac{16}{27} \quad (1.8)$$

This result is the well-known *Betz limit*.

The Strip Theory

The axial momentum theory above is developed on the assumption that there is no rotational motion in the turbine wake. To extend the theory to include the effects of this rotational motion, the rotor is modelled by an actuator disc which is divided into concentric, aerodynamically independent streamtubes or strips (Fig. 1.5).

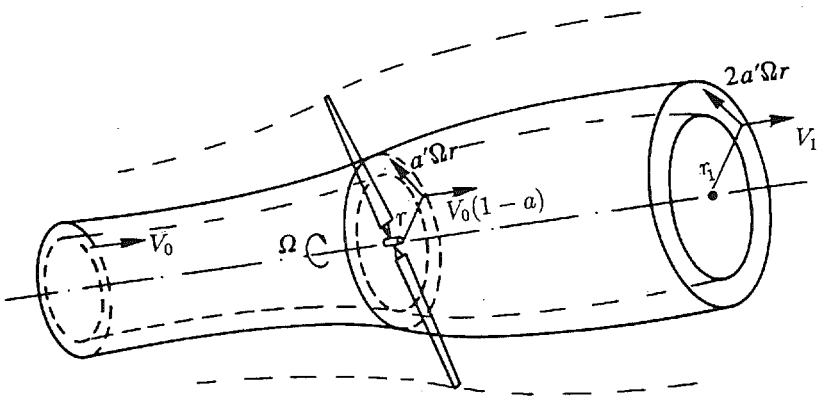


Figure 1.5: Streamtube model for wind turbine

Applying the axial momentum theory to a streamtube, whose width is dr , at radius, r , the elemental thrust is given by

$$dT = \rho \cdot 2\pi r dr \cdot V_0(1 - a) \cdot [V_0 - V_0(1 - 2a)]$$

or

$$dT = \frac{1}{2} \rho V_0^2 2\pi r 4a(1 - a) dr \quad (1.9)$$

Using conservation of angular momentum and assuming that there is no swirl upstream of the disc (Glauert 1935), angular momentum theory leads to the elemental torque

$$dQ = \rho \cdot 2\pi r dr \cdot V_0(1 - a) \cdot 2\omega r \cdot r \quad (1.10)$$

where ω is the angular velocity of the wake just behind the disc.

For convenience, we introduce the *tangential interference factor*, or *tangential induced velocity factor*, a' ,

$$a' = \frac{\omega}{\Omega} \quad (1.11)$$

where Ω is the angular velocity of the rotor. Then, Eq. 1.10 can be rewritten as

$$dQ = 2\rho V_0(1 - a)a'\Omega r^2 2\pi r dr \quad (1.12)$$

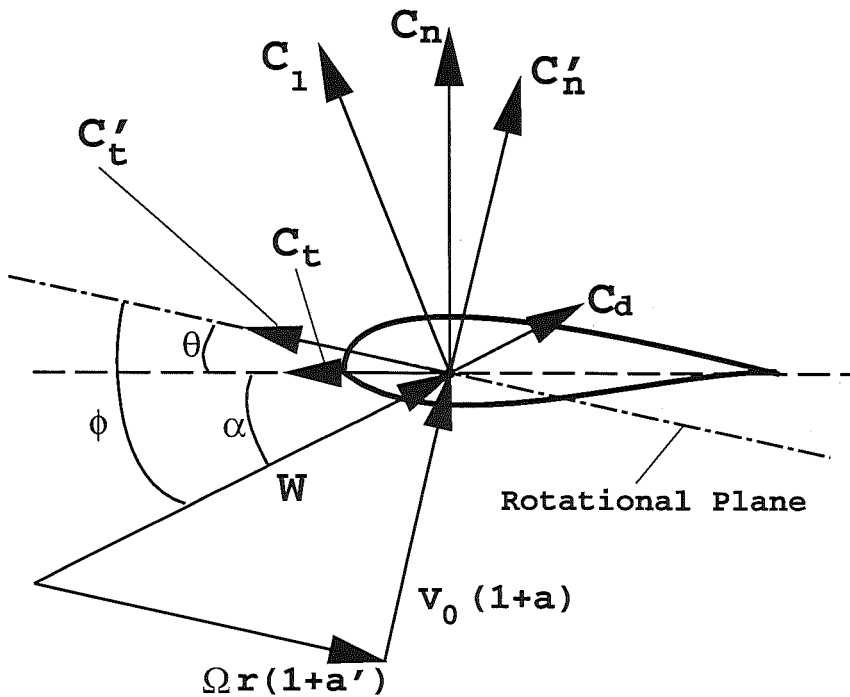


Figure 1.6: Inflow velocity and aerodynamic forces on blade element

If it is assumed that the blade element acts like a two-dimensional aerofoil, i.e. there are no aerodynamic interactions between the blade elements, the non-dimensional normal and tangential components of the forces acting on the blade element (Fig. 1.6) are

$$C'_n = C_l \cos \phi + C_d \sin \phi \quad (1.13)$$

$$C'_t = C_l \sin \phi - C_d \cos \phi \quad (1.14)$$

where C'_n is the force coefficient normal to the rotor disc and C'_t the force coefficient circumferential or tangential to the rotor disc; the prime ('') is used here to distinguish between these terms and the *normal force coefficient* of an aerofoil, C_n , and *tangential force coefficient* or *chordwise force coefficient* of an aerofoil, C_t , which will be frequently mentioned in the following chapters,

$$C_n = C_l \cos \alpha + C_d \sin \alpha \quad (1.15)$$

$$C_t = C_l \sin \alpha - C_d \cos \alpha \quad (1.16)$$

C_l and C_d are the two-dimensional aerofoil lift and drag coefficients, respectively, and functions of the angle of attack, α ,

$$\alpha = \phi - \theta \quad (1.17)$$

where θ is the blade pitch angle, and ϕ the inflow angle, which can be determined by

$$\tan \phi = \frac{V_0(1-a)}{\Omega r(1+a')} = \frac{1-a}{\lambda_r(1+a')} \quad (1.18)$$

where $\lambda_r = \lambda \bar{r}$ is the *local tip speed ratio*, $\lambda = \Omega R/V_0$ the *tip speed ratio*, and $\bar{r} = r/R$.

The elemental thrust and torque can then be expressed using blade element theory as follows:

$$dT = \frac{1}{2} \varrho W^2 B c C'_n dr \quad (1.19)$$

$$dQ = \frac{1}{2} \varrho W^2 B c C'_t r dr \quad (1.20)$$

where B is the number of blades, c the chord of the blade element, and W the inflow velocity

$$W = \sqrt{V_0^2 (1-a)^2 + \Omega^2 r^2 (1+a')^2} \quad (1.21)$$

Equating the thrust obtained from momentum theory, Eq. 1.9, to that from blade element theory, Eq. 1.19, gives

$$\frac{a}{1-a} = \frac{\sigma C'_n}{8 \sin^2 \phi} \quad (1.22)$$

where $\sigma = Bc/(\pi r)$ is the *local solidity*.

Similarly, equating the expressions for torque, Eq. 1.12 and Eq. 1.20, we obtain

$$\frac{a'}{1+a'} = \frac{\sigma C'_t}{8 \sin \phi \cos \phi} \quad (1.23)$$

If the induced velocity factors, a and a' , are determined, the rotor thrust coefficient, C_T , and *torque coefficient*, C_Q can be calculated by integrating Eq. 1.19 and Eq. 1.20, respectively,

$$C_T = \int_{\bar{R}_t}^1 \frac{Bc}{\pi R} \bar{W}^2 C'_n d\bar{r} \quad (1.24)$$

$$C_Q = \frac{Q}{\frac{1}{2} \rho V_0^2 \pi R^3} = \int_{\bar{R}_t}^1 \frac{Bc}{\pi R} \bar{W}^2 C'_t \bar{r} d\bar{r} \quad (1.25)$$

where the non-dimensional inflow velocity

$$\bar{W} = \frac{W}{V_0} = \sqrt{(1-a)^2 + \lambda_r^2 (1+a')^2} \quad (1.26)$$

and $\bar{R}_t = R_t/R$ with R_t being the radius of the blade root. The power coefficient can then be calculated from

$$C_P = \lambda C_Q \quad (1.27)$$

From Eqs. 1.13, 1.14, 1.17, 1.18, 1.22 and 1.23, a and a' are functions of the tip speed ratio λ and non-dimensional local radius \bar{r} . Obviously, the key to calculation of C_T , C_Q , and C_P is the determination of a and a' from Eqs. 1.22 and 1.23, which usually involves an iterative procedure.

The Effects of Number of Blades

In the momentum analysis above, the rotor is replaced by an actuator disc. This means that the rotor has infinite number of blades. In fact, the number of blades

is always finite. To account for this effect, the well-known *Prandtl tip loss factor*, F_t , is usually used,

$$F_t = \frac{2}{\pi} \arccos e^{-f} \quad (1.28)$$

where f can be approximately expressed as

$$f = \frac{B}{2} \frac{1 - \bar{r}}{\bar{r} \sin \phi} \quad (1.29)$$

Wilson and Lissaman (1974) applied the tip loss correction to a BEM formulation, obtaining

$$\frac{a}{1-a} = \frac{\sigma C'_n}{8 F \sin^2 \phi} \quad (1.30)$$

$$\frac{a'}{1+a'} = \frac{\sigma C'_t}{8 F \sin \phi \cos \phi} \quad (1.31)$$

A similar hub loss correction can also be obtained, but its effect on the turbine performance is much smaller than the tip correction.

Large Induced Velocity States

There are different flow states of a rotor in a wind stream, which are usually termed as:

- propeller state, when $a < 0$
- windmill brake state, when $0 \leq a \leq 0.5$
- turbulent wake state, when $0.5 < a \leq 1$
- vortex ring state, when $a > 1$

Only the *windmill brake state* and *turbulent wake state* are of interest for a wind turbine since in those cases $C_P \geq 0$.

When $a > 0.5$, from Eq. 1.5, there would be negative flow in the wake. This contravenes the assumption of one-dimensional flow and therefore the classic momentum theory breaks down. In this case, $C_T \neq 4a(1-a)$ and $C_P \neq 4a(1-a)^2$.

In fact, there is some evidence that the effect of the turbulent wake state starts at $a \approx 0.4$ (Glauert 1948), which is rather close to the optimum condition ($a = 1/3$).

To overcome this problem, several thrust coefficient formulas for large induced velocity states have been proposed on the basis of experimental investigations, for example,

- Glauert (1948): $C_T = 0.89 - 0.44a + 1.56a^2$, for $a > 0.4$
- Wilson (1981): $C_T = 0.578 + 0.96a$, for $a > 0.38$
- de Vries and den Blanken (1981): $C_T = 0.53 + 1.07a$, for $a > 0.4$
- Anderson *et al.* (1982): $C_T = 0.425 + 1.39a$, for $a > 0.326$

There is no strong evidence that one of the correlations above is more appropriate than the others, but the measurements of Wilmshurst *et al.* (1984) tend to support the correlations proposed by Wilson and by de Vries and den Blanken.

1.2.3 Vortex Wake Theory

Instead of estimating the induced velocities from the momentum equations, vortex wake methods directly calculate the velocities induced by the vortex system stemming from the rotor blades, *via* the Biot–Savart law.

The flow around a steadily rotating HAWT in a steady wind stream, \mathbf{V}_0 , parallel to the axis of rotation, can be considered as irrotational to first order. The velocity field, \mathbf{V} , in an earth-fixed coordinate system (Fig. 1.7) can be calculated from an unsteady perturbation potential φ , namely,

$$\mathbf{V} = \mathbf{V}_0 + \nabla\varphi(t, r, \psi, z) \quad (1.32)$$

where t is time, and r, ψ, z are cylindrical coordinates. In a rotor-fixed rotating coordinate system (r_r, ψ_r, z_r) , the flow is steady and rotational, but the perturbation velocity field is still irrotational because this cannot be changed by a mere

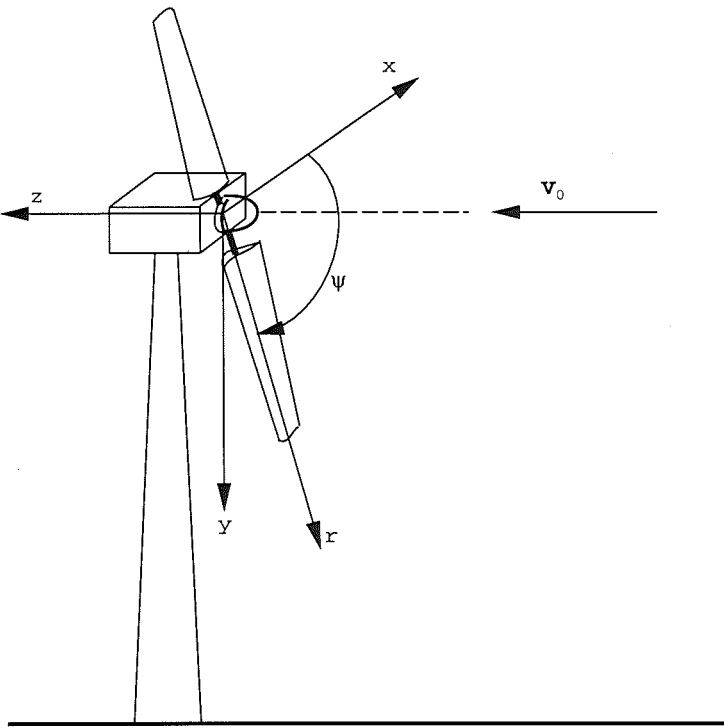


Figure 1.7: Coordinate system

coordinate transformation. Thus,

$$\mathbf{V} = \mathbf{V}_0 + \boldsymbol{\Omega} \times \mathbf{r} + \nabla \varphi(r_r, \psi_r, z_r) \quad (1.33)$$

where $\psi_r = \psi - \Omega t$.

Eq. 1.33 demonstrates that, although the flow in the rotating coordinate system is rotational, the perturbation velocities can be calculated from a potential in a way analogous to the airplane wing in rectilinear flight. However, there is one important difference between wings and rotor blades, the shape of the trailing vortex system. In the case of negligible perturbation velocities, the shape of the vortex sheet is determined by \mathbf{V}_0 and $\boldsymbol{\Omega} \times \mathbf{r}$ (rigid wake analysis). For relatively large perturbations, the shape is determined by the induced velocities and cannot be given a priori. Therefore, the shape and position of the trailing vortex sheet have to be assumed beforehand (prescribed wake analysis) or to be determined by an iteration procedure (free wake analysis). In the latter, the iteration involves extensive computation and usually takes the results of a rigid or prescribed wake

method as its initial values.

In the vortex wake analysis, the potential flow problem is solved by replacing the rotor blade and wake by a distribution of vortices, determining the strength of this distribution by fulfilling the boundary conditions, and then calculating the velocity field. A common way to cope with the blade is to view the blade as a vortex line, whose strength is usually concentrated on the quarter-chord of the aerofoil. This is called *lifting-line theory* and is widely used in vortex analysis of wind turbines (Miller *et al.* 1978, Gohard 1978, Miller 1983a, Miller 1983b, Miller 1984, Miller 1985, Afjeh and Keith 1986a, Afjeh and Keith 1986b, Afjeh and Keith 1989, Kotb and AbdelHaq 1992, Hernandez and Crespo 1987, Koh and Wood 1991a, Simoes and Graham 1992, Robison *et al.* 1995). While lifting-line theory is computationally simple and fast, it is well known that it is not valid for large variations in the downwash caused by the vortex wake. Therefore, some wind turbine codes use the more accurate *lifting-surface method* (Kocurek 1987, Rosen *et al.* 1990, Gould and Fiddes 1992, Lain *et al.* 1995) in which the blade is viewed as a wing of finite chord but zero thickness. A more sophisticated *panel method* was used by Preuss *et al.* (1980) to model finite-thickness blades in a vortex analysis of HAWTs.

In lifting-line based methods, the wake vortex filaments are generally modelled as straight lines of constant vortex strength. Afjeh and Keith (1986b), however, introduced vortex rings to represent the intermediate wake between the near and far wakes in order to reduce the computational time. A curved vortex model (Bliss *et al.* 1987) and a vortex box model (Egolf 1988) have been used in helicopter aerodynamics but, to date, have not been used for the analysis of wind turbines.

In vortex wake analysis, the vortex-induced velocity is directly calculated using the *Biot–Savart law* for inviscid, incompressible flow,

$$\mathbf{dv} = \frac{\Gamma}{4\pi} \frac{\mathbf{dl} \times \mathbf{r}}{|\mathbf{r}|^3} \quad (1.34)$$

where \mathbf{dv} is the velocity at an arbitrary spatial point $P(x, y, z)$, induced by an infinitesimal line vector, \mathbf{dl} , with vorticity Γ , whose direction abides by the “right-hand rule”; \mathbf{r} is the radius vector from the element \mathbf{dl} to the point P . For a vortex of infinite length (two-dimensional potential vortex) the Biot–Savart law reduces to

$$u = \frac{\Gamma}{2\pi r} \quad (1.35)$$

where r is the radius from this point vortex to the point P where the tangential induced velocity u is calculated.

Applying Eq. 1.34 to a spatial straight-line vortex from point $A(x_1, y_1, z_1)$ to point $B(x_2, y_2, z_2)$ with constant strength Γ , the velocity at point $P(x, y, z)$ induced by this straight-line vortex is

$$\mathbf{v} = \frac{\Gamma}{4\pi} \frac{\mathbf{r}_A \times \mathbf{r}_B}{|\mathbf{r}_A \times \mathbf{r}_B|^2} \left(\frac{\mathbf{r}_A \cdot \mathbf{r}_{AB}}{|\mathbf{r}_A|} - \frac{\mathbf{r}_B \cdot \mathbf{r}_{AB}}{|\mathbf{r}_B|} \right) \quad (1.36)$$

where

$$\mathbf{r}_A = (x - x_1)\mathbf{i} + (y - y_1)\mathbf{j} + (z - z_1)\mathbf{k}$$

$$\mathbf{r}_B = (x - x_2)\mathbf{i} + (y - y_2)\mathbf{j} + (z - z_2)\mathbf{k}$$

$$\mathbf{r}_{AB} = (x_2 - x_1)\mathbf{i} + (y_2 - y_1)\mathbf{j} + (z_2 - z_1)\mathbf{k}$$

The derivation of Eq. 1.36 and its expansion form Appendix A.

In free wake models, the perturbation velocity, $\nabla\varphi$, at the control point on the blade or in the wake is a summation of the velocities induced by the bound vortices on the blades and trailed vortices in the wake. As $\nabla\varphi$ is determined, the position, \mathbf{G} , of a wake vortex filament can be calculated, *via* Eq. 1.33, using the following formulation

$$\mathbf{G} = \begin{pmatrix} x \\ y \\ z \end{pmatrix} = \mathbf{V} \cdot t$$

Because the strength of the vortices is a function of \mathbf{G} in turn, an iteration procedure is needed in a free wake analysis.

1.2.4 Prescribed Wake Model

In a prescribed wake model, the geometry of the rotor wake is prescribed by so-called *prescription functions* usually as a function of the induced velocities at the rotor,

$$\mathbf{G} = \mathbf{G}(r, a, a')$$

Thus, the fixed geometry of the wake forms part of the input to the model.

In prescribed wake analysis, the trailed vorticities are distributed into the wake along the already known wake geometry. The velocity at the rotor induced by these vorticities is then estimated using the Biot–Savart law, Eq. 1.34, or Eq. 1.36. Because the shape of the wake depends on the induced velocities at the blade, an iteration procedure is usually involved in calculating the induced velocities from the Biot–Savart law. This iteration excludes any calculation of the induced velocities in the wake, which must be carried out in a free wake analysis to determine the wake geometry. Therefore, the prescribed wake method only requires a fraction of the computational power of a free wake model but can yield results of comparable accuracy if the wake is correctly prescribed.

At this point, it is necessary to emphasise that the level of precision of the wake geometry has proved to have only a small influence on the predicted rotor performance. Gould and Fiddes (1992) conclude that, for one example rotor, the power output and thrust loading are insensitive to the shape of wake. For that case, a prescribed cylindrical wake and a prescribed 35% expanded conical wake only differ by 3.6% in the power prediction and 1% in the thrust. Simoes and Graham (1992) found differences of less than 5% in power output between free and prescribed wake models. Afjeh and Keith (1986a), by comparing their simplified free wake model with those of Gohard (1978) and Miller (1983a), reached

similar conclusions. These results provide somewhat sounder ground for use of the prescribed wake model in the analysis of wind turbine aerodynamics.

In Chapter 2 a more detailed description is given of the prescribed wake model for HAWTs that will be used as an essential analysis tool in this study.

1.2.5 Unsteady and Three-Dimensional Aerodynamics

Rotational Effects

There has been a realisation that the performance of stall-controlled wind turbines is difficult to predict at high wind speeds. It is often observed that, at low tip speed ratios, measured power exceeds the level predicted traditionally using two-dimensional (2-D) aerofoil data. This is related to delay in aerofoil stall when three-dimensional (3-D) effects are significant.

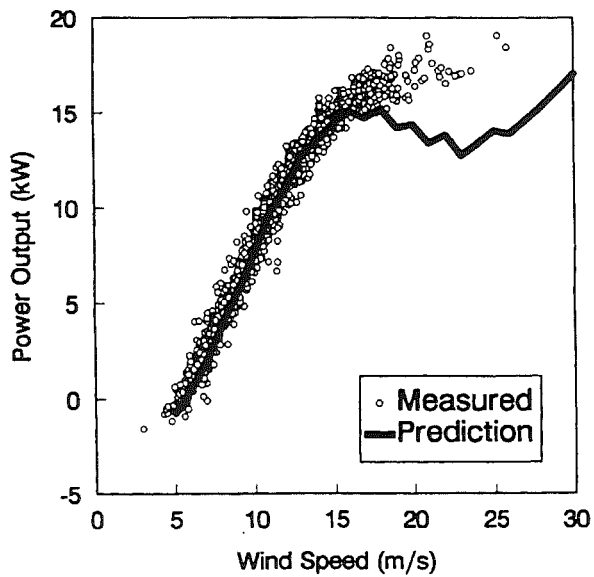


Figure 1.8: Comparison of predicted and measured CER power

Fig. 1.8 shows a comparison of measured and predicted rotor power output (Musial *et al.* 1990) for the NREL CER – Combined Experiment rotor. It clearly

demonstrates that the measured power is considerably higher than that predicted at high wind speeds. From both experimental observation and theoretical analysis, the phenomenon of stall delay, particularly manifest on the inboard portion of a rotating blade, has been identified as the main source of the discrepancy in the power output (de Vries 1979*b*, Viterna and Janetzke 1982, Milborrow 1985, Butterfield 1989*b*, Butterfield *et al.* 1992*a*, Hales 1991, Wood 1991, Ronsten 1992). Fig. 1.9, from Hansen and Butterfield (1993), shows the stall delay effects on the

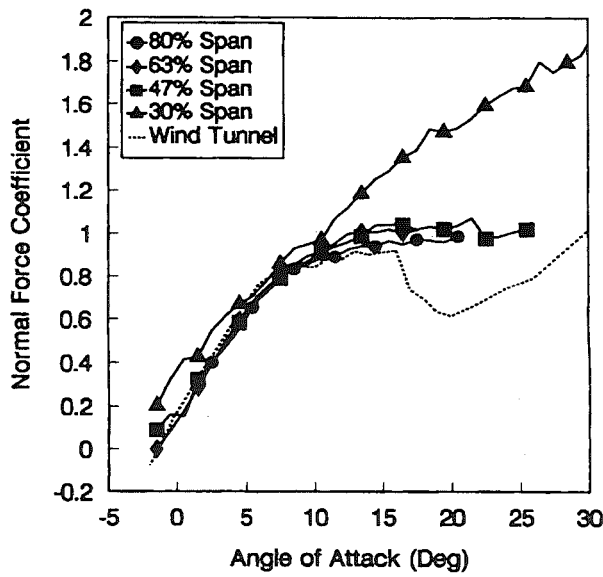


Figure 1.9: Normal force coefficients of CER blade aerofoil measured in field and in wind tunnel

aerofoil normal force coefficients at different spanwise stations, which produce the difference between the field measurements and the results calculated using 2-D aerofoil data illustrated in Fig. 1.8. The aerofoil on the rotating blade apparently does not experience the same drop in lift during stall as it does in the wind tunnel 2-D data. More surprisingly, the normal force at the 30% of span station continuously increases without any signs of stall drop-off.

In both the BEM theory and vortex wake models, the blade is conventionally divided into aerodynamically independent elements. It is assumed that there is

no aerodynamic interference between one blade element and another and that 2-D aerofoil lift and drag coefficients can be used on each element. In reality, there exists a spanwise flow along a rotating blade resulting in strong 3-D effects (McCroskey and Yaggy 1968, Young and Williams 1972). Much attention has been paid to this rotational effect. The outward radial (spanwise) flow generated by centrifugal pumping results in a Coriolis acceleration which acts as a favourable chordwise pressure gradient. This pressure gradient delays the boundary layer separation and increases the maximum lift coefficient (Banks and Gadd 1963, Harris 1966). Engineering stall delay models, based on experimental observation and simplified theoretical analysis of centrifugal and Coriolis terms, have been proposed for rotating wind turbine blades (Eggers and Digumarthi 1992, Snel *et al.* 1993, Tangler and Selig 1997, Du and Selig 1998). Numerical studies of stall delay due to 3-D rotational effects have also been performed through solutions of the N-S equations, a good review of which can be found in the work by Sorensen *et al.* (1997).

The 3-D effects due to rotation will be further addressed in Chapter 4.

Unsteady Aerodynamics

Wind turbines operate at all times in a extremely complex and unsteady flow. Aerodynamic forces acting on the blades vary consistently. The main factors which make a contribution to the unsteady aerodynamic forces on the blades are as follows:

- *yawed flow*: a rotating blade experiences a cyclic change in the incidence in yawed flow;
- *wind shear* in the atmospheric boundary layer: aerodynamic forces on the rotor are not balanced in condition of wind shear;
- *atmospheric turbulence and gust*: large scale eddies can cause a significant variation in both magnitude and direction of the inflow to the blade;

- *tower shadow*: the blade experiences an incidence fluctuation as it passes through the wake of the tower;
- *structural deformation of the blade*: flap and torsion add complexity to the dynamic analysis and the aerodynamic loads can be influenced by the motion of the blade;
- *control inputs* such as rotor yawing and blade feathering: these phenomena produce extra dynamic forces.

Obviously, aerodynamic loads must be well understood before the structural response can be accurately determined. Wind turbine failures, reduced machine life, and increased operating maintenance are all directly linked to unsteady aerodynamic loading. Thus, unsteady aerodynamics should play a very important role in the design and analysis of wind turbines and hence have recently been attracting the attention of wind turbine researchers. Aspects of unsteady aerodynamics of wind turbines have been well documented by Hansen and Butterfield (1993), Galbraith *et al.* (1990) and Robinson *et al.* (1995). There are no theories or models for wind turbines which can properly account for all of the unsteady factors listed above. The discussion here focuses mainly on dynamic stall.

The term *dynamic stall* refers to unsteady flow separation occurring on aerodynamic bodies which execute an unsteady motion. Dynamic stall phenomena are often observed during the operation of wind turbines and the forward or manoeuvering flight of helicopters. Dynamic stall may be encountered on propeller and turbomachinery blades and on the wings of rapidly manoeuvering fighter aircraft. The physics of the dynamic stall process is detailed by McCroskey (1981), Carr (1988) and Carr and Chandrasekhara (1996).

Dynamic stall is distinctively characterised by the formation and shedding of a discrete vortex, whose convection over the upper surface of the aerofoil induces a highly unsteady pressure field. Fig. 1.10 shows the development of aerofoil normal force and pitching moment coefficients along with the corresponding boundary

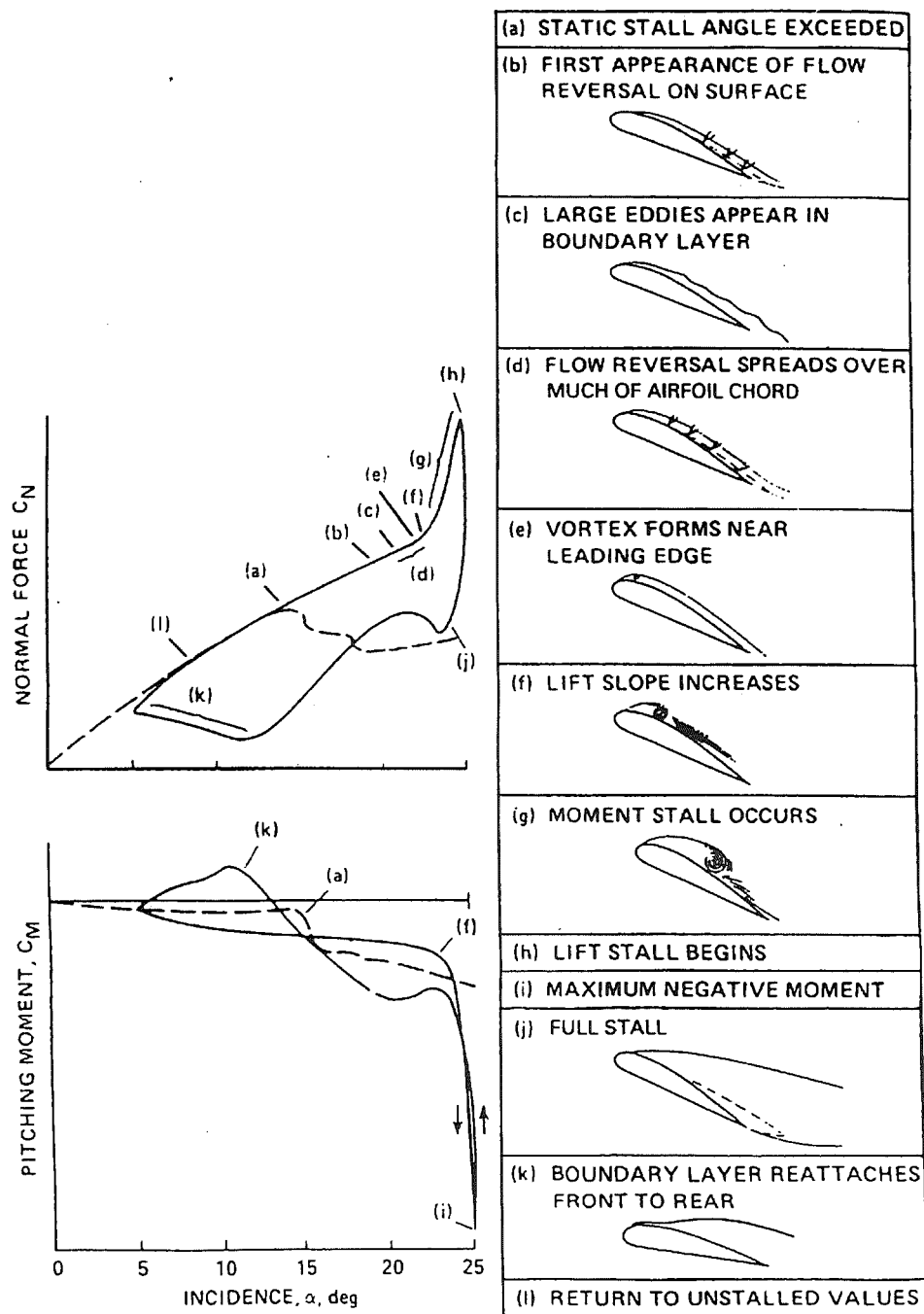


Figure 1.10: Events of dynamic stall on NACA 0012 aerofoil (Carr 1988)

layer behaviour for a NACA 0012 aerofoil oscillated in pitch. First, a vortex starts to develop near the aerofoil leading edge as the angle of attack is rapidly increased past the static stall angle. This vortex is then convected downstream over the aerofoil surface and causes an increase in lift due to the suction induced by the vortex. The magnitude of the lift increase depends on the strength of the vortex and its distance from the surface. The streamwise movement of the vortex depends on the aerofoil shape and the pitch rate. As the vortex is convected past the trailing edge, the pitching moment briefly attains its maximum negative value and then the magnitude of both lift and pitching moment start to drop rapidly. The flow over the aerofoil remains stalled until the angle of attack has decreased enough to enable flow reattachment. As a result of this sequence of flow events, the unsteady lift, drag, and pitching moment coefficients show a large degree of flow hysteresis when plotted as a function of incidence. The amount of hysteresis and the shape of the hysteresis loops vary in a highly nonlinear way with the amplitude of oscillation, mean angle of attack, and reduced frequency of oscillation.

Dynamic stall occurs on HAWTs where rather severe blade incidence variations are generated by particular inflow conditions, for example, during operation in yaw. In contrast to aerofoil static stall, the onset of stall on an aerofoil whose angle of attack is increasing rapidly can be delayed to an incidence which may exceed the static stall angle by a significant amount. Once dynamic stall occurs, however, the aerodynamic loads are generally more severe compared to steady stall and may cause substantial increases in the blade stresses and the control system loads. Therefore, dynamic stall is very challenging and important for design and analysis of wind turbines.

Prior to 1988 dynamic stall effects were not included in HAWT performance and loads analysis methods, whereas they were considered in VAWT analyses as early as in 1984 (Cardona 1984). In 1989 Butterfield (1989a) presented results that quantified both the existence of dynamic stall and its effect on rotor loads

by measuring pressure distributions on a 10 m HAWT. Dynamic stall was shown to occur under a variety of inflow conditions, including turbulence, tower shadow, and yawed flow. The existence of dynamic hysteresis resulted in significant increases in yaw loads. In a further study by Hansen *et al.* (1990), it is also found that stall hysteresis has a large influence on yaw moments on a rotor. Instantaneous pressure distributions measured on the rotor provide conclusive evidence that stall hysteresis is present and calculations show that the hysteresis increases the mean yaw moment dramatically (typically over 100%) and the cyclic yaw moments to a lesser extent. Results from the Combined Experiment, conducted by the National Renewable Energy Laboratory (NREL), clarify that unsteady aerodynamics exist during all operating conditions and that dynamic stall can exist for high yaw angle operation while stall hysteresis occurs for even small yaw angles (Huyer *et al.* 1996, Shipley *et al.* 1995a, Butterfield *et al.* 1992a). It is now common to consider the influence of dynamic stall in the study of HAWT unsteady aerodynamics *via* engineering or numerical models for dynamic stall (Ekaterinaris *et al.* 1998, Riziotis *et al.* 1996, Voutsinas and Riziotis 1996, Pierce and Hansen 1995, Hansen 1995, Thresher *et al.* 1986).

The development of empirical or semi-empirical engineering models for dynamic stall has been necessitated by the extremely complicated nature of the dynamic stall phenomena. These methods are based primarily on force and pitching moment data obtained from various wind tunnel tests, *e.g.* methods of Gangwani (1982) and of Ericsson and Reding (1972, 1987), the former of which is a time domain unsteady aerodynamic model based on oscillating aerofoil tests and the latter a combined analytical/empirical model incorporating several time-lag effects. Gormont (1973) developed a dynamic stall model derived from the so-called gamma function method (Harris *et al.* 1970), where the gamma function is an empirical function, which depends on aerofoil geometry and Mach number and is different for lift and moment stall. The Gormont method has been applied to analysis of the yaw dynamics of HAWTs (Hansen *et al.* 1990). A method of dynamic

stall prediction for helicopter rotors developed by ONERA (Petot 1983, Tran and Petot 1981) has also been applied to HAWT analysis (Bierbooms 1992, Yeznasni *et al.* 1992). In this method, linear, ordinary differential equations with constant coefficients are derived to describe the linear and nonlinear lift, drag, and moment coefficients. Bierbooms (1992) concluded that the ONERA method gave better results in hysteresis than the Gormont method but at the expense of more computer time, while Yeznasni *et al.* (1992) found that the ONERA model provided poorer results than the Gormont method for a NACA 4418 aerofoil on a 8.5 m test turbine and superior results for a NACA 64₂-xx aerofoil on a 500 KW rotor. Leishman and Beddoes (1989) have presented a unsteady model which still relies upon empirical constants but is more deeply founded in the physical mechanism of dynamic stall. This semi-empirical method has been developed in a form compatible with an indicial formulation and consists of three distinct subsystems, namely an attached flow solution for the unsteady linear forces, a separated flow solution for the nonlinear loading and a dynamic stall solution for the vortex-induced airloads. Results from the applications of this model to wind turbines demonstrate good agreement, in general, with measured data (Pierce and Hansen 1995, Coton *et al.* 1994).

As previously mentioned, due to the complicated nature of dynamic stall, the wind industry has been forced to develop and use empirical methods for dynamic predictions. However, recent progress in CFD and the tremendous increase in computing power have made possible the use of the full fluid dynamic governing equations for dynamic stall investigation and prediction. A good review of the computational methods applied to dynamic stall has been presented by Ekaterinariis and Platzer (1997). Numerical computation of dynamic stall is far from practical for day-to-day design use, especially the computation of 3-D dynamic stall, which is essential for a better understanding of 3-D flow over the wind turbine. This is mainly because these computations require very large computing times and the transitional and turbulent flow models need to be improved.

1.2.6 Experimental Studies

As in other aerodynamic areas, experimental study is indispensable to wind turbine aerodynamics. Numerous experiments on HAWTs have been performed over the last two decades. The experimental study is usually carried out by two means, *i.e.* operation in field and tests in wind tunnels.

Field Operation

Reliable aerodynamic measurements on wind turbines in field tests are both difficult and time consuming due to the stochastic character of the wind. Nevertheless, field experiments are necessary to better understand wind turbine aerodynamic behaviour and to aid design of cost-effective and reliable wind turbines, since they are conducted strictly under natural conditions.

Wind turbine field tests have already provided abundant aerodynamic data, helping improve the design of wind energy conversion systems and enhance the analysis of wind turbine aerodynamics. Among them, the most well-known experiment may be the Combined Experiment, later the Unsteady Aerodynamics Experiment, which has been being executed by NREL since its inauguration in 1987. The test HAWT is a 10 m diameter, three-bladed downwind machine whose blades are un-tapered without twist (Phase I, and II) and with twist (Phase III and IV). The test set-up and results have been extensively reported (Butterfield *et al.* 1992a, Butterfield *et al.* 1992b, Butterfield *et al.* 1992c, Shipley *et al.* 1995a, Robinson *et al.* 1995, Simms *et al.* 1995, Fingersh *et al.* 1995, Huyer *et al.* 1996, Acker and Hand 1999). Listed in Appendix B are the main geometric parameters of the NREL HAWT. The resulting field data have been used for development of new simulation methods and for validation of theoretical and numerical models (Duque *et al.* 1999, Du and Selig 1998, Tangler and Selig 1997, Pierce and Hansen 1995, Snel *et al.* 1993, Eggers and Digumarthi 1992, Hansen *et al.* 1990, Hartin 1990).

Butterfield *et al.* (1992a) analysed the data from Phase I and compared them

with wind tunnel test results. They identified the dynamic stall phenomena occurring for high yaw angles and stall hysteresis for even small yaw angles. Delayed stall was a very persistent phenomenon in all operating conditions. Stall delay was indicated by the existence of the leading edge suction peak through angles of attack up to 30° while the corresponding wind tunnel results showed this peak separating from the leading edge at 18°. Huyer *et al.* (1996) summarised the results from Phase II, concentrating on the analysis and discussion of the unsteady and 3-D aerodynamic behaviour for the wind turbine. The yaw effects, tower shadow effects, wind shear effects were all examined. The reduced data showed strong 3-D and unsteady effects on all sections of the blade. More interestingly, the movements of the suction pressure peak and the separation point were studied in detail, showing that the peak moved aftward along the chord and the separation point forward as the angle of attack increased. More recently, Acker and Hand (1999) have investigated the performance of the Phase IV rotor with twisted blades, indicating that the frequency of dynamic stall events on the blade of this rotor is significantly lower than that on the Phase II untwisted blade identified by Shipley *et al.* (1995a).

Besides NREL's Unsteady Aerodynamics Experiment, field tests have been systematically conducted by four other groups; Netherlands Energy Research Foundation (ECN), Delft University of Technology (DUT), Imperial College and Rutherford Appleton Laboratory (IC/RAL), and Risø National Laboratory (Risø). The field data from these five experimental programmes constitute the *IEA Annex XIV Database: Field Rotor Aerodynamics*, which has been documented in detail by Schepers *et al.* (1997). The database comprises pressure distributions on different blade sections, integrated blade loads (normal force, tangential force, and pitching moment coefficients), information about angle of attack, and gross rotor performance (thrust, torque, and power), etc. at various wind speeds and yaw angles, thus providing unique aerodynamic data for a number of wind turbine configurations for model validation and development.

Wind Tunnel Testing

Field experiments can provide comprehensive aerodynamic and dynamic information for wind turbines operating in natural conditions. However, such experiments are typically very time consuming, expensive and complicated through the large volumes of data and the extensive data reduction which are required. It is, therefore, often common to utilise wind tunnel testing which can be executed under controlled test conditions.

For accurate simulation of full-scale conditions in a wind tunnel the following similarity parameters should be the same for the full-scale turbine and for the wind tunnel model: the tip speed ratio λ , the Reynolds number R_e , and the tip Mach number M . These similarities cannot be simultaneously realised except in a compressed-air wind tunnel. For actual HAWTs, M is usually limited to 0.25 or 0.3 because of blade strength (centrifugal loads) and noise production. Therefore compressibility is not of great concern to wind turbine performance. The tip speed ratio is a determining factor of the performance as discussed in Section 1.2.2, and hence this similarity must be satisfied.

The Reynolds number for wind turbines is usually much lower than that for aeronautical vehicles. Therefore much experimental effort has been directed towards the development of aerofoils for wind turbines at low R_e and sometimes under icing conditions (Giguere and Selig 1997, Bloy and Robert 1993, Raghunathan *et al.* 1988, Jasinski *et al.* 1998, Hoskins *et al.* 1992). The aerofoil tests have by and large extended to high angles of attack because the blades of wind turbines commonly experience high incidences, especially those of stall-controlled wind turbines.

A large number of wind tunnel tests involving the measurement of wind turbine wakes have been carried out to analyse the wake characteristics and the interactions between turbines in a wind farm (*e.g.* Sforza *et al.* (1981) and Kirchhoff *et al.* (1990)). Grant *et al.* (1998) used particle image velocimetry (PIV) and laser sheet

visualisation (LSV) techniques to investigate the deflection of the tip vortices under various conditions of yaw and blade azimuth. Hurst *et al.* (1998) described a facility for the acquisition of simultaneous high quality PIV and unsteady surface pressures with high spatial and temporal resolution with the potential to provide detailed information for CFD validation.

Many wind tunnel tests on wind turbines are related to the validation of calculation models and the understanding of aerodynamic phenomena, such as stall characteristics and 3-D effects. Wilmshurst *et al.* (1984) made detailed measurements on a rotor and in its wake at a number of radial stations, investigating wind turbine performance in the high thrust region. Results were then compared with several empirical formulations for the turbulent wake state. The results from the wake measurements showed that high turbulence levels, generated at the rotor, persist and promote more rapid dissipation of the wake. Kotb and Schetz (1984) examined wind shear effects on wind turbine performance through wind tunnel tests. Clausen *et al.* (Clausen *et al.* 1987, Clausen and Wood 1988) carried out an experimental investigation to examine the validity of BEM theory and found that the theory underestimated the power contribution as a function of radius wherever the local angle of attack exceeded the angle that gives the maximum ratio of lift to drag in 2-D flow. Hernandez and Crespo (1987) and Nathan and Yin (1990) conducted wind tunnel tests to validate their performance prediction models. Stall delay and dynamic stall effects on the aerodynamic performance have also been investigated through experiments of HAWTs operating in wind tunnels (*e.g.* (Barnsley and Wellicome 1992, Bruining and Timmer 1992, Hemon *et al.* 1992)).

One major difficulty encountered in a wind tunnel test is the wall interference. For aerofoil tests, the wall interference can satisfactorily be corrected using conventional methods (Rae and Pope 1984). For wind tunnel tests on aerofoils at high angle of attack, where the wake blockage is large, the so-called wall pressure signature method may be used (Hackett *et al.* 1981). For full wind turbine test in a

wind tunnel, the tunnel wall interference may be very large because the expanding turbine wake produces serious blockage and the vortices, trailed and shed from the rotor into the wake, interact with the tunnel wall. For wind tunnel testing of wind turbines, therefore, the wall interference correction is a troublesome problem and correction methods have not widely been reported. Clayton and Filby (1984) studied the nature of the blockage in a open jet wind tunnel and identified that there is a point upstream of the rotor where the wind velocity has a notional value and this value is equivalent to the wind velocity at infinity in the ideal case. Nathan and Yin (1990) applied this method to their experimental data obtained from a model turbine test in an open jet section of a wind tunnel. Sayers and Ball (1983) proposed a velocity correction method that uses the drag measured on a rectangular flat plate in an open jet wind tunnel and claimed that this method would significantly increase the accuracy of the calculations made from wind turbine test results.

For a closed wind tunnel, the wall interference correction is even more difficult for wind turbine tests. In many tests, either scaled models or, simply, large wind tunnels are chosen to minimise the interference (*e.g.* Wei *et al.* 1990). However, the scaling of the wind turbine models is restricted by the blade strength because the rotational speed must be high for small-sized models in order to keep the tip speed ratio as high as expected. Also, large wind tunnels are not always available and they are expensive to run. The Aeronautical Research Institute of Sweden (FFA) and China Aerodynamics Research and Development Center (CARDC) have successfully used the wall pressure signature method to account for the tunnel wall interference with a turbine (Ronsten *et al.* 1995, Ronsten 1992, Ronsten *et al.* 1989, He and Jiang 1989). However, the distribution on the wall of the pressure taps, which acquire the wall pressure data necessary for the correction, is still a problem, because the wind turbine performance not only depends on the flow near the model but also is influenced by the wake. Loeffler and Steinhoff (1985) developed a multiple image method for computation of wind tunnel wall effects in ducted rotor experiments. This method may also be applied to wind tunnel

tests on conventional wind turbines. Nevertheless, the question of how to correct properly and effectively for wall interference in wind turbine tests in a closed wind tunnel still remains open.

1.3 Scope of the Study

This study is an investigation of unsteady aerodynamic modelling for HAWT performance prediction. The unsteady aspects addressed in this work include effects of variations in turbine inlet velocity due to operation in yawed flow, in the atmospheric boundary layer and in the tower wake. The unsteady and dynamic stall effects on the turbine aerodynamic performance and blade aerodynamic loads are modelled using an unsteady prescribed wake method which is coupled with an unsteady aerofoil model. In addition, the prescribed wake model is combined with a numerical representation of wind tunnel walls in a preliminary study of wind tunnel wall interference when the wind turbine is tested under unsteady conditions in a wind tunnel.

Although wind turbines and windmills have been used for centuries, the application of wind turbine aerodynamic technology to improve reliability and reduce the costs of wind-generated energy has only been pursued in earnest for the past twenty-odd years. Many fundamental aspects of wind turbine aerodynamics still remain to be explored. Accurate estimation of the unsteady aerodynamic characteristics of wind turbines is possibly the most significant modelling challenge.

During field operation, HAWTs always experience unsteady aerodynamic conditions. Yawed flows and tower shadow effects result in cyclic variations in the aerodynamic loads on the blades. Also, the aerodynamic performance of a HAWT can be affected by the interactions with other machines operating upwind in wind farms. The transient aerodynamic forces resulting from these unsteady factors have a significant impact on wind turbine operations. Reduced machine life due to

fatigue, increased maintenance, and severe transient power spiking are all typical effects. In a rapidly changing unsteady aerodynamic environment, unsteady loads can be four to five times larger than predicted steady-state values (Robinson *et al.* 1995). The 3-D stall delay due to rotational effects not only increases the blade loading, which affects the structural design and dynamic loads analysis, but also increases the difficulty in accurately predicting the power peak, which is particularly vital for design of stall-regulated HAWTs.

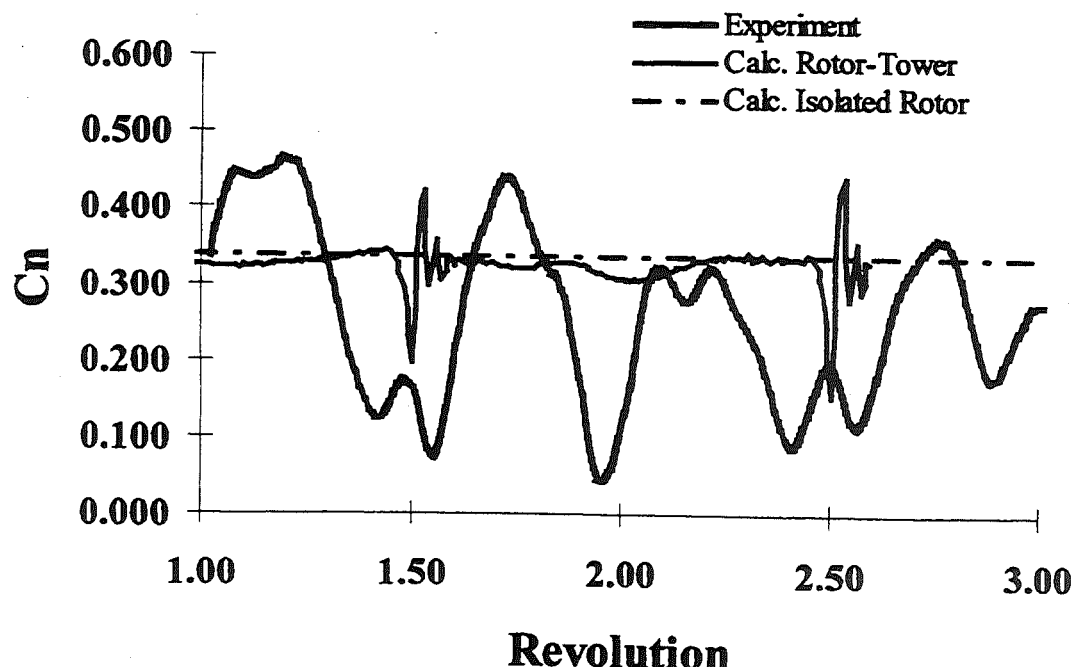


Figure 1.11: Comparison of N-S equations computation with experiment (Duque *et al.* 1999)

Although BEM theory has been used in dynamic load prediction, it is inadequate for calculation of the detailed unsteady aerodynamic information, as discussed in Section 1.2.1. The CFD studies which solve the unsteady N-S equations to obtain, theoretically speaking, an accurate representation of the wind turbine flowfield are promising but, at present, too time consuming. These methods are far from practical for day-to-day engineering design. Moreover, their accuracy remains to be improved. Fig. 1.11 shows a comparison for the NREL Combined Experi-

ment Phase II wind turbine, clearly demonstrating the disagreement between the N–S computation results and the fields data.

In vortex wake theories, the prescribed wake method requires much smaller computational time than the free wake method, and if modelled appropriately, can produce results of comparable accuracy to the latter. For this reason, a prescribed wake method has been adopted as the basic model in the present study. This model is extended to include yaw effects, wind shear effects and tower shadow effects. Coupled with an unsteady dynamic stall semi-empirical model as well as a 3-D stall delay model, this unsteady prescribed wake method comprehensively predicts the unsteady aerodynamic performance and characteristics of wind turbines.

Theoretical and computational models are often validated by comparison with data from wind tunnel tests. It is found, however, that the constraining effect of the wind tunnel walls is manifest in the closed wind tunnel (Grant *et al.* 1998). Clearly the interactions between the turbine, its wake and the tunnel walls are very complex. These interactions are more complex for unsteady cases, such as yawed operation. As mentioned in Section 1.2.6, the correction for closed wind tunnel wall interference is particularly challenging. In the present work, as a preliminary study, the wind tunnel walls are represented by distributed source panels and then interfaced with the turbine and its prescribed wake. This combination of the prescribed wake model with the numerical panel method provides a tool to analyse the wind tunnel wall effects on the wind turbines tested in closed wind tunnels.

This work will document the results from a study of unsteady aerodynamic modelling of HAWT performance, including

1. Modelling of the aerodynamic performance of HAWTs in uniform axial flow using a prescribed wake model;
2. Enhancement and development of the prescribed wake method for unsteady aerodynamic modelling;
3. Inclusion of 3-D effects into the unsteady model;

4. Modelling of tower shadow effects;
5. Study of the wind tunnel wall effects through the combination of the prescribed wake model with a panel method.

Obviously, the investigations presented in this work are directed at design and aerodynamic analysis of HAWTs.

1.4 Outline of the Dissertation

The main body of the dissertation is divided into seven chapters headed by this general introduction. With the exception of the last chapter, *Conclusions and Recommendations*, every chapter begins with an introduction, which briefly gives the background associated with the work in the chapter, and ends with a conclusive section, which highlights the conclusions drawn from the work documented in the chapter.

In Chapter 1, a discussion of status and prospects for wind energy is followed by remarks on wind energy technology. The bulk of the chapter is an introduction to HAWT aerodynamics, in which presented is the history and *status quo* as well as the methodology, theories and models used in HAWT aerodynamics. This provides some of the fundamental theory and background on which this thesis is based. Some experimental work on HAWT aerodynamics is also introduced briefly.

Chapter 2 introduces the prescribed wake model developed at the University of Glasgow and then documents the modelling of HAWT aerodynamic performance in uniform axial flow using this prescribed wake model. The formulation of the model and the calculation procedure are detailed. This chapter does not deal with unsteady aspects but the method presented in the chapter serves as a basic model that will be extended and enhanced in the following chapters to cope with the unsteady aerodynamic characteristics.

In Chapter 3, an unsteady prescribed wake model is described. In particular, the manner by which a semi-empirical unsteady dynamic stall model is coupled with the prescribed wake model to calculate the unsteady aerodynamic forces acting on the rotor blades is described.

In Chapter 4, the unsteady HAWT performance analysis is extended to include 3-D effects due to rotation. A stall delay model is amalgamated with the unsteady prescribed wake model, established in the above chapter, to give the 3-D correction.

Chapter 5 deals with the tower shadow problem. The tower shadow effects are first calculated directly from the unsteady prescribed wake model. After that, a very efficient near wake representation is integrated into the unsteady prescribed wake model to produce a hybrid scheme capable of predicting the blade aerodynamic characteristics together with high resolution loadings in the tower shadow region.

In Chapter 6, a combination of the prescribed wake model with a panel method, which models the wind tunnel walls, is established. The basic effect of the wind tunnel walls is therefore assessed. More importantly, this method demonstrates great potential to analyse and correct the wall interference for wind tunnel tests on wind turbines.

In Chapter 7, the general conclusions of the study are provided and recommendations for future work documented.

Chapter 2

Modelling of HAWT Aerodynamic Performance in Uniform Axial Flow

2.1 Introduction

The gross flow field around HAWTs has, in general, been reasonably well understood for some time (Hansen and Butterfield 1993). Knowledge of detailed aerodynamic effects are, however, still somewhat limited although recent experimental studies have led to increased understanding of unsteady flow phenomena on HAWTs as discussed in Section 1.2. The development of the wake of a HAWT, and hence its aerodynamic performance, are strongly influenced by these phenomena and consequently, mathematical models designed to give detailed solutions of HAWT aerodynamics should endeavour to account for these influences.

The BEM theory, popularly referring to Glauert (1935) and Wilson and Lissaman (1974), is widely used for turbine performance analysis if the gross performance such as power output is the main consideration. However, there are a number of situations where it is not reasonable to expect this theory and its

modified versions (Beans 1983, Jones 1983, Hansen *et al.* 1990, Manwell *et al.* 1991, Ackerman 1992, Wilson and Harman 1995) to offer the required accuracy. These methods do *not directly* take into account the induced effect of the turbine wake on the blades. The distribution of this induced flow is closely linked to the wake structure. The fact that the BEM models do not directly consider the wake structure imposes limits on the application of this type of model, particularly in cases when the wake is concentrated near the turbine. In fact, despite the advantage of a low computational overhead, the BEM theory rarely provides detailed time-dependent aerodynamic information accurately; this is particularly required if aeroelastic and/or aeroacoustic tailoring of the blades is to be achieved. Consequently, many studies have concentrated on the development of calculation schemes that model the turbine wake and its induced effect as an integral part of the solution.

Arguably the most comprehensive method for representing the turbine wake is the application of vortex theory in the form of a free wake analysis. In such a scheme the turbine wake is represented by filaments of trailing and, depending on operating conditions, shed vortices that convect downstream under the influence of the free stream and the global induced flow field. This type of method is fundamentally better suited to the complex flow fields generated by both HAWTs and VAWTs and is capable of accurately reproducing detailed distributed blade loads. The computational effort involved in such a scheme is, however, often prohibitive and, as a result, faster hybrid methods are usually preferred for design purposes.

Prescribed wake modelling has for many years been seen as an alternative to more intensive free wake methods in providing aerodynamic performance estimates for helicopter rotors. This approach has also been applied to wind turbines using both lifting-line and lifting-surface formulations (see Sections 1.2.1 and 1.2.3). The fundamental difference between a prescribed wake method and a free wake model lies in the manner in which the wake geometry is obtained. In free vortex

wake models the wake shape is created by consideration of self-induced velocities of the wake and can be either built up gradually over a number of time steps or obtained by a large number of successive gross distortions of the the entire wake geometry. Both of these techniques can be very time consuming and, although some innovative calculation strategies have evolved, the scope for substantial run-time reductions is limited. In prescribed wake models the detailed wake geometry is defined beforehand, thus avoiding the calculation of the wake self-induction. The prescribed wake method can yield results of comparable accuracy to a free wake method if the wake is correctly prescribed, while requiring only a fraction of the computational power. It is well suited to interactive design and has the potential to be coupled to aeroelastic and aeroacoustic analysis methods.

In this Chapter, the HAWT aerodynamic performance in steady, axial flow conditions is modelled based on the prescribed wake method developed at the University of Glasgow (Robison *et al.* 1995). This model uses simple prescription functions derived for HAWT wakes. The fully developed wake shape is obtained purely by consideration of the induced velocities at the blades. In this way the wake geometry can be viewed as part of the input to the problem rather than as part of the solution and so computation times are substantially reduced.

In the following sections enhancements to the basic prescribed wake model are described and its operating principles are discussed.

2.2 The Prescribed Wake Model

2.2.1 Assumptions and Coordinate Systems

In the study presented in this chapter, the following assumptions are used:

- the flow is inviscid and incompressible;
- the free stream is uniform and steady;

- the rotor is unyawed, *i.e.* the free stream is parallel to the axis of rotation;
- all blades are equally spaced and have identical geometry and aerodynamic characteristics.

The model uses both cartesian and cylindrical coordinate systems, whose original points both are at the centre of rotor, as shown in Fig. 1.7. The earth-fixed cartesian frame of reference (x, y, z) defines the gross flow field. The wind velocity is parallel to the z -axis and its direction defines the positive z -axis, which corresponds to the axis of rotation in the axial flow case. The x -axis lies horizontally along the 3 o'clock position and the y -axis is vertically downward.

For a rotational system, the local blade conditions are often defined more conveniently by the cylindrical coordinates (r, ψ, z). The r -axis lies along the blade. ψ describes the blade azimuthal position and is measured from the positive x -axis.

2.2.2 Blade Model

In order to provide a detailed assessment of the variation in aerodynamic forces across the blade span, each blade is divided into a number of spanwise elements that are considered to be aerodynamically independent. The blade division is carried out in a manner that yields a finer distribution of elements at the blade tip, so giving a more accurate representation of the rapidly changing aerodynamic conditions associated with this region.

The blade elements are defined by the positions of a series of element boundaries along the blade (see Fig. 2.1). There are two sets of control points defined in this study, namely blade element *control points*, positioned at the quarter chord of the mid span of each element, and blade element *boundary points*, positioned at the quarter chord of each element boundary. The wake-induced velocities calculated at the control points and at the boundary points are used to determine the blade loading and the wake shape, respectively.

The blade root section corresponds to the first blade element boundary, which is positioned at 0.1 of the blade radius R . The remaining element boundary distri-

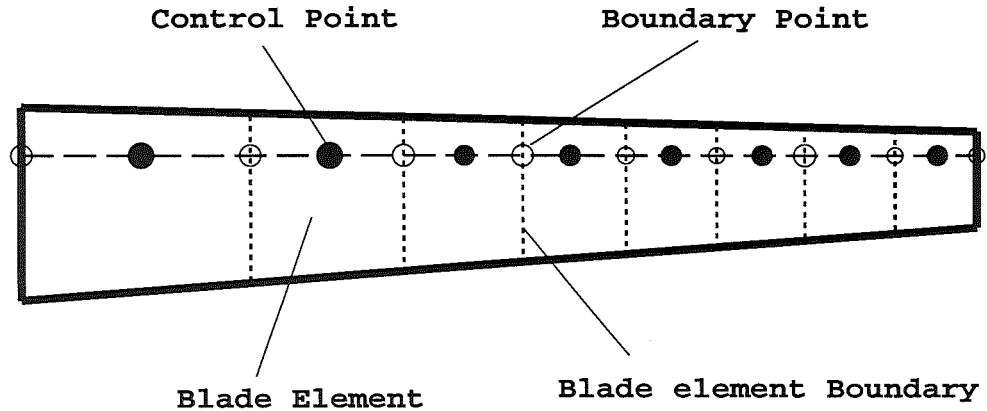


Figure 2.1: Representative blade element distribution

bution along each blade is achieved using the following “arc-cosine” relationship

$$\bar{r} = \frac{r}{R} = \frac{2}{\pi} \arccos \left(1 - \frac{i-1}{N_E} \right)$$

where N_E is the number of blade elements, and i the element boundary number ($i = 2, \dots, N_E + 1$). Therefore, there are N_E element control points and $(N_E + 1)$ boundary points.

If the root radius is R_t instead of $0.1 R$, more generally, the blade element boundary points are distributed according to

$$(\bar{r}_{bp})_i = \begin{cases} \bar{R}_t & \text{for } i = 1 \\ \bar{R}_t + \frac{\frac{2}{\pi} \arccos \left(1 - \frac{i-1}{N_E} \right) - 0.1}{0.9} (1 - \bar{R}_t) & \text{for } i = 2, \dots, N_E + 1 \end{cases} \quad (2.1)$$

where $\bar{R}_t = R_t/R$. The non-dimensional radial distance from the control point to the rotor centre is

$$(\bar{r}_{cp})_i = \frac{1}{2} [(\bar{r}_{bp})_i + (\bar{r}_{bp})_{i+1}] \quad i = 1, 2, \dots, N_E \quad (2.2)$$

The spanwise blade loading distribution is represented by a series of straight-line vortex filaments that lie along the quarter chord of each blade element, the strength, Γ_b , of which is evaluated by application of the Kutta–Joukowski theorem

on the basis of 2-D aerofoil data:

$$L = \rho W \Gamma_b dr$$

where L is the lift on the blade element and W the resultant inflow velocity at the blade element of width dr . The lift can also be expressed in the form,

$$L = \frac{1}{2} \rho W^2 C_l c dr$$

Thus, the bound vorticity for the i th blade element is then

$$(\Gamma_b)_i = \frac{1}{2} W_i C_l c_i \quad (2.3)$$

The spanwise distribution of bound circulation can therefore be obtained by applying Eq. 2.3 to the control point of each blade element.

2.2.3 Wake Model

As air passes through the wind turbine, energy is removed from the flow. This results in a deceleration of the flow in the streamwise direction. From continuity, the radius of the wake will increase as the axial convection velocity decreases. The axial deceleration of the flow is not an instantaneous phenomenon but begins ahead of the turbine and continues until the flow reaches a new equilibrium condition in the far field. Consequently, the wake may be viewed as consisting of two distinct regions. In the first of these, the *near wake*, large-scale changes in the wake geometry occur before the equilibrium state is achieved. Beyond this is the *far wake* which represents the far field equilibrium state of the flow.

Wake Vorticity

In the unyawed, uniform flow case, onset flow conditions remain constant around the azimuth and the wake is therefore composed solely of trailing vorticity, which is modelled as a discretised series of sequential, finite, straight-line vortex filaments extending downstream from the trailing edge of the blade element boundary, as shown in Fig. 2.2.

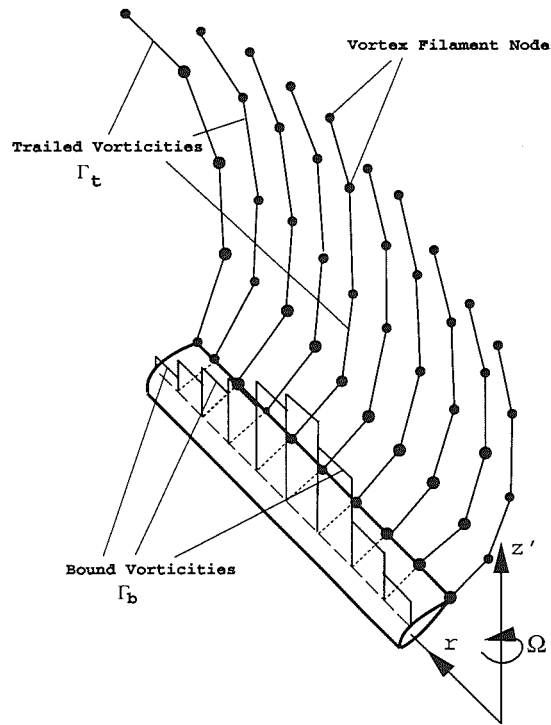


Figure 2.2: Vortex model of blade and rotor wake

The strength of the trailing vortex in the wake is defined to be the difference in bound vorticity between adjacent blade elements. Thus, the strength of the vortex trailing from the i th blade element boundary is given by

$$(\Gamma_t)_i = \begin{cases} (\Gamma_b)_1 & \text{for } i = 1 \\ (\Gamma_b)_i - (\Gamma_b)_{i-1} & \text{for } i = 2, \dots, N_E \\ -(\Gamma_b)_{N_E} & \text{for } i = N_E + 1 \end{cases} \quad (2.4)$$

It should be noted that the trailing vorticity is a vector, the strength of which is positive when its direction is downstream. Since the blade conditions are steady around the azimuth, the strength of the trailing vortex remains constant along the filament throughout the wake.

The Near Wake

Of the two wake regions, the near wake has the greatest influence on the induced velocity at the rotor and therefore the near wake must be prescribed carefully.

A major consideration is the extent of the near wake. The turbine wake structure varies with the operating tip speed ratio. The wake of a rotor operating at a low tip speed ratio is relatively extensive with the trailed vortex system being convected farther downstream from the blade in a given time period than if the rotor operates at a high tip speed ratio. Therefore it seems that the extent of the near wake region varies spatially, depending on the operating conditions. In the model, the physical extent of the near wake is expressed as a function of time, which is related to the tip speed ratio, λ ,

$$T_{nw} = \frac{7\pi\lambda}{4\Omega} \quad (2.5)$$

where T_{nw} is the time period during which the trailing vortex filament is convected from the blade to the *near wake cut-off* point.

In order to avoid the use of high order polynomials when describing the wake geometry, the near wake is divided into three sub-regions. As a result, the axial flow velocity may be described approximately by a linear function of time in each sub-region.

The Far Wake

The far wake describes the region extending downstream to infinity from the last point in the near wake, corresponding to $t = T_{nw}$. The flow field in the far wake represents the equilibrium state of the wake flow. Flow conditions are therefore assumed to remain steady throughout the far wake region, resulting in a cylindrical, axis-symmetric flow field.

Simple momentum theory dictates that the axial induced velocity in the far wake field is twice that at the turbine rotor (Eq. 1.5),

$$(v_z)_1 = 2v_z$$

where $(v_z)_1$ is the axial induced velocity in the far wake and v_z the axial induced velocity at the blade. In a blade element representation the turbine blade is mod-

elled as a series of connected elements that are aerodynamically independent of each other and to which this condition applies. In fact, considerable interaction of the wakes associated with adjacent elements would be expected as the turbine wake expands during its downstream development. This interaction would be particularly significant at the outer edge of the wake where large spanwise gradients in convection velocity exist. Therefore, it is not unreasonable to expect that $(v_z)_1 \neq 2v_z$ along the radial direction. It is necessary, for modelling purposes, to represent this behaviour appropriately in the wake prescription process. For this reason, the axial induced velocity in the far field is defined in terms of the axial induced velocity at the blade using a *far wake velocity parameter*, F , whose value varies along the span,

$$(v_z)_1 = Fv_z \quad (2.6)$$

The conditions in the far wake are achieved at time $t = T_{nw}$ under the following constraints:

1. Axial induced velocity increases from v_z to Fv_z at the start of the far wake;
2. Radial (induced) velocity decreases from v_r , the value at the blade, to zero at the start of the far wake.

These conditions then remain unchanged throughout the semi-infinite cylindrical far wake.

2.2.4 Wake Geometry Prescription

Determination of Wake Geometry Prescription Functions

The complex nature of the flow field means that the parameters which define the wake development are, to a great extent, interdependent. Thus, determination of appropriate prescription functions is problematic if detailed information on the wake structure for a variety of tip speed ratios is not available.

This was found to be a problem in this study as comprehensive and reliable test data were not available to assist in the model development. Therefore, a novel

hybrid prescribed/free wake scheme was developed to determine the optimum solution for the induced velocity functions, near wake cut-off criterion, and far wake velocity parameter. In this technique, an imaginary high-resolution grid, defining a series of node points, was positioned behind the turbine. This technique, which is illustrated for simplicity in a 2-D manner in Fig. 2.3, allowed the induced velocity components to be calculated in a free wake way at each node point and subsequently compared with those prescribed. By starting from an initial approx-

Grid points for induced velocity calculation

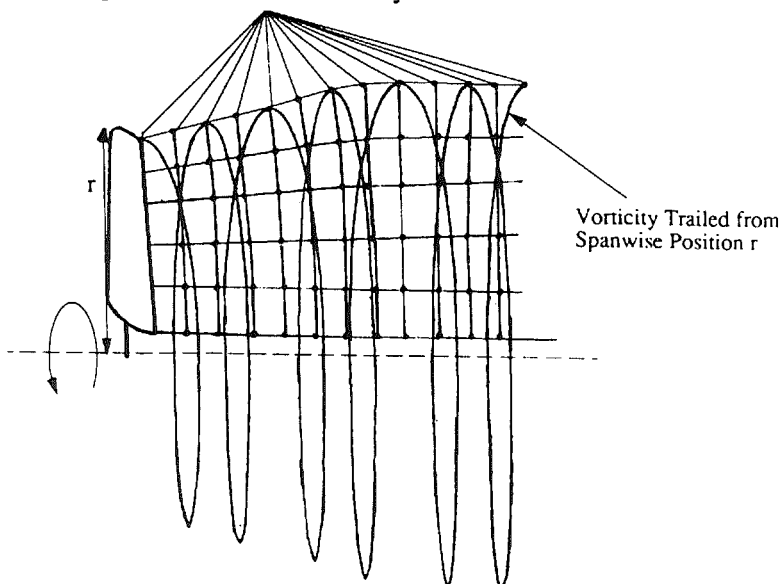


Figure 2.3: Imaginary grid behind a turbine blade in two dimensions: only the wake trailing from the tip is shown for clarity

imation to the required prescription functions, the information from these node points could be used in an iterative loop to provide feedback on the suitability of the current wake shape. This iterative process was continued until the feedback from the grid nodes matched the prescribed velocity distribution throughout the wake over a wide range of tip speed ratios.

It was found that the most appropriate wake geometry is obtained when the radial induced velocity variation is expressed as a quadratic function of time. The

corresponding axial induced velocity is defined as three sub-regions in each of which the velocity development is a linear function of time and 60%, 90%, and 100% of full axial deceleration is achieved, respectively. These relationships are applied over the entire near wake region which is assumed to reach the far wake state after a fixed time has elapsed. This time period, T_{nw} , depends on tip speed ratio. The corresponding spanwise variation in the far wake velocity parameter, F , can be expressed, to a good approximation, as a third-order polynomial of the non-dimensional local radius, \bar{r} . The wake prescription functions have been found to be relatively insensitive to realistic changes in blade planform, solidity and, consequently, the number of blades.

Wake Prescription Functions

Far Wake Axial Velocity Parameter

$$F = 1.1426 + 5.1906\bar{r} - 8.9882\bar{r}^2 + 4.0263\bar{r}^3 \quad (2.7)$$

Axial Development of the Wake

The axial flow velocity in the wake is prescribed as

$$(\bar{V}_z)_w = \begin{cases} 1 - a - \frac{21}{5}(F - 1)a\bar{t} & \text{for } \bar{t} \leq \frac{1}{7} \\ 1 - \frac{1}{2}(1 + F)a - \frac{7}{10}(F - 1)a\bar{t} & \text{for } \frac{1}{7} < \bar{t} \leq \frac{4}{7} \\ 1 - \frac{7 + 23F}{30}a - \frac{7}{30}(F - 1)a\bar{t} & \text{for } \frac{4}{7} < \bar{t} \leq 1 \\ 1 - Fa & \text{for } \bar{t} > 1 \end{cases} \quad (2.8)$$

where a is the axial induced velocity factor at the blade element boundary point,

$$a = -\frac{v_z}{V_0}$$

\bar{t} and $(\bar{V}_z)_w$ are the non-dimensional time and the non-dimensional axial flow velocity in the wake, respectively,

$$\bar{t} = \frac{t}{T_{nw}}$$

$$(\bar{V}_z)_w = \frac{(V_z)_w}{V_0}$$

with t being the time and $(V_z)_w$ the axial velocity in the wake.

It can be seen from Eq. 2.8 that the near wake ($\bar{t} = 0 \rightarrow 1$) is divided into three sub-regions in each of which the axial flow velocity is a linear function of time and that the axial flow velocity in the far wake ($\bar{t} > 1$) is a constant which corresponds to the value at the cut-off point ($\bar{t} = 1$).

The wake axial displacement is simply obtained by integration of the prescribed axial velocity over the associated time period and can be expressed as

$$\bar{z}_w = \begin{cases} \frac{7\pi}{4}(1-a)\bar{t} - \frac{147\pi}{40}(F-1)a\bar{t}^2 & \text{for } \bar{t} \leq 1/7 \\ \frac{\pi}{16}(F-1)a + \frac{7\pi}{4}\left(1 - \frac{1+F}{2}a\right)\bar{t} - \frac{49\pi}{80}(F-1)a\bar{t}^2 & \text{for } 1/7 < \bar{t} \leq 4/7 \\ \frac{47\pi}{240}(F-1)a + \frac{7\pi}{4}\left(1 - \frac{7+23F}{30}a\right)\bar{t} - \frac{49\pi}{240}(F-1)a\bar{t}^2 & \text{for } 4/7 < \bar{t} \leq 1 \\ \frac{2\pi}{5}(F-1)a + \frac{7\pi}{4}(1-Fa)\bar{t} & \text{for } \bar{t} > 1 \end{cases} \quad (2.9)$$

where the wake axial position z_w is normalised by the rotor radius,

$$\bar{z}_w = \frac{z_w}{R}$$

Radial Development of the Wake

The radial induced velocity in the wake is prescribed as

$$(\bar{v}_r)_w = \begin{cases} \bar{v}_r [1 - \bar{t}(2 - \bar{t})] & \text{for } \bar{t} \leq 1 \\ 0 & \text{for } \bar{t} > 1 \end{cases} \quad (2.10)$$

where \bar{v}_r and $(\bar{v}_r)_w$ are the non-dimensional radial induced velocities at the blade element boundary point and in the wake, respectively,

$$\bar{v}_r = \frac{v_r}{V_0}$$

$$(\bar{v}_r)_w = \frac{(v_r)_w}{V_0}$$

The wake radial position, r_w , can be obtained by integrating Eq. 2.10,

$$\bar{r}_w = \frac{r_w}{R} = \begin{cases} \bar{r} + \frac{7}{4}\pi\bar{v}_r\bar{t} \left[1 - \bar{t} \left(1 - \frac{\bar{t}}{3} \right) \right] & \text{for } \bar{t} \leq 1 \\ \bar{r} + \frac{7}{12}\pi\bar{v}_r & \text{for } \bar{t} > 1 \end{cases} \quad (2.11)$$

where \bar{r} is the non-dimensional local radius of the blade element boundary.

During the construction of the initial wake structure, the radial induced velocity at the blade is not available since the full wake is not available. In this case, the wake radial displacement can not be determined by Eq. 2.11. Therefore, an initial strategy for the wake radial development has been proposed. The radial development of the wake from the blade to the near wake cut-off point is defined in a similar manner to the axial development. In the three sub-regions, the radial position of the wake element is determined by a linear function of time and 60%,

90%, and 100% of full radial expansion are achieved, respectively,

$$\bar{r}_w = \begin{cases} \bar{r} + \frac{21}{5} (\bar{r}_1 - \bar{r}) \bar{t} & \text{for } \bar{t} \leq 1/7 \\ \frac{1}{2}(\bar{r} + \bar{r}_1) + \frac{7}{10} (\bar{r}_1 - \bar{r}) \bar{t} & \text{for } 1/7 < \bar{t} \leq 4/7 \\ \frac{1}{30}(7\bar{r} + 23\bar{r}_1) + \frac{7}{30} (\bar{r}_1 - \bar{r}) \bar{t} & \text{for } 4/7 < \bar{t} \leq 1 \\ \bar{r}_1 & \text{for } \bar{t} > 1 \end{cases} \quad (2.12)$$

where \bar{r}_1 is the non-dimensional local radius of the wake element, which is determined by the application of continuity,

$$\bar{r}_1 = \sqrt{\frac{1-a}{1-Fa}} \cdot \bar{r} \quad (2.13)$$

It should be noted that the initial strategy, Eq. 2.12, is applied only during the construction of the initial wake structure. Once the initial wake has been built up, Eq. 2.11 is used for the axial development.

From Eqs. 2.7 through 2.13, it can be seen that the wake velocities and wake geometry in their non-dimensional form are functions neither of the freestream speed V_0 nor of the rotational angular speed Ω . They are instead functions of only the tip speed ratio λ , the combination of V_0 and Ω .

2.3 Performance Calculation

2.3.1 Discretisation

As described in Section 2.2.2, the blade is divided into N_E elements with $(N_E + 1)$ element boundaries (Fig. 2.1). The first blade boundary corresponds to the root section and the $(N_E + 1)$ th to the tip. The blade element is represented by a bound vortex lying on the quarter chord of the element. The radial positions of the i th

element control point and boundary point are $(\bar{r}_{cp})_i$ (Eq. 2.2) and $(\bar{r}_{bp})_i$ (Eq. 2.1), respectively.

For discretisation, a revolution of the rotor is equally divided into N_T time steps. The azimuthal angle at the j th step is

$$\psi_j = \frac{2\pi}{N_T}(j - 1) \quad (2.14)$$

Therefore, the azimuthal position of the k th blade at the j th time step is

$$\psi_{j,k} = \psi_j + \frac{2\pi}{B}(k - 1) \quad (2.15)$$

where $j = 1, 2, \dots, N_T$ and $k = 1, 2, \dots, B$.

In the wake there are $(N_E + 1)$ helical vortex filaments trailing from each blade element boundary and convecting downstream to infinity. These vortex filaments are composed of straight-line elements, each of which corresponds to a time step. When the wake vortex element is downstream far enough, its induction at the blade is negligible. For this reason, the far wake is cut off after N_C cycles and beyond this cut-off point the wake is neglected. Thus, each wake vortex filament has $(N_T \cdot N_C)$ elements, which are defined by their nodes at the two ends (Fig. 2.2).

The time step interval is

$$\Delta t = \frac{2\pi}{\Omega N_T}$$

or in its non-dimensional form,

$$\Delta \bar{t} = \frac{\Delta t}{T_{nw}} = \frac{8}{7\lambda N_T} \quad (2.16)$$

Therefore, the total time for a vortex element to convect downstream from the blade to the wake far end is

$$\bar{T} = N_T \cdot N_C \cdot \Delta \bar{t} = \frac{8N_C}{7\lambda}$$

The j th wake element node in the n th wake cycle corresponds to the time

$$\begin{cases} \bar{t}_{j,n} = [j - 1 + (n - 1)N_T] \Delta \bar{t} \\ j = 1, 2, \dots, N_T \\ n = 1, 2, \dots, N_C \end{cases} \quad (2.17)$$

If we can obtain the axial induced velocity factor $(a_{bp})_{i,j}$ and the normalized radial induced velocity $(\bar{v}_r)_{i,j}^{bp}$ at the blade element boundary point $[(\bar{x}_{bp})_{i,j}, (\bar{y}_{bp})_{i,j}, (\bar{z}_{bp})_{i,j}]$,

$$\left\{ \begin{array}{l} (\bar{x}_{bp})_{i,j} = (\bar{r}_{bp})_i \cos \psi_j \\ (\bar{y}_{bp})_{i,j} = (\bar{r}_{bp})_i \sin \psi_j \\ (\bar{z}_{bp})_{i,j} = 0 \\ i = 1, 2, \dots, N_E + 1 \\ j = 1, 2, \dots, N_T \end{array} \right. \quad (2.18)$$

where i and j denote the blade radial and azimuthal positions, respectively, then substitution of $(a_{bp})_{i,j}$, $(\bar{v}_r)_{i,j}^{bp}$, and $\bar{t}_{j,n}$ for a , \bar{v}_r , and \bar{t} in Eq. 2.9 and Eq. 2.11, or Eq. 2.12 for initial wake, gives the axial and radial positions, $(\bar{z}_w)_{i,j,k,n}$ and $(\bar{r}_w)_{i,j,k,n}$, of the node of the wake element trailing from the i th blade element boundary of the k th blade after $\bar{t}_{j,n}$ time. This wake node position can therefore be expressed, in the cartesian coordinate system, as

$$\left\{ \begin{array}{l} \bar{x}_w(i, j, k, n) = (\bar{r}_w)_{i,j,k,n} \cos \psi_{j,k} \\ \bar{y}_w(i, j, k, n) = (\bar{r}_w)_{i,j,k,n} \sin \psi_{j,k} \\ \bar{z}_w(i, j, k, n) = (\bar{z}_w)_{i,j,k,n} \end{array} \right. \quad (2.19)$$

It should be noted that the last node point of one wake filament cycle is the first point of the following cycle,

$$\bar{x}_w(i, N_T + 1, k, n) = \bar{x}_w(i, 1, k, n + 1)$$

$$\bar{y}_w(i, N_T + 1, k, n) = \bar{y}_w(i, 1, k, n + 1)$$

$$\bar{z}_w(i, N_T + 1, k, n) = \bar{z}_w(i, 1, k, n + 1)$$

2.3.2 Blade Loading and Rotor Performance

Bound Vorticity

The non-dimensional local radius of the control point can be calculated from Eq. 2.2. Then the position of the control point of the i th element at the j th

azimuth is defined, in the cartesian coordinate system, as

$$\begin{cases} (\bar{x}_{cp})_{i,j} = (\bar{r}_{cp})_i \cos \psi_j \\ (\bar{y}_{cp})_{i,j} = (\bar{r}_{cp})_i \sin \psi_j \\ (\bar{z}_{cp})_{i,j} = 0 \\ i = 1, 2, \dots, N_E \\ j = 1, 2, \dots, N_T \end{cases} \quad (2.20)$$

If the induced velocity at the (i, j) th control point is denoted by

$$(\mathbf{v}_{cp})_{i,j} = (v_x)_{i,j}^{cp} \mathbf{i} + (v_y)_{i,j}^{cp} \mathbf{j} + (v_z)_{i,j}^{cp} \mathbf{k}$$

or

$$\frac{(\mathbf{v}_{cp})_{i,j}}{V_0} = (\bar{v}_x)_{i,j}^{cp} \mathbf{i} + (\bar{v}_y)_{i,j}^{cp} \mathbf{j} + (\bar{v}_z)_{i,j}^{cp} \mathbf{k} \quad (2.21)$$

Then the radial and tangential induced velocities, $(v_r)_{i,j}^{cp}$ and $(v_\psi)_{i,j}^{cp}$, can be determined by

$$\begin{bmatrix} (\bar{v}_r)_{i,j}^{cp} \\ (\bar{v}_\psi)_{i,j}^{cp} \end{bmatrix} = \begin{bmatrix} (v_r)_{i,j}^{cp}/V_0 \\ (v_\psi)_{i,j}^{cp}/V_0 \end{bmatrix} = \begin{bmatrix} \cos \psi_j & \sin \psi_j \\ -\sin \psi_j & \cos \psi_j \end{bmatrix} \begin{bmatrix} (\bar{v}_x)_{i,j}^{cp} \\ (\bar{v}_y)_{i,j}^{cp} \end{bmatrix} \quad (2.22)$$

Thus, the axial and tangential inflow velocities $(V_z)_{i,j}^{cp}$ and $(V_\psi)_{i,j}^{cp}$ are expressed as

$$(\bar{V}_z)_{i,j}^{cp} = \frac{(V_z)_{i,j}^{cp}}{V_0} = 1 + (\bar{v}_z)_{i,j}^{cp} \quad (2.23)$$

$$(\bar{V}_\psi)_{i,j}^{cp} = \frac{(V_\psi)_{i,j}^{cp}}{V_0} = \lambda (\bar{r}_{cp})_i - (\bar{v}_\psi)_{i,j}^{cp} \quad (2.24)$$

and the resultant inflow velocity $W_{i,j}^{cp}$ at the (i, j) th control point is obtained from

$$\bar{W}_{i,j}^{cp} = \frac{W_{i,j}^{cp}}{V_0} = \sqrt{[(\bar{v}_r)_{i,j}^{cp}]^2 + [(\bar{V}_\psi)_{i,j}^{cp}]^2 + [(\bar{V}_z)_{i,j}^{cp}]^2} \quad (2.25)$$

The axial and tangential induced velocity factors at the blade element control point are

$$(a_{cp})_{i,j} = -(\bar{v}_z)_{i,j}^{cp} \quad (2.26)$$

and

$$(a'_{cp})_{i,j} = -\frac{(\bar{v}_\psi)_{i,j}^{cp}}{\lambda (\bar{r}_{cp})_i} \quad (2.27)$$

From Eq. 2.3, the bound vorticity $(\Gamma_b)_{i,j}$ at the (i,j) th control point is assessed from

$$(\bar{\Gamma}_b)_{i,j} = \frac{(\Gamma_b)_{i,j}}{4\pi V_0 R} = \frac{1}{8\pi} \bar{W}_{i,j}^{cp} \bar{c}_i (C_l)_{i,j} \quad (2.28)$$

where $\bar{c}_i = c_i/R$ with c_i being the chord of the i th blade element, and $(C_l)_{i,j}$ is the 2-D lift coefficient of the i th blade element at the angle of attack $\alpha_{i,j}$,

$$\alpha_{i,j} = \phi_{i,j} - \theta_i \quad (2.29)$$

where θ_i is the pitch angle of the i th blade element, and the inflow angle

$$\phi_{i,j} = \arctan \frac{(\bar{V}_z)_{i,j}^{cp}}{(\bar{V}_\psi)_{i,j}^{cp}} \quad (2.30)$$

Force Coefficients

From the angle of attack $\alpha_{i,j}$, the element drag coefficient $(C_d)_{i,j}$ can also be determined, and therefore, the element normal and tangential force coefficients are

$$\begin{bmatrix} (C_n)_{i,j} \\ (C_t)_{i,j} \end{bmatrix} = \begin{bmatrix} \cos \alpha_{i,j} & \sin \alpha_{i,j} \\ \sin \alpha_{i,j} & -\cos \alpha_{i,j} \end{bmatrix} \begin{bmatrix} (C_l)_{i,j} \\ (C_d)_{i,j} \end{bmatrix} \quad (2.31)$$

From Eq. 1.13 and 1.14,

$$\begin{bmatrix} (C'_n)_{i,j} \\ (C'_t)_{i,j} \end{bmatrix} = \begin{bmatrix} \cos \phi_{i,j} & \sin \phi_{i,j} \\ \sin \phi_{i,j} & -\cos \phi_{i,j} \end{bmatrix} \begin{bmatrix} (C_l)_{i,j} \\ (C_d)_{i,j} \end{bmatrix} \quad (2.32)$$

Rotor Performance Coefficients

Let

$$\begin{cases} l = j + \frac{N_T}{B}(k-1) \\ j = 1, 2, \dots, N_T + 1 \\ k = 1, 2, \dots, B \end{cases} \quad (2.33)$$

and

$$m = \begin{cases} l & l \leq N_T \\ l - N_T & l > N_T \end{cases} \quad (2.34)$$

According to Eqs. 1.24, 1.25, and 1.27, the rotor performance may be calculated by simple summation as,

$$(C_T)_j = \frac{1}{\pi} \sum_{k=1}^B \sum_{i=1}^{N_E} [\bar{W}_{i,m}^{cp}]^2 (C'_n)_{i,j} \bar{c}_i [(\bar{r}_{bp})_{i+1} - (\bar{r}_{bp})_i] \quad (2.35)$$

$$(C_Q)_j = \frac{1}{\pi} \sum_{k=1}^B \sum_{i=1}^{N_E} [\bar{W}_{i,m}^{cp}]^2 (C'_t)_{i,j} \bar{c}_i (\bar{r}_{cp})_i [(\bar{r}_{bp})_{i+1} - (\bar{r}_{bp})_i] \quad (2.36)$$

and

$$(C_P)_j = \lambda (C_Q)_j \quad (2.37)$$

where j is the blade azimuthal index. The average values of the rotor thrust, torque, and power coefficients over a revolution may be obtained from

$$C_T = \frac{B}{N_T} \sum_{j=1}^{N_T/B} (C_T)_j \quad (2.38)$$

$$C_Q = \frac{B}{N_T} \sum_{j=1}^{N_T/B} (C_Q)_j \quad (2.39)$$

and

$$C_P = \lambda C_Q \quad (2.40)$$

Steady Axial Flow Case

In fact, Eqs. 2.21 through 2.40 are in general suited to unsteady flow cases. For steady axial flow, the iterative process demonstrates some unsteady phenomena before the full steady wake is built up. Once the construction of the steady wake is completed, these expressions are simpler. In this case, the induced velocities and inflow velocity at the blade are independent of the azimuthal angle,

$$\begin{bmatrix} (\bar{v}_r)_i^{cp} \\ (\bar{v}_\psi)_i^{cp} \\ (\bar{v}_z)_i^{cp} \end{bmatrix} = \begin{bmatrix} \cos \psi_j & \sin \psi_j & 0 \\ -\sin \psi_j & \cos \psi_j & 0 \\ 0 & 0 & 1 \end{bmatrix} \begin{bmatrix} (\bar{v}_x)_{i,j}^{cp} \\ (\bar{v}_y)_{i,j}^{cp} \\ (\bar{v}_z)_{i,j}^{cp} \end{bmatrix} \quad (2.41)$$

and

$$\bar{W}_i^{cp} = \sqrt{[(\bar{v}_r)_i^{cp}]^2 + [1 + (\bar{v}_z)_i^{cp}]^2 + [\lambda(\bar{r}_{cp})_i - (\bar{v}_\psi)_i^{cp}]^2} \quad (2.42)$$

It follows that

$$\phi_i = \arctan \frac{1 + (\bar{v}_z)_i^{cp}}{\lambda(\bar{r}_{cp})_i - (\bar{v}_\psi)_i^{cp}} \quad (2.43)$$

$$\alpha_i = \phi_i - \theta_i \quad (2.44)$$

$$\begin{bmatrix} (C_n)_i \\ (C_t)_i \end{bmatrix} = \begin{bmatrix} \cos \alpha_i & \sin \alpha_i \\ \sin \alpha_i & -\cos \alpha_i \end{bmatrix} \begin{bmatrix} (C_l)_i \\ (C_d)_i \end{bmatrix} \quad (2.45)$$

$$\begin{bmatrix} (C'_n)_i \\ (C'_t)_i \end{bmatrix} = \begin{bmatrix} \cos \phi_i & \sin \phi_i \\ \sin \phi_i & -\cos \phi_i \end{bmatrix} \begin{bmatrix} (C_l)_i \\ (C_d)_i \end{bmatrix} \quad (2.46)$$

$$C_T = \frac{B}{\pi} \sum_{i=1}^{N_E} [\bar{W}_i^{cp}]^2 (C'_n)_i \bar{c}_i [(\bar{r}_{bp})_{i+1} - (\bar{r}_{bp})_i] \quad (2.47)$$

$$C_Q = \frac{B}{\pi} \sum_{i=1}^{N_E} [\bar{W}_i^{cp}]^2 (C'_t)_i \bar{c}_i (\bar{r}_{cp})_i [(\bar{r}_{bp})_{i+1} - (\bar{r}_{bp})_i] \quad (2.48)$$

2.3.3 Induced Velocity

It is clear that the key to calculation of the rotor aerodynamic loads and performance is the determination of the velocity at the blade induced by the trailing vortices in the wake. The strength $(\Gamma_t)_{i,j}$ of a wake vortex element trailing from the i th blade element boundary at the j th azimuth is estimated by

$$(\bar{\Gamma}_t)_{i,j} = \frac{(\Gamma_t)_{i,j}}{4\pi V_0 R} = \begin{cases} (\bar{\Gamma}_b)_{1,j} & \text{for } i = 1 \\ (\bar{\Gamma}_b)_{i,j} - (\bar{\Gamma}_b)_{i-1,j} & \text{for } i = 2, \dots, N_E \\ -(\bar{\Gamma}_b)_{N_E,j} & \text{for } i = N_E + 1 \end{cases} \quad (2.49)$$

where $j = 1, 2, \dots, N_T$.

Influence Coefficients of Induced Velocity

A wake vortex element is defined by its two end points, whose coordinates are

$$[\bar{x}_w(i, j, k, n), \bar{y}_w(i, j, k, n), \bar{z}_w(i, j, k, n)]$$

and

$$[\bar{x}_w(i, j+1, k, n), \bar{y}_w(i, j+1, k, n), \bar{z}_w(i, j+1, k, n)]$$

respectively. Let

$$\mathbf{r}_A = [\bar{x} - \bar{x}_w(i, j, k, n)] \mathbf{i} + [\bar{y} - \bar{y}_w(i, j, k, n)] \mathbf{j} + [\bar{z} - \bar{z}_w(i, j, k, n)] \mathbf{k}$$

$$\mathbf{r}_B = [\bar{x} - \bar{x}_w(i, j+1, k, n)] \mathbf{i} + [\bar{y} - \bar{y}_w(i, j+1, k, n)] \mathbf{j} + [\bar{z} - \bar{z}_w(i, j+1, k, n)] \mathbf{k}$$

$$\begin{aligned} \mathbf{r}_{AB} = & [\bar{x}_w(i, j+1, k, n) - \bar{x}_w(i, j, k, n)] \mathbf{i} + [\bar{y}_w(i, j+1, k, n) - \bar{y}_w(i, j, k, n)] \mathbf{j} + \\ & + [\bar{z}_w(i, j+1, k, n) - \bar{z}_w(i, j, k, n)] \mathbf{k} \end{aligned}$$

where $i = 1, 2, \dots, N_E$, $j = 1, 2, \dots, N_T$, $k = 1, 2, \dots, B$, and $n = 1, 2, \dots, N_C$. According to Eq. 1.36, the induced velocity at a point $(\bar{x}, \bar{y}, \bar{z})$ due to the trailing vortex filament element is then determined by

$$\frac{\mathbf{v}_{i,j,k,n}(\bar{x}, \bar{y}, \bar{z})}{V_0} = -\bar{\Gamma} \frac{\mathbf{r}_A \times \mathbf{r}_B}{|\mathbf{r}_A \times \mathbf{r}_B|^2} \left(\frac{\mathbf{r}_A \cdot \mathbf{r}_{AB}}{|\mathbf{r}_A|} - \frac{\mathbf{r}_B \cdot \mathbf{r}_{AB}}{|\mathbf{r}_B|} \right) \quad (2.50)$$

where the minus sign ($-$) is added since a positive trailing vorticity induces negative velocity components. $\bar{\Gamma}$ is the non-dimensional strength of the (i, j, k, n) th trailing vortex element and it must appropriately be chosen from Eq.2.49.

Eq. 2.50 can be re-expressed as

$$(\bar{v}_x)_{i,j,k,n} \mathbf{i} + (\bar{v}_y)_{i,j,k,n} \mathbf{j} + (\bar{v}_z)_{i,j,k,n} \mathbf{k} = -\bar{\Gamma} \mathbf{I}_{i,j,k,n}^t$$

$$\mathbf{I}_{i,j,k,n}^t = (I_x^t)_{i,j,k,n} \mathbf{i} + (I_y^t)_{i,j,k,n} \mathbf{j} + (I_z^t)_{i,j,k,n} \mathbf{k} = \frac{\mathbf{r}_A \times \mathbf{r}_B}{|\mathbf{r}_A \times \mathbf{r}_B|^2} \left(\frac{\mathbf{r}_A \cdot \mathbf{r}_{AB}}{|\mathbf{r}_A|} - \frac{\mathbf{r}_B \cdot \mathbf{r}_{AB}}{|\mathbf{r}_B|} \right)$$

where the superscript t denotes the contribution of the trailing vorticity, and $(I_x^t)_{i,j,k,n}$, $(I_y^t)_{i,j,k,n}$, and $(I_z^t)_{i,j,k,n}$ are called the *influence coefficients* of induced velocity due to the (i, j, k, n) th vortex element,

$$\begin{cases} (I_x^t)_{i,j,k,n} = \frac{(\mathbf{r}_A \times \mathbf{r}_B) \cdot \mathbf{i}}{|\mathbf{r}_A \times \mathbf{r}_B|^2} \left(\frac{\mathbf{r}_A \cdot \mathbf{r}_{AB}}{|\mathbf{r}_A|} - \frac{\mathbf{r}_B \cdot \mathbf{r}_{AB}}{|\mathbf{r}_B|} \right) \\ (I_y^t)_{i,j,k,n} = \frac{(\mathbf{r}_A \times \mathbf{r}_B) \cdot \mathbf{j}}{|\mathbf{r}_A \times \mathbf{r}_B|^2} \left(\frac{\mathbf{r}_A \cdot \mathbf{r}_{AB}}{|\mathbf{r}_A|} - \frac{\mathbf{r}_B \cdot \mathbf{r}_{AB}}{|\mathbf{r}_B|} \right) \\ (I_z^t)_{i,j,k,n} = \frac{(\mathbf{r}_A \times \mathbf{r}_B) \cdot \mathbf{k}}{|\mathbf{r}_A \times \mathbf{r}_B|^2} \left(\frac{\mathbf{r}_A \cdot \mathbf{r}_{AB}}{|\mathbf{r}_A|} - \frac{\mathbf{r}_B \cdot \mathbf{r}_{AB}}{|\mathbf{r}_B|} \right) \end{cases} \quad (2.51)$$

Using Eqs. 2.33 and 2.34, the influence coefficients can be re-written as

$$\begin{cases} I_x^t(i, m, k, n) = (I_x^t)_{i,j,k,n} \\ I_y^t(i, m, k, n) = (I_y^t)_{i,j,k,n} \\ I_z^t(i, m, k, n) = (I_z^t)_{i,j,k,n} \\ i = 1, 2, \dots, N_E + 1 \\ j = 1, 2, \dots, N_T \\ k = 1, 2, \dots, B \\ n = 1, 2, \dots, N_C \end{cases} \quad (2.52)$$

The conversion of the second subscript from j to m ($m = 1, 2, \dots, N_T$) is made for the convenience of the following expression and calculation of the induced velocities.

The vortex element trailing from the i th blade element boundary at the j th azimuth keeps its strength $(\Gamma_t)_{i,j}$ unchanged during its convection downstream. This makes it convenient to summarise the influence coefficients into

$$\left\{ \begin{array}{l} (I_x^t)_{i,j} = \sum_{k=1}^B \sum_{n=1}^{N_C} I_x^t(i, j, k, n) \\ (I_y^t)_{i,j} = \sum_{k=1}^B \sum_{n=1}^{N_C} I_y^t(i, j, k, n) \\ (I_z^t)_{i,j} = \sum_{k=1}^B \sum_{n=1}^{N_C} I_z^t(i, j, k, n) \end{array} \right. \quad (2.53)$$

where the azimuthal index is denoted by j instead of by m .

Induced Velocities

The velocity components at a point $(\bar{x}, \bar{y}, \bar{z})$ induced by the trailing vortex system can be calculated *via* the influence coefficients,

$$\left\{ \begin{array}{l} \bar{v}_x(\bar{x}, \bar{y}, \bar{z}) = - \sum_{i=1}^{N_E+1} \sum_{j=1}^{N_T} (\bar{\Gamma}_t)_{i,j} (I_x^t)_{i,j} \\ \bar{v}_y(\bar{x}, \bar{y}, \bar{z}) = - \sum_{i=1}^{N_E+1} \sum_{j=1}^{N_T} (\bar{\Gamma}_t)_{i,j} (I_y^t)_{i,j} \\ \bar{v}_z(\bar{x}, \bar{y}, \bar{z}) = - \sum_{i=1}^{N_E+1} \sum_{j=1}^{N_T} (\bar{\Gamma}_t)_{i,j} (I_z^t)_{i,j} \end{array} \right. \quad (2.54)$$

Substitution of $(\bar{x}_{cp})_{i,j}$, $(\bar{y}_{cp})_{i,j}$, and $(\bar{z}_{cp})_{i,j}$ (Eq. 2.20) in Eq. 2.54 yields the non-dimensional induced velocity components at the (i, j) th control point of the blade element,

$$\left\{ \begin{array}{l} (\bar{v}_x)_{i,j}^{cp} = \bar{v}_x((\bar{x}_{cp})_{i,j}, (\bar{y}_{cp})_{i,j}, (\bar{z}_{cp})_{i,j}) \\ (\bar{v}_y)_{i,j}^{cp} = \bar{v}_y((\bar{x}_{cp})_{i,j}, (\bar{y}_{cp})_{i,j}, (\bar{z}_{cp})_{i,j}) \\ (\bar{v}_z)_{i,j}^{cp} = \bar{v}_z((\bar{x}_{cp})_{i,j}, (\bar{y}_{cp})_{i,j}, (\bar{z}_{cp})_{i,j}) \end{array} \right. \quad (2.55)$$

where $i = 1, 2, \dots, N_E$ and $j = 1, 2, \dots, N_T$, and they should not be confused with those i and j indices inside the sum operators in Eq. 2.54.

The induced velocity at the blade element boundary point may be obtained using interpolation or extrapolation through the induced velocities at the blade element control points. However, this has been found inappropriate for many cases mainly due to the sensitivity of the trailing vortex induction to the vortex core and to the distance between the vortex and the calculation point. Therefore, an appropriate way to calculate the induced velocities at the blade element boundary point $[(\bar{x}_{bp})_{i,j}, (\bar{y}_{bp})_{i,j}, (\bar{z}_{bp})_{i,j}]$ (Eq. 2.18) is again the application of Eq. 2.54,

$$\begin{cases} (\bar{v}_x)_{i,j}^{bp} = \bar{v}_x((\bar{x}_{bp})_{i,j}, (\bar{y}_{bp})_{i,j}, (\bar{z}_{bp})_{i,j}) \\ (\bar{v}_y)_{i,j}^{bp} = \bar{v}_y((\bar{x}_{bp})_{i,j}, (\bar{y}_{bp})_{i,j}, (\bar{z}_{bp})_{i,j}) \\ (\bar{v}_z)_{i,j}^{bp} = \bar{v}_z((\bar{x}_{bp})_{i,j}, (\bar{y}_{bp})_{i,j}, (\bar{z}_{bp})_{i,j}) \end{cases} \quad (2.56)$$

where $i = 1, 2, \dots, N_E + 1$ and $j = 1, 2, \dots, N_T$. Then the radial and tangential components at the blade element boundary point are

$$\begin{bmatrix} (\bar{v}_r)_{i,j}^{bp} \\ (\bar{v}_\psi)_{i,j}^{bp} \end{bmatrix} = \begin{bmatrix} \cos \psi_j & \sin \psi_j \\ -\sin \psi_j & \cos \psi_j \end{bmatrix} \begin{bmatrix} (\bar{v}_x)_{i,j}^{bp} \\ (\bar{v}_y)_{i,j}^{bp} \end{bmatrix} \quad (2.57)$$

Therefore, the axial and tangential induced velocity factors at the blade element boundary point are

$$(a_{bp})_{i,j} = -(\bar{v}_z)_{i,j}^{bp} \quad (2.58)$$

and

$$(a'_{bp})_{i,j} = -\frac{(\bar{v}_\psi)_{i,j}^{bp}}{\lambda (\bar{r}_{bp})_i} \quad (2.59)$$

Vortex Core

Application of the Biot–Savart law to the vortex system can, under certain flow conditions, introduce numerical instabilities, *i.e.* where a vortex element passes very close to or lies on the calculation point, such as the blade control point under

consideration. In order to avoid such a problem, the idea of a finite vortex core may be utilised. The Biot–Savart law is, therefore, applied to the flow beyond the core radius while a modified relationship between induced velocity and perpendicular distance from the vortex element is used inside the viscous core. This technique results in a more representative estimate of the induced velocity.

For a 2-D vortex the rule that the tangential induced velocity u is inversely proportional to the radius r (see Eq. 1.35) must break down within the small vortex core to avoid an unphysical singularity at the vortex itself because the velocity at the vortex point can never be infinite in reality. The simplest application of this vortex core concept involves considering the velocity induced at a control point to be zero if the control point lies within the vortex core. It has been found in this study, however, that this formulation may also develop numerical divergency during the iteration due to the discontinuity of the induced velocity at the core radius. In fact, viscous effects will adjust the flow in the centre region of the vortex, resulting in smooth, bounded velocity distribution (Rule and Bliss 1998, Corsiglia *et al.* 1973). For this reason, several models for the vortex core have been proposed (Rule and Bliss 1998, Vatistas *et al.* 1991, Scully 1975, Burgers 1948, Lamb 1932).

In the model of Vatistas *et al.* (1991), the tangential velocity in the core is non-dimensionally expressed by

$$\bar{u} = \frac{\bar{r}_c}{(1 + \bar{r}_c^{2n})^{1/n}}$$

where

$$\bar{u} = \frac{u}{\Gamma/(2\pi R_c)}$$

$$\bar{r}_c = \frac{r_c}{R_c}$$

r_c is the distance between the core centre and the point under consideration in the core, R_c is the core radius and n is an integer constant. When $n \rightarrow \infty$, the Vatistas model corresponds to the well-known Rankine model, in which the vortex rotates as a solid body within its core; when $n = 1$, the Vatistas model corresponds to the

Scully model,

$$u = \frac{\Gamma}{2\pi r_c} \frac{\bar{r}_c^2}{1 + \bar{r}_c^2}$$

Full developed vortices seem to exhibit rather simple functional behaviour within the core, which has led to the common use of the Scully algebraic core model (Rule and Bliss 1998).

Vatistas *et al.* (1991) have demonstrated that when $n = 2$ the Vatistas vortex core model

$$\bar{u} = \frac{\bar{r}_c}{\sqrt{1 + \bar{r}_c^4}} \quad (2.60)$$

provides the best fit to a series of sets of experimental data. For this reason and owing to its relatively smooth connection with the Biot–Savart law at the core radius, Eq. 2.60 is modified for a 3-D vortex element in the present study and then applied to calculate the induced velocity within the vortex core.

2.3.4 Procedure of Calculation

The numerical procedure for implementing the prescribed wake model for the calculation of HAWT aerodynamic performance in unyawed flow is outlined in Fig. 2.4 and involves an iterative process which is designed to obtain a convergent solution for the wake geometry and the blade loading. The complete calculation scheme is described in detail as follows:

1. Input of System Parameters

The parameters required to be input to the model include

- number of blade elements N_E
- number of time steps per revolution N_T
- number of wake cycles N_C

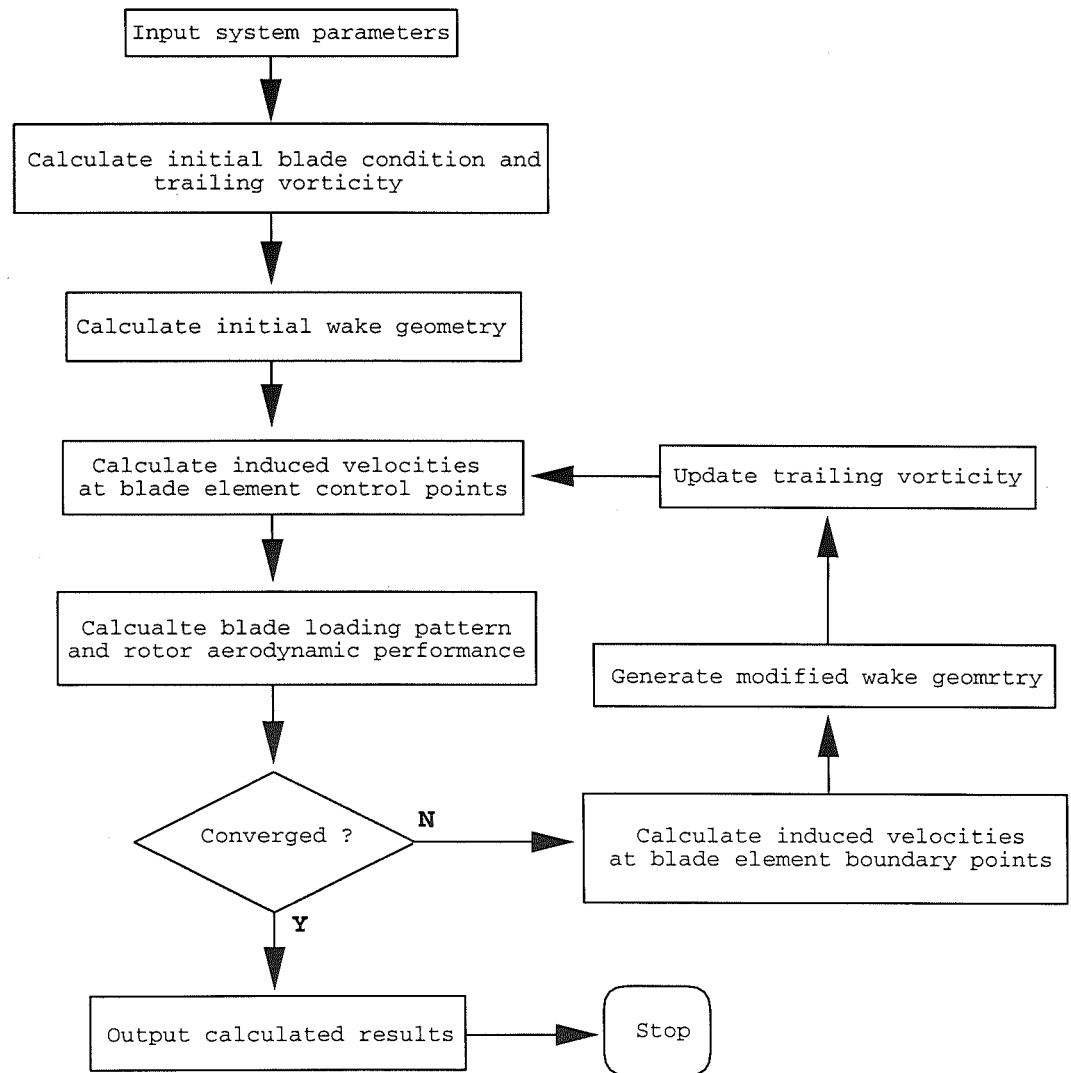


Figure 2.4: Flow chart of the calculation scheme for the steady prescribed wake model

- number of blades B
- tip speed ratio λ
- rotor radius R
- blade root radius R_t
- blade chord spanwise distribution c_i
- blade pitch spanwise distribution θ_i
- variation of 2-D aerofoil data C_l and C_d with angle of attack

It should be noted that in order to break the cycle down into discrete steps the number of time steps per revolution, N_T , must be exactly divisible by the number of blades, B , namely (N_T/B) must be an integer.

2. Calculation of Initial Blade Condition

Results from the prescribed wake model are independent of the initial inputs to it unless the initial blade condition involves reversed flow. However, good initial values can substantially reduce the overall computational times in which the prescribed wake model obtains convergent results. The initial values for the main iteration of the prescribed wake model are obtained using the BEM theory described in Section 1.2.2. Wilson and Lissaman (1974) proposed a simple iterative procedure in the well-known PROP code to determine the induced velocity factors a and a' . Unfortunately, this iteration is not always converged. Since it is found that the results from BEM theory are good initial values for the prescribed wake model, it is important to obtain a convergent solution from the BEM theory. Therefore, an iterative procedure using linear interpolation is utilised in the study. The iteration takes place within a region where only a single solution exists and is described as follows.

Eqs. 1.30 and 1.31 can be rearranged as

$$f_a(a, a') = \sigma C'_n (1 - a) - 8 F a \sin^2 \phi = 0 \quad (2.61)$$

$$f_t(a, a') = \sigma C'_t (1 + a') - 8 F a' \sin \phi \cos \phi = 0 \quad (2.62)$$

Thus, the solutions $a = a_*$ and $a' = a'_*$ must satisfy Eqs. 2.61 and 2.62.

Let the p th iteration result of the axial induced velocity factor a be a_p . Then the corresponding tangential induced velocity factor a'_p , which satisfies Eqs. 2.62, can be obtained using the following iteration,

$$\begin{cases} (a'_p)_{q+1} = \frac{(a'_p)_{q-1} f_t(a_p, (a'_p)_q) - (a'_p)_q f_t(a_p, (a'_p)_{q-1})}{f_t(a_p, (a'_p)_q) - f_t(a_p, (a'_p)_{q-1})} \\ q = 1, 2, \dots \end{cases} \quad (2.63)$$

If the two values $(a'_p)_{q-1}$ and $(a'_p)_q$ are chosen such that $f_t(a_p, (a'_p)_{q-1})$ and $f_t(a_p, (a'_p)_q)$ are of opposite sign, namely,

$$f_t(a_p, (a'_p)_{q-1}) \cdot f_t(a_p, (a'_p)_q) < 0 \quad q = 1, 2, \dots$$

and this is maintained from the start to the finish of the process of iteration Eq. 2.63, $(a'_p)_{q+1}$ converges to a'_p . From Eq. 2.61, the factor a can be obtained using the same iterative method as follows:

$$\begin{cases} a_{p+1} = \frac{a_{p-1} f_a(a_p, a'_p) - a_p f_a(a_{p-1}, a'_{p-1})}{f_a(a_p, a'_p) - f_a(a_{p-1}, a'_{p-1})} \\ p = 1, 2, \dots \end{cases} \quad (2.64)$$

If the two values a_{p-1} and a_p are chosen such that $f_a(a_{p-1}, a'_{p-1})$ and $f_a(a_p, a'_p)$ are of opposite sign, namely,

$$f_a(a_{p-1}, a'_{p-1}) \cdot f_a(a_p, a'_p) < 0 \quad q = 1, 2, \dots$$

and this is maintained from the start to the finish of the process of iteration Eq. 2.64, a_{p+1} converges to a_* .

Finally, a'_* corresponding to a_* is calculated by the iteration Eq. 2.63.

Once all of the induced velocity factors, $(a_{bp})_{i,j}$ and $(a'_{bp})_{i,j}$, at the blade element boundary points are determined, the induction factors at the blade element control points can be approximated by

$$(a_{cp})_{i,j} = \frac{1}{2}[(a_{bp})_{i,j} + (a_{bp})_{i+1,j}]$$

$$(a'_{cp})_{i,j} = \frac{1}{2}[(a'_{bp})_{i,j} + (a'_{bp})_{i+1,j}]$$

Then the $(N_E \cdot N_T)$ bound vorticities $(\bar{\Gamma}_b)_{i,j}$ ($i = 1, 2, \dots, N_E$, and $j = 1, 2, \dots, N_T$) can be calculated from Eq. 2.28, where the inflow velocity is obtained from

$$\bar{W}_{i,j}^{cp} = \sqrt{[1 - (a_{cp})_{i,j}]^2 + \lambda^2 (\bar{r}_{cp})_i^2 [1 + (a'_{cp})_{i,j}]^2}$$

instead of from Eq. 2.25.

From Eq. 2.49, $[(N_E + 1) \cdot N_T]$ trailing vorticities $(\bar{\Gamma}_t)_{i,j}$ ($i = 1, 2, \dots, N_E + 1$, and $j = 1, 2, \dots, N_T$) are obtained.

3. Construction of Initial Wake Geometry

Using the results from the BEM theory, the initial wake geometry can be determined from the prescription functions (Eqs. 2.9 and 2.12). The cartesian coordinates of the wake elements are then calculated from Eq. 2.19.

4. Calculation of the induced velocities at the Blade Element Control Points

The Biot–Savart law is applied to calculate the induced velocities at the blade element control points (Eq. 2.55) *via* the induced velocity influence coefficients.

5. Calculation of the Performance

Based on the results from the vortex theory above, the aerodynamic parameters, such as blade angle of attack, inflow velocity, bound vorticity, aerodynamic

forces on the blades, and the rotor performance as well, are calculated as detailed in Section 2.3.2.

6. Calculation of the induced velocities at the Blade Element Boundary Points

Usually, the results obtained in Step 5 above do not compare well in the first few iterations with the previous iterative results. Therefore, a new wake structure should be created. For this reason, the Biot–Savart law is again applied to compute the induced velocities at the blade element boundary points (Eq. 2.56). The axial induced velocity factor (Eq. 2.58) and radial induced velocity (Eq. 2.57) are then calculated for the generation of the new wake.

7. Modification of Wake Structure

Based on the newly calculated induced velocities at the blades, a new wake structure (Eq. 2.19) for the current blade position is generated with the aid of the prescription functions (Eqs. 2.9 and 2.11).

8. Modification of Trailing Vorticities

From Eq. 2.49, $[(N_E + 1) \cdot B]$ trailing vorticities $(\bar{\Gamma}_t)_{i,m}$ are obtained, where $i = 1, 2, \dots, N_E + 1$, and the azimuthal index m is determined by Eqs. 2.33 and 2.34. In this way, the trailing vorticities at the current positions of the blades are updated.

The blades then move to the next azimuthal position (Eqs. 2.18 and 2.20). The calculation goes back to Step 4 above and repeats Steps 4 to 8 until global convergence of the wake shape with the loading distribution is achieved.

2.4 Results and Discussion

Gross Rotor Performance

The primary aim of the present prescribed wake model is to provide a means of obtaining accurate estimates of turbine aerodynamic performance for use as an integral part of the design process of HAWTs. The power output of the wind turbine is a very important parameter for the wind turbine aerodynamic performance, as wind turbines are used to extract energy from the wind.

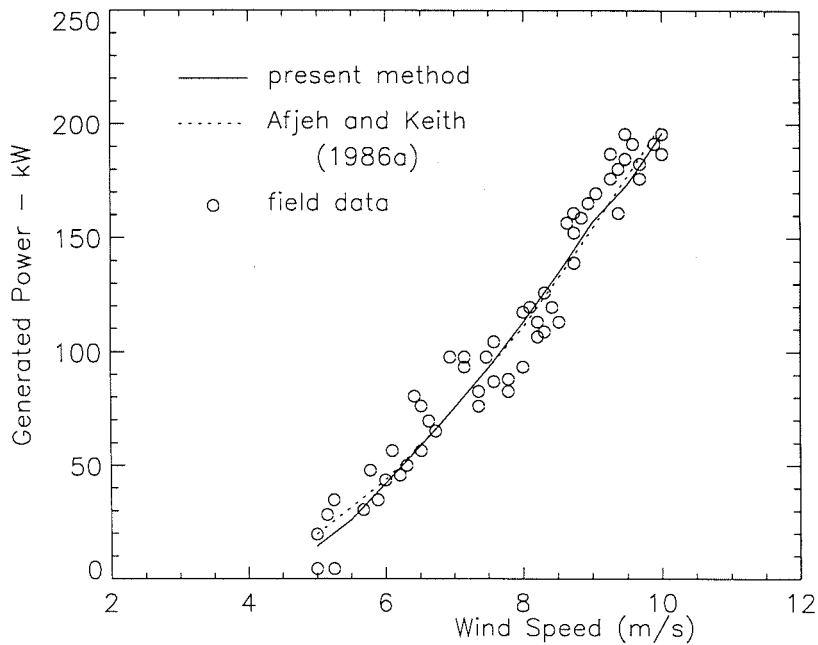


Figure 2.5: Comparison of generated power for MOD–OA turbine

Fig. 2.5 shows the generated power results for the MOD–OA turbine predicted by the prescribed wake model and compared with field measurements (Spera and Janetzke 1981). The results are also compared in the figure with the numerical predictions obtained from the free wake method of Afjeh and Keith (1986a), since free wake analysis is the most sophisticated means of predicting HAWT performance.

It should be noted that the predicted rotor power values have been converted to the generator power outputs by accounting for the efficiency and drive train loss. The predicted values from the prescribed wake model compare well with both the field data and the free wake analysis over the entire range of operating conditions, especially at moderate wind speeds.

The largest differences between the prescribed and free wake predictions can be seen to occur at low wind speeds or high tip speed ratios, although both predictions fall within the scatter of the field data. At the high tip speed ratio, the turbine wake has a compact structure, resulting in highly concentrated vorticity in close proximity to the blades. This type of flow regime can cause problems for vortex techniques through blade–vortex and vortex–vortex interactions. Under these conditions, the tip vortex interaction effects are particularly appreciable and the lifting-line assumption is no longer valid for the sections close to the blade tip since large variations occur in the chordwise pressure distribution (Afjeh and Keith 1986a). This leads to inaccurate prediction of the turbine aerodynamic performance for both the prescribed and free wake methods.

There are also small differences in the predictions between the prescribed and free wake methods at high wind speeds, or low tip speed ratios. Under these conditions the proportion of the blade operating in stall increases, which can be seen from Fig. 2.6 showing the variations in angle of attack along the blade at $V_0 = 10$ m/s and $V_0 = 5$ m/s, respectively. One reason for the differences when operating in this flow regime could be a lack of reliable aerodynamic data for the aerofoil in the post stall regime. Additionally, 3-D effects become highly significant when a large portion of the blade is operating in separated flow, as discussed in Section 1.2.5. Therefore, the quasi 2-D flow assumption used in the model gives an inaccurate representation of the aerodynamic conditions at these high wind speeds.

The differences between the prescribed and free wake models may also result, though not mainly, from the manner in which the wake is prescribed. Fig. 2.7 illustrates the difference in the far wake velocity parameter F between the pre-

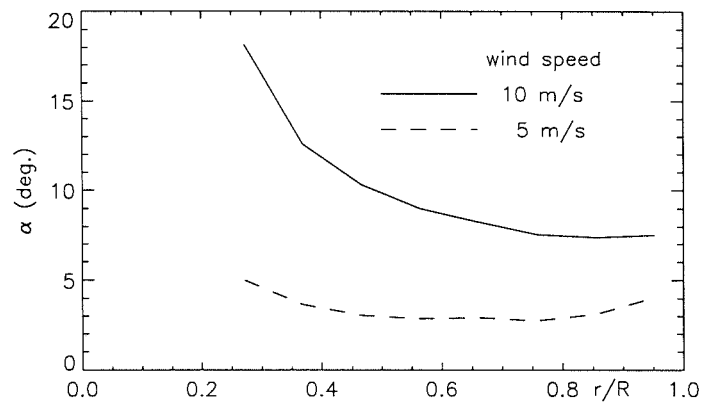


Figure 2.6: Calculated angle of attack for MOD-OA turbine at $V_0 = 10$ m/s and $V_0 = 5$ m/s

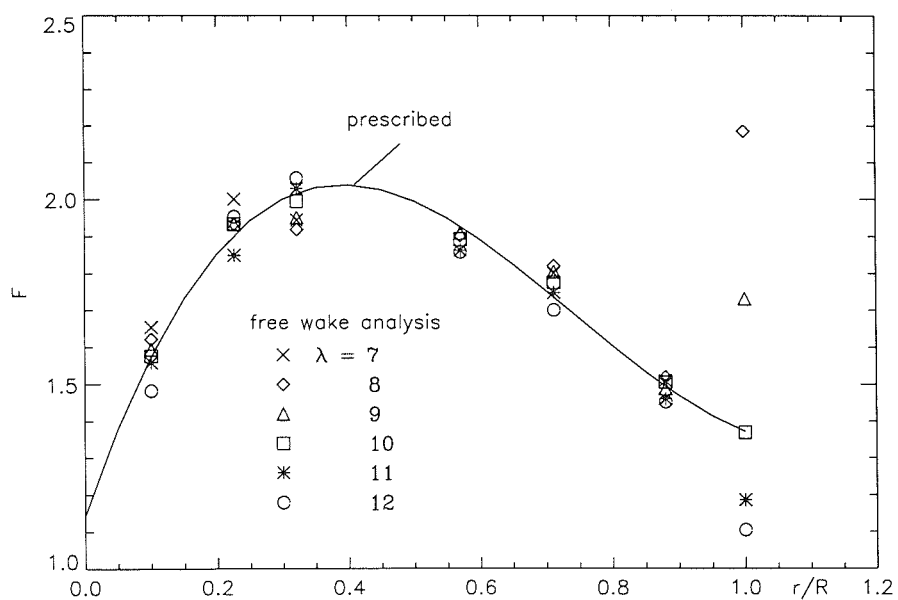


Figure 2.7: Comparison of far wake velocity parameter

scribed wake model and free wake calculation (Robison *et al.* 1994) for a rotor consisting of two blades with a constant pitch angle of 4° and a taper ratio of 0.25. The prescribed values, which correspond to the best fit curve through the hybrid prescribed/free wake estimates and are independent of the tip speed ratio, cannot cover all results from the free wake analysis at various tip speed ratios, especially in the tip region where it is difficult to accurately evaluate average induced velocities due to the extremely steep velocity gradients which exist near the wake boundaries. In order to improve the accuracy of the wake prescription, the prescribed value of F at the tip has been modified through an empirical linear function of tip speed ratio.

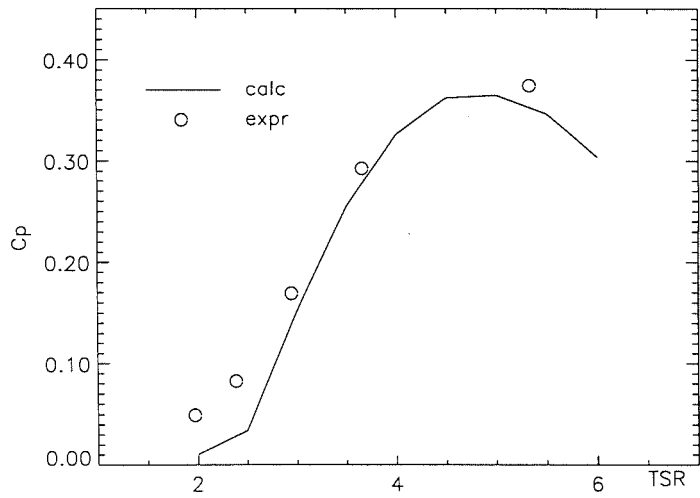


Figure 2.8: Comparison of rotor power coefficient for NREL UAE Phase IV turbine

Fig. 2.8 shows a comparison between field measurements (Schepers *et al.* 1997) on the NREL Unsteady Aerodynamics Experiment (UAE) Phase IV turbine and the rotor power coefficient predicted by the prescribed wake model. The description of the wind turbine can be found in Appendix B. Analogously to the comparison for the turbine MOD-OA, it seems that the prescribed wake model underestimates the rotor power at low and high tip speed ratios while the prediction compares well with the field data at moderate tip speed ratios. The reasons for

this are likely to be similar to those discussed above in the previous MOD–OA case. It is anticipated that the level of the agreement at the low tip speed ratios could be improved if the 3-D effects are included in the prescribed wake model.

High Tip Speed Ratio Cases

In its present form, the model is not designed to deal with large scale reversed flow regions. This should be borne in mind when results are required at high tip speed ratios, where various reverse flow states may be induced.

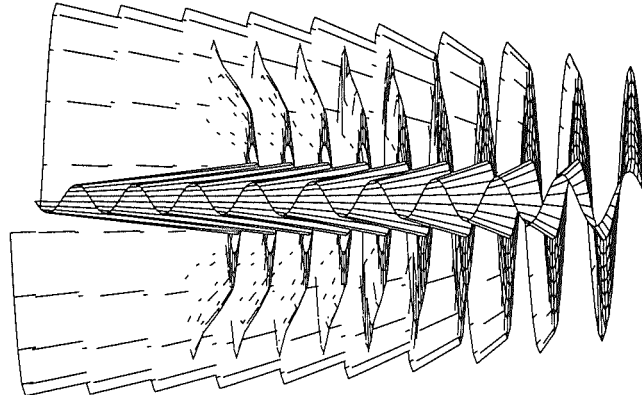


Figure 2.9: Calculated wake structure for MOD–OA turbine at $V_0 = 5 \text{ m/s}$

Figs. 2.9 and 2.10 present the wake structures calculated for the MOD–OA turbine using the prescribed wake model at $V_0 = 5 \text{ m/s}$ ($\lambda = 16$) and $V_0 = 10 \text{ m/s}$ ($\lambda = 8$), respectively. In the figures the flow direction is from right to left and, for clarity, the structure trailed from only one blade is shown. Noticeable in the figures is the high convection rate of the wake filaments that emanate from the blade root. This occurs because the blockage associated with the turbine nacelle

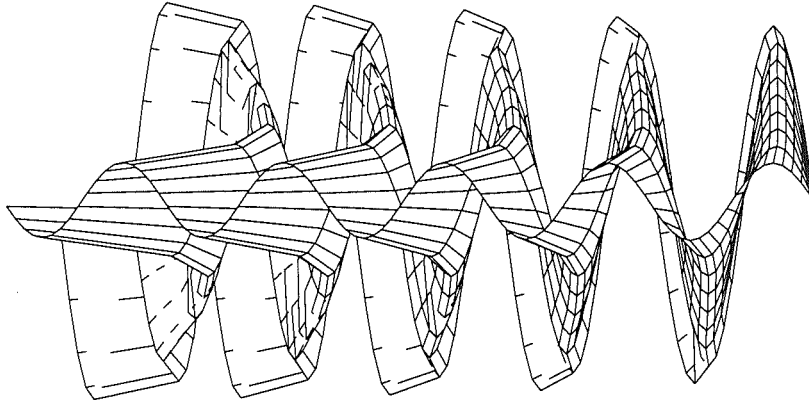


Figure 2.10: Calculated wake structure for MOD–OA turbine at $V_0 = 10 \text{ m/s}$

is not represented in the calculation. For comparison, the wakes are cut off at the same non-dimensional time $\bar{t} = 0.7143$ in the both figures. It can be seen, more importantly, that the wake structure at $V_0 = 5 \text{ m/s}$ is more compact than that at $V_0 = 10 \text{ m/s}$. This can be attributed to the lower wind speed and relatively higher induced velocity; the latter can be viewed from Fig. 2.11, where the calculated axial induced velocity factors at these two wind speeds are compared.

Since the prescribed wake model was not developed to deal with large scale reverse flow regions, the unrepresentative wake shapes at high tip speed ratios produce artificially high induced velocities at the blades in a prescribed wake model. This feature makes the prescribed wake model underestimate the rotor power at high tip speed ratios, as revealed in Figs. 2.5 and 2.8. When the tip speed ratio is high enough, the high induced velocities produce a more condensed wake structure, which, more severely, results in a divergent iteration, a problem also reported by Koh and Wood (1991*b*). For example, the calculation for the NREL UAE Phase

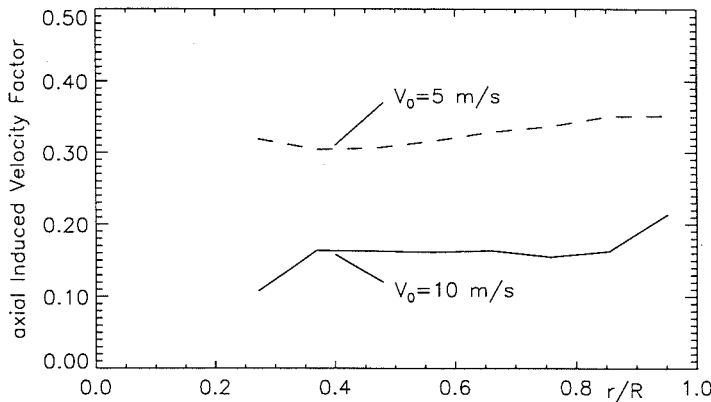


Figure 2.11: Induced velocity factor for MOD–OA turbine at $V_0 = 10 \text{ m/s}$ and $V_0 = 5 \text{ m/s}$

IV turbine fails to converge at $\lambda = 6.5$, which is rather high for this machine.

In the present study the wake is prescribed using simple geometry prescription functions derived from consideration of momentum theory. Vortex roll-up is not modelled in the prescribed wake method. However, there is strong evidence that vortices trailed from the rotor blades tend to roll up into discrete, concentrated tip vortices which remain approximately in the cycloidal trace of the blade tips (McCroskey 1995). Fig. 2.12 gives the calculated bound circulation distributions for the MOD–OA turbine blade, from which it can be seen that the bound vorticities near the tip and near the root are of the same order. Therefore, it is expected that there would be a root vortex roll-up for a HAWT, addition to the existence of a strong tip vortex, which has been clearly shown by Savino and Nyland (1983) through field-based flow visualisation studies under low power generation conditions. It is possible that modelling of the tip and root roll-up may improve the level of accuracy of the prescribed wake model at high tip speed ratios.

At high tip speed ratios the HAWT blade may induce a turbulent wake state at a certain downstream distance, where there are highly complex changes in the

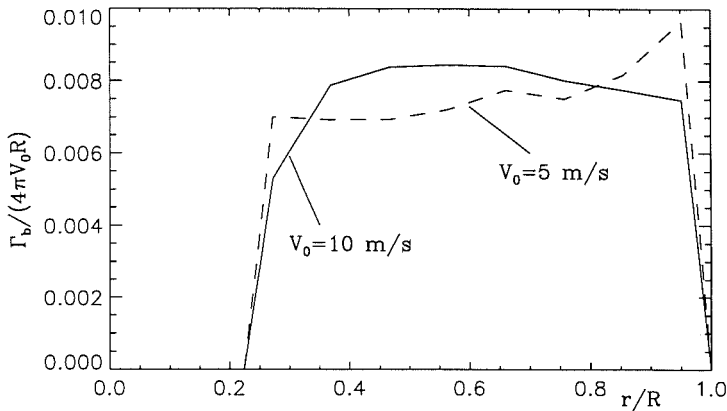


Figure 2.12: Bound circulation distribution along the MOD–OA turbine blade

trailing vortex structures. The strictly inviscid theory of Helmholtz and Kelvin is applied for the distribution of the wake vorticities in the prescribed wake model. In reality, the viscous nature of the flow must be always appreciated. At certain downstream distances, viscous forces cause the dissipation and breakdown of the vortex structure (Spalart 1998). It can be imaged that the dissipation of the wake vorticity in the HAWT turbulent wake state is particularly significant. Although precise influence of turbulence on the dynamics of the vortex structure is unclear, several models for vorticity dissipation have been proposed (Lamb 1932, Squire 1965, Owen 1970, Corsiglia *et al.* 1973, Saffman 1973). Appropriate accounting of vortex diffusion may eliminate the divergent problem in the prescribed wake model at high tip speed ratios and make calculated results more reliable.

Vortex Core Size

Fully developed vortices seem to exhibit rather simple functional behaviour within the core, which has led to several empirical and semi-empirical vortex models. However, it is necessary for the most models to adjust the core size for every configuration of interest usually through fitting to relative experimental data. This limits the model to either fitting data or makes the choice of the vortex size arbit-

rary.

Basuno (1992) examined the influence of the vortex size on the aerodynamic performance of a VAWT, indicating that a choice of too small a core size would not produce a convergent solution. In other words, the vortex core size must be set to be large enough to eliminate the singularity. It was also found that there were no significant differences in the performance if the core size R_c varied from 0.1% to 1% of the blade chord.

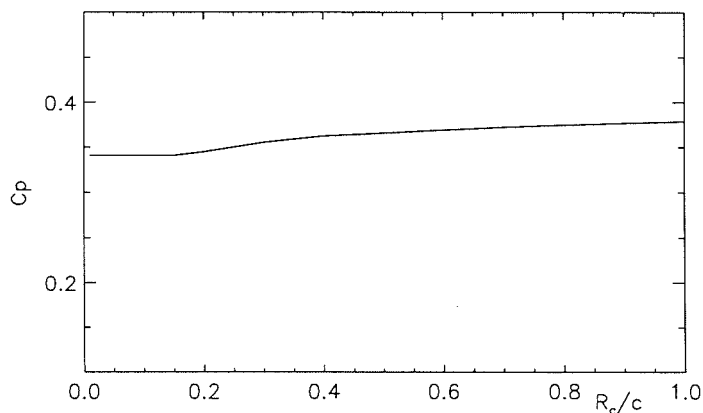


Figure 2.13: Influence of vortex core size on power coefficient for the MOD–OA turbine at $\lambda = 10$

Fig. 2.13 shows the power coefficient variation of the MOD–OA rotor with different sizes of vortex core at $\lambda = 10$. When the core size is increased from $R_c = 0.01c$ to $R_c = 0.15c$ there is little change in the power coefficient. Beyond that the power coefficient gradually increases with the increasing core size.

According to Landahl (1981), vortex sizes before breakdown may be expected to be of the order of 0.06 of the blade chord. However, Miller (1985) indicated that reasonable agreement with the test data resulted only after the core size R_c was increased by a factor of 10, to 0.6 of the blade chord. This may be related to the influence of turbulence. Most vortex cores are turbulent. The motion is irregular and the rate of diffusion much greater than if the flow were laminar. In order to avoid arbitrary choice, the vortex core size is fixed to be $R_c = 0.6c$, as suggested by Miller, for all wind turbine configurations studied.

Blade Aerodynamic Loading

Table 2.1: Overview of NREL UAE Phase I field datasets (source: NREL)

Dataset No.	1	2	3	4	5	6
Mean Vel. (m/s)	12.5	12.3	12.5	12.3	15.9	15.9
Mean Yaw (deg.)	0.4	-0.2	-19.7	9.9	-17.2	-30.1
Vel. S.D. (m/s)	0.62	0.48	0.40	0.33	0.62	0.92
Yaw S.D. (deg.)	2.28	2.31	5.03	1.75	7.97	1.89
Min. Vel. (m/s)	11.0	11.5	11.6	12.0	14.0	13.7
Max. Vel. (m/s)	13.2	13.1	12.9	13.1	16.8	16.9
Min. Yaw (deg.)	-5.2	-4.9	-30.3	6.6	-30.4	-34.8
Max. Yaw (deg.)	4.3	5.0	-7.3	13.0	2.9	-27.1
No. of Cycles	6	6	6	7	7	5

Table 2.2: Overview of NREL UAE Phase I field datasets (source: Schepers *et al.* 1997)

Dataset No.	1	2	3	4
Mean Vel. (m/s)	10.5	19.2	6.1	7.8
Mean Yaw (deg.)	1.3	1.6	-35.4	21.4
Vel. S.D. (m/s)	1.05	1.98	0.59	0.47
Yaw S.D. (deg.)	5.40	8.71	4.91	11.94
Min. Vel. (m/s)	8.4	14.8	4.8	6.7
Max. Vel. (m/s)	14.1	24.4	7.0	8.8
Min. Yaw (deg.)	-14.3	-17.3	-43.9	-3.5
Max. Yaw (deg.)	16.8	20.3	-20.9	47.2
No. of Cycles	72	72	18	18

While overall performance is a useful indicator of gross predictive capability, it is more informative to examine load variations at various locations along the

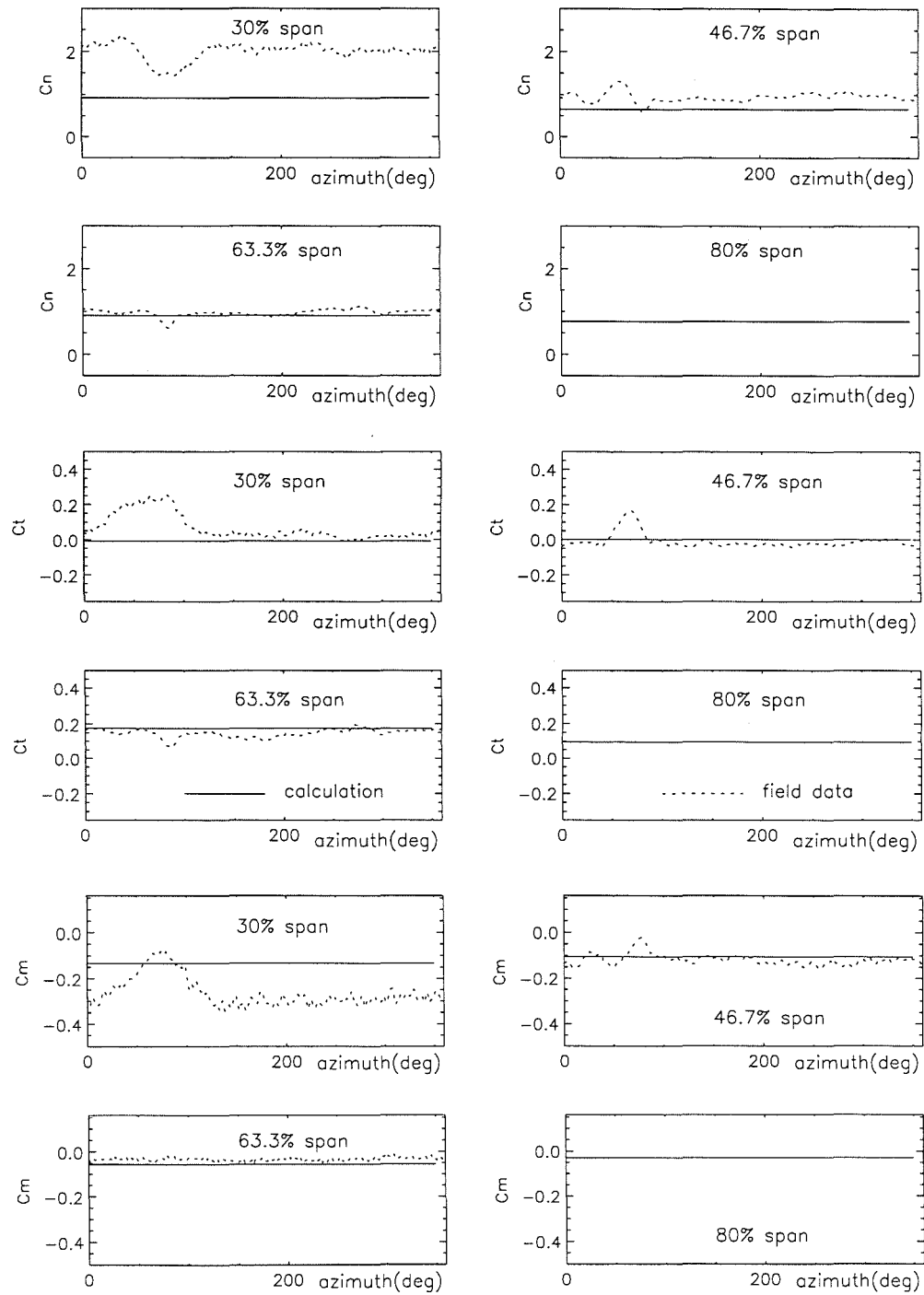


Figure 2.14: Comparison of predicted blade aerodynamic loading with field data of NREL UAE Phase I at $V_0 = 12.5$ m/s and $\gamma = 0.4^\circ$

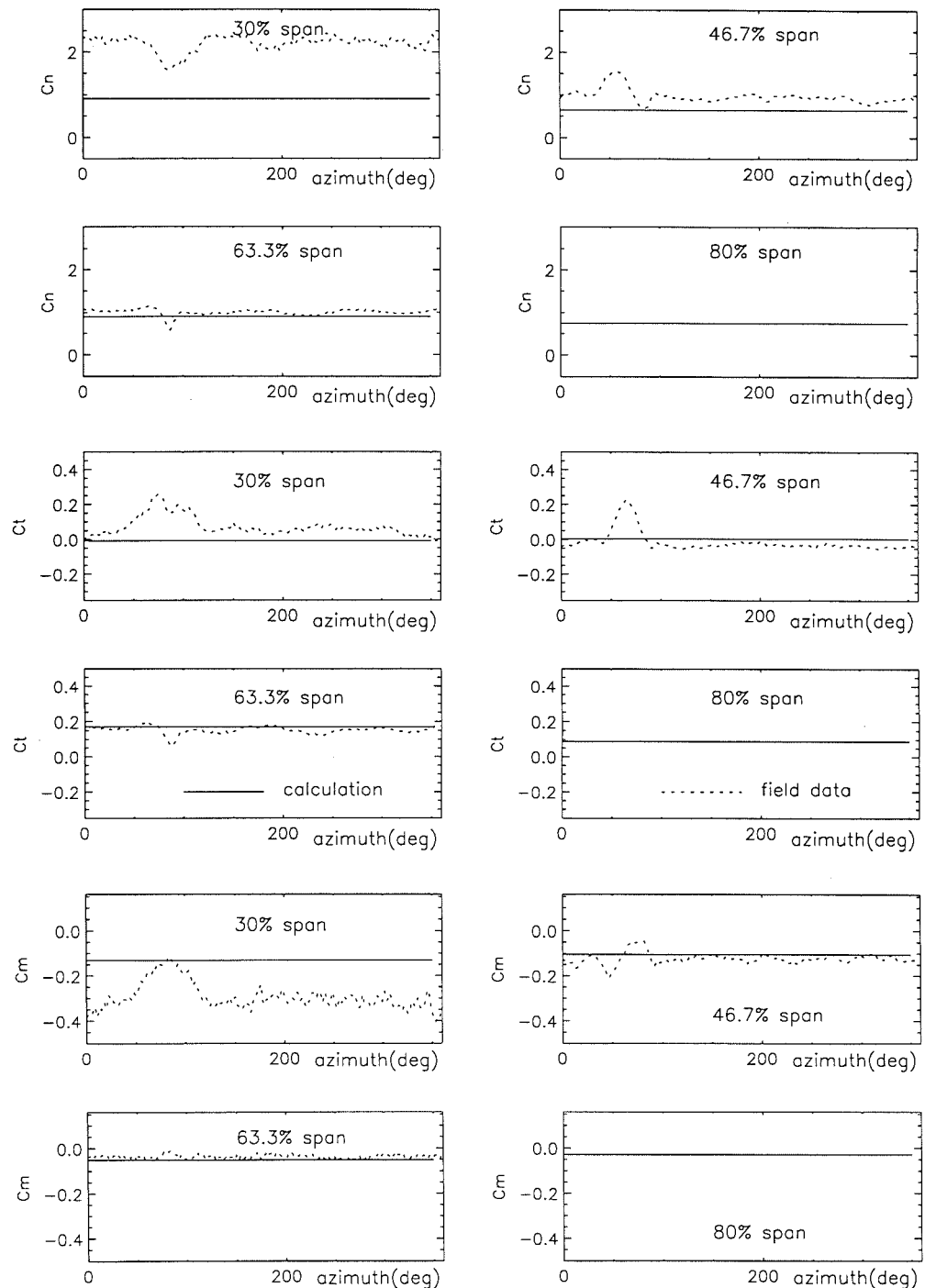


Figure 2.15: Comparison of predicted blade aerodynamic loading with field data of NREL UAE Phase I at $V_0 = 12.3$ m/s and $\gamma = -0.2^\circ$

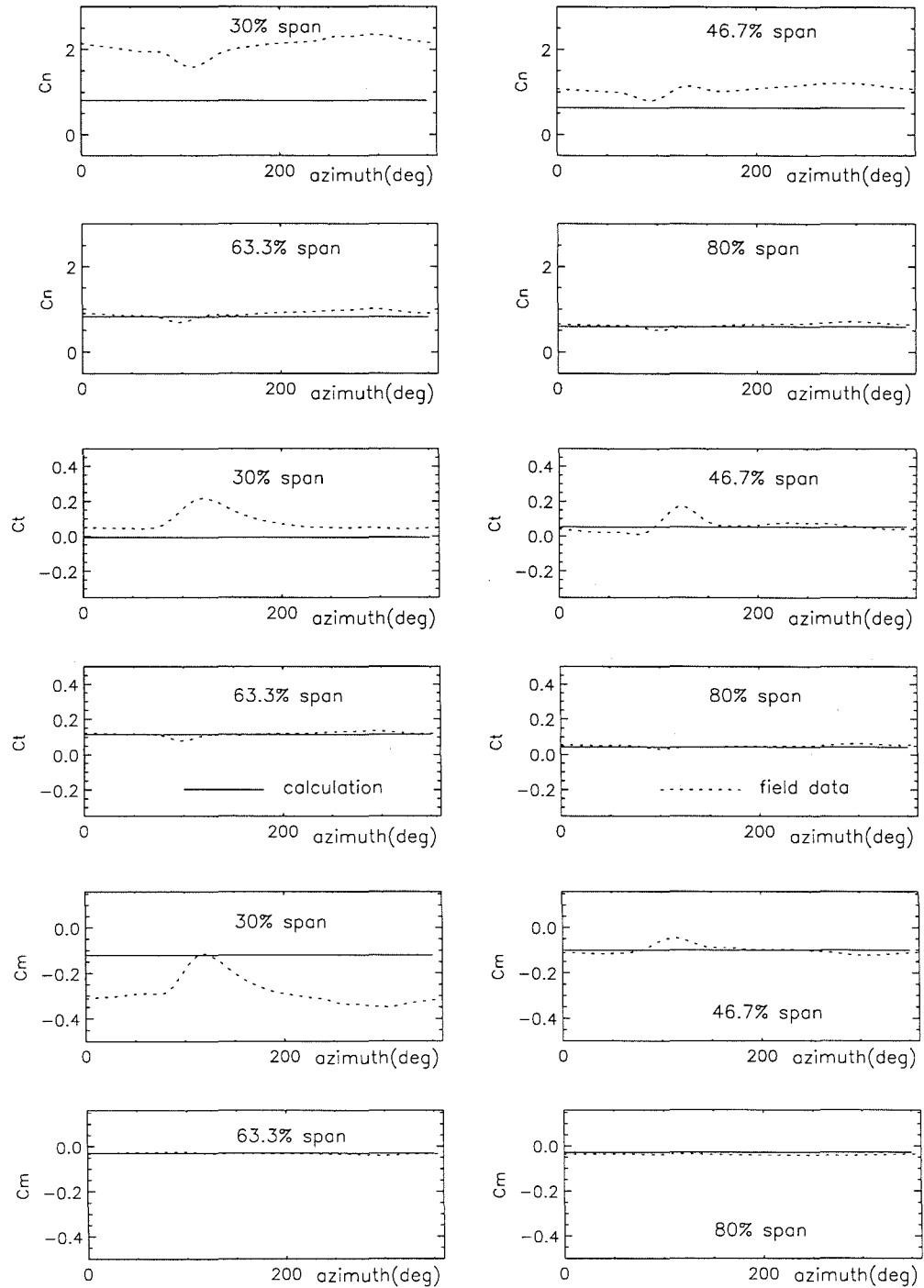


Figure 2.16: Comparison of predicted blade aerodynamic loading with field data of NREL UAE Phase I at $V_0 = 10.5$ m/s and $\gamma = 1.3^\circ$

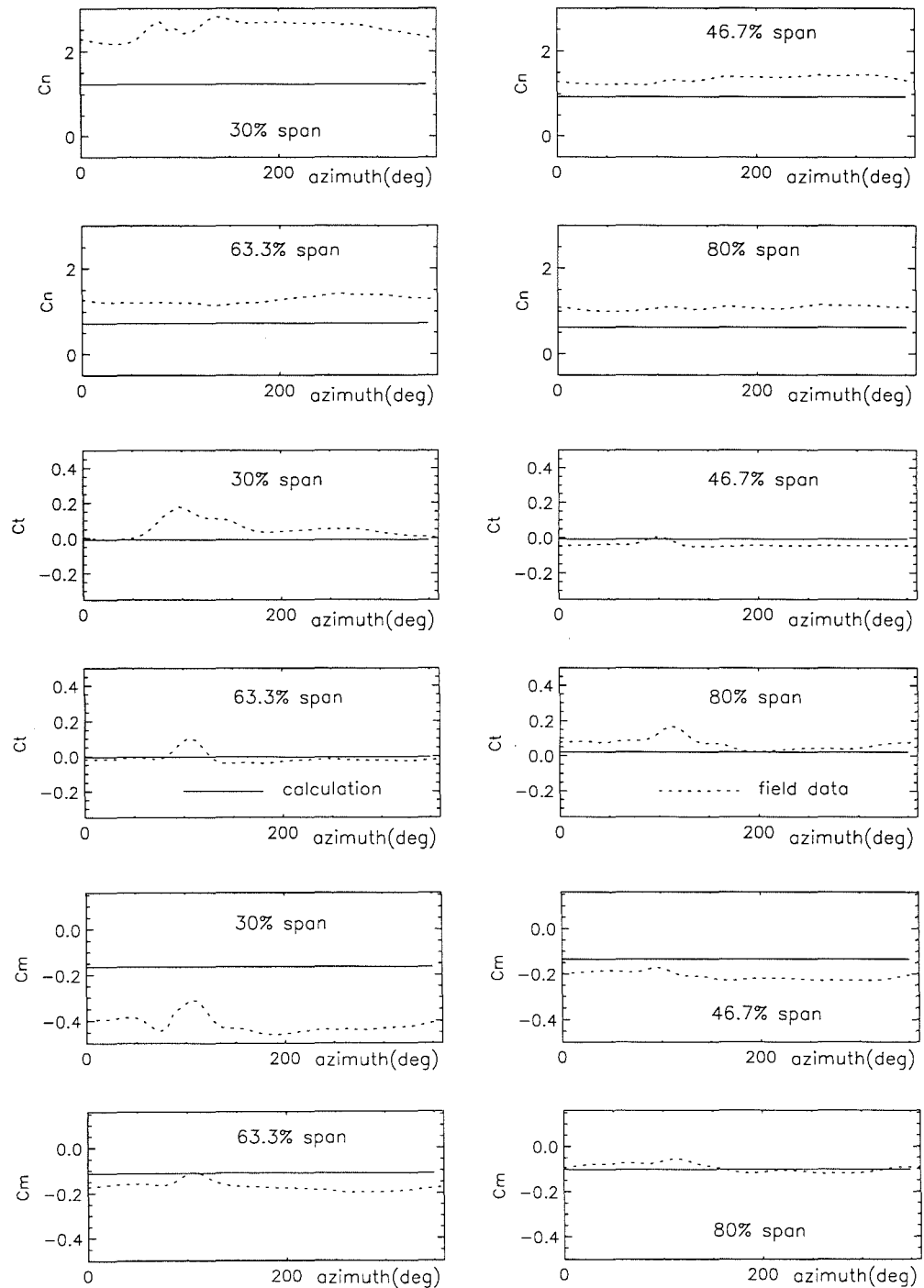


Figure 2.17: Comparison of predicted blade aerodynamic loading with field data of NREL UAE Phase II at $V_0 = 19.2$ m/s and $\gamma = 1.6^\circ$

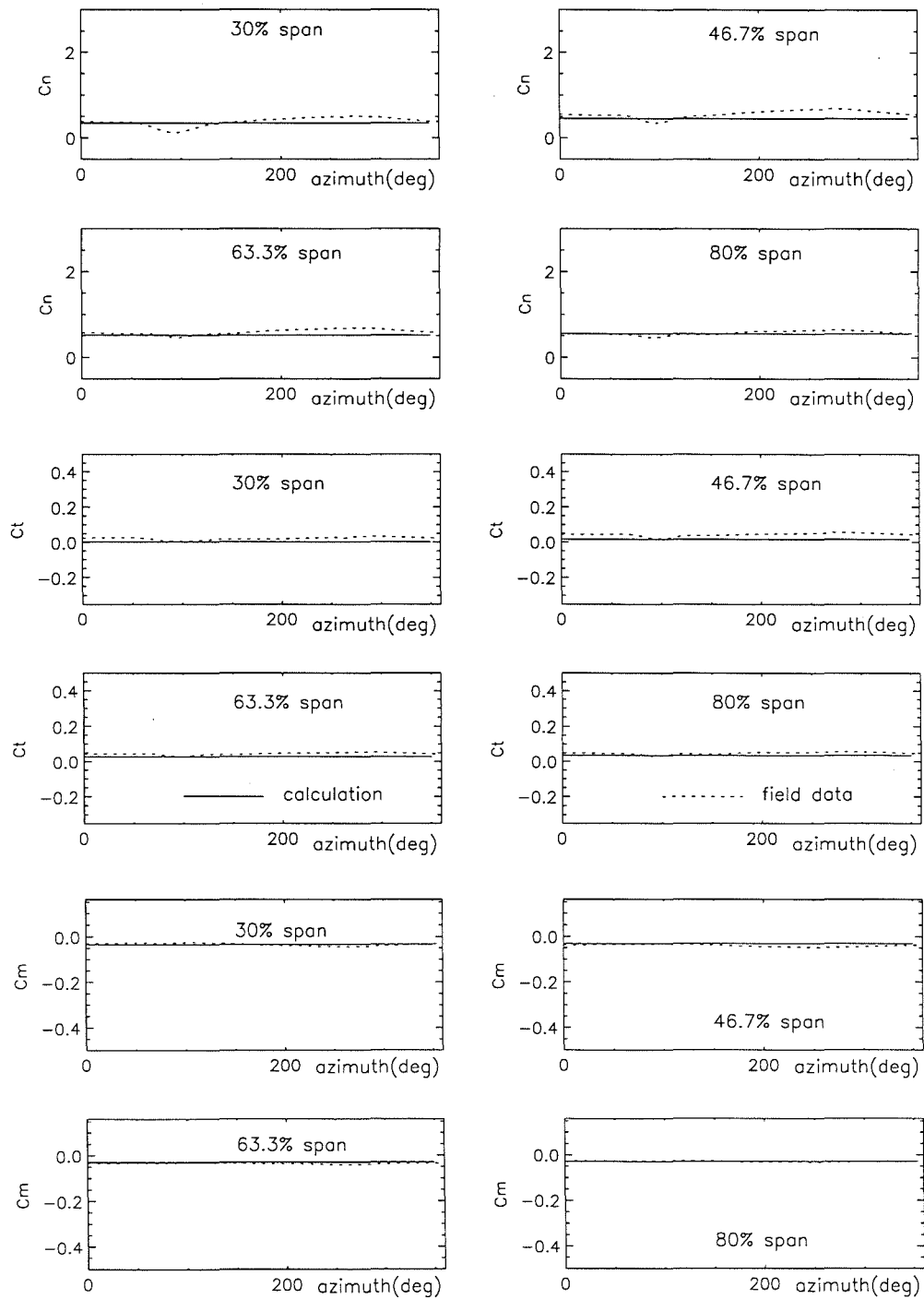


Figure 2.18: Comparison of predicted blade aerodynamic loading with field data of NREL UAE Phase N at $V_0 = 7.1 \text{ m/s}$ and $\gamma = 0.4^\circ$

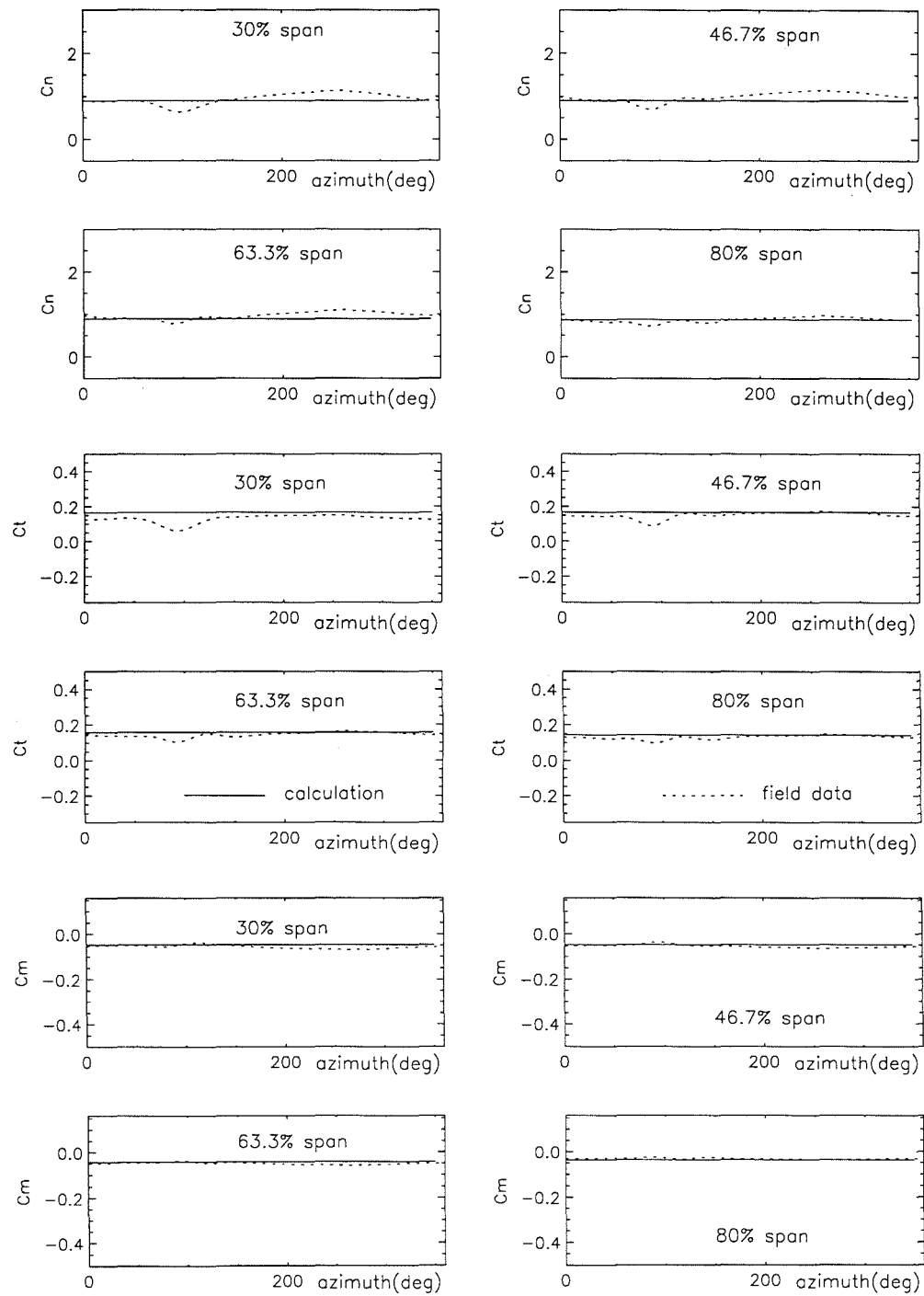


Figure 2.19: Comparison of predicted blade aerodynamic loading with field data of NREL UAE Phase M at $V_0 = 10.4$ m/s and $\gamma = -1.5^\circ$

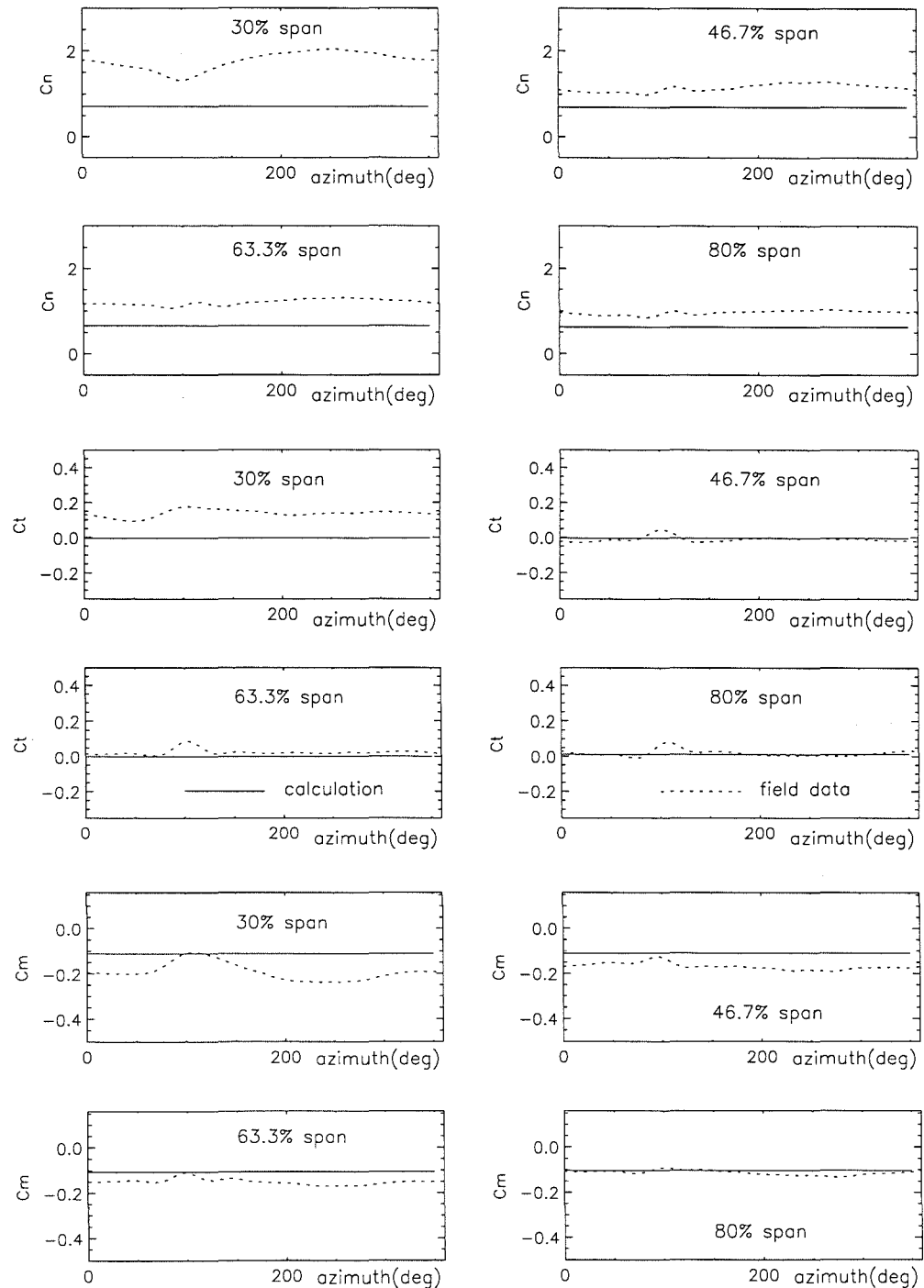


Figure 2.20: Comparison of predicted blade aerodynamic loading with field data of NREL UAE Phase N at $V_0 = 15.9$ m/s and $\gamma = 0.3^\circ$

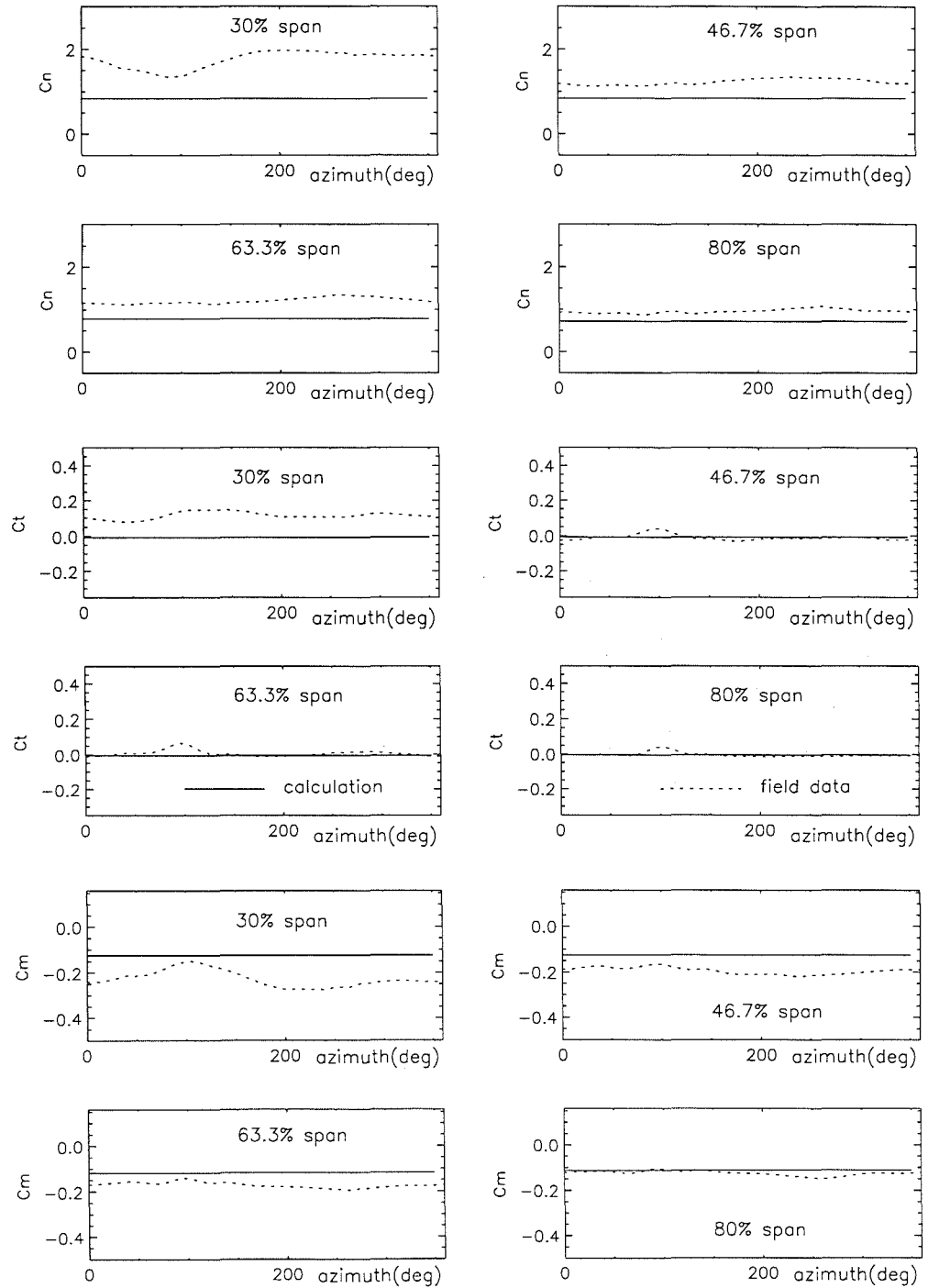


Figure 2.21: Comparison of predicted blade aerodynamic loading with field data of NREL UAE Phase M at $V_0 = 19.3$ m/s and $\gamma = 1.0^\circ$

Table 2.3: Overview of NREL UAE Phase IV field datasets (source: Schepers *et al.* 1997)

Dataset No.	1	2	3	4	5	6	7	8	9
Mean Vel. (m/s)	7.1	10.4	15.9	19.3	6.7	6.8	9.9	10.3	12.5
Mean Yaw (deg.)	0.4	-1.5	0.3	1.0	-38.2	-18.7	21.9	41.4	-21.2
Vel. S.D. (m/s)	0.97	0.76	1.75	2.25	0.49	0.74	0.70	1.35	2.35
Yaw S.D. (deg.)	7.42	0.73	7.36	16.50	10.14	5.92	2.90	4.47	8.06
Min. Vel. (m/s)	5.1	8.5	11.8	12.6	5.7	5.6	8.5	6.9	8.4
Max. Vel.(m/s)	8.6	12.5	20.5	24.3	8.1	8.1	11.3	12.1	17.0
Min. Yaw (deg.)	-19.0	-27.0	-21.0	-39.8	-59.3	-33.6	14.8	22.9	-38.1
Max. Yaw (deg.)	22.0	17.7	18.2	45.1	-2.4	-3.4	29.5	49.6	-0.2
No. of Cycles	72	72	72	72	18	18	18	18	18

blade span. For this reason, NREL's UAE HAWTs were chosen as the basis for comparison of the model with available field data. The data in this study came from Phases II and IV of the experiment (Butterfield *et al.* 1992c, Schepers *et al.* 1997) which utilised untwisted and twisted rectangular planform blades (see Appendix B), respectively. For comparison with the numerical model, the field data were azimuth-averaged over a series of cycles on the basis of yaw angle and wind speed. Tables 2.1, 2.2 and 2.3 give overviews of the NREL AUE field data which will be used for comparisons in this chapter and the following chapters. Each of the tables contains the mean, minimum, maximum and standard deviation values of wind velocity and yaw angle within the indicated number of cycles over which the data were azimuth-averaged. The field data in Table 2.1, were provided by NREL from their database according to certain criteria specified by the University of Glasgow. More details of the field data described in Tables 2.2 and 2.3 can be found in the ECN report (Schepers *et al.* 1997) and on the accompanying compact disc.

Figs. 2.14 to 2.21 show comparisons of the aerofoil normal force, tangential force, and pitching moment coefficients between the prescribed wake model and the field data at four spanwise blade locations in unyawed cases. For the cases of $V_0 = 12.5$ m/s and $V_0 = 12.3$ m/s of Phase II (Figs. 2.14 and 2.15), the field data are unavailable at the 80% span station where only calculated results are presented.

It can be seen from these comparisons that the normal force coefficient C_n , chordwise force coefficient C_t , and pitching moment coefficient C_m calculated using the prescribed wake model compare well with the experiment at blade outboard sections, except at very high wind speeds ($V_0 = 19.2$ m/s in Fig. 2.17 and $V_0 = 19.3$ m/s in Fig. 2.21) and in the region of tower shadow which is not represented in the numerical model. However, there are generally big discrepancies between the model and the field data at blade inboard stations where the angle of attack is well in excess of the static 2-D stall incidence. The variations in the blade incidence calculated corresponding to the above unyawed flow cases (Figs. 2.14 to 2.21) are illustrated in Figs. 2.22 and 2.23.

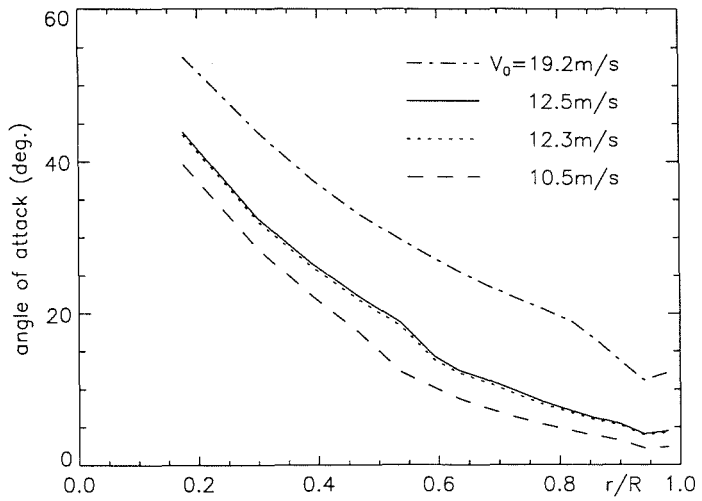


Figure 2.22: Variation in angle of attack along the blade of NREL UAE Phase II turbine in unyawed flow

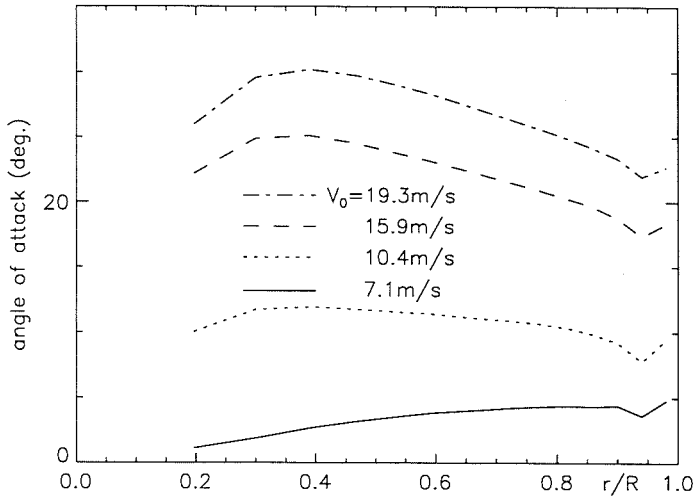


Figure 2.23: Variation in angle of attack along the blade of NREL UAE Phase IV turbine in unyawed Flow

In Figs. 2.18 and 2.19, the calculated results compare well with the field data not only at the outboard stations but also at the inboard stations while the corresponding angles of attack at all blade sections are lower than the stall angle. These results demonstrate the basic capability of the model accurately to represent blade aerodynamic loads in head-on flows when the local blade incidence is below the static stall incidence.

The differences between the model and experiment at most inboard locations mainly result from the 3-D effects, which are significant in separated flow regions for rotating blades. This phenomenon is viewed particularly in Figs. 2.17, 2.20 and 2.21 where the angle of attack even at the 80% span station is higher than the static stall angle. These results illustrate the inappropriate use of the 2-D aerofoil data in the model, which cannot account for the rotational effects.

It should be noted that the yaw angle is zero and the free stream speed is also fixed during the calculation procedure while there are small mean yaw angles for the field data as indicated in Figs. 2.14 to 2.21. These small differences in the yaw angles have little influence on the comparison between the model and experiment.

However, both the wind speed and yaw angle naturally vary around their mean values for the UAE field operations. For example, during the collection of the field data in Fig. 2.21, the wind speed varied from 12.6 m/s to 24.3 m/s and the yaw angle from -39.8° to 45.1° while their mean values were 19.3 m/s and 1° , respectively. Therefore, the experimental blade loads vary with azimuthal angle, unlike the calculation results which are constants with azimuth variation. Yawed flow will be dealt with in the following chapter.

2.5 Conclusions

A prescribed wake model for the prediction of the aerodynamic performance of HAWTs operating in steady axial flow has been presented. This method can be used not only to estimate the gross rotor performance but also to calculate the detailed aerodynamic characteristics such as blade loading, incidence information, and wake structure, etc. A vortex core model has been introduced to improve both the numerical convergency and accuracy of the calculation.

Power predictions obtained using the model show good agreement with field data over a range of operating conditions. Compared with experiment, the model apparently predicts the power better than it does the normal force on inboard sections of the blade. This is because the majority of the rotor power is produced by the outboard sections at which the model gives good predictions of the aerodynamic force coefficients. The model predictions also exhibit levels of accuracy associated with a free wake method. However, the prescribed wake model underestimates the rotor power output at low tip speed ratios as most prediction methods do. This results from the 2-D assumption of the flow around the blades. The model also shows incompleteness at very high tip speed ratios where the wake behind the rotor is in a turbulent wake state, either partly or wholly. Overcoming this problem provides a focus for future work.

The predicted aerodynamic loads on the blades using the model are encouraging. The normal force, tangential force, and pitching moment are well repres-

ented by the model up to the static stall angle, compared to the field data. At inboard spanwise locations which usually experience deep stall, there are big differences in the blade loads between the model and experiment although the variation trends are the same in all cases. This can mainly be attributed to rotational effects on the blade flow and it is envisaged that this will be improved by the inclusion of 3-D effects in the model.

Chapter 3

Unsteady Prescribed Wake Model

3.1 Introduction

Wind Turbines operate at all times in an unsteady aerodynamic environment. Factors such as atmospheric turbulence, wind shear, skewed flow, and the influence of the turbine tower on the blades, etc., all have significant effects on turbine blade inflow conditions. The cumulative effect of these phenomena results in the blade experiencing unsteady loading, which plays an important role in both the aerodynamic performance of the turbine and the fatigue life of its structure. Obviously, the aerodynamic loads must be well understood before the structural response can be accurately determined.

For HAWTs operating in a yawed inflow, the loading distribution on the turbine blades varies with azimuth and is characterised by changes in the blade incidence. Unsteady effects are manifest if the reduced frequency of the effective pitching of the turbine blade is high enough. In some cases the unsteadiness becomes severe and results in dynamic stall, which, as indicated by Shipley *et al.* (1995a), can influence a significant region of the rotor disc. The loads produced under these circumstances can be much higher than the equivalent steady-state loads and may have important life cycle implications for a wind turbine. As a result, this phenomenon has received much interest in the past few years and it becomes

clear that a comprehensive aerodynamic prediction scheme must be capable of modelling such effects.

The prescribed wake model presented in the previous chapter has shown the ability to provide detailed estimates of the aerodynamic conditions on the turbine blades in head-on flow with a satisfactory level of accuracy. In this chapter the prescribed wake model is extended to the case of yawed inflow. In the yawed case, not only is the wind velocity no longer parallel to the axis of rotation, but also there are additional shed vorticities in the wake due to the variation of the blade loads with time. Once yawed inflow is included in the model, wind shear effects can also be easily taken into account.

Both BEM theory and vortex wake theory for wind turbines in yaw use quasi-steady assumptions. In unsteady inflow conditions, however, the variations in the aerodynamic loads on the turbine blades are no longer in steady manner. In fact, both experimental and theoretical studies have revealed that dynamic stall can exist for high yaw angle operation and stall hysteresis occurs even for small yaw angles (Huyer *et al.* 1996, Shipley *et al.* 1995a, Butterfield *et al.* 1992a, Munduate and Coton 1999). The dynamic stall process in wind-tunnel tests on pitching and oscillating aerofoils is characterised by the formation and convection of a shedding vortex during which significant and high transient loading occurs (McCroskey *et al.* 1975, Carr *et al.* 1977, Huyer *et al.* 1988). Under certain conditions lift coefficients as great as five times their maximum static counterparts are produced during early formation of this vortex. Although the blades on a stall-regulated wind turbine do not pitch and oscillate, yawing of the rotor disc caused by changes in wind direction may induce similar dynamic conditions. Therefore, the unsteady and dynamic stall aspects must be appropriately modelled in order to calculate accurately the aerodynamic performance of wind turbines.

In the following sections of this chapter, the prescribed wake model is extended to the case of yawed inflow and wind shear conditions. In addition, the dynamic

stall model of Leishman and Beddoes (1989) is coupled to the prescribed wake scheme to give the unsteady aerodynamic loads on the blades. Results from the coupled model are discussed in detail.

3.2 Prescribed Wake Model in Yawed and Shear Flow

3.2.1 Coordinate Systems and Wind Input

The three coordinate systems used in the model for yawed flow are shown in Fig. 3.1. The origin points all are at the centre of rotor. The wind coordinate system (x, y, z) defines the gross flow field and the wake structure behind the turbine. The yawed, shearing wind velocity V_∞ is parallel to the z -axis and its direction defines the positive z -axis, the angle between which and the axis of rotation is the yaw angle. The y -axis is vertically downward and the x -axis horizontally points to the right when viewed from upwind along the wind direction. When the wind is inclined to the positive x -axis, the yaw angle γ is defined to be positive.

The turbine coordinate system (x', y', z') is used to define the parameters associated with the turbine and the local blade conditions as well. The z' -axis lies along the axis of rotation and the x' -axis lies horizontally along the 3 o'clock position. The y' -axis is vertically downward and identical to the y -axis. Parameters in the wind coordinate system can be transformed to those corresponding in the turbine coordinate system using the following transformation

$$\begin{bmatrix} x' \\ y' \\ z' \end{bmatrix} = \begin{bmatrix} \cos \gamma & 0 & \sin \gamma \\ 0 & 1 & 0 \\ -\sin \gamma & 0 & \cos \gamma \end{bmatrix} \begin{bmatrix} x \\ y \\ z \end{bmatrix} \quad (3.1)$$

For a rotational system, the local blade conditions are often defined more conveniently by the cylindrical coordinates (r, ψ, z') . The r -axis lies along the blade.

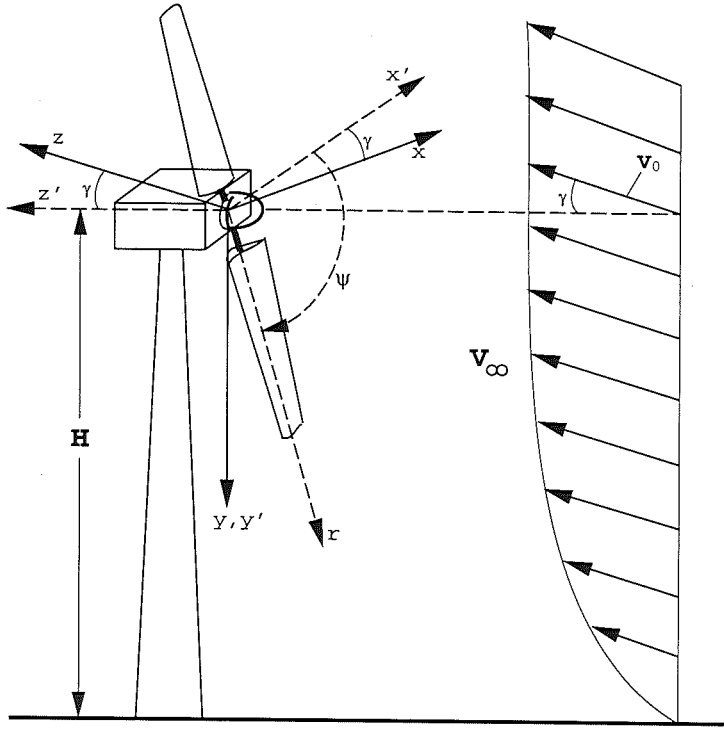


Figure 3.1: Illustration of coordinate systems in yawed flow

ψ describes the blade azimuthal position and is measured clockwise from the positive x -axis. Thus, the blade element boundary points and control points in the turbine coordinate system are

$$\left\{ \begin{array}{l} (\bar{x}'_{bp})_{i,j} = (\bar{r}_{bp})_i \cos \psi_j \\ (\bar{y}'_{bp})_{i,j} = (\bar{r}_{bp})_i \sin \psi_j \\ (\bar{z}'_{bp})_{i,j} = 0 \\ i = 1, 2, \dots, N_E + 1 \\ j = 1, 2, \dots, N_T \end{array} \right. \quad (3.2)$$

$$\left\{ \begin{array}{l} (\bar{x}'_{cp})_{i,j} = (\bar{r}_{cp})_i \cos \psi_j \\ (\bar{y}'_{cp})_{i,j} = (\bar{r}_{cp})_i \sin \psi_j \\ (\bar{z}'_{cp})_{i,j} = 0 \\ i = 1, 2, \dots, N_E \\ j = 1, 2, \dots, N_T \end{array} \right. \quad (3.3)$$

and can be re-expressed as

$$\left\{ \begin{array}{l} (\bar{x}_{bp})_{i,j} = (\bar{r}_{bp})_i \cos \gamma \cos \psi_j \\ (\bar{y}_{bp})_{i,j} = (\bar{r}_{bp})_i \sin \gamma \cos \psi_j \\ (\bar{z}_{bp})_{i,j} = (\bar{r}_{bp})_i \sin \gamma \sin \psi_j \\ i = 1, 2, \dots, N_E + 1 \\ j = 1, 2, \dots, N_T \end{array} \right. \quad (3.4)$$

$$\left\{ \begin{array}{l} (\bar{x}_{cp})_{i,j} = (\bar{r}_{cp})_i \cos \gamma \cos \psi_j \\ (\bar{y}_{cp})_{i,j} = (\bar{r}_{cp})_i \sin \gamma \cos \psi_j \\ (\bar{z}_{cp})_{i,j} = (\bar{r}_{cp})_i \sin \gamma \sin \psi_j \\ i = 1, 2, \dots, N_E \\ j = 1, 2, \dots, N_T \end{array} \right. \quad (3.5)$$

in the wind coordinate system. Meanwhile, the yawed free stream velocity, V_∞ , can be resolved into radial, tangential, and axial components (see Fig. 3.2),

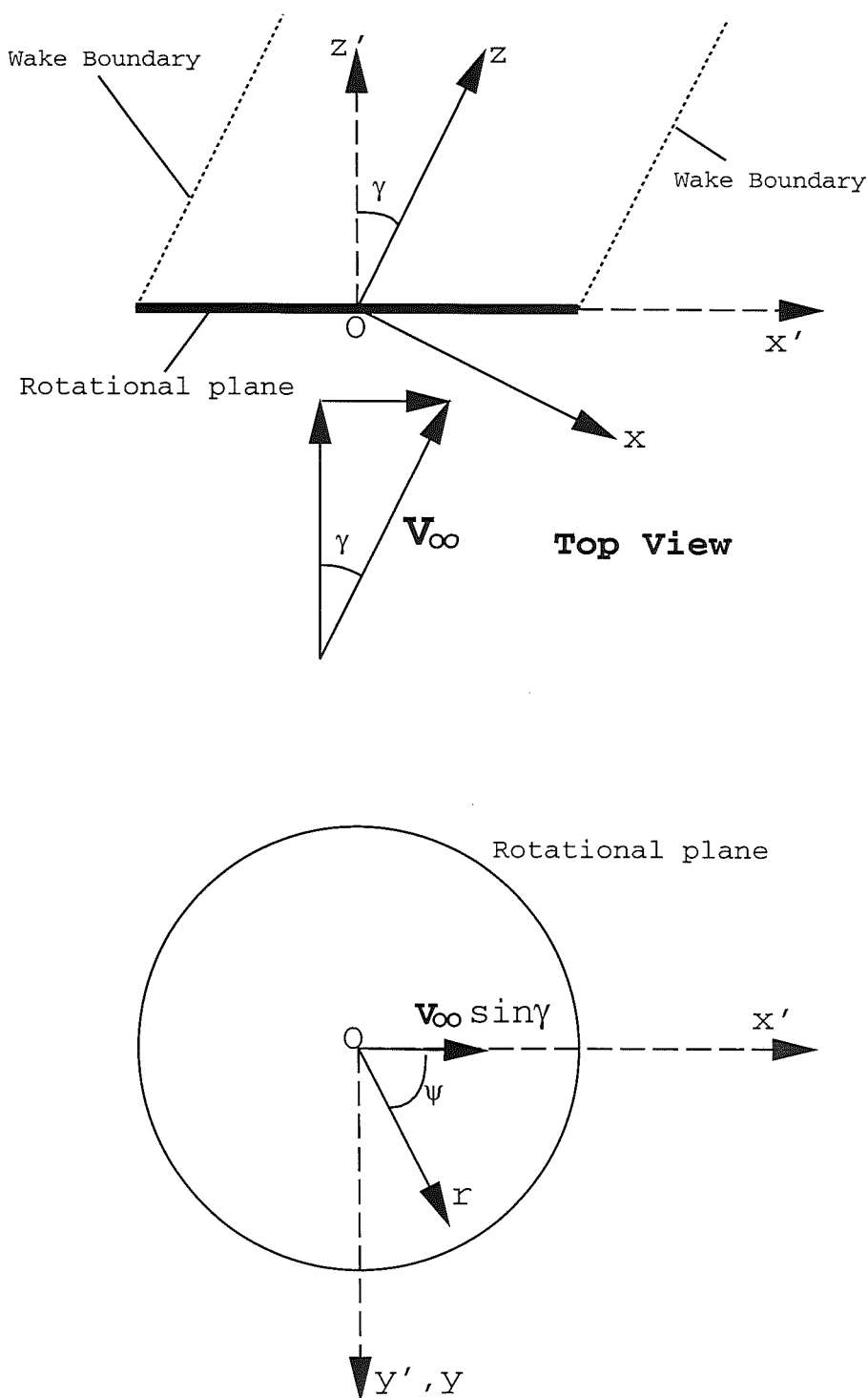
$$V_\infty = V_\infty \sin \gamma \cos \psi \mathbf{e}_r - V_\infty \sin \gamma \sin \psi \mathbf{e}_\psi + V_\infty \cos \gamma \mathbf{e}_{z'} \quad (3.6)$$

where \mathbf{e}_r , \mathbf{e}_ψ , and $\mathbf{e}_{z'}$ are the unit vectors in the radial, tangential, and axial directions, respectively.

There always exists an atmospheric boundary layer, which results in a wind shear velocity distribution. The change in mean velocity with height above the ground is often described by the simple power law as

$$V(h) = V(h_0) \left(\frac{h}{h_0} \right)^\eta$$

where h is the height above the ground, h_0 is the reference height, and $V(h_0)$ is the reference velocity at the height h_0 . The exponent η is called the shear exponent and varies with terrain factor. The wind shear exponents at different terrains can be found from de Vries (1979a) and Hunt (1981), and for an open plain terrain the value of η is about 1/6.



View from Upwind in Axial Direction

Figure 3.2: Geometry of yawed inflow

For a wind turbine it is convenient to choose the turbine centre height H as the reference height and hence the wind velocity V_0 at this height as the reference velocity. Thus, the wind shear velocity distribution across the turbine disc can be expressed as

$$\bar{V}_\infty = \frac{V_\infty}{V_0} = \left(1 - \frac{\bar{r} \sin \psi}{\bar{H}}\right)^\eta \quad (3.7)$$

where the velocity is normalised by V_0 and the parameters associated with length are normalised by the turbine radius R , as done in the previous chapter; $\bar{H} = H/R$.

The effective tip speed ratio is

$$\lambda_e = \frac{\Omega R + V_\infty \sin \gamma \sin \psi}{V_\infty \cos \gamma}$$

or

$$\lambda_e = \frac{\lambda}{\bar{V}_\infty \cos \gamma} + \tan \gamma \sin \psi \quad (3.8)$$

It is obvious from Eq. 3.8 that, for a given wind turbine at a given yaw angle and at a given condition of wind shear, the blade aerodynamic performance depends not only on the tip speed ratio $\lambda = \Omega R/V_0$ but also on the blade azimuthal angle ψ .

3.2.2 Wake Prescription

In order to determine prescription functions appropriate to yawed wake structures, the hybrid free/prescribed wake method, discussed previously in Section 2.2.4, was applied to a range of operating conditions, including yaw angles of up to 60° . It was found that the principal effect on the wake structure occurred through the loading imbalance on the disc and that, when the induced velocity variation resulting from this imbalance was fed into the existing wake prescription functions for unyawed flow, an adequate representation of the yawed wake was obtained. Thus, the prescription functions developed for unyawed flow were found to be universally applicable to yawed flow when applied in the wind coordinate system.

The prescription functions were not derived in conditions of wind shear. However, the wind shear effects can be included in the prescribed wake model if a quasi-steady assumption is appropriately made. Under this assumption, the non-dimensional wake velocity and displacement, $(\bar{V}_z)_w$ and \bar{z}_w , in the wind direction are prescribed as

$$\frac{(\bar{V}_z)_w}{\bar{V}_\infty} = \begin{cases} 1 - a - \frac{21}{5}(F - 1)a\bar{t} & \text{for } \bar{t} \leq \frac{1}{7} \\ 1 - \frac{1}{2}(1 + F)a - \frac{7}{10}(F - 1)a\bar{t} & \text{for } \frac{1}{7} < \bar{t} \leq \frac{4}{7} \\ 1 - \frac{7 + 23F}{30}a - \frac{7}{30}(F - 1)a\bar{t} & \text{for } \frac{4}{7} < \bar{t} \leq 1 \\ 1 - Fa & \text{for } \bar{t} > 1 \end{cases} \quad (3.9)$$

$$\frac{\bar{z}_w}{\bar{V}_\infty} = \begin{cases} \frac{7\pi}{4}(1 - a)\bar{t} - \frac{147\pi}{40}(F - 1)a\bar{t}^2 & \text{for } \bar{t} \leq 1/7 \\ \frac{\pi}{16}(F - 1)a + \frac{7\pi}{4} \left(1 - \frac{1 + F}{2}a\right)\bar{t} - \frac{49\pi}{80}(F - 1)a\bar{t}^2 & \text{for } 1/7 < \bar{t} \leq 4/7 \\ \frac{47\pi}{240}(F - 1)a + \frac{7\pi}{4} \left(1 - \frac{7 + 23F}{30}a\right)\bar{t} - \frac{49\pi}{240}(F - 1)a\bar{t}^2 & \text{for } 4/7 < \bar{t} \leq 1 \\ \frac{2\pi}{5}(F - 1)a + \frac{7\pi}{4}(1 - Fa)\bar{t} & \text{for } \bar{t} > 1 \end{cases} \quad (3.10)$$

The radial development of the wake takes the form of Eqs. 2.10 and 2.11, or 2.12 during the stage of the initial construction of the wake. Thus, the wake node position can be expressed, in the wind cartesian coordinate system (see Figs. 3.1

and 3.2), as

$$\left\{ \begin{array}{l} \bar{x}_w(i, j, k, n) = (\bar{r}_w)_{i,j,k,n} \cos \gamma \cos \psi_{j,k} \\ \bar{y}_w(i, j, k, n) = (\bar{r}_w)_{i,j,k,n} \sin \gamma \cos \psi_{j,k} \\ \bar{z}_w(i, j, k, n) = (\bar{r}_{bp})_i \sin \gamma \cos \psi_{j,k} + (\bar{z}_w)_{i,j,k,n} \\ i = 1, 2, \dots, N_E + 1 \\ j = 1, 2, \dots, N_T \\ k = 1, 2, \dots, B \\ n = 1, 2, \dots, N_C \end{array} \right. \quad (3.11)$$

where $(\bar{r}_w)_{i,j,k,n}$ is obtained from Eq. 2.12 during the initial wake construction and from Eq. 2.11 as long as the intial wake has been created, $(\bar{z}_w)_{i,j,k,n}$ is obtained from Eq. 3.10, the indices (i, j, k, n) denote the wake filament traile from the i th element boundary of the k th blade at the j th azimuthal position for the n th wake cycle.

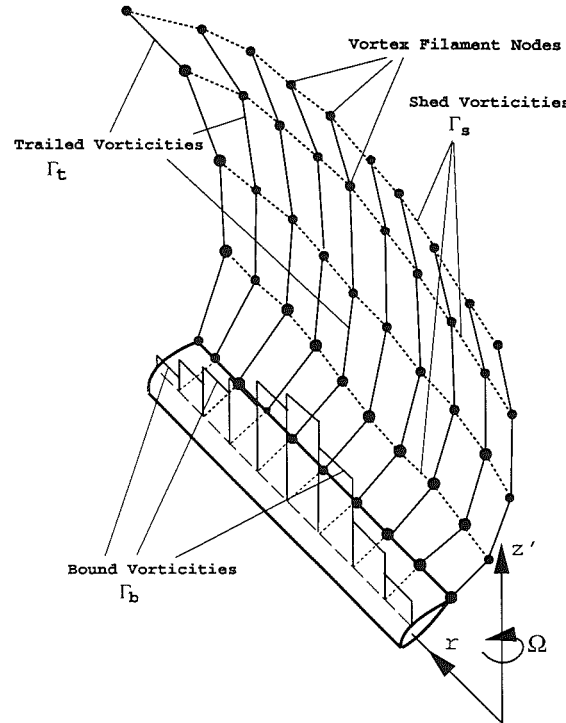


Figure 3.3: Sketch of vortex system

3.2.3 Induced Velocities

As stated above, the flow conditions around the blade in yawed inflow vary with time or azimuthal angle, ψ . The angle of attack at the blade is therefore no longer constant around the azimuth. This change in blade incidence with time requires the introduction of shed vorticity into the wake to account for the temporal changes in bound circulation. In this case the wake consists not only of the trailed vorticity but also of the shed vorticity, as shown in Fig. 3.3. The strength $(\Gamma_s)_{i,j}$ of a wake vortex element shed from the i th blade element at the j th azimuth position is estimated by

$$(\bar{\Gamma}_s)_{i,j} = \frac{(\Gamma_s)_{i,j}}{4\pi V_0 R} = \begin{cases} (\bar{\Gamma}_b)_{i,1} - (\bar{\Gamma}_b)_{i,N_T} & \text{for } j = 1 \\ (\bar{\Gamma}_b)_{i,j} - (\bar{\Gamma}_b)_{i,j-1} & \text{for } j = 2, 3, \dots, N_T \end{cases} \quad (3.12)$$

where $i = 1, 2, \dots, N_E$.

A shed vortex element in the wake is defined by its two end points, whose coordinates are

$$[\bar{x}_w(i, j, k, n), \bar{y}_w(i, j, k, n), \bar{z}_w(i, j, k, n)]$$

and

$$[\bar{x}_w(i+1, j, k, n), \bar{y}_w(i+1, j, k, n), \bar{z}_w(i+1, j, k, n)]$$

respectively. Let

$$\mathbf{r}_A = [\bar{x} - \bar{x}_w(i, j, k, n)] \mathbf{i} + [\bar{y} - \bar{y}_w(i, j, k, n)] \mathbf{j} + [\bar{z} - \bar{z}_w(i, j, k, n)] \mathbf{k}$$

$$\mathbf{r}_B = [\bar{x} - \bar{x}_w(i+1, j, k, n)] \mathbf{i} + [\bar{y} - \bar{y}_w(i+1, j, k, n)] \mathbf{j} + [\bar{z} - \bar{z}_w(i+1, j, k, n)] \mathbf{k}$$

where $(\bar{x}, \bar{y}, \bar{z})$ is the point at which the induced velocity is calculated. Similarly to the induction of the trailed vortex, the influence coefficients, $(I_x^s)_{i,j,k,n}$, $(I_y^s)_{i,j,k,n}$, and $(I_z^s)_{i,j,k,n}$, of induced velocity due to the (i, j, k, n) th shed vortex element are

determined by

$$\left\{ \begin{array}{l} (I_x^s)_{i,j,k,n} = \frac{(\mathbf{r}_A \times \mathbf{r}_B) \cdot \mathbf{i}}{|\mathbf{r}_A \times \mathbf{r}_B|^2} \left(\frac{\mathbf{r}_A \cdot \mathbf{r}_{AB}}{|\mathbf{r}_A|} - \frac{\mathbf{r}_B \cdot \mathbf{r}_{AB}}{|\mathbf{r}_B|} \right) \\ (I_y^s)_{i,j,k,n} = \frac{(\mathbf{r}_A \times \mathbf{r}_B) \cdot \mathbf{j}}{|\mathbf{r}_A \times \mathbf{r}_B|^2} \left(\frac{\mathbf{r}_A \cdot \mathbf{r}_{AB}}{|\mathbf{r}_A|} - \frac{\mathbf{r}_B \cdot \mathbf{r}_{AB}}{|\mathbf{r}_B|} \right) \\ (I_z^s)_{i,j,k,n} = \frac{(\mathbf{r}_A \times \mathbf{r}_B) \cdot \mathbf{k}}{|\mathbf{r}_A \times \mathbf{r}_B|^2} \left(\frac{\mathbf{r}_A \cdot \mathbf{r}_{AB}}{|\mathbf{r}_A|} - \frac{\mathbf{r}_B \cdot \mathbf{r}_{AB}}{|\mathbf{r}_B|} \right) \end{array} \right. \quad (3.13)$$

Using Eqs. 2.33 and 2.34, these influence coefficients can be re-written as

$$\left\{ \begin{array}{l} I_x^s(i, m, k, n) = (I_x^s)_{i,j,k,n} \\ I_y^s(i, m, k, n) = (I_y^s)_{i,j,k,n} \\ I_z^s(i, m, k, n) = (I_z^s)_{i,j,k,n} \\ i = 1, 2, \dots, N_E \\ j = 1, 2, \dots, N_T \\ k = 1, 2, \dots, B \\ n = 1, 2, \dots, N_C \end{array} \right. \quad (3.14)$$

The vortex element shedding from the i th blade element at the j th azimuth keeps its strength $(\Gamma_s)_{i,j}$ unchanged during its convection downstream. This makes it convenient to summarise the influence coefficients into

$$\left\{ \begin{array}{l} (I_x^s)_{i,j} = \sum_{k=1}^B \sum_{n=1}^{N_C} I_x^s(i, j, k, n) \\ (I_y^s)_{i,j} = \sum_{k=1}^B \sum_{n=1}^{N_C} I_y^s(i, j, k, n) \\ (I_z^s)_{i,j} = \sum_{k=1}^B \sum_{n=1}^{N_C} I_z^s(i, j, k, n) \end{array} \right. \quad (3.15)$$

The velocity components at a point $(\bar{x}, \bar{y}, \bar{z})$ induced by the wake vortex system can be calculated *via* the influence coefficients associated with the trailed and shed

vorticities,

$$\left\{ \begin{array}{l} \bar{v}_x(\bar{x}, \bar{y}, \bar{z}) = - \sum_{i=1}^{N_E+1} \sum_{j=1}^{N_T} (\bar{\Gamma}_t)_{i,j} (I_x^t)_{i,j} - \sum_{i=1}^{N_E} \sum_{j=1}^{N_T} (\bar{\Gamma}_s)_{i,j} (I_x^s)_{i,j} \\ \bar{v}_y(\bar{x}, \bar{y}, \bar{z}) = - \sum_{i=1}^{N_E+1} \sum_{j=1}^{N_T} (\bar{\Gamma}_t)_{i,j} (I_y^t)_{i,j} - \sum_{i=1}^{N_E} \sum_{j=1}^{N_T} (\bar{\Gamma}_s)_{i,j} (I_y^s)_{i,j} \\ \bar{v}_z(\bar{x}, \bar{y}, \bar{z}) = - \sum_{i=1}^{N_E+1} \sum_{j=1}^{N_T} (\bar{\Gamma}_t)_{i,j} (I_z^t)_{i,j} - \sum_{i=1}^{N_E} \sum_{j=1}^{N_T} (\bar{\Gamma}_s)_{i,j} (I_z^s)_{i,j} \end{array} \right. \quad (3.16)$$

Substitution of $(\bar{x}_{cp})_{i,j}$, $(\bar{y}_{cp})_{i,j}$, and $(\bar{z}_{cp})_{i,j}$ (Eq. 3.5) as well as $(\bar{x}_{bp})_{i,j}$, $(\bar{y}_{bp})_{i,j}$, and $(\bar{z}_{bp})_{i,j}$ (Eq. 3.4) in Eq. 2.54 yields the non-dimensional induced velocity components at the blade,

$$\left\{ \begin{array}{l} (\bar{v}_x)_{i,j}^{cp} = \bar{v}_x((\bar{x}_{cp})_{i,j}, (\bar{y}_{cp})_{i,j}, (\bar{z}_{cp})_{i,j}) \\ (\bar{v}_y)_{i,j}^{cp} = \bar{v}_y((\bar{x}_{cp})_{i,j}, (\bar{y}_{cp})_{i,j}, (\bar{z}_{cp})_{i,j}) \\ (\bar{v}_z)_{i,j}^{cp} = \bar{v}_z((\bar{x}_{cp})_{i,j}, (\bar{y}_{cp})_{i,j}, (\bar{z}_{cp})_{i,j}) \end{array} \right. \quad (3.17)$$

$$\left\{ \begin{array}{l} (\bar{v}_x)_{i,j}^{bp} = \bar{v}_x((\bar{x}_{bp})_{i,j}, (\bar{y}_{bp})_{i,j}, (\bar{z}_{bp})_{i,j}) \\ (\bar{v}_y)_{i,j}^{bp} = \bar{v}_y((\bar{x}_{bp})_{i,j}, (\bar{y}_{bp})_{i,j}, (\bar{z}_{bp})_{i,j}) \\ (\bar{v}_z)_{i,j}^{bp} = \bar{v}_z((\bar{x}_{bp})_{i,j}, (\bar{y}_{bp})_{i,j}, (\bar{z}_{bp})_{i,j}) \end{array} \right. \quad (3.18)$$

The induced velocities at the blade element boundary points (Eq. 3.18) are directly used to determine the wake geometry since the prescription functions are applicable to the yawed case in the wind coordinate system. In order to determine the aerodynamic loads on the blade, the induced velocities (Eq. 3.17) at the blade element control points in the wind coordinate system are usually transformed into the radial, tangential and axial components,

$$\begin{bmatrix} (\bar{v}_r)_{i,j}^{cp} \\ (\bar{v}_\psi)_{i,j}^{cp} \\ (\bar{v}_{z'})_{i,j}^{cp} \end{bmatrix} = \begin{bmatrix} \cos \psi & \sin \psi & 0 \\ -\sin \psi & \cos \psi & 0 \\ 0 & 0 & 1 \end{bmatrix} \begin{bmatrix} \cos \gamma & 0 & \sin \gamma \\ 0 & 1 & 0 \\ -\sin \gamma & 0 & \cos \gamma \end{bmatrix} \begin{bmatrix} (\bar{v}_x)_{i,j}^{cp} \\ (\bar{v}_y)_{i,j}^{cp} \\ (\bar{v}_z)_{i,j}^{cp} \end{bmatrix} \quad (3.19)$$

The non-dimensional resultant inflow velocity is then

$$\bar{W}_{i,j}^{cp} = \sqrt{[(\bar{V}_r)_{i,j}^{cp}]^2 + [(\bar{V}_\psi)_{i,j}^{cp}]^2 + [(\bar{V}_{z'})_{i,j}^{cp}]^2} \quad (3.20)$$

where

$$(\bar{V}_r)_{i,j}^{cp} = (\bar{V}_\infty)_{i,j}^{cp} \sin \gamma \cos \psi_j + (\bar{v}_r)_{i,j}^{cp}$$

$$(\bar{V}_\psi)_{i,j}^{cp} = \lambda (\bar{r}_{cp})_i + (\bar{V}_\infty)_{i,j}^{cp} \sin \gamma \sin \psi_j - (\bar{v}_\psi)_{i,j}^{cp}$$

$$(\bar{V}_{z'})_{i,j}^{cp} = (\bar{V}_\infty)_{i,j}^{cp} \cos \gamma + (\bar{v}_{z'})_{i,j}^{cp}$$

and

$$(\bar{V}_\infty)_{i,j}^{cp} = \left[1 - \frac{(\bar{r}_{cp})_i \sin \psi_j}{\bar{H}} \right]^\eta$$

The inflow angle is

$$\phi_{i,j} = \arctan \frac{(\bar{V}_{z'})_{i,j}^{cp}}{(\bar{V}_\psi)_{i,j}^{cp}} \quad (3.21)$$

The prescribed wake calculation procedure in the yawed case is similar to that in the head-on flow case (Fig. 2.4) but, all of the equations used in the calculation must be replaced by those associated with yaw.

3.3 The Unsteady Aerofoil Model

3.3.1 Introduction

The prescribed wake model developed for HAWTs in yaw is actually a quasi-steady model, in which the inflow conditions are treated as a steady state for every time step and hence many unsteady aerodynamic aspects, such as dynamic stall, are not included. The requirements for accurate calculation of the unsteady aerodynamic characteristics have recently become more stringent as extremely large transient

forces from unsteady aerodynamics cause early fatigue failure of blades, hubs, generators and power transfer (gear box) components.

Dynamic stall on HAWT blades has been shown to occur under a variety of inflow conditions. Field-based experimental studies have clarified that unsteady aerodynamics exist during all operating conditions and that dynamic stall can exist for high yaw angle operation while stall hysteresis occurs for even small yaw angles (Huyer *et al.* 1996, Shipley *et al.* 1995a, Butterfield *et al.* 1992a). The existence of dynamic stall and dynamic hysteresis results in significant increases in blade loads. For accurate wind turbine performance and structural response predictions, it is essential to incorporate a realistic representation of the blade aerodynamics in regimes involving fully attached flow and both partial and complete flow separations, including dynamic stall. All these flow regimes are greatly influenced by the unsteady forcing conditions encountered by the blades during operation in yaw. Even if separation effects and dynamic stall are not encountered in yawed flow cases, there are still local unsteady aerodynamic effects on the blade loading due to the combined effects of time-dependent incidence changes and skewed wake structure which cannot be neglected.

Recently, there has been significant progress in the computational prediction of dynamic stall on aerofoils (Ekaterinaris and Platzer 1997). Because of the extremely large amount of computing resource required and a variety of numerical problems associated with the CFD solvers, however, these methods are still impractical for use in day-to-day routine turbine design investigations. Therefore, an alternative to calculation of unsteady aerodynamics is to make use of empirical and semi-empirical unsteady aerodynamic modelling procedures, which have been developed to estimate approximately the rotor loads in the helicopter industry due to the extremely complicated nature of the dynamic stall phenomena during helicopter forward flight.

Most empirical dynamic stall models rely heavily on the analysis of wind tunnel data from 2-D aerofoil tests, and hence, are subject to limitations to their formulation and generality in application. These methods have, however, been shown to

give significant improvements in rotor design capability. A semi-empirical model was formulated by Leishman and Beddoes (Leishman and Beddoes 1989, Leishman 1987a, Leishman 1987b) to represent the unsteady lift, drag, and pitching moment characteristics of an aerofoil undergoing dynamic stall. This model still relies upon empirical constants but is more deeply founded in the physical mechanism of dynamic stall. In the model, unsteady effects during attached flow conditions are simulated by the superposition of indicial aerodynamic responses. Non-linearities in aerofoil behaviour, related to small amounts of trailing edge separation, are represented using a Kirchhoff flow model. The movement of the unsteady flow separation point is related to the static separation position *via* a deficiency function. The onset of leading edge separation (and hence, dynamic stall) is identified using a criterion based on the attainment of critical leading edge pressure which is further related to the normal force. For unsteady conditions a lag in the normal force response to changes in angle of attack and a lag in the leading edge pressure response with respect to normal force are taken into consideration. The induced vortex force and the associated pitching moment are represented empirically in a time-dependent manner during dynamic stall. This model is very efficient owing to its explicit algebraic format.

In the present unsteady prescribed wake model, unsteady loads on the blades are modelled by coupling the prescribed wake method to the unsteady aerofoil model of Leishman and Beddoes. The formulation of the Leishman–Beddoes model is briefly described in the following sections.

3.3.2 Attached Flow Behaviour

Indicial Responses

By definition, an indicial function is the response to a disturbance which is applied instantaneously at time zero and held constant thereafter. That is a response to a step change in forcing. A variation in forcing is implemented as a series of steps (sampled forcing) and the response is built up by superposition, formally expressed

by Duhamel's integral (*e.g.* Bisplinghoff 1996). The total indicial response can conveniently be split into two components; one to solve for the circulatory loading which builds up quickly and asymptotes to the appropriate steady-state loading, and the other for the initial loading which is impulsive (non-circulatory) and decays rapidly with time. Thus, the indicial normal force coefficient due to a step change, $\Delta\alpha$, in angle of attack at the quarter chord can be written as

$$\Delta C_n^\alpha(S) = \left[C_{n_\alpha} (\phi_\alpha^C)_n + \frac{4}{M} (\phi_\alpha^I)_n \right] \Delta\alpha \quad (3.22)$$

where C_{n_α} is the normal force slope and can be approximated by the lift slope. The non-dimensional time S represents the distance travelled at the resultant velocity W by the aerofoil in semi-chords,

$$S = \frac{2Wt}{c}$$

The circulatory and impulsive response coefficients, $(\phi_\alpha^C)_n$ and $(\phi_\alpha^I)_n$, are approximated in terms of exponential functions as (Leishman 1988, Beddoes 1984),

$$(\phi_\alpha^C)_n = 1 - A_1 \exp(-b_1\beta^2 S) - A_2 \exp(-b_2\beta^2 S)$$

$$(\phi_\alpha^I)_n = \exp\left(-\frac{S}{S_\alpha^n}\right)$$

where the coefficients $A_1 = 0.3$, $A_2 = 0.7$, $b_1 = 0.14$, and $b_2 = 0.53$ have been determined as a consequence of experimental and theoretical analyses for the standard Beddoes–Leishman model (Beddoes 1984); β is the compressibility correction parameter,

$$\beta = \sqrt{1 - M^2}$$

with M being the local Mach number, and

$$S_\alpha^n = \frac{1.5M}{1 - M + \pi\beta M^2(A_1 b_1 + A_2 b_2)}$$

The indicial pitching moment coefficient due to a step change $\Delta\alpha$ can be expressed as

$$\Delta C_m^\alpha(S) = \left[\left(\frac{1}{4} - \frac{x_{ac}}{c} \right) C_{n_\alpha} (\phi_\alpha^C)_n - \frac{1}{M} (\phi_\alpha^I)_m \right] \Delta\alpha \quad (3.23)$$

where x_{ac} is the position of the aerofoil aerodynamic centre measured from the leading edge in the chordwise direction, and

$$(\phi_\alpha^I)_m = A_3 \exp\left(-\frac{S}{b_3 S_\alpha^m}\right) + A_4 \exp\left(-\frac{S}{b_4 S_\alpha^m}\right)$$

with $A_3 = 1.5$, $A_4 = -0.5$, $b_3 = 0.25$, $b_4 = 0.1$, and

$$S_\alpha^m = \frac{1.6(A_3 b_4 + A_4 b_3)M}{b_3 b_4 (1 - M)}$$

Similarly, for a step change in pitch rate about the quarter chord,

$$\Delta q = \frac{\Delta \dot{\alpha} c}{W}$$

the indicial responses can be written, if the aerofoil boundary condition is satisfied at the 3/4-quarter chord, as

$$\Delta C_n^q(S) = \left[C_{n\alpha} (\phi_\alpha^C)_n + \frac{2}{M} (\phi_q^I)_n \right] \frac{\Delta q}{2} \quad (3.24)$$

$$\Delta C_m^q(S) = \left[-\frac{\pi}{8\beta} (\phi_q^C)_m - \frac{7}{12M} (\phi_q^I)_m \right] \Delta q \quad (3.25)$$

where

$$(\phi_q^I)_n = \exp\left(-\frac{S}{S_q^n}\right)$$

$$(\phi_q^C)_m = 1 - \exp(-b_5 \beta^2 S)$$

$$(\phi_q^I)_m = \exp\left(-\frac{S}{S_q^m}\right)$$

with $b_5 = 0.5$, and

$$S_q^n = \frac{1.5M}{1 - M + 2\pi\beta M^2(A_1 b_1 + A_2 b_2)}$$

$$S_q^m = \frac{11.2M}{15(1 - M) + 3\pi M^2 \beta b_5}$$

Recursive Method

Circulatory Response

For an aerofoil undergoing pitch about an axis at the quarter chord, the upwash velocity at the three-quarter chord is given by

$$w_e = W\alpha + \dot{\alpha}\frac{c}{2} = W\alpha + W\frac{q}{2} \quad (3.26)$$

where w_e represents the effective boundary condition at the three-quarter chord including the time history effect of the aerofoil shed wake. Using Duhamel's superposition integral, this boundary condition can be written as

$$w_e(S) = w(0)\phi(S) + \int_0^S \frac{dw(\sigma)}{d\sigma} \phi(S - \sigma) d\sigma \quad (3.27)$$

where $w(0)$ is the initial value of the upwash, σ a time variable and ϕ an indicial response function.

For discrete forcing, the above expression associated with the circulatory response can be written in a recursive form, denoting the current sample by N , as

$$\begin{aligned} w_e(N) = & W(0)\alpha(0) + W(N) \sum_{j=0}^N \Delta\alpha(j) - X_1(N) - Y_1(N) + \\ & + \alpha(N) \sum_{j=0}^N \Delta W(j) - X_2(N) - Y_2(N) + \\ & + \frac{c}{2} \sum_{j=0}^N \Delta\dot{\alpha}(j) - X_3(N) - Y_3(N) \end{aligned} \quad (3.28)$$

where the differences in the angle of attack, resultant inflow velocity, and incidence change rate between two continuous samples are

$$\Delta\alpha(j) = \alpha(j) - \alpha(j - 1)$$

$$\Delta W(j) = W(j) - W(j - 1)$$

$$\Delta\dot{\alpha}(j) = \dot{\alpha}(j) - \dot{\alpha}(j - 1)$$

$X_i(N)$ and $Y_i(N)$ ($i = 1, 2, 3$) are the deficiency functions which represent the time history effect due to the shed wake and are given in terms of the indicial function $(\phi_\alpha^C)_n$ as

$$X_i(N) = X_i(N - 1) \exp(-b_1 \beta^2 \Delta S) + A_1 \Delta_i \exp(-b_1 \beta^2 \Delta S/2)$$

$$Y_i(N) = Y_i(N - 1) \exp(-b_2 \beta^2 \Delta S) + A_2 \Delta_i \exp(-b_2 \beta^2 \Delta S/2)$$

where

$$\Delta_1 = W(N) \Delta \alpha(N)$$

$$\Delta_2 = \alpha(N) \Delta W(N)$$

$$\Delta_3 = \frac{c}{2} \Delta \dot{\alpha}(N)$$

$$\Delta S = \frac{2W(N) \Delta t}{c}$$

Thus, the effective angle of attack under the unsteady attached flow condition can approximately be obtained by

$$\alpha_e = \frac{w_e(N)}{W(N)} \quad (3.29)$$

and the normal force coefficient corresponding to the circulatory response is

$$C_n^C(N) = C_{n_\alpha} (\alpha_e - \alpha_0) \quad (3.30)$$

where α_0 is the zero-lift angle of attack.

For the circulatory pitching moment component, a similar approach can be adopted to obtain

$$C_m^C(N) = \left(\frac{1}{4} - \frac{x_{ac}}{c} \right) C_n^C(N) - \frac{\pi}{8\beta} \left[\frac{c \sum_{j=0}^N \Delta \dot{\alpha}(j)}{W(N)} - X_4(N) \right] \quad (3.31)$$

where

$$X_4(N) = X_4(N-1) \exp(-b_5 \beta^2 \Delta S) + \Delta q(N) \exp(-b_5 \beta^2 \Delta S/2)$$

$$\Delta q(N) = \frac{\dot{\alpha}(N) c}{W(N)} - \frac{\dot{\alpha}(N-1) c}{W(N-1)}$$

Impulsive Response

Numerical algorithms for the impulsive normal force and pitching moment responses can be obtained in a way similar to that above and to Beddoes's (1984). The normal force coefficient due to the impulsive response is

$$\begin{aligned} C_n^I(N) &= \frac{4 S_\alpha^n}{M} [D_\alpha(N) - D_1(N) + D_W(N) - D_2(N)] + \\ &\quad + \frac{S_q^n}{M} [D_q(N) - D_3(N)] \end{aligned} \tag{3.32}$$

where

$$D_\alpha(N) = \Delta \alpha(N) / \Delta S$$

$$D_W(N) = \alpha(N) \Delta W(N) / [W(N) \Delta S]$$

$$D_q(N) = \Delta q(N) / \Delta S$$

and

$$D_1(N) = D_1(N-1) \exp\left(-\frac{\Delta S}{S_\alpha^n}\right) + [D_\alpha(N) - D_\alpha(N-1)] \exp\left(-\frac{\Delta S}{2 S_\alpha^n}\right)$$

$$D_2(N) = D_2(N-1) \exp\left(-\frac{\Delta S}{S_\alpha^n}\right) + [D_W(N) - D_W(N-1)] \exp\left(-\frac{\Delta S}{2 S_\alpha^n}\right)$$

$$D_3(N) = D_3(N-1) \exp\left(-\frac{\Delta S}{S_q^n}\right) + [D_q(N) - D_q(N-1)] \exp\left(-\frac{\Delta S}{2 S_q^n}\right)$$

The impulsive response of the pitching moment coefficient is obtained by

$$\begin{aligned}
 C_m^I(N) = & -\frac{S_\alpha^m A_3 B_3}{M} [D_\alpha(N) - D_4(N)] \\
 & -\frac{S_\alpha^m A_4 B_4}{M} [D_\alpha(N) - D_5(N)] - \\
 & -\frac{7S_q^m}{12M} [D_q(N) - D_6(N)]
 \end{aligned} \tag{3.33}$$

where

$$\begin{aligned}
 D_4(N) &= D_4(N-1) \exp\left(-\frac{\Delta S}{S_\alpha^m b_3}\right) + [D_\alpha(N) - D_\alpha(N-1)] \exp\left(-\frac{\Delta S}{2S_\alpha^m b_3}\right) \\
 D_5(N) &= D_5(N-1) \exp\left(-\frac{\Delta S}{S_\alpha^m b_4}\right) + [D_\alpha(N) - D_\alpha(N-1)] \exp\left(-\frac{\Delta S}{2S_\alpha^m b_4}\right) \\
 D_6(N) &= D_6(N-1) \exp\left(-\frac{\Delta S}{S_q^m}\right) + [D_q(N) - D_q(N-1)] \exp\left(-\frac{\Delta S}{2S_q^m}\right)
 \end{aligned}$$

3.3.3 Leading Edge Separation

The most crucial aspect of the modelling of dynamic stall is the identification and representation of the conditions for the onset of leading edge separation. Beddoes (1978) determined that, although under time-dependent forcing conditions the pressure gradient on the aerofoil at a given angle of attack was significantly modified, it was possible to predict the onset of leading edge separation using a criterion in which the attainment of a critical local leading pressure was the primary factor. In application, the leading edge pressure is related to the normal force coefficient, C_n , so that it is possible to obviate the need to compute aerofoil pressures. From analysis of aerofoil static data, a critical static normal force coefficient, C_{n_1} , may be obtained which corresponds to the critical pressure for the leading edge separation onset. In practice, however, C_{n_1} can be obtained from the static value of C_n that corresponds to either the break in the pitching moment or the chordwise force at stall.

For dynamic conditions, there is a lag in the unsteady normal force coefficient $C_n(t)$ with respect to changes in angle of attack; however, there is also a lag in the leading edge pressure response with respect to $C_n(t)$ (Beddoes 1983). Thus, for an increasing angle of attack, the lag in the leading edge pressure response results in the critical pressure being achieved at a higher value of C_n than for the quasi-steady case. This mechanism significantly contributes to the overall delay in the onset of dynamic stall.

To implement the critical pressure criterion under unsteady conditions, a first-order lag may be applied to unsteady $C_n(t)$. For a discretely sampled system, this compensation may be expressed in a recursive form as

$$C'_n(N) = C_n(N) - D_p(N) \quad (3.34)$$

where

$$C_n(N) = C_n^C(N) + C_n^I(N)$$

$$D_p(N) = D_p(N-1) \exp\left(-\frac{\Delta S}{S_p}\right) + [C_n(N) - C_n(N-1)] \exp\left(-\frac{\Delta S}{2S_p}\right)$$

The constant S_p can be determined empirically from test data. Thus, the leading edge separation is initiated when $C'_n > C_{n_1}$. Furthermore, if the value of C'_n is monitored throughout the calculation into stall, it may be used as an indicator for flow re-attachment when $C'_n < C_{n_1}$.

3.3.4 Trailing Edge Separation

Kirchhoff Flow Theory

A phenomenon that appears to be involved in most types of stall is progressive trailing edge flow separation. This movement of the trailing edge separation point has been observed in HAWT experiments (Huyer *et al.* 1996).

The associated loss of circulation with the development of separation at the trailing edge introduces non-linearities in the lift, drag, and pitching moment behaviour. The accurate solution for these non-linear relationships can only come from

coupled boundary layer/separation calculations. Alternatively, the Leishman–Beddoes model uses the Kirchhoff flow theory to account approximately for the effects of separation on the linear solution. In the Kirchhoff flow model, which was

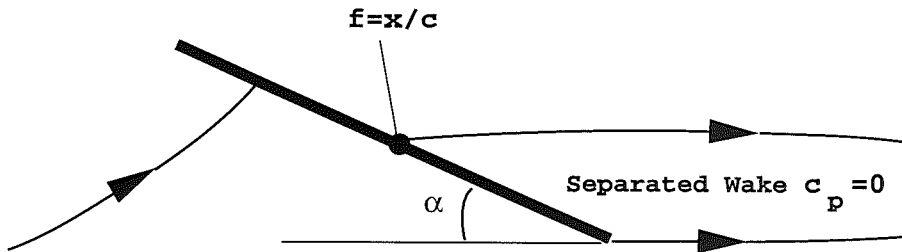


Figure 3.4: Kirchhoff flow model for separated flow past a flat plate

reviewed by Thwaites (1960) and Woods (1961), the pressure in the wake of the separated flow region on a 2-D flat plate is assumed to be zero and the lift is then related to the separation point $x/c = f$ (Fig. 3.4),

$$C_n = C_{n_\alpha} \left(\frac{1 + \sqrt{f}}{2} \right)^2 (\alpha - \alpha_0) \quad (3.35)$$

Thus, if the separation point can be determined, it is then a trivial calculation to determine the normal force. The relationship between the separation point and the angle of attack can be deduced from aerofoil wind tunnel data by re-arranging Eq. 3.35,

$$f = 4 \left[\sqrt{\frac{C_n}{C_{n_\alpha} (\alpha - \alpha_0)}} - \frac{1}{2} \right]^2 \quad (3.36)$$

Through investigation of a series of aerofoils, Eq. 3.36 can be generalised in a fitted exponential format as

$$f = \begin{cases} 1 - 0.3 \exp \left[\frac{\alpha - \alpha_1}{S_1} \right] & \text{for } \alpha \leq \alpha_1 \\ 0.04 + 0.66 \exp \left[\frac{\alpha_1 - \alpha}{S_2} \right] & \text{for } \alpha > \alpha_1 \end{cases} \quad (3.37)$$

where the coefficients S_1 and S_2 define the static stall characteristic, while α_1 defines the break point corresponding to $f = 0.7$. S_1 , S_2 , and α_1 can easily be

determined from the wind tunnel static lift data.

A general expression for the pitching moment coefficient, C_m , cannot be obtained from Kirchhoff flow theory. In the Leishman–Beddoes model, the variation of the ratio C_m/C_n (allowing for the zero-lift moment) is fitted in a least square method, from the aerofoil static data, to the form

$$\frac{C_m}{C_n} = k_0 + k_1 (1 - f) + k_2 \sin(\pi f^\mu) \quad (3.38)$$

where k_0 represents the offset of the aerodynamic centre from the quarter-chord axis, k_1 gives the direct effect on the centre of pressure due to the growth of the separated flow region, and k_2 helps describe the shape of the moment break at stall. The values of k_0 , k_1 , k_2 , and μ can be adjusted for different aerofoils, as necessary, to give the best reconstruction of C_m/C_n .

For small angles of attack, the tangential force (leading edge thrust) coefficient C_t (Eq. 1.16) can be approximated by

$$C_t = C_l \alpha - C_d \quad (3.39)$$

Substitution of the results from the Kirchhoff theory

$$C_l = C_{l_\alpha} \alpha \left(\frac{1 + \sqrt{f}}{2} \right)^2$$

$$C_d = C_{d_\alpha} \alpha^2 \left(\frac{1 - \sqrt{f}}{2} \right)^2$$

into Eq. 3.39 yields

$$C_t = C_{l_\alpha} \alpha^2 \sqrt{f}$$

This may be related to the normal force coefficient in a more generalised way,

$$C_t = C_{n_\alpha} (\alpha - \alpha_0) \sqrt{f} \sin \alpha \quad (3.40)$$

Unsteady Trailing Edge Separation

For unsteady conditions, there is a lag in the leading edge pressure response with respect to normal force and the lagged normal force coefficient C'_n is obtained by Eq. 3.34. The corresponding angle of attack becomes

$$\alpha'(N) = \frac{C'_n(N)}{C_{n_\alpha}} + \alpha_0 \quad (3.41)$$

Substitution of Eq. 3.41 into Eq. 3.37 yields the trailing edge separation point associated with the lag in the leading edge pressure response,

$$f'(N) = \begin{cases} 1 - 0.3 \exp \left[\frac{\alpha'(N) - \alpha_1}{S_1} \right] & \text{for } \alpha'(N) \leq \alpha_1 \\ 0.04 + 0.66 \exp \left[\frac{\alpha_1 - \alpha'(N)}{S_2} \right] & \text{for } \alpha'(N) > \alpha_1 \end{cases} \quad (3.42)$$

In addition to the aerofoil unsteady pressure response, there is also an unsteady boundary layer response, the effect of which on the trailing edge separation point may be represented by applying a first-order lag to the value of f' . For a sampled system,

$$f''(N) = f'(N) - D_f(N) \quad (3.43)$$

where

$$D_f(N) = D_f(N-1) \exp \left(-\frac{\Delta S}{S_f} \right) + [f'(N) - f'(N-1)] \exp \left(-\frac{\Delta S}{2S_f} \right)$$

The constant S_f can be evaluated from unsteady aerofoil test data. Thus, the value of f'' is used to obtain the non-linear forces and pitching moment *via* Eqs. 3.35, 3.40 and 3.38.

3.3.5 Modelling of Dynamic Stall

The general case of dynamic stall involves the formation of a vortex near the leading edge of the aerofoil which subsequently separates from the upper surface and is transported downstream over the chord. In the Leishman–Beddoes dynamic stall

model, the total accumulated vortex normal force coefficient C_n^v under unsteady conditions is allowed to decay exponentially with time and is also updated by a new increment. For a sampled system,

$$C_n^v(N) = C_n^v(N-1) \exp\left(-\frac{\Delta S}{S_v}\right) + [C_v(N) - C_v(N-1)] \exp\left(-\frac{\Delta S}{2S_v}\right) \quad (3.44)$$

where

$$C_v(N) = C_n^C(N) \left\{ 1 - \left[\frac{1 + \sqrt{f''(N)}}{2} \right]^2 \right\} \quad (3.45)$$

The centre of pressure on the aerofoil also varies with the chordwise position of the shedding vortex and will achieve a maximum value when the vortex reaches the trailing edge after a non-dimensional time period τ_{vl} . A general representation of the centre of pressure behaviour (aft of quarter-chord) due to the dynamic stall vortex is empirically formulated as

$$(CP)_v = 0.25 \left(1 - \cos \frac{\pi \tau_v}{\tau_{vl}} \right) \quad (3.46)$$

where τ_v is denoted as the non-dimensional vortex time, $0 \leq \tau_v \leq 2\tau_{vl}$, *i.e.* $\tau_v = 0$ at the onset of dynamic stall and $\tau_v = \tau_{vl}$ when the vortex reaches the trailing edge. Both the vortex decay non-dimensional time constant S_v and the non-dimensional time for the vortex to traverse the chord τ_{vl} can be obtained statistically from a variety of dynamic stall test data. Thus, the increment in pitching moment about the quarter-chord due to dynamic stall is given by

$$C_m^v = -(CP)_v \cdot C_n^v \quad (3.47)$$

Abrupt airloading changes occur when the critical condition for the leading edge separation is met, *i.e.* $C'_n > C_{n_1}$. At this point the accumulated vortex lift is assumed to start to convect over the chord. During the vortex convection process the vortex force is assumed to behave according to Eqs. 3.44 and 3.45 but, the accumulation is terminated when the vortex reaches the trailing edge at $\tau_v = \tau_{vl}$. At the same time, the ongoing pressure changes due to the vortex shedding process are sufficient to accelerate the forward movement of the trailing edge separation;

this is accomplished by halving the S_f non-dimensional time constant. After the vortex passes the aerofoil trailing edge the effect of the vortex-induced lift on the aerofoil behaviour decays rapidly, which is accomplished by halving the non-dimensional vortex decay time constant S_v for the period $\tau_{vl} \leq \tau_v \leq 2\tau_{vl}$.

3.3.6 Unsteady Aerodynamic Loads

Having presented the attached flow behaviour, which is split into the circulatory and impulsive responses in an indicial form, and the separated flow behaviour including dynamic stall, the aerodynamic forces and moment can now be summarised as follows.

Normal Force

The non-linear term associated with the trailing edge separation is

$$C_n^f = C_n^C \left(\frac{1 + \sqrt{f''}}{2} \right)^2 \quad (3.48)$$

where C_n^C is obtained by Eq. 3.30 and f'' by Eq. 3.43. Thus, the total unsteady normal force coefficient is

$$C_n = C_n^f + C_n^I + C_n^v \quad (3.49)$$

where C_n^I is calculated from Eq. 3.32 and, in the dynamic stall case, C_n^v is obtained from Eq. 3.44.

Chordwise Force

After the onset of gross separation, the Kirchhoff modification to the chordwise force, Eq. 3.40, becomes invalid and an alternative procedure has been adopted. In the model, the chord force is related to the separation point simply by introducing an additional term in the expression, *i.e.*

$$C_t^f = k_t \eta_t C_n^C \sqrt{f''} \sin \alpha_e \quad (3.50)$$

where k_t is called the chordwise force efficiency which can be estimated from aerofoil test data and is usually close to unity, and

$$\eta_t = \begin{cases} (f'')^{K_f (C'_n - C_{n_1})} & \text{for } C'_n > C_{n_1} \\ 1 & \text{for } C'_n \leq C_{n_1} \end{cases} \quad (3.51)$$

where the increased rate at which the chordwise force in dynamic stall case is lost (and hence the onset of drag divergence) is represented using the empirical constant K_f . The tangential force coefficient is given by

$$C_t = C_t^f + (C_n^I + C_n^v) \sin \alpha \quad (3.52)$$

Pitching Moment

From Eq. 3.38, the contribution of the movement of the centre of pressure due to the trailing edge separation is

$$C_m^f = C_{m_0} + \{k_0 + k_1(1 - f'') + k_2 \sin [\pi (f'')^\mu]\} C_n^f \quad (3.53)$$

where C_{m_0} is the zero-lift pitching moment coefficient. The total pitching moment coefficient is then given by

$$C_m = C_m^C + C_m^f + C_m^I + C_m^v \quad (3.54)$$

where C_m^C and C_m^I are obtained from Eqs. 3.31 and 3.33 respectively and, in the dynamic stall case, C_m^v is obtained from Eq. 3.47.

3.4 Model Coupling

In the present study, the prescribed wake model and Leishman–Beddoes dynamic stall model are combined into the unsteady prescribed wake model to calculate the unsteady aerodynamic performance of HAWTs. The calculation procedure is illustrated in Fig. 3.5.

The Leishman–Beddoes unsteady aerodynamic model requires information such as the reduced pitching rates, the local relative velocity and the instantaneous

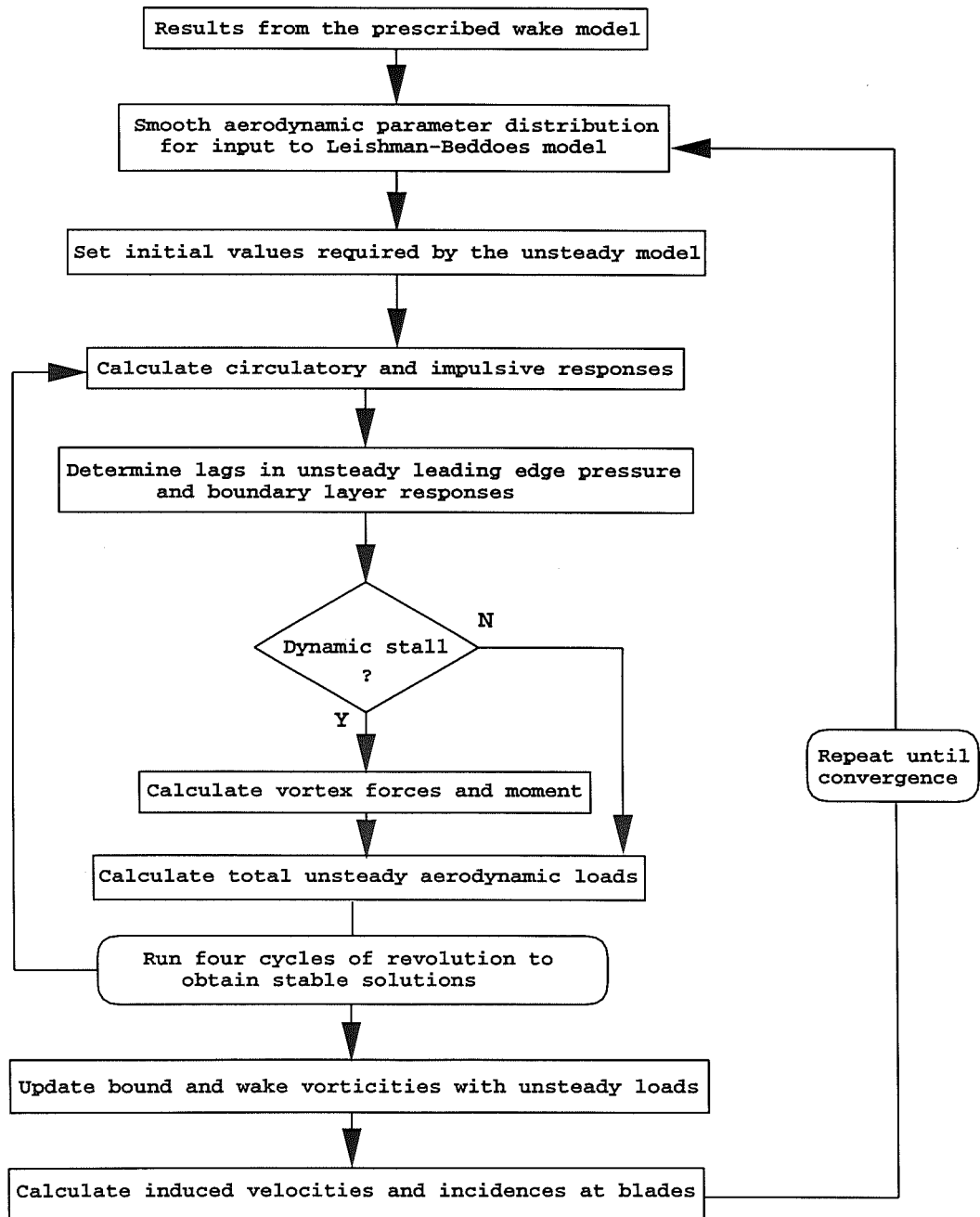


Figure 3.5: Flow chart of the calculation Scheme for the unsteady prescribed wake model

angle of attack that the turbine blade experiences. In the unsteady prescribed wake model, this information is provided by initial application of the prescribed wake scheme using static aerodynamic characteristics. The results from the prescribed wake model are then input to the unsteady model as initial values and, the unsteady aerodynamic characteristics of the blade are calculated.

As the stability of the indicial approach can be sensitive to the calculation time step, the number of azimuthal steps is appropriately increased in the unsteady calculation stage; the aerodynamic information at the additional steps is obtained using interpolation. A smoothing process, which can be required by the Leishman–Beddoes model, is applied to the variations of velocity and angle of attack with azimuthal position. Furthermore, in order to obtain stable solutions for the unsteady forcing, a series of iterations are conducted on a cycle-by-cycle basis when the recursive calculations are carried out for the sampled system. It has been found that the repeatability of calculations is very good between the third cycle and those following, an outcome similar to other numerical studies of dynamic stall (*e.g.* Guilmineau and Queutey 1999).

The application of the Leishman–Beddoes model gives an unsteady aerodynamic blade loading which is different from the quasi-steady results obtained from the prescribed wake model. This difference results in a redistribution of the bound vorticity along the blade and consequently of the trailed and shed vorticities in the wake. The changes in the wake vorticities influence the blade loading in turn *via* the induced velocity. Therefore, a global iteration process must be implemented to achieve an appropriate distribution of the induced velocities and the aerodynamic loads on the blades. Based on the wake geometry and hence the influence coefficients from the quasi-steady prescribed wake model, this reconstruction iteration is very fast.

In modelling the performance of an aerofoil in unsteady flow, the indicial technique described above implicitly includes the induced effect of the shed wake structure downstream of *the aerofoil* (see Section 3.3.2). Meanwhile, the wake structure generated in the prescribed wake method contains filaments of shed vorticity and

their induced effect on the blade flow field is calculated directly by application of the Biot–Savart law. Consequently, coupling of the two schemes is hindered by this duplicative effect. This can be overcome by selectively neglecting the shed wake terms from the prescribed wake model and calculating the induced effect *via* the unsteady aerofoil performance scheme. In this case, only the influence of the wake element on the blade element from which it is shed is removed from the prescribed wake model. Let $(\bar{x}_{cp})_{i,j}$, $(\bar{y}_{cp})_{i,j}$ and $(\bar{z}_{cp})_{i,j}$ (Eq. 3.5) be the cartesian coordinates of the blade element at which the induced velocity is evaluated. The induced velocities at the (i,j) th blade element control point are then estimated, in the unsteady calculation stage, by

$$(\bar{v}_x)_{i,j}^{cp} = - \sum_{q=1}^{N_T} \left[\sum_{p=1}^{N_E+1} (\bar{\Gamma}_t)_{p,q} (I_x^t)_{p,q} + \sum_{\substack{p=1 \\ p \neq i}}^{N_E} (\bar{\Gamma}_s)_{p,q} (I_x^s)_{p,q} \right] \quad (3.55)$$

$$(\bar{v}_y)_{i,j}^{cp} = - \sum_{q=1}^{N_T} \left[\sum_{p=1}^{N_E+1} (\bar{\Gamma}_t)_{p,q} (I_y^t)_{p,q} + \sum_{\substack{p=1 \\ p \neq i}}^{N_E} (\bar{\Gamma}_s)_{p,q} (I_y^s)_{p,q} \right] \quad (3.56)$$

$$(\bar{v}_z)_{i,j}^{cp} = - \sum_{q=1}^{N_T} \left[\sum_{p=1}^{N_E+1} (\bar{\Gamma}_t)_{p,q} (I_z^t)_{p,q} + \sum_{\substack{p=1 \\ p \neq i}}^{N_E} (\bar{\Gamma}_s)_{p,q} (I_z^s)_{p,q} \right] \quad (3.57)$$

where the non-dimensional trailed and shed vorticities are calculated using the unsteady loading from the Leishman–Beddoes model while the influence coefficients are assumed to remain unchanged.

3.5 Results and Discussion

Gross Rotor Performance

The ability of the model to predict gross wind turbine performance in yawed flow is illustrated in Fig. 3.6. In this figure the power coefficients calculated for

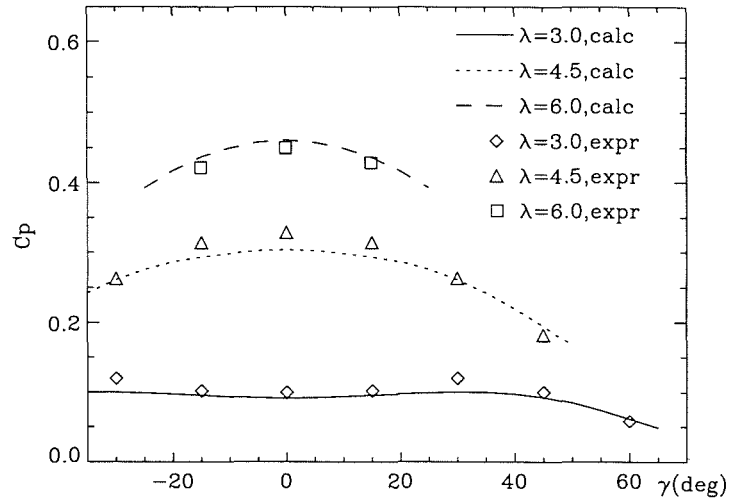


Figure 3.6: Comparison of predicted and measured power coefficients for the WG500 turbine in yaw

the WG500 turbine are compared with wind tunnel measurements (Ronsten *et al.* 1995) over a range of tip speed ratios and yaw angles. The problems associated with obtaining accurate estimates of rotor power from a wind tunnel based test are well documented. A unique aspect of this particular test, however, was that the measured data were corrected using an established technique based on measured wall pressure to reflect performance in an unconstrained flow. It is clear from the figure that the level of agreement between calculation and experiment is generally very high and that trends in the experimental data are well represented by the calculation. One interesting aspect of the results presented in the figure is that at a tip speed ratio $\lambda = 3$ the maximum power coefficient does not correspond to the head-on flow case. This occurs because the angle of incidence on a large portion of the blade is so high in the zero yaw case that a large section of the blade is continually stalled. At moderate yaw angles, however, the blades pass in and out of stall and thus experience a periodic recovery in performance. It is particularly significant that the model is able accurately to represent this effect.

Wind Shear Effect

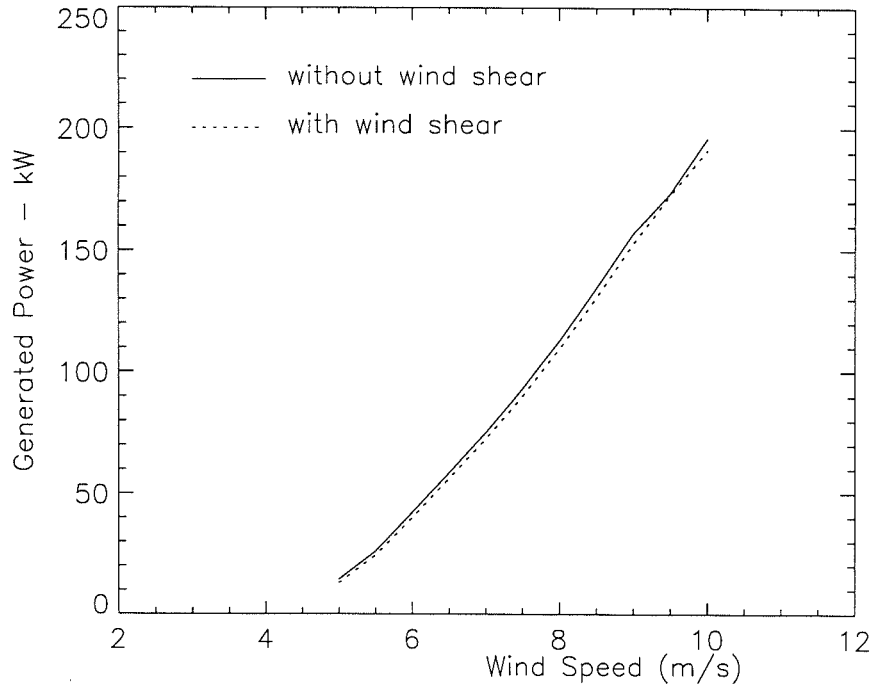


Figure 3.7: Comparison of generated power coefficients predicted for the MOD–OA turbine in unyawed flow

Fig. 3.7 gives a comparison of the power output from the MOD–OA HAWT generator calculated with and without wind shear. For the wind shear case, the shear exponent was chosen to be $\eta = 1/6$ for demonstration of the wind shear effect. The generated power with wind shear is slightly lower than that without wind shear.

The effect of wind shear on the turbine blade aerodynamic loads is illustrated in Fig. 3.8, where the shear exponent was assumed to be $\eta = 1/6$ again. This figure clearly shows the cyclic variation of the section normal force with azimuth under the wind shear condition. This additional loading imbalance, particularly evident at blade outboard sections, may have important influences on the turbine fatigue life. By comparing Fig. 3.9 with Fig. 2.16, it seems that the results calculated

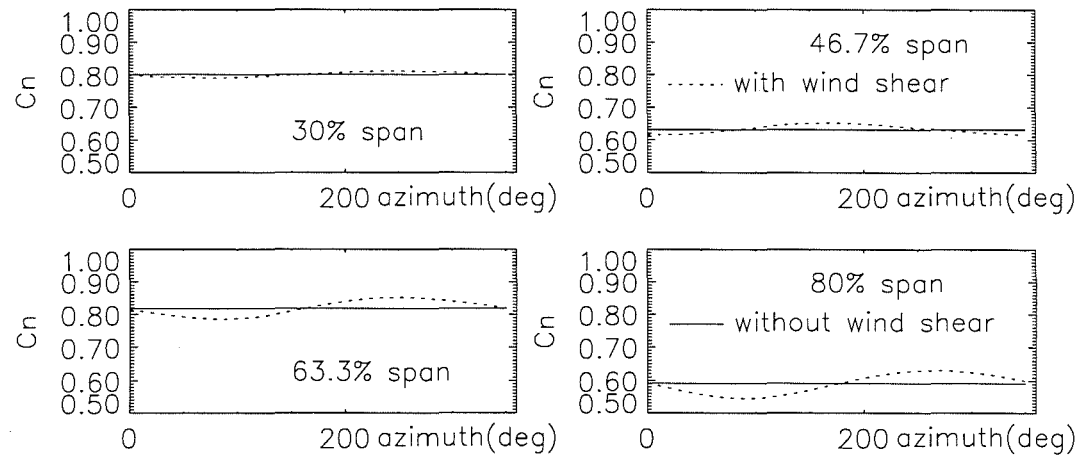


Figure 3.8: Comparison of predicted normal force coefficient with and without wind shear for NREL UAE Phase I turbine at $V_0 = 10.5 \text{ m/s}$ and $\gamma = 1.3^\circ$

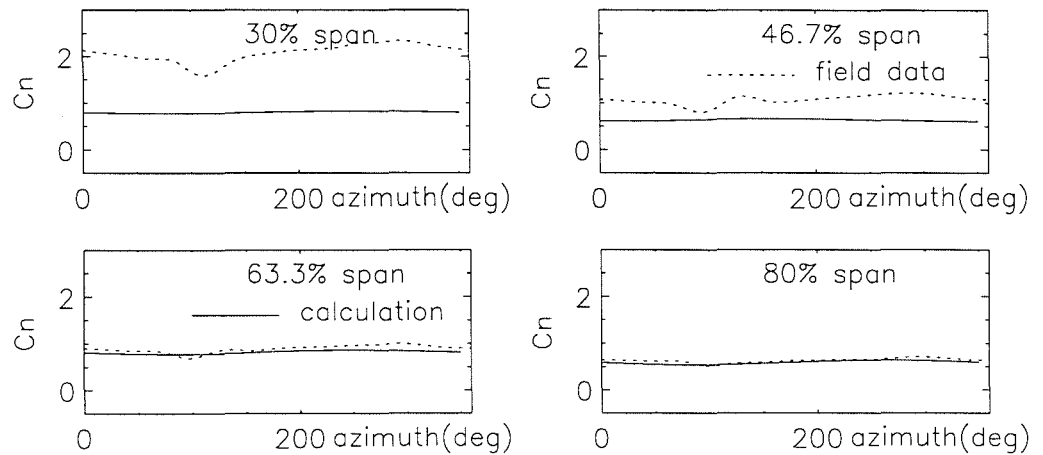


Figure 3.9: Comparison of predicted normal force coefficient in condition of wind shear with field data of NREL UAE Phase I at $V_0 = 10.5 \text{ m/s}$ and $\gamma = 1.3^\circ$

with wind shear correlate slightly better with field data than without wind shear. In the following comparisons and discussion, however, there are no wind shear effects presented in the calculated results since complete wind velocity profiles are unavailable in the field data.

Blade Aerodynamic Loading

The primary aim of the unsteady prescribed wake model is to provide a means of obtaining accurate estimates of unsteady aerodynamic loads on the blades, which then can be used in the analysis of dynamic and structural responses. NREL's UAE HAWTs were again chosen as the basis for comparison due to available field data associated with unsteady blade loads.

It should be noted that the free stream speed and yaw angle are fixed during the calculation procedure. For the field experiment, however, both of these parameters naturally vary around their mean values. The variation in the measured field data from the constant wind speed and steady yaw condition can be considerable, although this effect is to a large extent minimised by azimuth averaging over a number of revolutions. Nevertheless, in the comparisons that follow this may be the reason that the predicted blade loads lack the apparent higher-frequency content exhibited by much of the field data.

Figs. 3.10 to 3.19 show comparisons of the aerofoil normal force, tangential force, and pitching moment coefficients between the prescribed wake model and field data at four spanwise blade locations for a variety of wind speeds and a variety of yaw angles. Generally, the model compares well with the field data from the two NREL wind turbines and captures the main features of the loading pattern on outboard sections of the blade where most of the turbine power is produced. In addition, the level of agreement between the prediction and experiment at low wind speeds (low blade angle of attack) is better than at high wind speeds (high blade angle of attack). The reason for this will be discussed below.

In these examples, the yaw angle is as high as -35.4° for the NREL untwisted-

blade rotor of the Phase II and 41.4° for the twisted-blade rotor of the Phase IV machine according to the available field data. It seems in these ranges of yaw angle that the influence of yaw angle on the correlation of calculation with experiment is very small. In other words, at the same wind speed (Figs. 3.12 and 3.13) or nearly the same wind speed (Figs. 3.10 and 3.11 as well as Figs. 3.16 and 3.17), the levels of agreement between the model and field data are not significantly different at different yaw angles. This illustrates the applicability of the unsteady prescribed wake model to the yawed flow case.

One interesting aspect of Fig. 3.15 is the sharp downward deviation in the predicted pitching moment coefficient at 30% of span as the blade reaches approximately 230° azimuth. This is accompanied by a corresponding rise in the normal force coefficient and is produced by predicted vortex shedding. Although there is a difference in the amplitude and phasing between the prediction and the field data, the field data clearly exhibit a similar response at around 290° azimuth suggesting that vortex shedding does, in fact, take place. The differences may result from the substitutive uses of the vortex constants S_v and τ_{vl} of the NACA0012 aerofoil because these dynamic stall parameters are not available for the S809 aerofoil at present. It is expected that use of the real values of S_v and τ_{vl} for the S809 aerofoil would mitigate these discrepancies. Also, the model captures the trend of the extremely acute load variations exhibited by the field data in Figs. 3.18 and 3.19 for the second half of revolution, although the magnitude is not particularly represented by the model.

On the other hand, it can be seen from comparisons between Figs. 3.11 and 3.12 and between Figs. 3.14 and 3.15 that the level of agreement between calculation and measurement deteriorates with increased wind speed. This is particularly clear in Figs. 3.16 through 3.20 where the figures are arranged in order of increasing velocity. Compared to the untwisted blade (Figs. 3.10 to 3.15), the comparison of the calculated results with field data is much better for the twisted blade (Figs. 3.16 to 3.20) at the inboard blade stations where the angles of attack

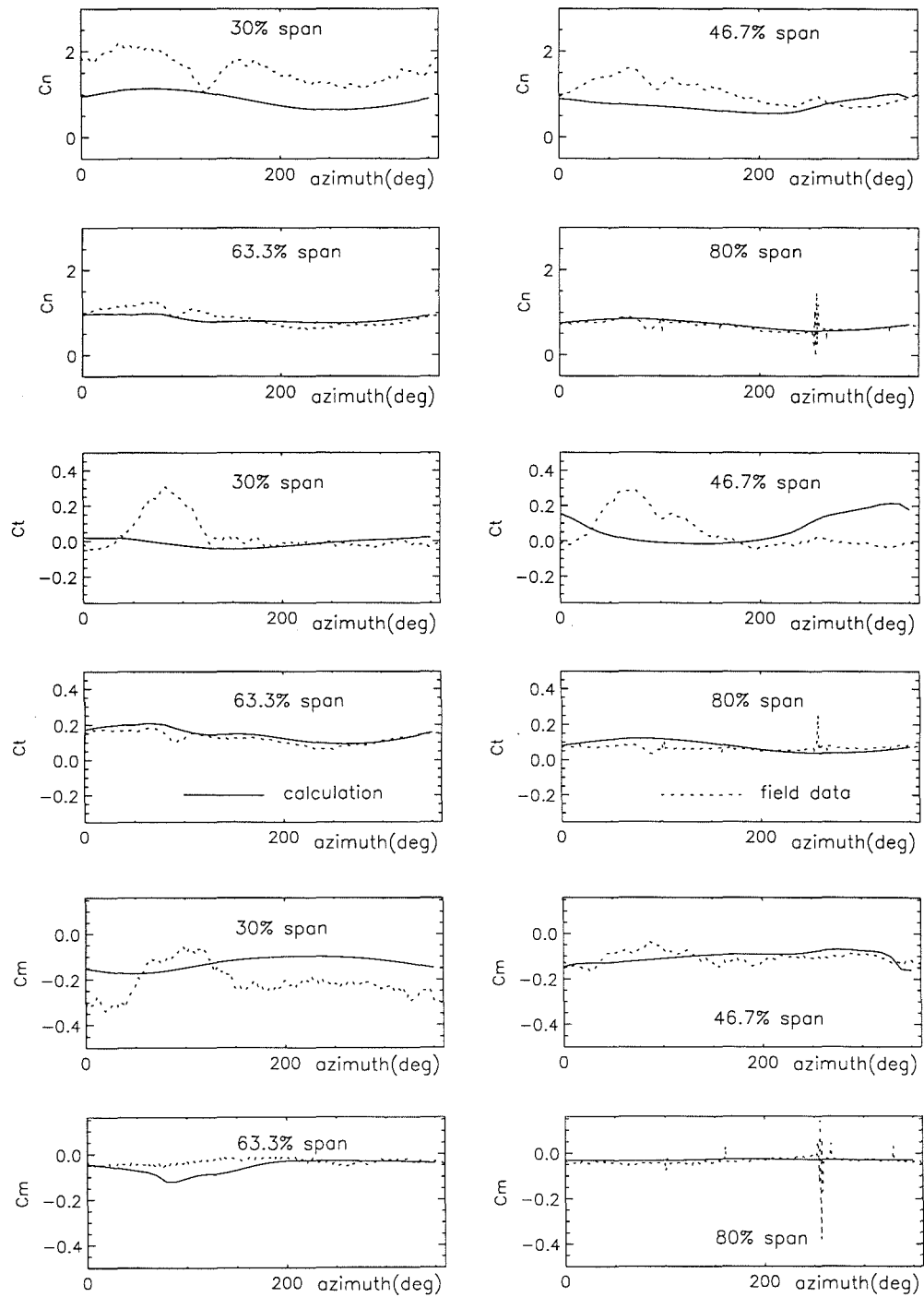


Figure 3.10: Comparison of predicted blade aerodynamic loading with field data of NREL UAE Phase I at $V_0 = 12.5$ m/s and $\gamma = -19.7^\circ$

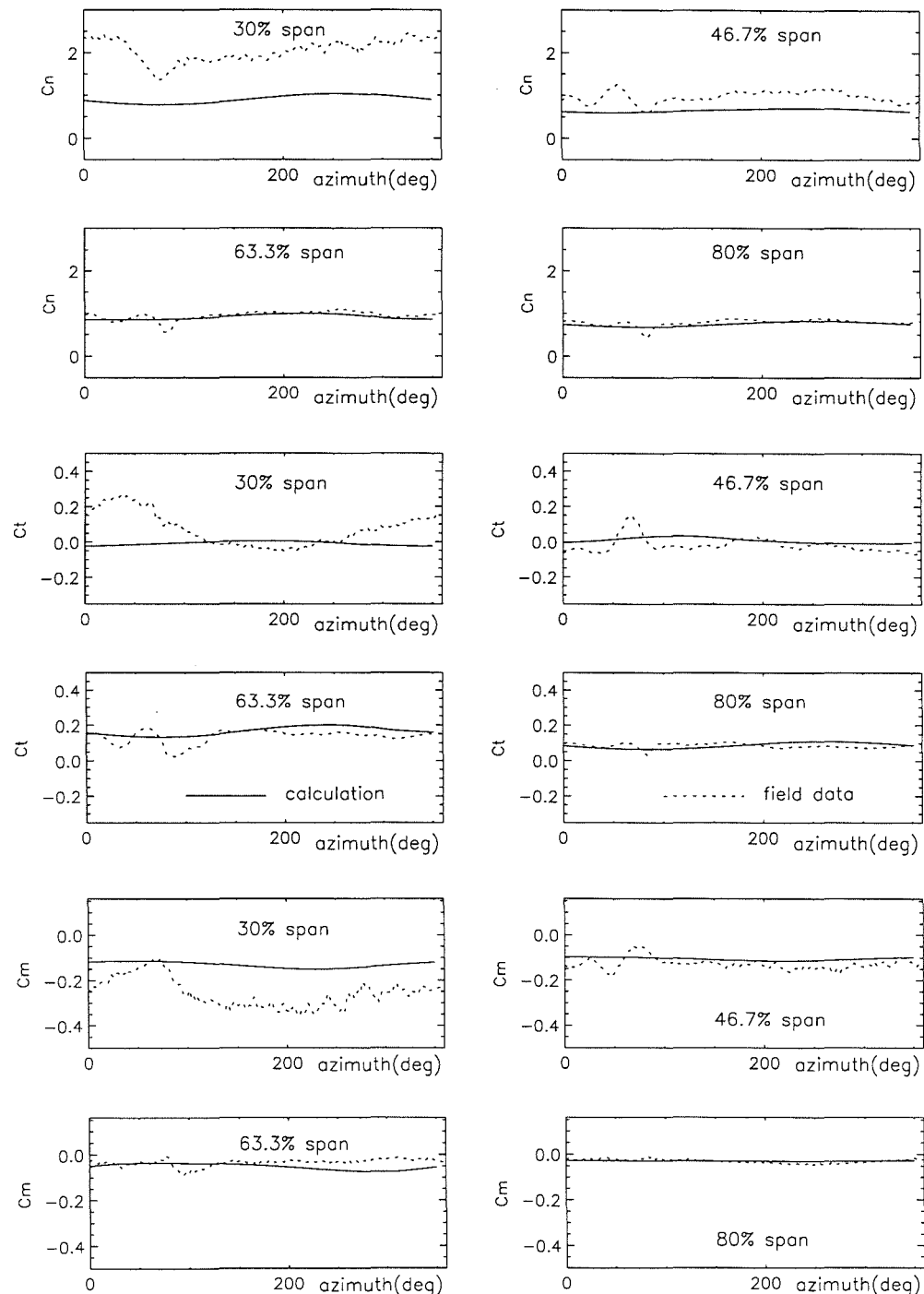


Figure 3.11: Comparison of predicted blade aerodynamic loading with field data of NREL UAE Phase I at $V_0 = 12.3$ m/s and $\gamma = 9.9^\circ$

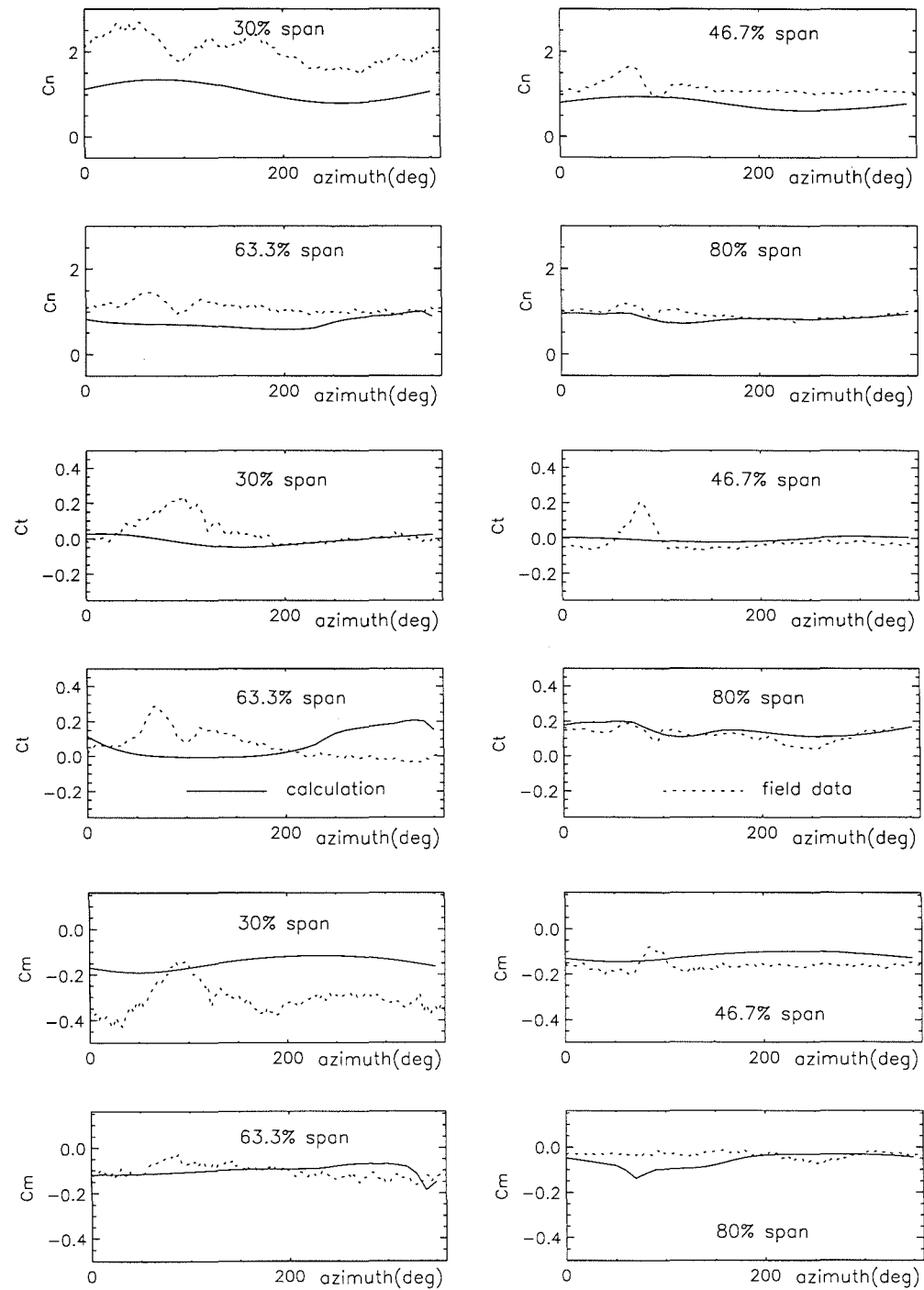


Figure 3.12: Comparison of predicted blade aerodynamic loading with field data of NREL UAE Phase I at $V_0 = 15.9$ m/s and $\gamma = -17.2^\circ$

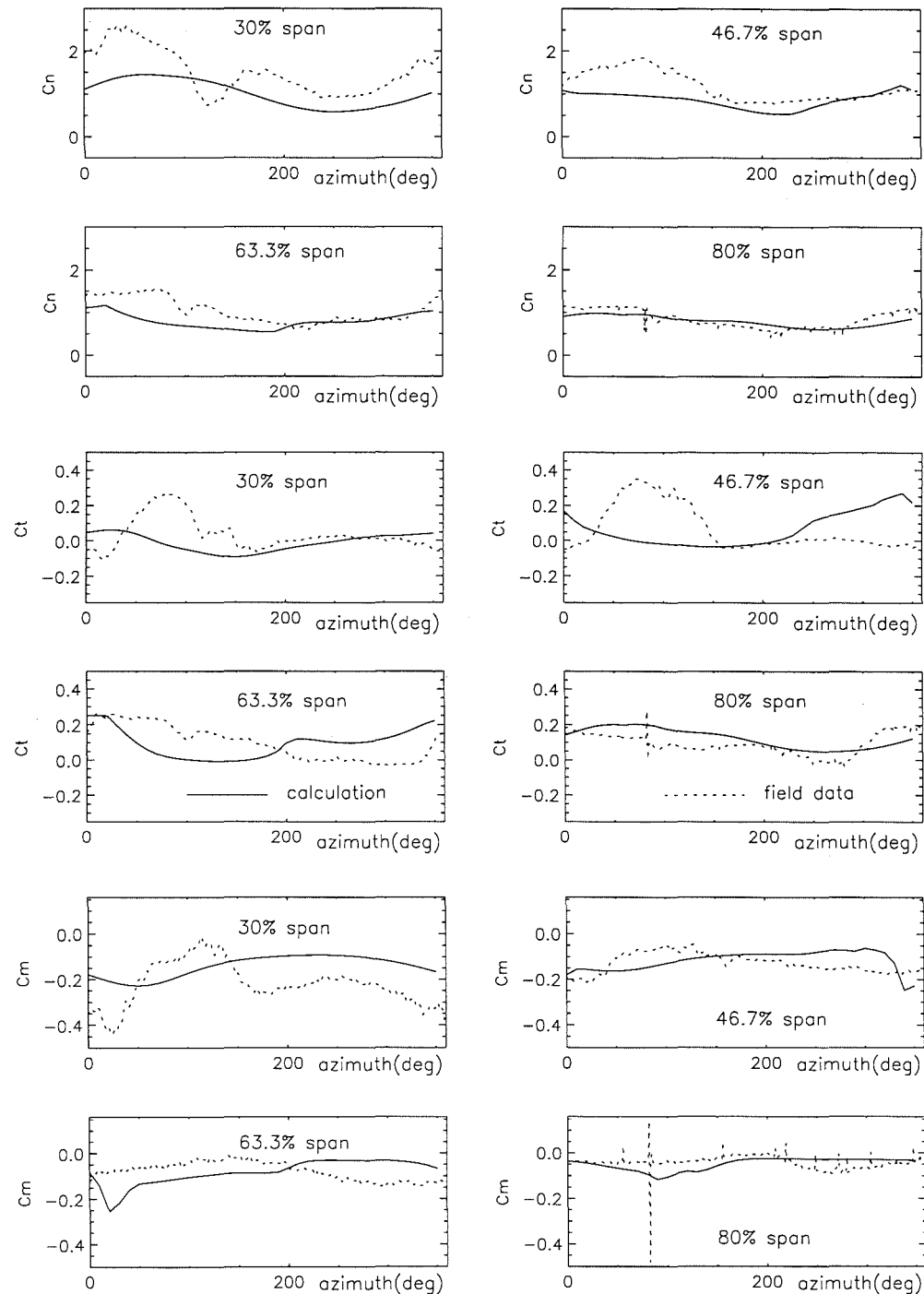


Figure 3.13: Comparison of predicted blade aerodynamic loading with field data of NREL UAE Phase I at $V_0 = 15.9$ m/s and $\gamma = -30.1^\circ$

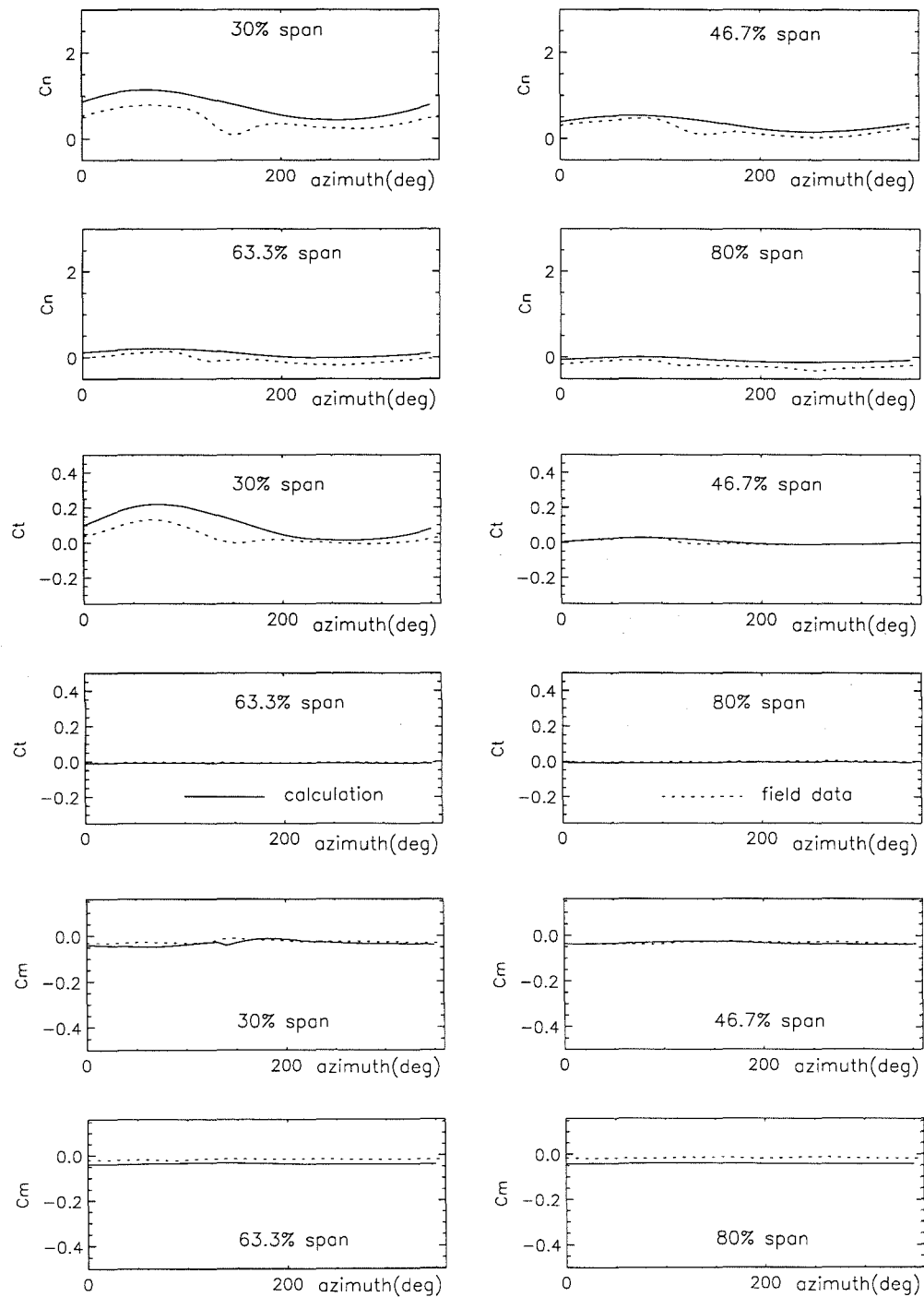


Figure 3.14: Comparison of predicted blade aerodynamic loading with field data of NREL UAE Phase I at $V_0 = 6.1$ m/s and $\gamma = -35.4^\circ$

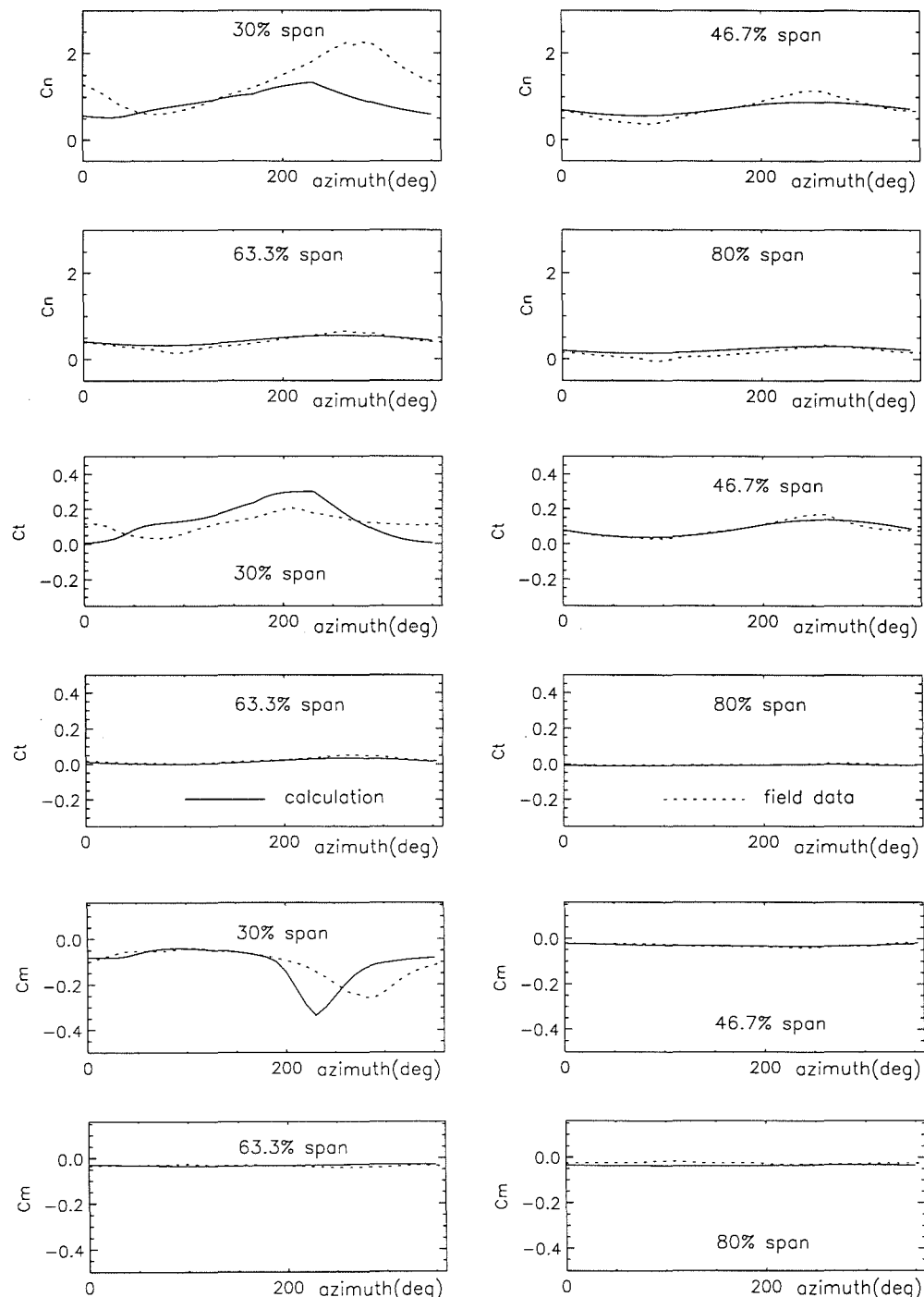


Figure 3.15: Comparison of predicted blade aerodynamic loading with field data of NREL UAE Phase I at $V_0 = 7.8$ m/s and $\gamma = 21.4^\circ$

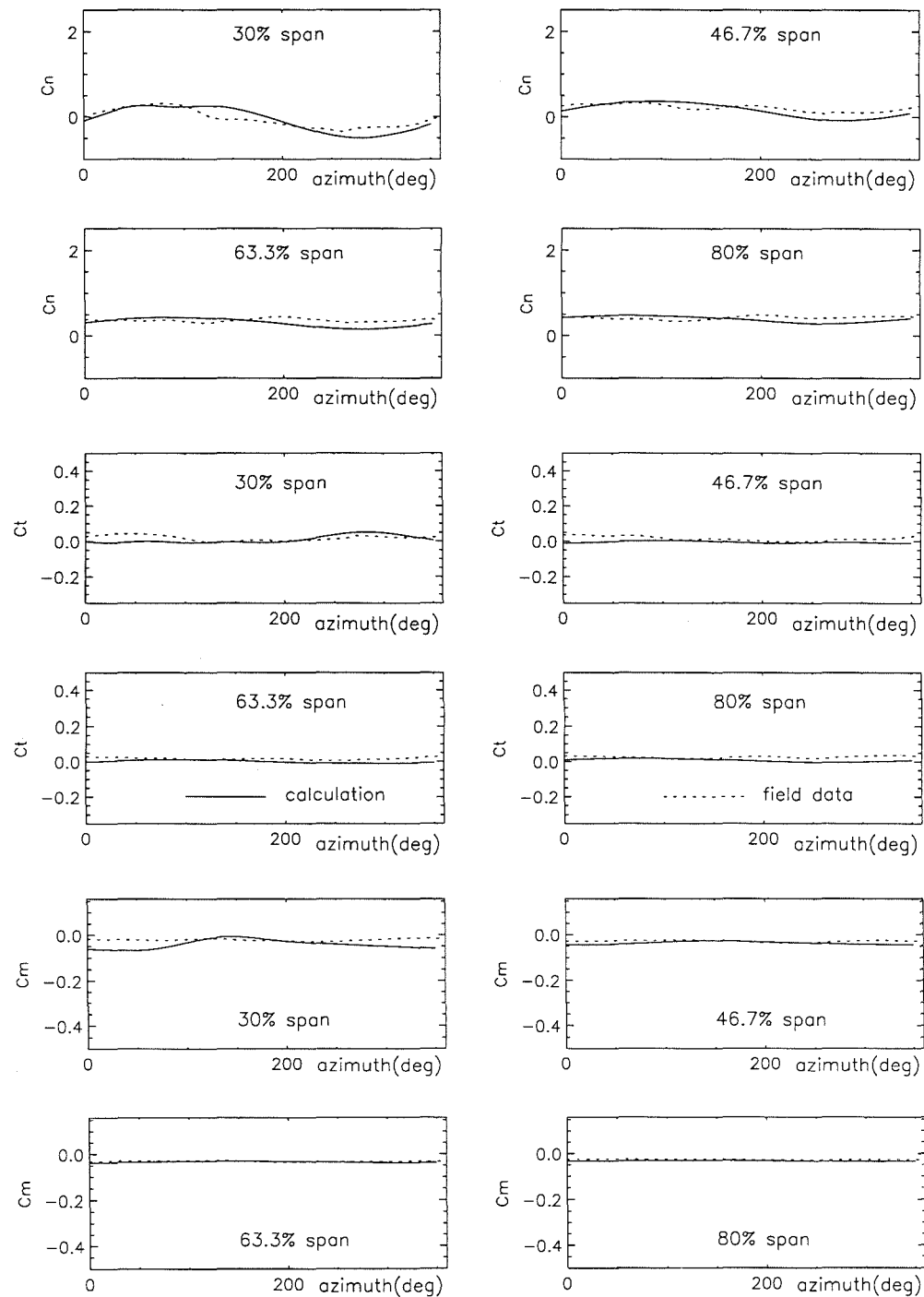


Figure 3.16: Comparison of predicted blade aerodynamic loading with field data of NREL UAE Phase IV at $V_0 = 6.7$ m/s and $\gamma = -38.2^\circ$

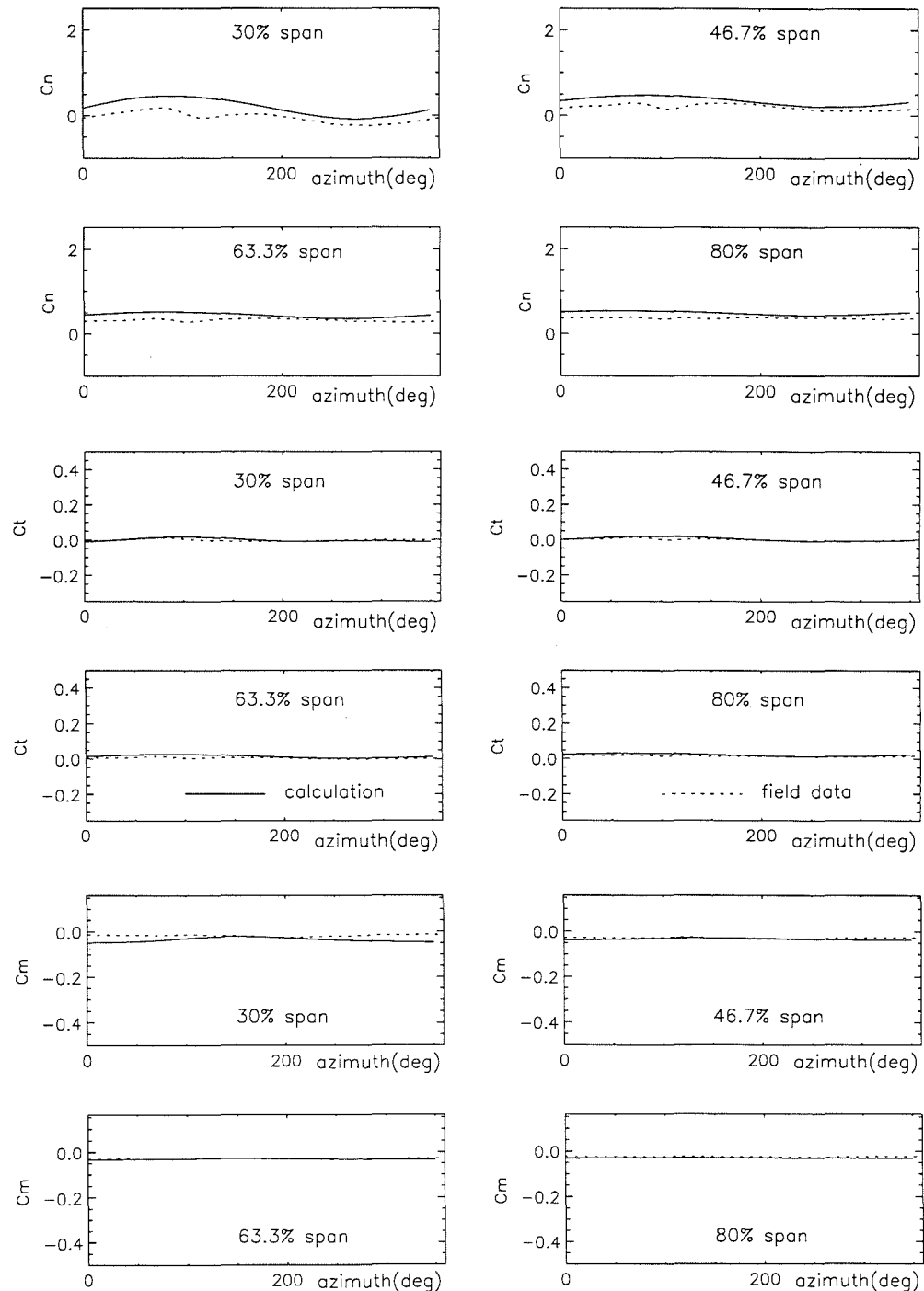


Figure 3.17: Comparison of predicted blade aerodynamic loading with field data of NREL UAE Phase N at $V_0 = 6.8$ m/s and $\gamma = -18.7^\circ$

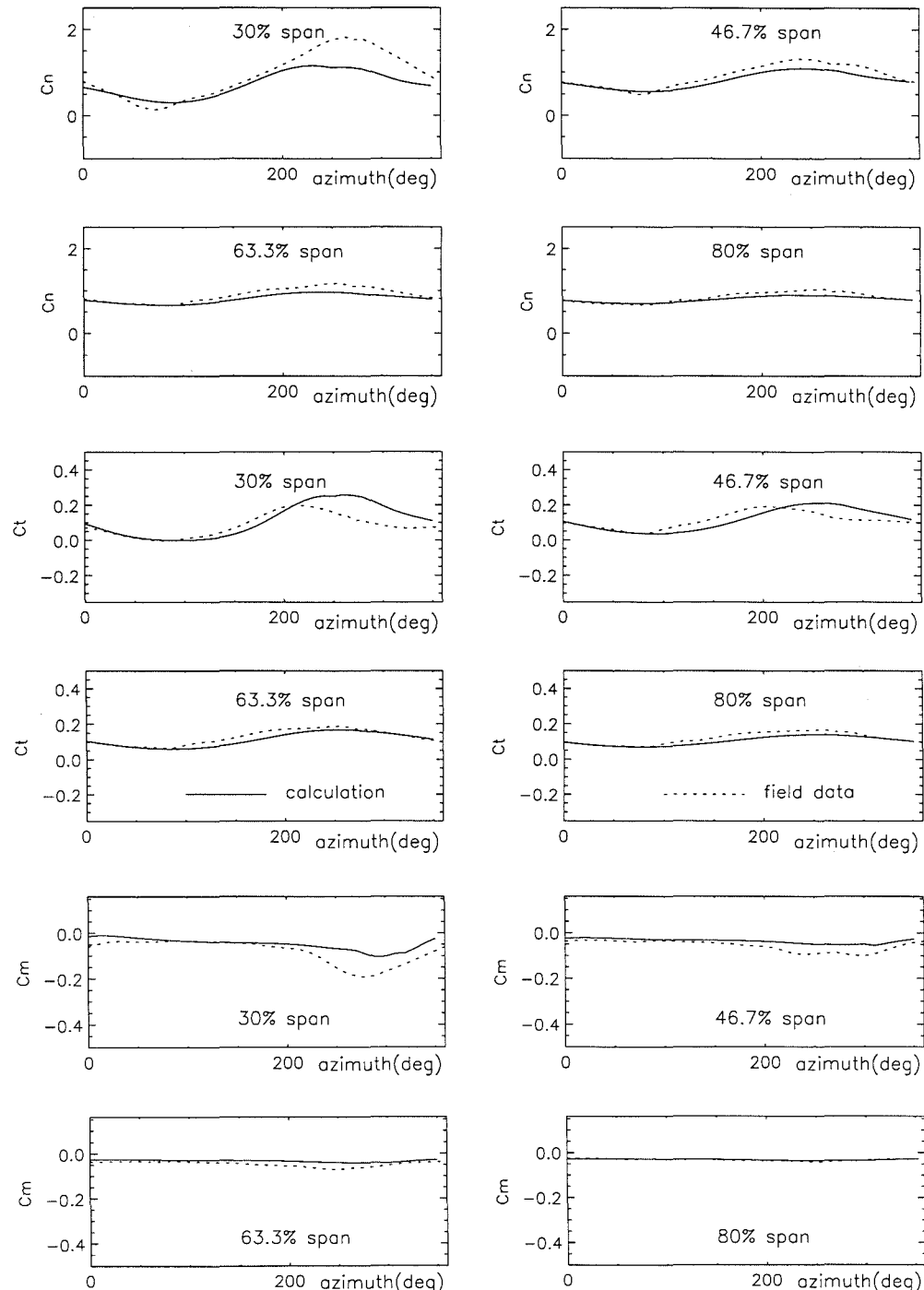


Figure 3.18: Comparison of predicted blade aerodynamic loading with field data of NREL UAE Phase IV at $V_0 = 9.9$ m/s and $\gamma = 21.9^\circ$

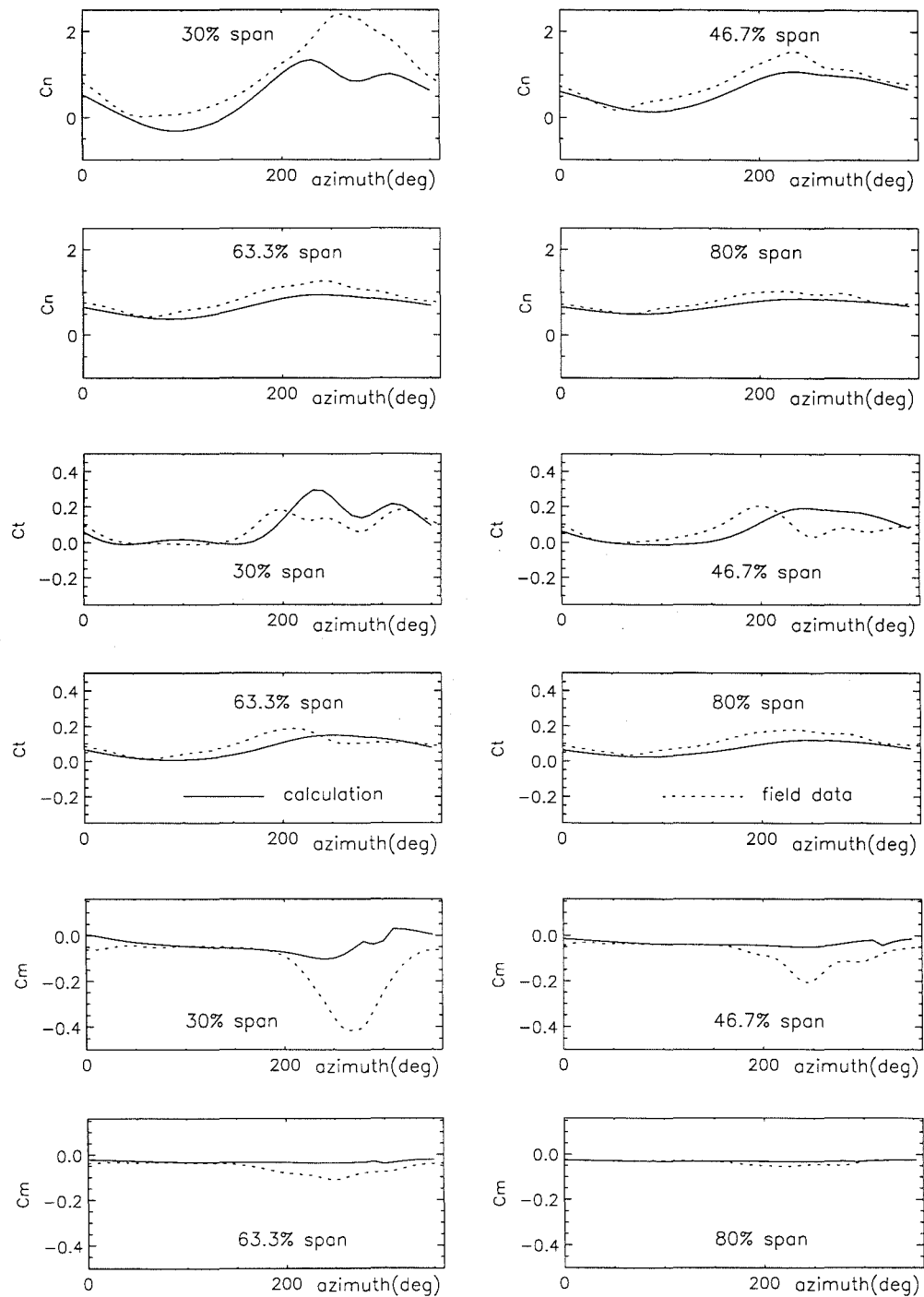


Figure 3.19: Comparison of predicted blade aerodynamic loading with field data of NREL UAE Phase IV at $V_0 = 10.3$ m/s and $\gamma = 41.4^\circ$

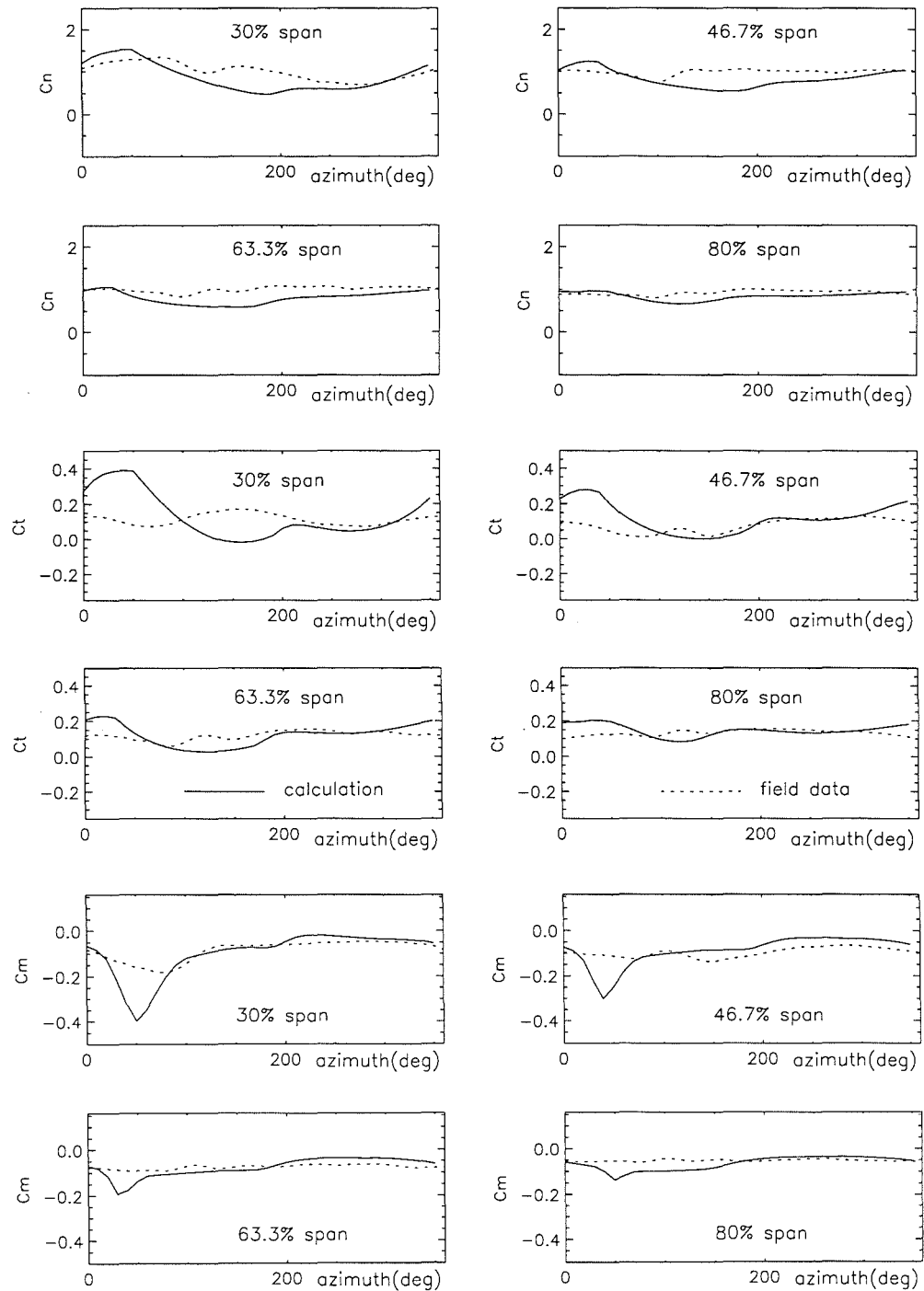


Figure 3.20: Comparison of predicted blade aerodynamic loading with field data of NREL UAE Phase IV at $V_0 = 12.5$ m/s and $\gamma = -21.2^\circ$

are reduced due to the twist. Nevertheless, there are large discrepancies, especially at high wind speeds, between the predictions and the experimental data towards the blade root. This is in addition to the expected divergence of the prediction and experiment in the tower shadow region, because tower shadow effects are not included at this stage. A number of factors influence the quality of prediction at inboard sections of the blade. These are discussed below.

Applicability of the Model

The ability of the unsteady prescribed wake model to calculate the unsteady aerodynamic characteristics of the wind turbine and its blades has been demonstrated by a large number of comparisons between prediction and experiment (Figs. 3.10 to 3.20), and the quality of prediction is very good if the angles of attack of the blade sections are below the static stall angle. However, given that the Leishman–Beddoes model was developed as a performance estimation tool for helicopter rotors, other aspects of it may be inappropriate for calculations on wind turbine rotors where the free stream speeds and rotation rates are normally much lower than for a helicopter. Niven and Galbraith (1997) concluded, through investigations and comparisons of wind tunnel data with the dynamic stall model, that the Leishman–Beddoes model was unable to predict the incidence at which dynamic stall vortex shedding was observed in wind tunnel tests at Mach numbers less than 0.15. The inability of the basic model to predict stall recovery during pitch down at low wind speeds has also been highlighted elsewhere (Niven *et al.* 1989). The present version of the Leishman–Beddoes dynamic stall model should be upgraded to give a better representation of these effects.

Idealisation of Kirchhoff Flow

The local angles of attack experienced by the inboard blade sections are higher than the static stall angle in most operating conditions. For example, the calculated blade incidences at the four blade sections are presented in Fig. 3.21 for NREL UAE Phase II at $V_0 = 15.9$ m/s and $\gamma = -30.1^\circ$ corresponding to Fig. 3.13. With the exception of the 80%-span location, all of the blade sections achieve incidence values beyond that of static

stall. This behaviour exposes a potential weakness in the manner in which the Leishman–Beddoes model represents the non-linear response due to trailing edge separation. In essence, the method is based on the performance characteristics of the blade aerofoil section obtained from steady 2-D wind tunnel tests. These data are, however, not applied directly but are used, *via* the Kirchhoff flow relations, to determine a best-fit idealised variation in boundary layer separation point with incidence (Eq. 3.37). The unsteady response of the blade is then predicted by applying a lag function to the movement of the separation point. The main difficulty with this approach lies in the unsuitability of the idealised separation point curve in the post stall region. This is mainly due to the assumption of a constant base pressure, which does not depend on angle of attack or degree of separation, in the separated flow region in Kirchhoff flow. It is also, however, a consequence of the inability of the idealised separation curve to represent non-linearities in the movement of the separation point. Fig. 3.22 illustrates these effects by comparing the measured lift characteristics of the S809 aerofoil with those resulting from the application of the Kirchhoff flow model *via* the best-fit separation line. Clearly, neither the magnitude nor the trend of the wind tunnel data are well predicted in the post-stall region by the idealised representation. This deficiency will inevitably influence the quality of prediction from the unsteady prescribed wake model at high angles of attack.

Despite these apparent weaknesses in the modelling approach, it is unlikely that they would fully account for the discrepancies apparent in the case of high angle of attack. In fact, preliminary analysis of the comparisons above would suggest that any improvements made to the model would result in a deterioration in the level of agreement between prediction and experiment for some cases. For instance, if the aerofoil lift characteristics (Fig. 3.22) could be well represented beyond an incidence of 40° in the model, Fig. 3.21 would indicate that the calculated values of C_n at 30%-span station would be even lower than the calculated ones presented in Fig. 3.13.

3-D Effects

A more plausible explanation for the poor level of correspondence between the field data and the predictions is the combined influence of 3-D and rotational effects. There are various indications that, at the most inboard stations, the blade would not stall in the manner predicted by 2-D data (Hansen and Butterfield 1993, Ronsten 1992) but, rather, that stall would be delayed to higher incidence. This kind of delayed static stall has been attributed to 3-D and rotational effects. As indicated by Snel *et al.* (1993), for rotating blades, significant radial flows only develop in the separated flow region. This can have a considerable effect on the chordwise pressure distribution and, in particular, can produce significantly increased suction in the separated region. In fact, in strongly 3-D flows, the angle at which C_n stall occurs is dictated by this effect rather than simply by the movement of the trailing edge separation point.

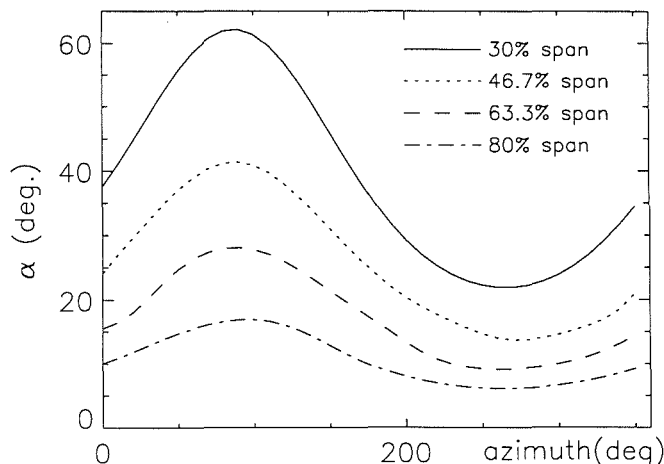


Figure 3.21: Variation in angle of attack with azimuth for NREL UAE Phase I at $V_0 = 15.9$ m/s and $\gamma = -30.1^\circ$

As a result, it is common for wind turbine field data to exhibit increased C_n values, beyond the 2-D limit, on inboard blade sections that are operating at very high incidence. It is not surprising, therefore, that the predicted normal

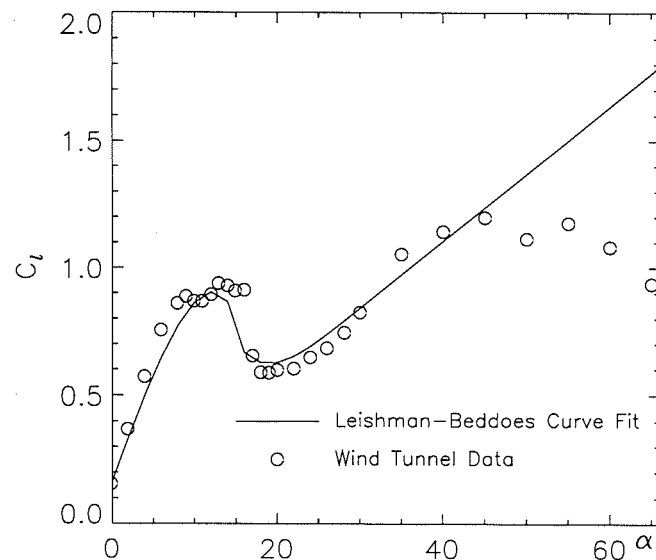


Figure 3.22: Comparison of the Kirchhoff flow model with wind tunnel measurements on the S809 aerofoil

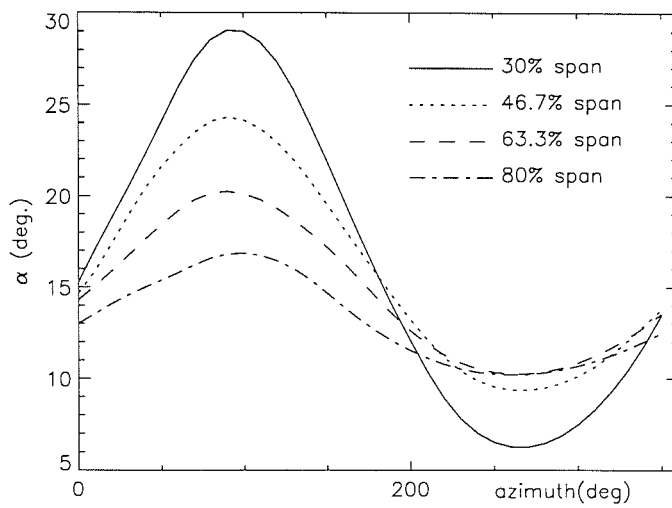


Figure 3.23: Variation in angle of attack with azimuth for NREL UAE Phase N at $V_0 = 12.5$ m/s and $\gamma = -21.2^\circ$

forces and nose-down pitching moments are much lower than the field data at the 30%-span station where the angle of attack is generally well above the static stall angle. This phenomenon can also be observed at other spanwise stations where the angle of attack exceeds the stall angle, for example, in Fig. 3.21 corresponding to Fig. 3.13 for the first half-revolution at the 46.7%- and 63.3%-span stations. At outboard stations where the angle of attack is low, the calculation results match the measured data very well because the rotational effects in the attached flow regime are minimal (Eggers and Digumarthi 1992).

Typical HAWT blades are usually twisted such that the entire blade is at the same, or nearly the same, angle of attack for a given wind velocity. Thus, the variation in incidence with spanwise location is not normally as severe as that illustrated in Fig. 3.21. In other words, the 30%-span section of a twisted blade may not experience incidence values as high as 60° shown in Fig. 3.21. Nevertheless, as shown in Fig. 3.23 where the calculated angle of attack is illustrated for the NREL's UAE Phase IV rotor consisting of twisted blades, some blade sections do go through both attached and separated flows within a revolution in yawed flow and therefore experience the 3-D effects. This unsteadiness will inevitably affect the wind turbine fatigue life. In order to provide accurate blade aerodynamic loads, the 3-D and rotational effects must appropriately be modelled and this modelling will be dealt with in the following chapter.

3.6 Conclusions

An unsteady aerodynamic model for HAWT performance prediction, based on a prescribed wake method, has been developed for yawed flow and/or wind shear. The model is capable of predicting both steady unyawed flow and yawed flow performance. The unsteady and dynamic stall characteristics of the blade, owing to skewed inflow, are represented by the coupling of the Leishman–Beddoes semi-empirical dynamic stall model with the prescribed wake model. Several test examples show that the calculated results, in terms of both the predicted gross

rotor performance and detailed blade airloads, generally compare well with wind tunnel measurements and field data. The blade loading distribution is well represented by the model up to the static stall angle.

Clearly, there are still areas of improvement within the modelling strategy, particularly in relation to high angle of attack. *Firstly*, the present model lacks a tower shadow representation. Modelling work on this aspect will be presented in Chapter 5. *Secondly*, the unsteady aerofoil prediction scheme is not ideally suited to very high angles of attack in its present form. The unsteady model also requires some specific modifications to become directly applicable to low-speed flows on the type of aerofoils used on wind turbines. This is a consequence of the history of the dynamic stall model in its use for high-speed flows on helicopter rotors. *Finally*, the 3-D effects on rotating blades, which are the main source of the differences in the inboard section characteristics between prediction and measurement, must be represented for precise prediction of the HAWT aerodynamic performance.

Chapter 4

Unsteady HAWT Performance with Three-Dimensional Effects

4.1 Introduction

The prediction of HAWT performance has been traditionally carried out using relatively simple estimation codes (Hansen and Butterfield 1993). These have, until relatively recently, been considered adequate for day-to-day design use because of their ability to produce an acceptable estimate of the gross turbine performance. As blade designs have evolved, however, it has become clear that these simple schemes have some specific deficiencies which limit the useful information which can be generated by them. In particular, they often neglect unsteady aerodynamic effects and, just as importantly, the influence of rotation on flow development. Attempts have been made to address these two problems and, in this respect, much progress had been made in understanding and predicting the unsteady aerodynamic environment in which wind turbines operate (Robinson *et al.* 1995). An unsteady prescribed wake model has been presented in the last chapter and this model has demonstrated the capability of predicting the unsteady aerodynamic characteristics of HAWT rotors and blades. The impact of work of this type on the aeroelastic tailoring of future blade designs should not be underestimated.

More recently, much attention has been focussed on the manner in which 3-D rotational effects are manifest on wind turbine blades. It has been established, for example, that measured pressure distributions on inboard blade sections differ considerably from their 2-D counterparts (Butterfield *et al.* 1992a). This has been primarily associated with a delayed stall on rotating blades. In fact, the 3-D effects on a rotating blade were shown as early as 1947 by the experiment of Himmelskamp on an airscrew, the results of which were reproduced and reviewed by Schlichting (1979). The experiment showed that the maximum value of the lift coefficient, $C_{l\max}$, of an aerofoil section in a rotating environment exceeds the $C_{l\max}$ of the same aerofoil section held stationary in a free stream. The results also indicated that in moving toward the centre of the rotor the stall delay became more and more pronounced.

Throughout the development of rotary-wing aircraft, consideration of 3-D rotational effects on rotor performance has remained rather academic. Sears and his colleagues at Cornell University published a series of papers presenting their work on the laminar boundary layer problem on a rotating blade (Sears 1950, Fogarty and Sears 1950, Fogarty 1951, Tan 1953, Rott and Smith 1956). Because of the assumptions made by those researchers, the chordwise and radial momentum equations were decoupled and the chordwise velocity at stations several chord lengths from the axis of rotation was independent of the spanwise velocity due to rotation; hence, the separation was unaffected by rotation. Therefore, their results had few differences from the boundary layer separation problem of the conventional fixed wing.

The analysis from Mager (1954), however, showed that the cross-flow is an important factor affecting separation in a 3-D laminar boundary layer. Banks and Gadd (1963) derived a set of equations that were coupled through the Coriolis and centrifugal force terms. The solution to this problem showed that laminar separation was delayed due to rotation. In fact, they found that, for the extreme inboard sections, the boundary layer was completely stabilised against separation

by a linear adverse external-velocity gradient. The conclusions drawn by Banks and Gadd were confirmed by other more rigorous and detailed analyses (McCroskey and Yaggy 1968, Dwyer and McCroskey 1970). A possible explanation is that for a rotating blade the fluid particles of the boundary layer are subject to a strong centrifugal force, which throws the fluid outward, and to Coriolis forces which acts like an additional chordwise pressure drop. The boundary layer thickness is reduced by the radial flow (centrifugal pumping), which becomes important as stall develops. Meanwhile the separation is shifted to a higher angle of attack by favourable pressure gradient caused by the Coriolis force. As a result, higher $C_{l\max}$ is achieved on a rotating blade than on a non-rotating wing (Schlichting 1979, Dress 1976, Harris 1966).

With the development of high-speed supercomputers and the emergence of more sophisticated analyses, modern CFD methods have been used to investigate the 3-D effects on rotating blades. Narramore and Vermeland (1992) used a full N-S solver with an algebraic turbulence model to calculate the increase in lift and reduction in drag obtained near the stall of a propeller blade. The computations of the lift coefficients along the span showed that stall is delayed by the rotational effects and that the effect is particularly pronounced for the inboard blade stations. They concluded that the stall delay phenomenon described by Banks and Gadd also occurs for turbulent flows.

Recent studies of the development of spanwise flows on wind turbine blades also indicate that the strongest effects appear to be confined to regions of separated flow on the blades. This modifies the pressure distribution in the separated region and, consequently, 3-D chordwise pressure distributions often bear little resemblance to their 2-D counterparts (Ronsten 1992).

Several models have been proposed to address the problem of 3-D rotational effects. Generally, these have been either based on sound physical principles, or developed on the basis of more complex solutions of the rotational flow problem. Eggers and Digumarthi (1992) presented a scaling model based on approximate

power series solutions of the N–S equations in which the effects of centrifugal force and Coriolis force on spanwise flows and pressure distributions are considered to be of primary importance while the centrifugal force effects on these chordwise quantities are assumed to be of secondary importance. However, this approximate model involves the use of wind tunnel data for the pressure on the blade. The engineering method of Snel *et al.* (1993) evaluates the first-order effects of blade rotation on stall characteristics by way of the solution of a simplified form of the 3-D boundary layer equations. This method relates the increment in lift due to stall delay to the local blade solidity, c/r . Quantitatively their results appear to overpredict the effects of rotation on $C_{l\max}$ by a considerable amount. Tangler and Selig (1997) applied the stall delay model of Corrigan and Schillings (1994) to prediction of HAWT rotor performance. They concluded that the empirical model appears to quantify the first-order effects of rotation and that empirical constants used in the method required further evaluation. Nevertheless, these techniques have been applied with varying degrees of success and their results have been very encouraging. More recently, one particularly notable technique has been that due to Du and Selig (1998), which is based on the analysis of laminar boundary layers developing under the influence of rotational effects. Despite the laminar flow limitation, this scheme has been shown to correlate well with field test data.

The present study extends the unsteady aerodynamic prediction scheme for HAWTs, which is described in detail in Chapter 3, to include 3-D effects *via* a series of correction factors based on the method of Du and Selig. For unsteady calculations, the prescribed wake model is coupled to the unsteady aerofoil performance method of Leishman and Beddoes which is modified to represent 3-D rotational effects in the present study. The basis for the 3-D modification is the delay in the forward movement of the separation point. This delay directly modifies the predicted normal force and, together with consideration of the likely chordwise loading distribution, provides the basis for corrections to the tangential force and pitching moment.

The predictions of the modified scheme are contrasted with the basic 2-D predictions and compared with test data. It is shown that significantly improved correlation with the field data is achieved when the 3-D effects are included. For completeness the influence that these effects have on the gross performance prediction is also examined and is shown to be most significant at low tip speed ratios.

4.2 The Stall Delay Model

4.2.1 Solution of the Boundary Layer Equations

3-D Terms

The 3-D incompressible steady boundary layer equations in a blade-attached cylindrical coordinate system (Fig. 4.1) are given by

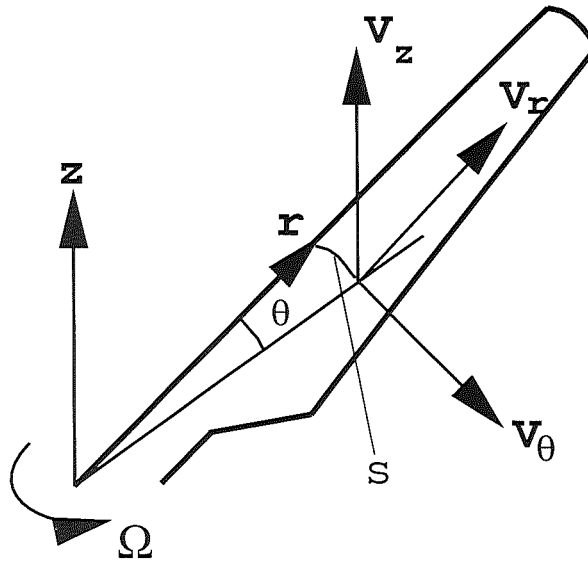


Figure 4.1: Coordinate system attached to rotating blade

$$V_r \frac{\partial V_r}{\partial r} + V_\theta \frac{\partial V_r}{\partial \theta} + V_z \frac{\partial V_r}{\partial z} = -\frac{1}{\varrho} \frac{\partial p}{\partial r} + \frac{1}{\varrho} \frac{\partial \tau_r}{\partial z} + \frac{(V_\theta - \Omega r)^2}{r} \quad (4.1)$$

$$V_r \frac{\partial V_\theta}{\partial r} + V_\theta \frac{\partial V_r}{\partial \theta} + V_z \frac{\partial V_\theta}{\partial z} = -\frac{1}{\varrho} \frac{\partial p}{r \partial \theta} + \frac{1}{\varrho} \frac{\partial \tau_\theta}{\partial z} + 2\Omega V_r - \frac{V_r V_\theta}{r} \quad (4.2)$$

$$\frac{V_r}{r} + \frac{\partial V_r}{\partial r} + \frac{\partial V_\theta}{r \partial \theta} + \frac{\partial V_z}{\partial z} = 0 \quad (4.3)$$

They are the r -momentum, θ -momentum, and continuity equations, respectively. It has been assumed that the surface on which the boundary layer develops is in the plane of rotation $z = 0$. τ_r and τ_θ are the shear stresses in the r - and θ -directions, respectively.

From the momentum equations, the 3-D terms can clearly be identified. The θ -momentum equation (Eq. 4.2) contains the Coriolis-force term ($2\Omega V_r$) and coordinate curvature term ($V_r V_\theta / r$). The r -momentum equation (Eq. 4.1) contains the centrifugal-force term that consists of a coordinate curvature term (V_θ^2 / r), a Coriolis-force component ($-2V_\theta \Omega r$) and the formal centrifugal force ($\Omega^2 r$) resulting from the rotation of the coordinate system.

Separation Model

The momentum integral equations for a 3-D boundary layer in an incompressible flow can be obtained by integrating the boundary layer equations in the normal direction and have been derived by many researchers. In the analyses carried out by Snel *et al.* (1994) and Lakshminarayana and Govindan (1981), an order of magnitude analysis technique is adopted for the rotating system. In the 3-D formulation, the non-linear convective terms are presented in their 2-D form, while the important 3-D effects of centrifugal and Coriolis forces are preserved. Similar to the approximation made by Banks and Gadd (1963), the external chordwise velocity outside the boundary layer is assumed by Du and Selig (1998) to be

$$V_\theta(z = \infty) = V_\infty(1 - k s)$$

where k is a constant representing the velocity gradient and s is the arc length measured from the leading edge along the surface of the blade section r .

Integrating the integral boundary layer equations from the leading edge up to the laminar separation point, s , produces an equation associated with a separation factor in the form

$$ks = f_s \left(\lambda, \frac{s}{r} \right) \quad (4.4)$$

The separation factor ks is a function of the tip speed ratio λ and the point of laminar separation.

Having numerically calculated the separation factor ks , which determines the separation point on the rotating blade surface, for different values of λ and s/r , Du and Selig proposed

$$ks = 1.6 \frac{s}{r} \frac{C_1 - \left(\frac{s}{r} \right)^{C_3/\lambda}}{C_2 + \left(\frac{s}{r} \right)^{C_3/\lambda}} \quad (4.5)$$

to approximate Eq. 4.4. The separation factor for a 2-D flow without rotation is $ks = 0.1267$. For a 3-D blade in rotation, therefore, the increase in (ks) compared with the non-rotating 2-D case is given by

$$\Delta(ks) = \frac{1.6 \frac{s}{r}}{0.1267} \frac{C_1 - \left(\frac{s}{r} \right)^{C_3/\lambda}}{C_2 + \left(\frac{s}{r} \right)^{C_3/\lambda}} - 1 \quad (4.6)$$

where C_1 , C_2 , and C_3 are correction factors. On the basis of numerical solutions, it has been found that C_1 and C_2 vary approximately from 0.8 to 1.2 and C_3 varies from 0.4 to 1.0. In this study, the parameters C_1 , C_2 , and C_3 are all set to unity.

In light of the empirical and approximate nature of the correction, the ratio s/r is replaced by the blade local solidity parameter c/r and Eq. 4.6 is then re-expressed as

$$\Delta(ks) = \frac{1.6 \frac{c}{r}}{0.1267} \frac{C_1 - \left(\frac{c}{r} \right)^{C_3/\lambda}}{C_2 + \left(\frac{c}{r} \right)^{C_3/\lambda}} - 1 \quad (4.7)$$

4.2.2 3-D Correction to 2-D Aerofoil Data

As indicated above, separation of the flow around a rotating blade is delayed due to rotational effects and the pressure distribution in the separated region can be

significantly altered by the development of strong spanwise flow. The combination of these two effects produces a delay in the stalling process which must be modelled in order to accurately predict wind turbine blade aerodynamics.

Obviously, the stall delay results in an increase in lift and a decrease in drag. With the aid of the separation factor model, the increment in the lift coefficient and decrement in the drag coefficient have been suggested as

$$\Delta C_l = f_l [(C_l)_p - (C_l)_{2D}] \quad (4.8)$$

$$\Delta C_d = f_d [(C_d)_{2D} - (C_d)_{\alpha=0}] \quad (4.9)$$

where $(C_l)_{2D}$ and $(C_d)_{2D}$ are the 2-D aerofoil lift and drag coefficients, $(C_d)_{\alpha=0}$ is the 2-D aerofoil drag coefficient at $\alpha = 0$, and the theoretical 2-D aerofoil lift coefficient $(C_l)_p$ is given by

$$(C_l)_p = 2\pi(\alpha - \alpha_0)$$

The empirical modification factors f_l and f_d are based on Eq. 4.7,

$$f_l = \frac{1}{2\pi} \left[\frac{1.6 \frac{c}{r}}{0.1267} \frac{C_1 - \left(\frac{c}{r}\right)^{\frac{C_3}{\Lambda^{\frac{3}{2}}}}}{C_2 + \left(\frac{c}{r}\right)^{\frac{C_3}{\Lambda^{\frac{3}{2}}}}} - 1 \right] \quad (4.10)$$

$$f_d = \frac{1}{2\pi} \left[\frac{1.6 \frac{c}{r}}{0.1267} \frac{C_1 - \left(\frac{c}{r}\right)^{\frac{C_3}{2\Lambda^{\frac{3}{2}}}}}{C_2 + \left(\frac{c}{r}\right)^{\frac{C_3}{2\Lambda^{\frac{3}{2}}}}} - 1 \right] \quad (4.11)$$

where the parameter Λ is a modified tip speed ratio given by

$$\Lambda = \frac{\lambda}{1 + \lambda^2}$$

Finally, the 3-D lift and drag coefficients can be calculated from

$$(C_l)_{3D} = (C_l)_{2D} + \Delta C_l \quad (4.12)$$

$$(C_d)_{3D} = (C_d)_{2D} + \Delta C_d \quad (4.13)$$

4.3 Correction for Unsteady 3-D Effects

Once the 3-D C_l and C_d are obtained, the calculation of the 3-D static normal force and chord force coefficients is trivial:

$$(C_n)_{3D} = (C_l)_{3D} \cos \alpha + (C_d)_{3D} \sin \alpha \quad (4.14)$$

$$(C_t)_{3D} = (C_l)_{3D} \sin \alpha - (C_d)_{3D} \cos \alpha \quad (4.15)$$

Unsteady aerodynamic forces acting on the blade cannot, however, be calculated directly from Eqs. 4.14 and 4.15 since the static aerofoil data do not fully represent the unsteady flow phenomena such as the movement of separation point with time. Therefore, the 3-D aerofoil data must carefully and appropriately be incorporated into the unsteady aerodynamic model. The manner in which this accomplished is described below.

4.3.1 Normal Force

If it is assumed that the Kirchhoff formula, Eq. 3.35, holds for 3-D cases, the variation of the 3-D trailing edge separation point can then be related to the 3-D normal force coefficient by re-writing Eq. 3.36,

$$f_{3D} = 4 \left[\sqrt{\frac{(C_n)_{3D}}{C_{n_\alpha} (\alpha - \alpha_0)}} - \frac{1}{2} \right]^2 \quad (4.16)$$

Obviously, for a given tip speed ratio f_{3D} is a function not only of angle of attack, as in the 2-D case, but also of local radius r ,

$$f_{3D} = g(\alpha, r) \quad (4.17)$$

For unsteady conditions, there is a lag in the leading edge pressure response with respect to normal force. Application of this lag to $(C_n)_{3D}$, as Eq. 3.34, yields a substitutive normal force coefficient $(C'_n)_{3D}$. Correspondingly, the angle of attack becomes (Eq. 3.41)

$$\alpha' = \frac{(C'_n)_{3D}}{C_{n_\alpha}} + \alpha_0 \quad (4.18)$$

Substitution of α' into Eq. 4.17 gives the trailing edge separation point associated with the lag in the leading edge pressure response,

$$f'_{3D} = g(\alpha', r) \quad (4.19)$$

The separation point f'_{3D} now depends on the angle of attack, radial position of the blade element, and tip speed ratio. Therefore, the variation of the 3-D separation point is impossible to be generalised in a simple explicit algebraic form as Eq. 3.37. In the present procedure, f'_{3D} is obtained by interpolation with Eq. 4.17 represented by a look-up table rather than using the exponential function of the original Leishman–Beddoes dynamic stall model (Eq. 3.42). This approach is similar to that adopted by Pierce and Hansen (1995) when matching the separation point curve with 2-D experimental data.

In addition to the aerofoil unsteady pressure response, there is also an unsteady boundary layer response, the effects of which on the trailing edge separation point may be represented by applying a first-order type lag to f'_{3D} ,

$$f''_{3D} = f'_{3D} - D_f \quad (4.20)$$

where the compensation function D_f , similarly to the 2-D case for a sampled system, is given by

$$D_f(N) = D_f(N-1) \exp\left(-\frac{\Delta S}{S_f}\right) + [f'_{3D}(N) - f'_{3D}(N-1)] \exp\left(-\frac{\Delta S}{2S_f}\right)$$

Similarly, for 3-D dynamic stall Eq. 3.45 becomes

$$C_v(N) = C_n^C(N) \left\{ 1 - \left[\frac{1 + \sqrt{f''_{3D}(N)}}{2} \right]^2 \right\}$$

Thus, the normal force component due to the dynamic stall vortex can be calculated by Eq. 3.44.

Finally, the unsteady 3-D normal force coefficient can be expressed as

$$C_n = C_{n_\alpha} \left(\frac{1 + \sqrt{f''_{3D}}}{2} \right)^2 (\alpha_e - \alpha_0) + C_n^I + C_n^v \quad (4.21)$$

4.3.2 Chordwise Force

Following Eq. 3.50, the 3-D chordwise force coefficient associated with the nonlinear separation may be expressed as

$$C_t^f = k_t \eta_t \sqrt{f''_{3D}} C_{n_\alpha} (\alpha_e - \alpha_0) \sin \alpha_e \quad (4.22)$$

For a given aerofoil, the chordwise force efficiency k_t for the 2-D case is fixed and is usually close to unity due to the large peak suction in the leading edge area. For rotational cases, however, where 3-D effects are manifest, the aerofoil loading depends both on the angle of attack and on the distance of the blade section from the centre of rotation. As a consequence, the 3-D k_t will be different for the same aerofoil section at different spanwise positions and would be difficult to determine in advance as an input to the calculation. As a result, determination of the chordwise thrust for 3-D cases is problematic using this method and, consequently, an alternative procedure has been developed.

If the change in shear stress on the aerofoil surface is negligible, the increment in the chordwise thrust coefficient due to 3-D effects can be expressed as

$$\Delta C_t = - \int \Delta c_p d\left(\frac{y}{c}\right)$$

where Δc_p denotes the increment in the pressure coefficient on the aerofoil and y the coordinate perpendicular to the chord. Since the rotational effects are minimal in the attached flow regime and manifest in the separated flow region as stated previously, the increase in the surface pressure may be considered to be primarily restricted to the separation region (Fig. 4.2). Further, if to a first order, it is assumed that the change in pressure is constant throughout the separated flow region, it can be related to the change in normal force by the expression

$$\Delta c_p = - \frac{\Delta C_n}{1 - f} \quad (4.23)$$

where

$$\Delta C_n = C_{n_\alpha} \left[\left(\frac{1 + \sqrt{f''_{3D}}}{2} \right)^2 - \left(\frac{1 + \sqrt{f''_{2D}}}{2} \right)^2 \right] (\alpha_e - \alpha_0)$$

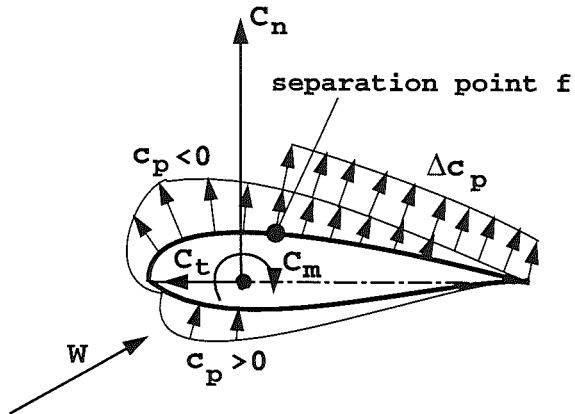


Figure 4.2: Illustration of assumed change in pressure due to 3-D effects

Thus the change in C_t can be approximated by

$$\Delta C_t = -\frac{\Delta C_n}{1 - f_{3D}''} \frac{y_f}{c} \quad (4.24)$$

where y_f is the vertical distance between the separation point f and the chord line.

With this modification, the unsteady 3-D chordwise force coefficient is then calculated from

$$C_t = (C_t)_{2D} + \Delta C_t \quad (4.25)$$

where the 2-D chordwise force coefficient $(C_t)_{2D}$ is obtained from Eq. 3.52.

4.3.3 Pitching Moment

It is expected that the increment in the quarter-chord pitching moment coefficient, ΔC_m , due to 3-D effects will be related to the change in the normal force coefficient, ΔC_n , and the location of separation, f . It is also understandable that positive ΔC_n produces negative ΔC_m if the change in pressure which produces the increase in normal force mainly takes place in the separated flow region. Following this argument, the increment in pitching moment can be expressed as

$$\Delta C_m = \int_f^1 \Delta c_p \left(\frac{x}{c} - \frac{1}{4} \right) d\left(\frac{x}{c}\right) + \int_{y_f/c}^0 \Delta c_p \left(\frac{y}{c} \right) d\left(\frac{y}{c}\right) \quad (4.26)$$

If, once again, the change in pressure is considered to be approximately constant throughout the separated flow region, Eq. 4.26 can then be written as

$$\Delta C_m = -\frac{\Delta C_n}{1-f} \left[\int_f^1 \left(\frac{x}{c} - \frac{1}{4} \right) d\left(\frac{x}{c}\right) + \int_{y_f/c}^0 \left(\frac{y}{c} \right) d\left(\frac{y}{c}\right) \right]$$

For 3-D unsteady cases, the above expression reduces to

$$\Delta C_m = -\frac{\Delta C_n}{2} \left[\frac{1+2f''_{3D}}{2} - \frac{y_f^2}{c^2(1-f''_{3D})} \right] \quad (4.27)$$

Thus, when using Eq. 3.54 to calculate the total pitching moment coefficient in the 3-D case

$$C_m = C_m^C + C_m^f + C_m^I + C_m^v$$

the contribution of the movement of the centre of pressure due to the trailing edge separation is

$$C_m^f = C_{m_0} + \{k_0 + k_1(1-f''_{3D}) + k_2 \sin[\pi(f''_{3D})^\mu]\} (C_n^f)_{2D} + \Delta C_m \quad (4.28)$$

with

$$(C_n^f)_{2D} = C_{n_\alpha} \left(\frac{1+\sqrt{f''_{2D}}}{2} \right)^2 (\alpha_e - \alpha_0)$$

4.4 Results and Discussion

In this section, the general capability of the modelling strategy will be demonstrated by comparisons with field and wind tunnel test data. In particular, comparison will be made with blade forces and moments for a wide range of inflow conditions to demonstrate the generality of the model and the level of improvement in load prediction that can be realised by 3-D correction on inboard blade sections.

Gross Rotor Performance

For many years, the aerodynamic models used in the design of wind turbines relied entirely on 2-D test data and did not include any allowance for 3-D effects.

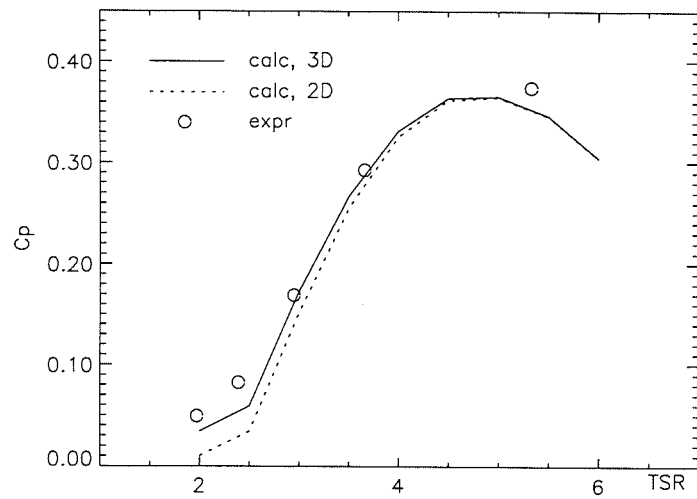


Figure 4.3: Comparison of rotor power coefficient for NREL UAE Phase N turbine

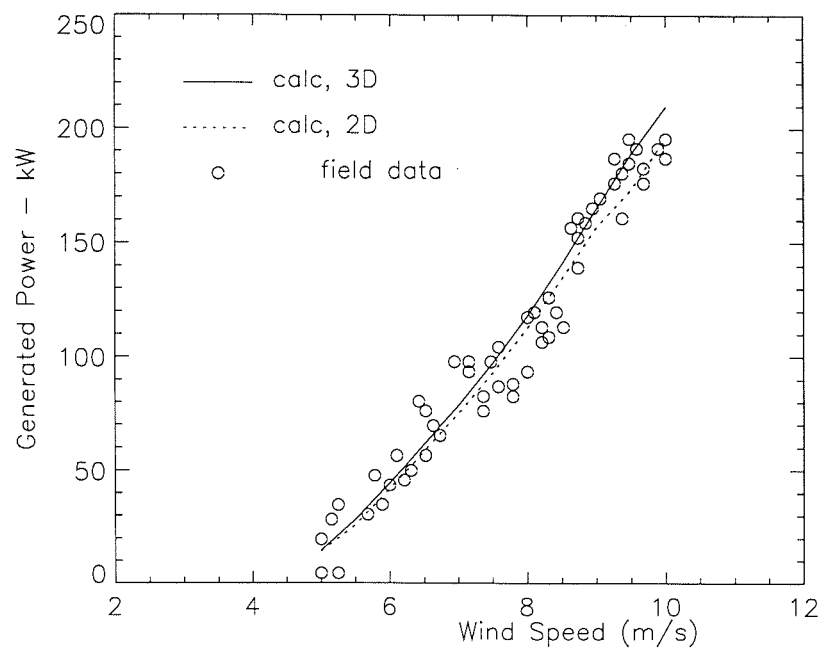


Figure 4.4: Comparison of generated power for MOD-OA turbine

However, it is well known that using 2-D aerofoil wind tunnel data designers were not able to predict high wind speed performance accurately on stall-controlled turbines (Hansen and Butterfield 1993), resulting in underestimates of the peak rotor power. This is attributed to the unavailability of the aerofoil stall characteristics and absence of the 3-D rotational effects. The present model allows an assessment of the 3-D effects on the turbine power prediction to be made by comparing 2-D and 3-D predictions with field data. Such comparisons are presented in Figs. 4.3 and 4.4 for the NREL UAE Phase IV and MOD-OA turbines, respectively.

In Fig. 4.3, it may be observed that the general form of both predictions follows the measured data points at moderate tip speed ratios but deviates from the data at the extremes of the range. There are many possible reasons for this and some of them have been discussed in Section 2.4 but, for the present purpose, it is more interesting to focus on the differences between the 2-D and 3-D predictions. At high tip speed ratios the two predictions are identical but, as the tip speed ratio is decreased, the two curves steadily diverge. As they do so, the 3-D prediction remains consistently closer to the field data. This is an interesting result because it might be expected that influence of the rotational speed would be most severe at high tip speed ratios. In fact, the local angle of incidence at each blade section increases as the tip speed ratio is reduced and more separated flow appears on the blade. The blade then becomes more susceptible to 3-D effects and, consequently, predictions at high wind speeds, or low tip speed ratios, are more sensitive to the influence of 3-D effects.

The result presented above is, to some extent, mirrored in Fig. 4.4 where predictions are compared with field measurements collected on the MOD-OA wind turbine (Spera and Janetzke 1981). The figure also provides a good illustration of the capability of the present scheme over a range of wind speeds. The inclusion of 3-D rotational effects in the model improves the level of agreement between the calculation and field data. In particular, as in the previous case, the biggest improvement occurs at high wind speeds while there are smaller 3-D effects at low wind speeds.

Blade Aerodynamic Loading

The 3-D rotational effects on the detailed blade aerodynamic loads tend to be insignificant at low wind speeds where the blade angle of attack is low. This conclusion can be drawn from the comparison of Fig. 3.16 with Fig. 4.5, in which there are few differences between the calculated results with and without 3-D effects. In the following discussion, therefore, the blade aerodynamic loadings calculated with 3-D effects at low wind speeds will not be presented because they are little different from their 2-D counterparts that can be found in the last two chapters.

The effect that the 3-D corrections have on the predictive capacity of the model is illustrated in Figs. 4.6 and 4.7 for nominally non-yawed and yawed cases, respectively, of the NREL UAE Phase II. Compared to the 2-D calculations presented previously in Figs. 2.14 and 3.12, the level of correspondence between the field data and the normal force coefficient predictions with the 3-D corrections at inboard blade sections is clearly much better. Not only is the general shape of the loading pattern consistent with the field data but the quantitative agreement is also significantly improved.

It is interesting to note that the normal force predictions on outboard blade sections show little influence of 3-D effects. This is entirely consistent with the observation that on outboard blade sections, where the local blade incidence is relatively low and little flow separation exists, 3-D effects are minimised.

Unlike the marked change in the predicted normal force coefficient trace, there is little evidence of any significant effect on the chordwise thrust coefficient. While both the 2-D and 3-D predicted chordwise force coefficients for the head-on flow case (Figs. 2.14 and 4.6) compare satisfactorily with the measured data, the 3-D corrections have no practical improvement on the C_t predictions for the yawed case (Fig. 4.7) even on the inboard blade sections. Nevertheless, given the well-known difficulties in accurately determining C_t values (McCroskey 1995), the level

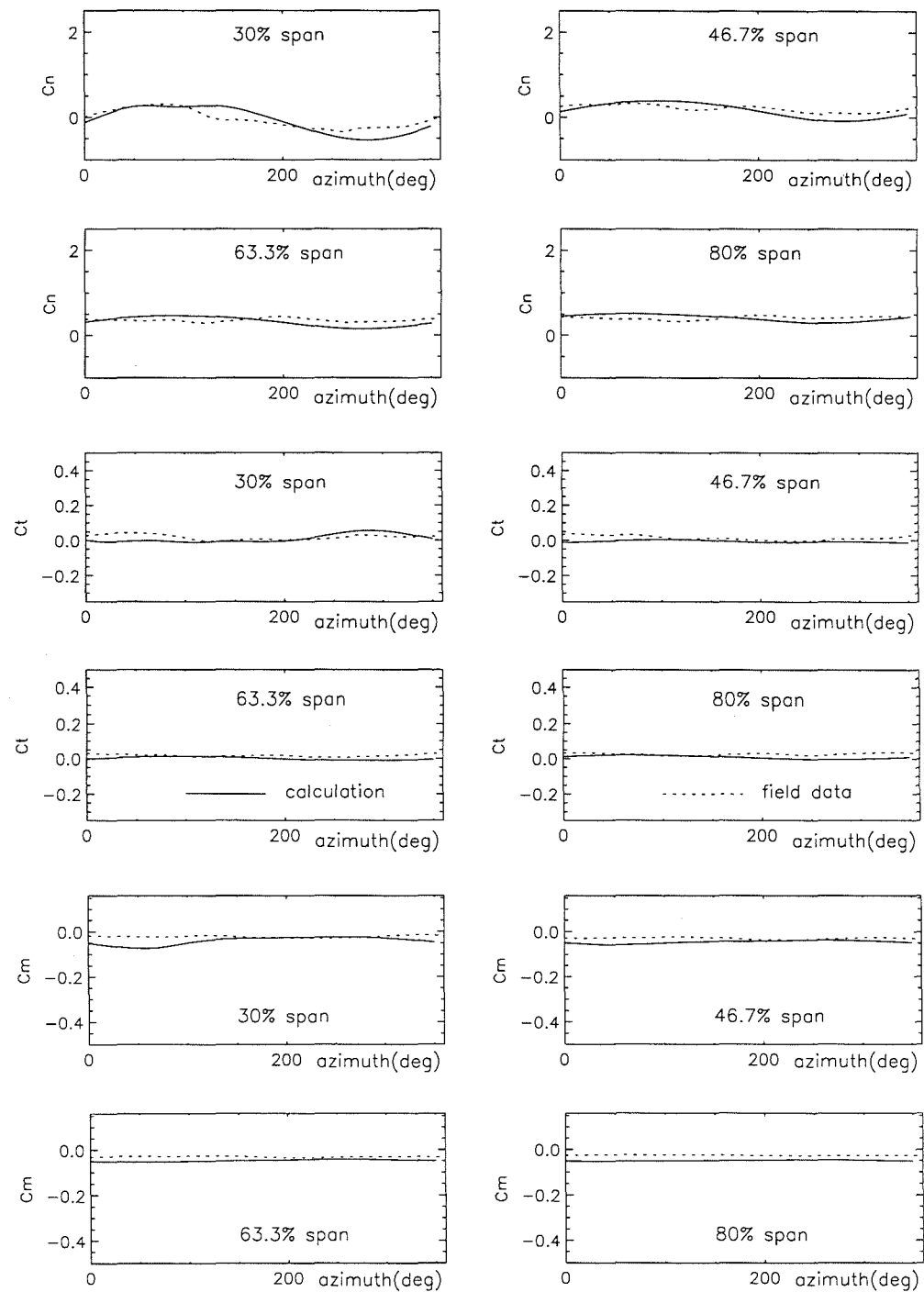


Figure 4.5: Comparison of predicted 3-D blade aerodynamic loading with field data of NREL UAE Phase N at $V_0 = 6.7$ m/s and $\gamma = -38.2^\circ$

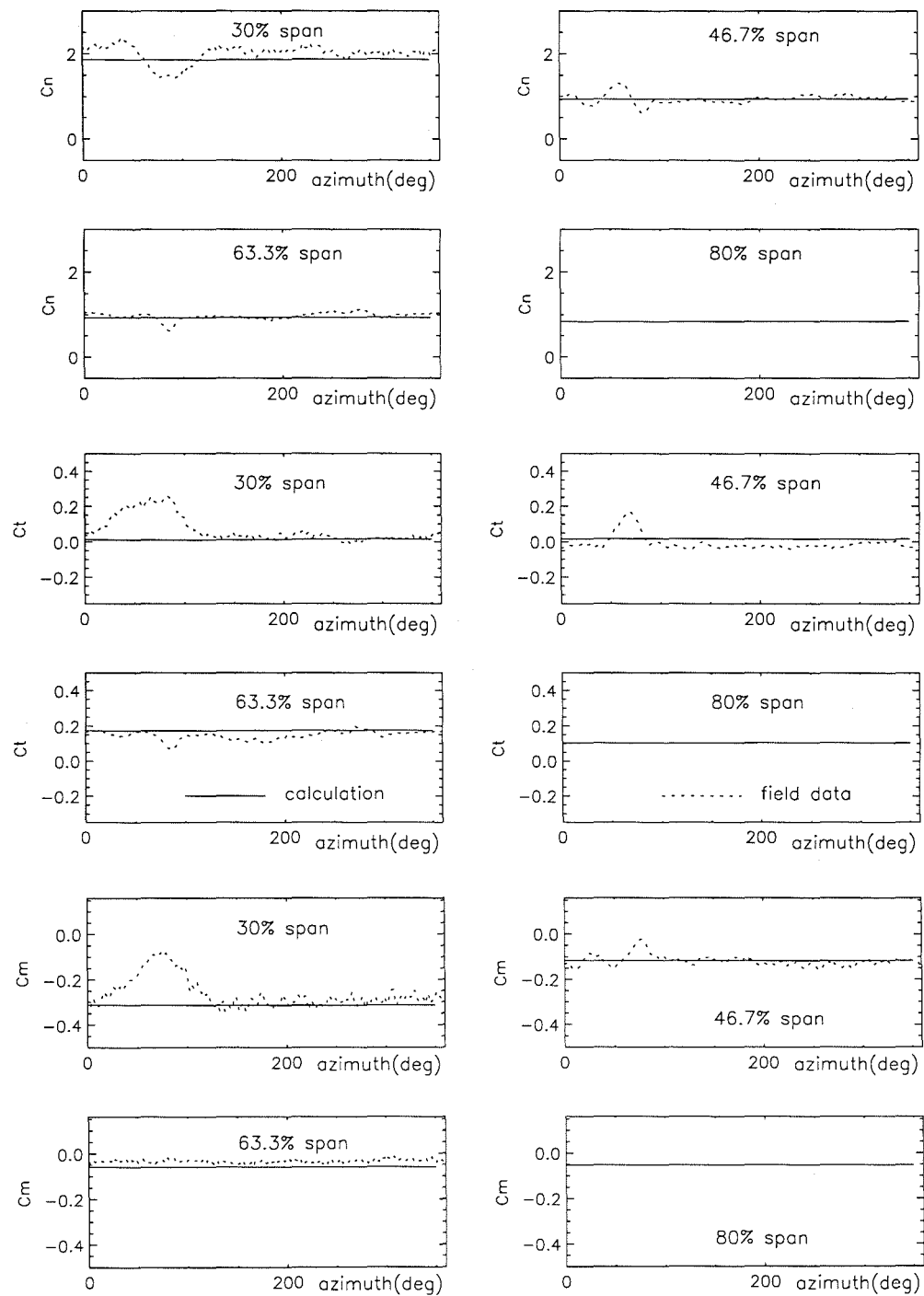


Figure 4.6: Comparison of predicted 3-D blade aerodynamic loading with field data of NREL UAE Phase I at $V_0 = 12.5$ m/s and $\gamma = 0.4^\circ$

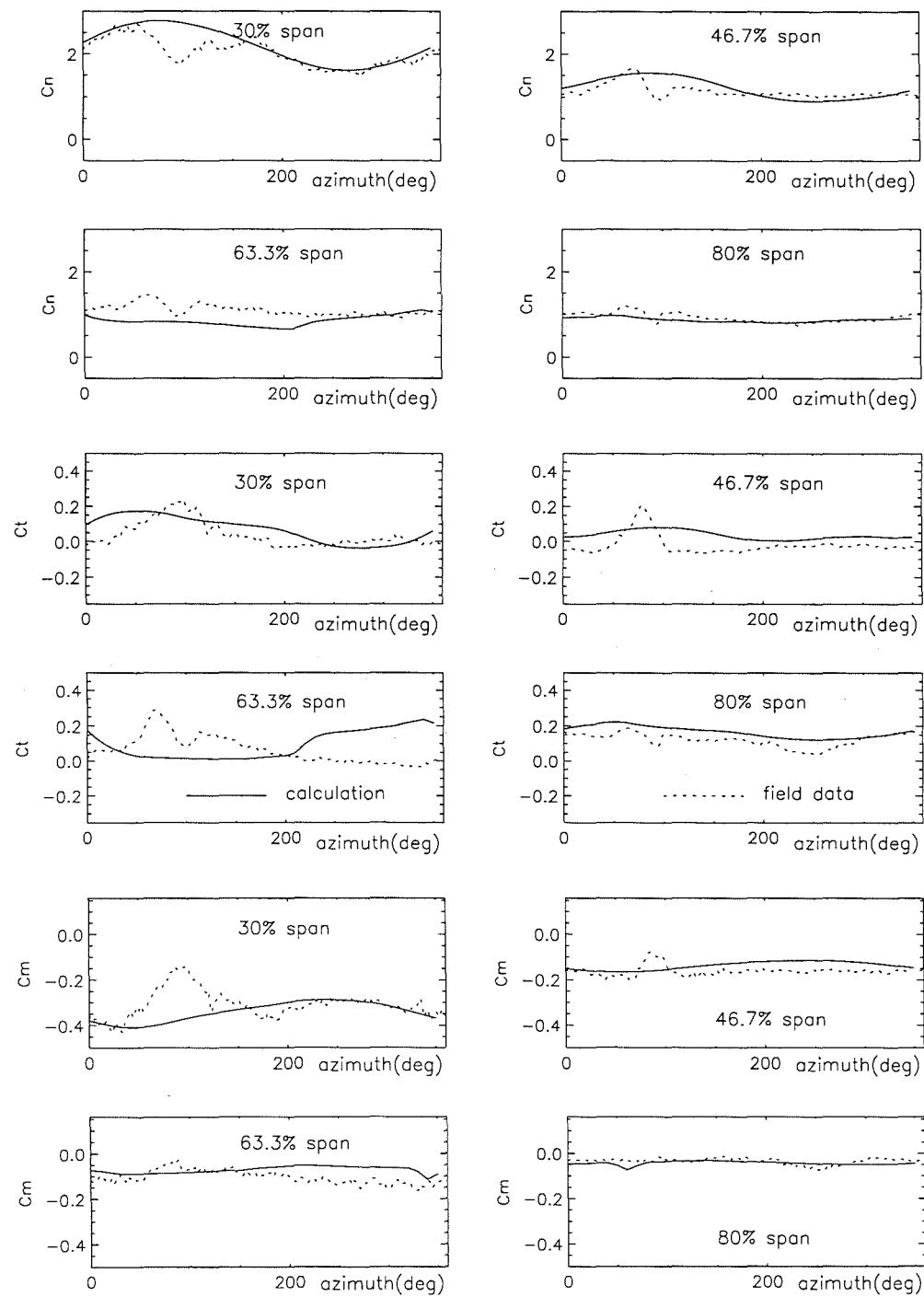


Figure 4.7: Comparison of predicted 3-D blade aerodynamic loading with field data of NREL UAE Phase I at $V_0 = 15.9$ m/s and $\gamma = -17.2^\circ$

of correspondence between the predictions and experiment is generally good.

Of the three coefficients presented in the figures, it may be anticipated that the pitching moment would be particularly sensitive to 3-D effects. Indeed, there is a marked difference in the pitching moment coefficient between the results predicted with and without 3-D effects and, as in the case of the normal force, there is a clear effect on the most inboard section. Given that the pitching moment depends not merely on the integrated normal force but also on the location of the centre of pressure, it is somewhat surprising that the present 3-D correction model greatly improves the C_m predictions since 3-D effects have an influence both on the normal force and on the movement of the centre of pressure.

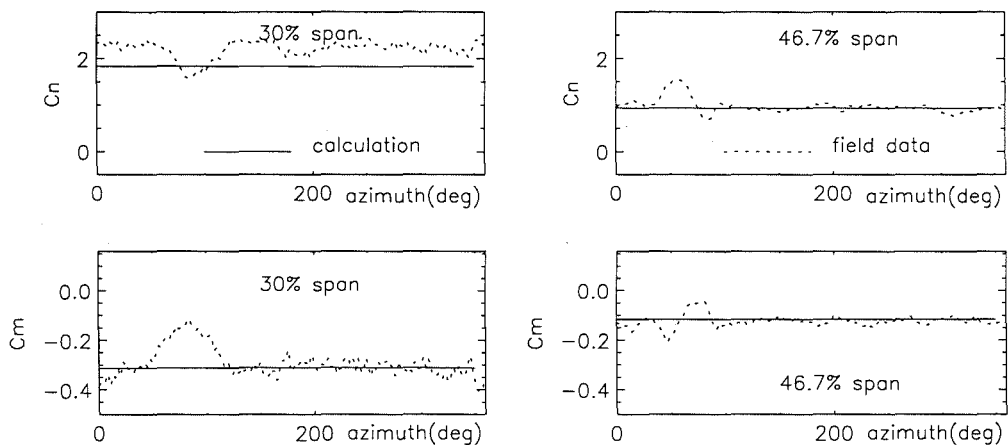


Figure 4.8: Comparison of predicted 3-D blade aerodynamic loading with field data of NREL UAE Phase I at $V_0 = 12.3$ m/s and $\gamma = -0.2^\circ$

Given that 3-D rotational effects have little influence on the tangential force and on the outboard section normal force and pitching moment, Figs. 4.8 through 4.16 only give comparisons of the 3-D calculated normal force and pitching moment coefficients with the field data at the 30%- and 46.7%-span stations of the untwisted and twisted blades for the two NREL machines. Compared to their 2-D counterparts presented in Sections 2.4 and 3.5, the level of agreement in both the normal force and the pitching moment coefficients between the model with 3-D

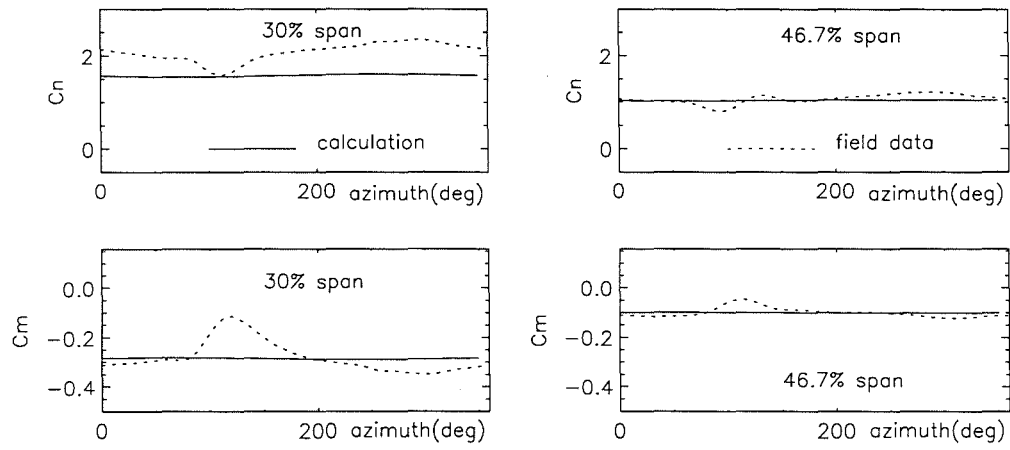


Figure 4.9: Comparison of predicted 3-D blade aerodynamic loading with field data of NREL UAE Phase I at $V_0 = 10.5$ m/s and $\gamma = 1.3^\circ$

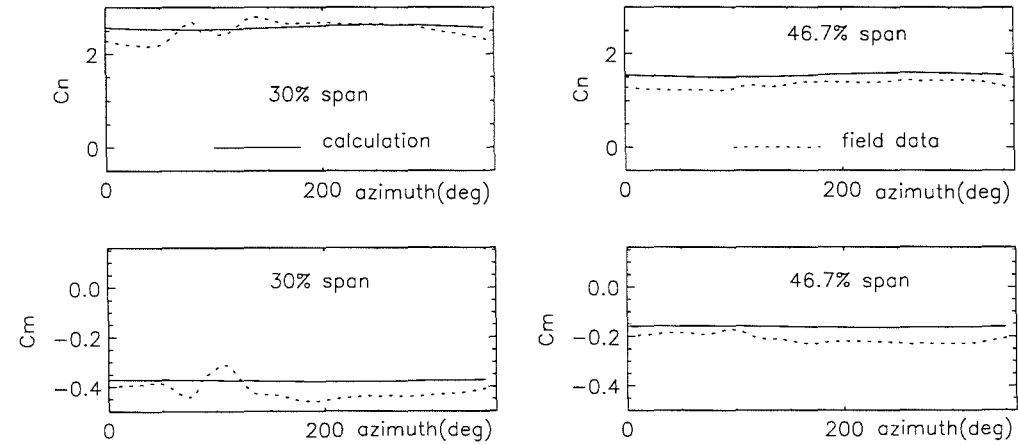


Figure 4.10: Comparison of predicted 3-D blade aerodynamic loading with field data of NREL UAE Phase I at $V_0 = 19.2$ m/s and $\gamma = 1.6^\circ$

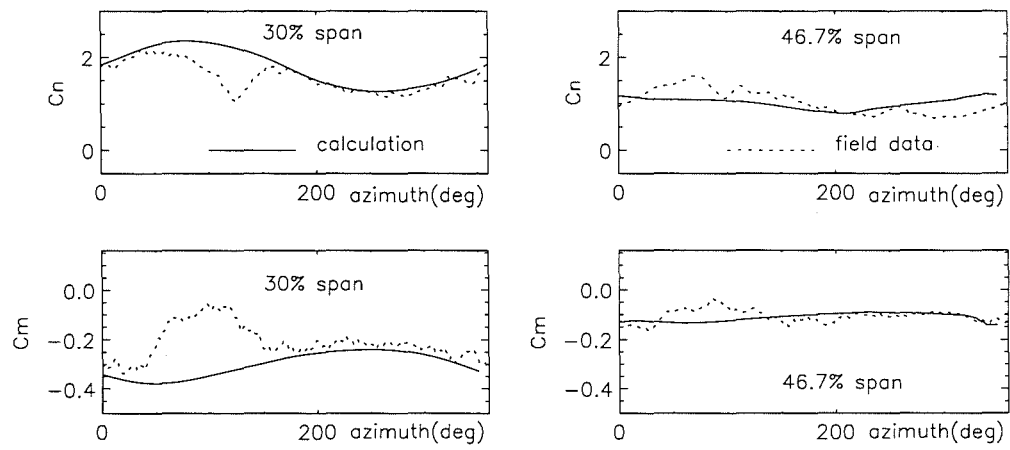


Figure 4.11: Comparison of predicted 3-D blade aerodynamic loading with field data of NREL UAE Phase I at $V_0 = 12.5$ m/s and $\gamma = -19.7^\circ$

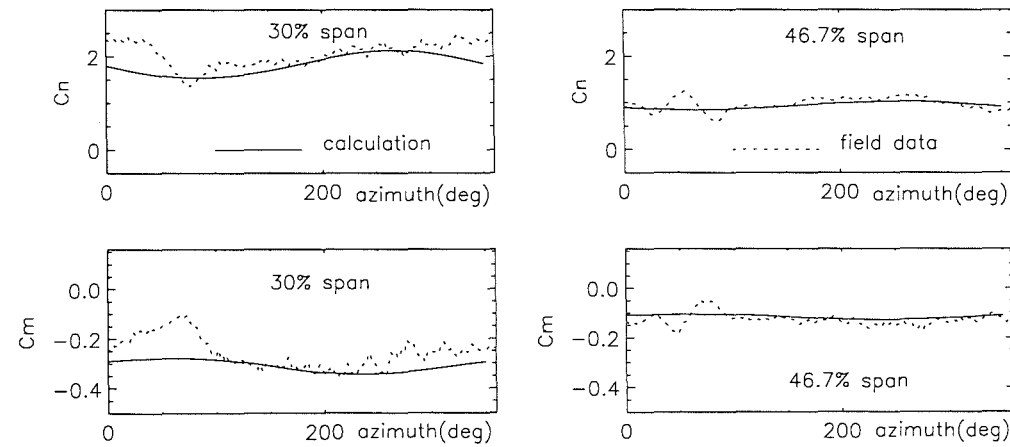


Figure 4.12: Comparison of predicted 3-D blade aerodynamic loading with field data of NREL UAE Phase I at $V_0 = 12.3$ m/s and $\gamma = 9.9^\circ$

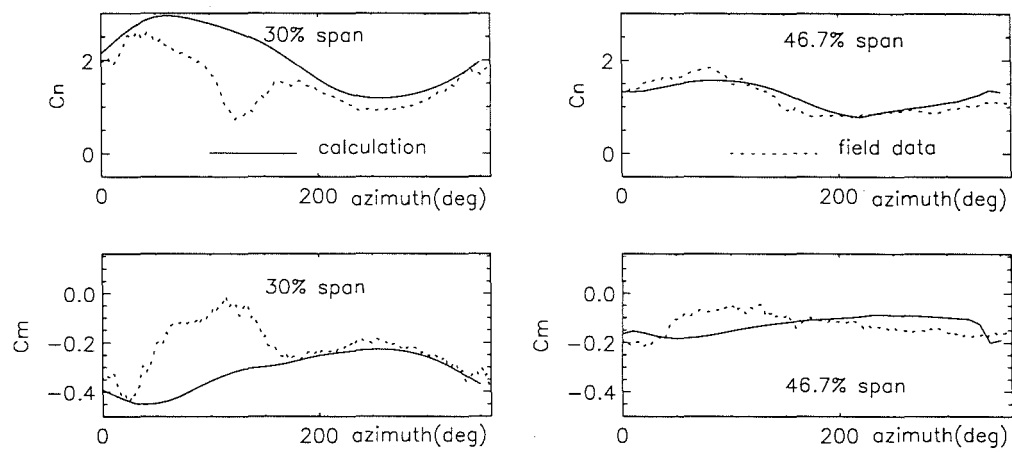


Figure 4.13: Comparison of predicted 3-D blade aerodynamic loading with field data of NREL UAE Phase I at $V_0 = 15.9$ m/s and $\gamma = -30.1^\circ$

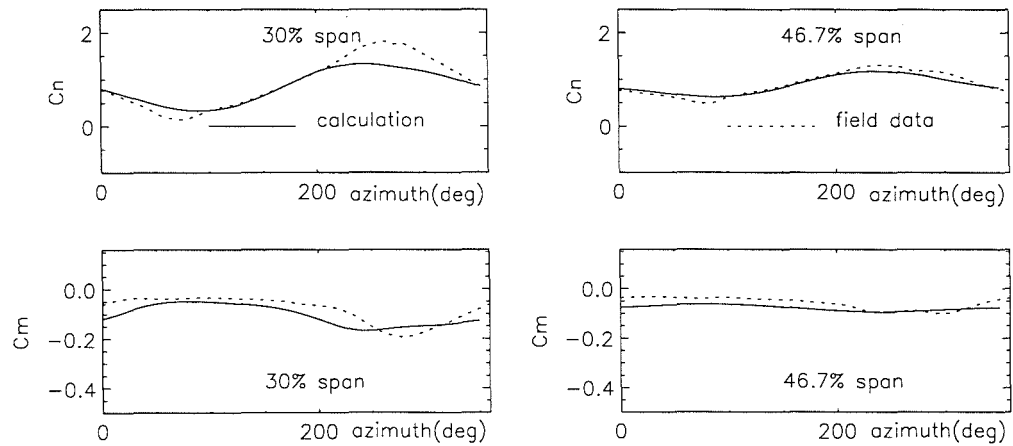


Figure 4.14: Comparison of predicted 3-D blade aerodynamic loading with field data of NREL UAE Phase IV at $V_0 = 9.9$ m/s and $\gamma = 21.9^\circ$

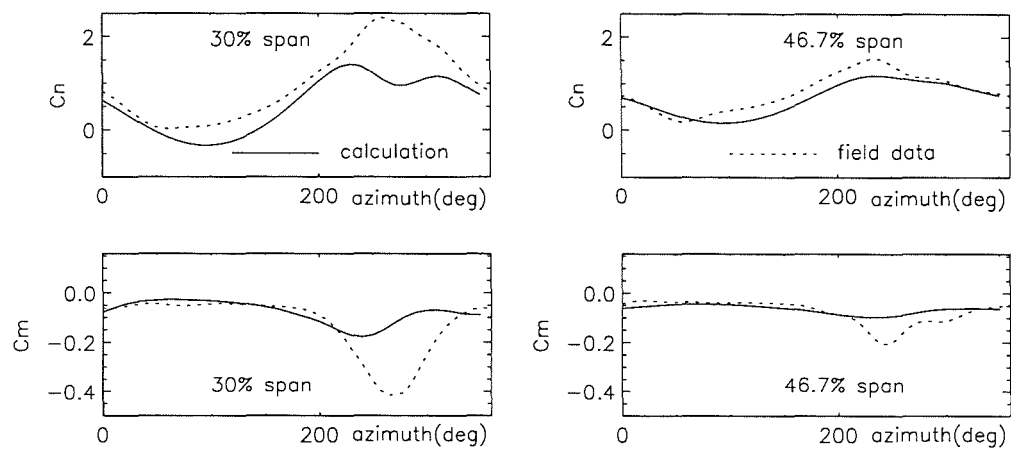


Figure 4.15: Comparison of predicted 3-D blade aerodynamic loading with field data of NREL UAE Phase M at $V_0 = 10.3$ m/s and $\gamma = 41.4^\circ$

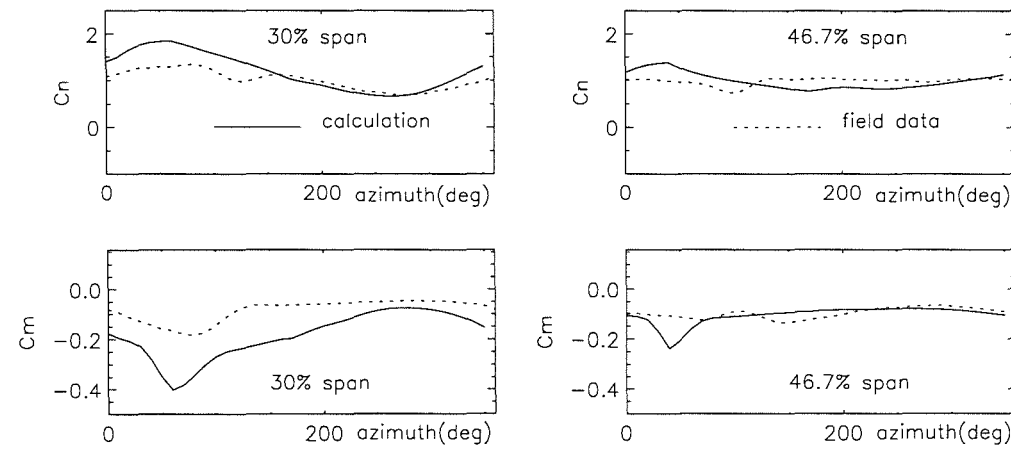


Figure 4.16: Comparison of predicted 3-D blade aerodynamic loading with field data of NREL UAE Phase M at $V_0 = 12.5$ m/s and $\gamma = -21.2^\circ$

correction and field data is considerably improved. Therefore, the 3-D corrections developed in this chapter appear to be appropriate to both twisted and untwisted blades.

It has been demonstrated that the present model is capable of predicting both the gross and detailed performance of wind turbine rotors. Despite this, there is scope to improve the 3-D unsteady aerodynamic calculation. It can be seen, for example, that there are obvious discrepancies between the calculated and measured normal force coefficients at the 30% span in Figs. 4.8 and 4.9 while all the predicted aerodynamic coefficients in Fig. 4.6 and the predicted C_m at both spanwise sections as well as C_n at the 46.7%-span station in Figs. 4.8 and 4.9 coincide well with the field data. Furthermore, there are discrepancies between the model and measurements in Fig. 4.10 except for C_n at the 30%-span station. Such differences can also be seen in the results for the yawed cases presented in Figs. 4.11 to 4.13. This kind of disagreement appears not only for the untwisted blades but also for the twisted blades of the NREL UAE Phase IV turbine (Figs. 4.14 to 4.16), although the inclusion of the 3-D rotational effects has clearly improved the predictions. This can be attributed in part to the extremely wide-ranging variations in the wind speed and yaw angle during the collection of the field data, the effect of which has been discussed in Sections 2.4 and 3.5. On the other hand, the basic Leishman-Beddoes model uses 2-D wind tunnel test data. These data may not be suitable for the 3-D case. For example, the critical value of C_{n_1} for the leading edge separation onset under rotational effects can be different from the 2-D value. However, the 3-D value of C_{n_1} for the NREL turbine blade is not available in the present 3-D calculations and, therefore, is replaced by the 2-D value. This can influence the 3-D calculated results. Overcoming the weaknesses of the unsteady aerodynamic model with 3-D effects should provide a focus for future work.

In order to improve the 3-D calculation, a better understanding is needed of the flow mechanisms inherent in these rotational effects. The radial flow in the boundary layer of a rotating blade is affected by a number of factors, such as the

chordwise and spanwise pressure distributions, the centrifugal and Coriolis force fields, and the freestream velocity field. For a HAWT in yaw, the oblique flow to local sections of the blade varies with azimuthal position. This results in a cyclic radial flow which thins the boundary layer from the root to the tip or from the tip to the root depending on the azimuthal position of the blade. The stall delay model used here does not consider the influence of the radial flow directly arising from the yawed flow. Moreover, the stall delay model used in this study is based on the analysis of the 3-D laminar integral boundary layer equations that involve the centrifugal pumping and Coriolis force terms, the effects of which, for the semi-empirical model of Du and Selig, could not be obtained directly from the solution of these equations. Rather, they were obtained through fitting to the numerical solutions of the equations. In order to reproduce accurately the numerical results, the empirical constants used in the model should be adjusted corresponding to the rotor and flow condition under consideration. This cannot be done because the empirical constants depend on a number of factors which are difficult to determine. It is possible that the level of correlation between the 3-D calculation and measurement would be further improved if the constants were adjustable from blade section to section and from flow condition to condition. To achieve this, it is necessary to conduct more both experimental and theoretical studies into 3-D flows on rotating blades.

The present 3-D correction scheme is based on the work of Du and Selig which, together with the others available for empirical 3-D effect corrections (Eggers and Digumarthi 1992, Snel *et al.* 1993, Corrigan and Schillings 1994), is based on the analysis of laminar boundary layer behaviour. Most flows around wind turbine blades are, however, turbulent in natural conditions. Therefore, the key to understanding stall on rotating blades is, as stated by Dwyer and McCroskey (1970), the study of the influence of rotation on the *turbulent* regions of the boundary layer rather than the laminar portion of the boundary layer. Although there have been some numerical solutions of turbulent boundary layers on rotating blades (*e.g.* Narramore and Vermeland 1992, Lakshminarayana and Govindan 1981),

the question of how the results of such models can be embodied in empirical models, which can easily be incorporated into wind turbine performance prediction methods, still remains open.

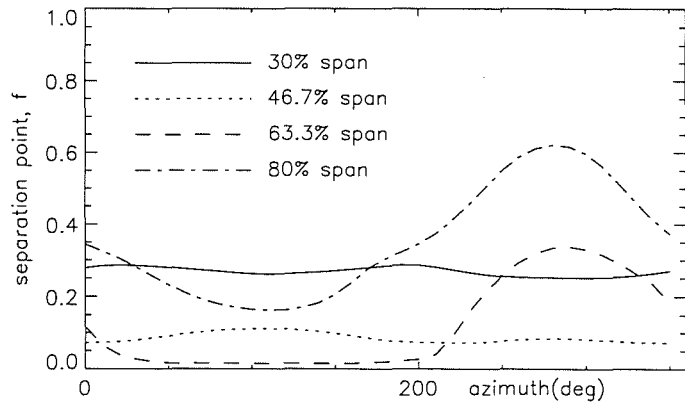


Figure 4.17: Calculated separation point for NREL UAE Phase I turbine blade at $V_0 = 15.9$ m/s and $\gamma = -17.2^\circ$

Some deficiencies of the ideal Kirchhoff flow model, which is used in the unsteady prescribed wake model, have been discussed in Section 3.5. These are inherited by the 3-D unsteady model and inevitably affect the calculated results from the model. For example, the 3-D separation point in this study is determined from Eq. 4.16 which is a direct extension of the Kirchhoff flow formula Eq. 3.36. The Kirchhoff flow model is based not only on the assumption of constant pressure in the separated wake but also on a totally 2-D analysis. Therefore, the value of the separation point derived from the Kirchhoff flow may not fully represent the real separation point. This may be one of the reasons that the calculated aerofoil tangential force coefficient C_t in Fig. 4.7 does not correlate well with the field data. In this figure even the trend of the predicted C_t at 63.3%-span station does not follow the field data. From the Kirchhoff flow formula Eq. 3.40, C_t is proportional to the square root of the separation point, \sqrt{f} . Thus, the C_t variation is strongly determined by the f value (see Fig. 4.17), which may not be appropriately predicted

due to the idealisation of the Kirchhoff flow. Although it is difficult, as stated previously, to accurately determine C_t values from pressure data, as was the case in the field test, refinement of the Leishman–Beddoes dynamic stall model will improve calculated results.

It should be noted that, since the NREL wind turbines are downwind-configured machines, the field data exhibit significant tower shadow effects which are not modelled in this chapter. The influence of tower shadow is particularly severe on inboard blade sections and can be clearly observed as a significant dip in the field data near the centre of the tower wake. In addition to this localised effect, it is likely that the changes here influence the measured loading in the surrounding region. Consequently, it is difficult to determine the extent to which the lack of correspondence between the prediction and experiment in the first half of the cycle arises from the tower shadow effect. It has become clear that the unsteady aerodynamic effects produced during tower shadow are complex, and therefore the tower shadow problem will be addressed specifically in the following chapter.

4.5 Conclusions

An unsteady aerodynamic model for HAWT performance prediction, based on a prescribed wake vortex method, has been extended to consider 3-D rotational effects. The method incorporates an unsteady aerofoil performance model which has been modified, on the basis of semi-empirical stall delay corrections, to allow for the consideration of 3-D and rotational flow effects. It has been demonstrated that application of the proposed 3-D modifications can improve the prediction of both the gross rotor performance and the detailed aerodynamic loads on the blades. In general, the method is shown to give accurate predictions over a wide range of operating conditions and inflow angles. The substantial improvement in the prediction of aerodynamic force and moment coefficients is, however, confined mainly to inboard blade sections and depends on inflow conditions on the blades. For the case of the NREL UAE Phase II at $V_0 = 12.5$ m/s and $\gamma = 0.4^\circ$, for

example, the 3-D calculated normal force and pitching moment at 30% of span (Fig. 4.6) are as high as twice their 2-D counterparts (Fig. 2.14) and the normal force at 46.7% of span is increased by 45% by the 3-D correction. Little change takes place further outboard. Given that most of the 3-D effect is confined to inboard blade sections, it is not surprising that the 3-D corrections have little influence on the production of turbine power. The exception to this is at high wind speeds or low tip speed ratios when separated flow and hence 3-D effects influence more of the blade radius.

It is clear from the above that two aspects of the 3-D corrections are significant. Firstly, the evolution of turbine blade design has been such that future benefits are likely to come from a combination of aerodynamics and materials through aeroelastic tailoring. This can be achieved effectively if the aerodynamic information supplied to the aeroelastic model is of high quality across the entire blade. Obviously 3-D effects must be considered for this to be the case. Secondly, designs that rely on stall regulation at high wind speed will benefit from more accurate power prediction at low tip speed ratios. It is in this regime that the inclusion of 3-D effects has a beneficial influence on the predicted aerodynamic performance.

Whilst the 3-D corrections presented here have significantly improved the prediction of the HAWT aerodynamic performance, the 3-D stall delay model requires further refinement. This will only be achieved through more experimental and theoretical investigations of 3-D flow effects on rotating blades.

Chapter 5

Tower Shadow Problem

5.1 Introduction

The sources of unsteadiness which influence the operating environment of a HAWT are numerous and have been well documented (Galbraith *et al.* 1990, Hansen and Butterfield 1993, Robinson *et al.* 1995, Huyer *et al.* 1996). These include the influence of atmospheric turbulence, wind shear, yawed rotor operation and, in the case of wind farms, the disturbance created by other turbines in close proximity. Among them, the influence of the yawed flow and wind shear has been modelled using an unsteady prescribed wake scheme in Chapter 3.

For wind turbines another important unsteady effect comes from the interaction between the blade and supporting tower. It is understandable that the effect of the tower on the upwind rotor is small. However, a further complication arises in the case of downwind-configured machines. These machines experience a disturbance as the blade passes through the wake, or shadow, of the support tower. In addition to producing a velocity deficit and high turbulence, this shadow region may contain secondary sources of unsteadiness resulting from vortex shedding from the tower itself. The primary effect is, however, the velocity deficit and, depending on the particular geometry of the blades and the tower, the effects of this may have severe implications for the operating life and general performance of the turbine. For this reason, it is necessary to develop appropriate modelling techniques which will allow

this effect to be properly represented at an early stage in the design process. The present work, therefore, concentrates on integrating a tower shadow model with a fully unsteady calculation scheme for yawed flow on HAWTs.

In its simplest form, tower shadow may be considered as a region of velocity deficit which produces changes in angle of attack and resultant velocity experienced by the blade. The frequency and severity of these changes is often such that the local aerodynamic response of the blade is highly unsteady (Robinson *et al.* 1995). To date, consideration of this phenomenon has been somewhat limited. In fact, there are few publications which discuss tower shadow effects in detail, although both experimental and theoretical studies into the problem have been carried out (Powles 1983, Wilmhurst *et al.* 1985, Graham and Brown 1999, Thresher *et al.* 1986, Duque *et al.* 1999). When Thresher *et al.* (1986) used a computer code to analyse the blade dynamic loads, the tower shadow effects were not the main concern; instead, the velocity deficit in the tower shadow was included in passing only as a deterministic excitation. In the work of Duque *et al.* (1999), a state-of-the-art N-S solver is used to examine the rotor/tower interactions but, in comparison to the experiment, the computed tower wake interaction has neither the same duration nor amplitude as the experiment mainly due to grid density mismatches in the analysis. Nevertheless, given the complicated nature of the tower shadow problem which can induce huge fluctuations in the blade incidence and dynamic pressure, the significance of any effort to address this problem should not be underestimated.

In this chapter, a tower shadow model is firstly included directly in the prescribed wake scheme which has been presented in the previous chapters. This simple model produces a low resolution of the tower shadow effects and hence only provides a general investigation of the tower shadow problem. Dynamic and aeroelastic analyses generally require high temporal resolution of tower shadow effects. To provide this kind of detail, a near wake model is coupled with the prescribed wake scheme to form a method which is capable of producing high tem-

poral resolution in the tower shadow domain whilst minimising the computational overhead for the gross calculation of the turbine performance. Comparisons are then made between the low and high resolution tower shadow models, and both are compared with measured data.

5.2 Velocity Profile in the Tower Wake

Tower shadow is typically a region of greatly reduced wind speed and high turbulence through which the wind turbine blade must pass once per revolution. The azimuthal angles ψ_1 and ψ_2 at which the blade enters and leaves the shadow, respectively, vary with the blade spanwise location r and, for the yawed case, can be determined by the following formulae,

$$\psi_1 = \arccos \frac{Z_t \sin \gamma + \frac{1}{2} B_t}{r \cos \gamma} \quad (5.1)$$

$$\psi_2 = \arccos \frac{Z_t \sin \gamma - \frac{1}{2} B_t}{r \cos \gamma} \quad (5.2)$$

where Z_t is the distance from the yawing axis to the rotor rotation plane, and B_t is the tower shadow width (see Fig. 5.1).

It is anticipated that the velocity profile behind the tower depends on the shape of tower. Usually a cosine function is used to model the tower shadow velocity deficit. For a cylindrical supporting tower, the shadow region, modelled with a pie-shaped section from ψ_1 to ψ_2 , is assumed to have a velocity profile of the form

$$\frac{\tilde{V}}{V_\infty} = 1 - \frac{D_V}{2} \left[1 + \cos \frac{2\pi \left(\psi_t - \frac{\pi}{2} \right)}{2\psi_0} \right] \quad (5.3)$$

where \tilde{V} is the velocity within tower shadow and D_V the maximum velocity deficit; the shadow half angle ψ_0 and shadow azimuth angle ψ_t corresponding to a blade section r at the azimuth ψ (Fig. 5.1) are generally determined by

$$\psi_0 = \arctan \frac{B_t}{2r \sin \psi_1} \quad (5.4)$$

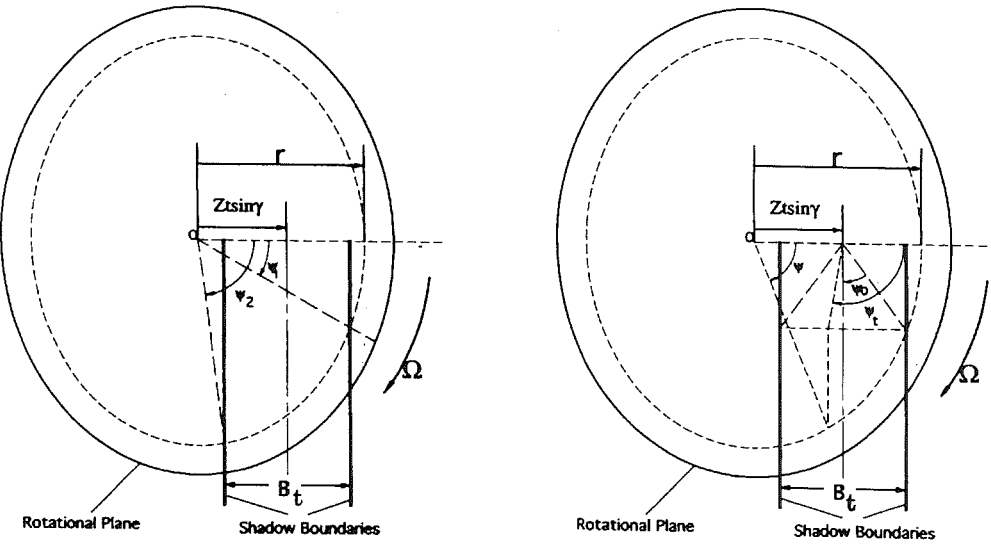


Figure 5.1: Definitions of tower shadow and its parameters

$$\psi_t = \frac{\pi}{2} - \arctan \frac{r \cos \gamma \cos \psi - Z_t \sin \gamma}{r \sin \psi_t} \quad (5.5)$$

Obviously, the tower shadow width B_t and maximum value of velocity deficit D_V mainly depend on the streamwise distance downstream and Reynolds number. Applying basic linear momentum theory to Eq. 5.3, B_t and D_V can be related to the drag coefficient C_d of a 2-D circular cylinder which has a diameter D :

$$C_d = \frac{B_t}{D} \left(1 - \frac{3}{4} D_V \right) D_V \quad (5.6)$$

The variation of C_d with Reynolds number, $R_e = V_\infty D / \nu$, can be found in many references (e.g. Schlichting 1979) and is reproduced in Fig. 5.2. It is worthy to note that the cylinder drag is very sensitive to R_e when R_e ranges from 2×10^5 to 5×10^5 ; C_d falls markedly from about 1.2 for $R_e = 2 \times 10^5$ to 0.3 for $R_e = 5 \times 10^5$. This implies that either the shadow width or the maximum velocity deficit changes sharply with Reynolds number within this region. This kind of change may particularly be of importance for the NREL Unsteady Aerodynamics Experiment, the field data of which are used to validate the model. This is because most operating Reynolds numbers for its support tower lie between $R_e = 2 \times 10^5$ and $R_e = 5 \times 10^5$.

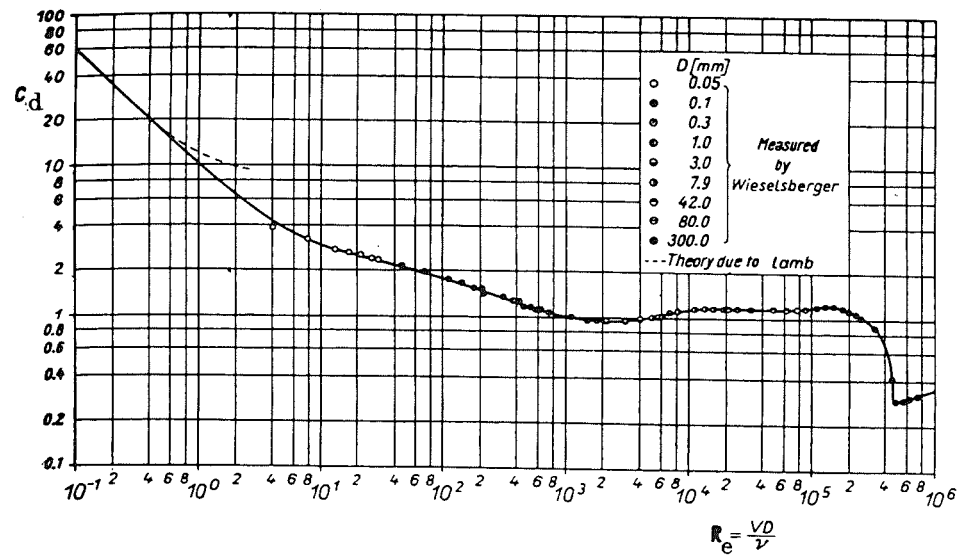


Figure 5.2: Drag coefficient for circular cylinders as a function of the Reynolds number

A study of tower shadow on the NREL UAE indicated that the maximum velocity deficit at particular locations behind the tower could fluctuate from 10% to 90% of the freestream velocity when the mean values were between 25% and 30% (Shipley *et al.* 1995*b*). Therefore, Eq. 5.3 is a time-averaged expression. Variations of the shadow width and velocity deficit are systematically demonstrated by the results from wind tunnel tests carried out by Snyder and Wentz (1981) for Reynolds numbers from 1.74×10^5 to 7.58×10^5 . Three cylinder diameters downstream of the cylinder centreline, the maximum velocity deficit varies with R_e from less than 10% to a little greater than 30% of the freestream. It appears that the tower shadow width depends very much on the type of boundary layer separation, *i.e.* laminar or turbulent separation. At the higher Reynolds numbers, the corresponding tower shadow width is about 2.5 times the tower diameter whereas, at lower Reynolds numbers, the tower shadow is wider.

The critical value of R_e , at which laminar and turbulent separations are distinguished, varies with both the degree of turbulence in the free stream and the roughness of the tower surface. The natural conditions of a wind turbine field would be much different from the controlled environment of wind tunnel tests.

This should, if possible, be taken into consideration when field data are compared with calculations which rely on input from wind tunnel tests.

5.3 Low Resolution Tower Shadow Effects

5.3.1 Wake Prescription with Tower Shadow Effects

The effect of tower shadow can be introduced into the prescribed wake model by representing the incoming wind velocity in the tower shadow domain by the velocity in the tower wake \tilde{V} (Eq. 5.3). In this way, the non-dimensional wake velocity $(\bar{V}_z)_w$ and displacement \bar{z}_w in the wind direction are, according to Eqs. 3.9 and 3.10, can be prescribed as

$$\frac{(\bar{V}_z)_w}{\frac{\tilde{V}}{V_\infty} \bar{V}_\infty} = \begin{cases} 1 - a - \frac{21}{5}(F-1)a\bar{t} & \text{for } \bar{t} \leq \frac{1}{7} \\ 1 - \frac{1}{2}(1+F)a - \frac{7}{10}(F-1)a\bar{t} & \text{for } \frac{1}{7} < \bar{t} \leq \frac{4}{7} \\ 1 - \frac{7+23F}{30}a - \frac{7}{30}(F-1)a\bar{t} & \text{for } \frac{4}{7} < \bar{t} \leq 1 \\ 1 - Fa & \text{for } \bar{t} > 1 \end{cases} \quad (5.7)$$

$$\frac{\bar{z}_w}{\frac{\tilde{V}}{V_\infty} \bar{V}_\infty} = \begin{cases} \frac{7\pi}{4}(1-a)\bar{t} - \frac{147\pi}{40}(F-1)a\bar{t}^2 & \text{for } \bar{t} \leq 1/7 \\ \frac{\pi}{16}(F-1)a + \frac{7\pi}{4} \left(1 - \frac{1+F}{2}a\right) \bar{t} - \frac{49\pi}{80}(F-1)a\bar{t}^2 & \text{for } 1/7 < \bar{t} \leq 4/7 \\ \frac{47\pi}{240}(F-1)a + \frac{7\pi}{4} \left(1 - \frac{7+23F}{30}a\right) \bar{t} - \frac{49\pi}{240}(F-1)a\bar{t}^2 & \text{for } 4/7 < \bar{t} \leq 1 \\ \frac{2\pi}{5}(F-1)a + \frac{7\pi}{4}(1-Fa)\bar{t} & \text{for } \bar{t} > 1 \end{cases} \quad (5.8)$$

Thus, the induced velocities at the blades can be calculated using the prescribed wake method (Chapter 3). The aerodynamic information from the prescribed wake model is then input to the three-dimensionally enhanced Leishman–Beddoes unsteady aerodynamic model and the 3-D airloads on the blades are then obtained (Chapter 4).

5.3.2 Results and Discussion

It is understandable that rotor power predictions which include tower shadow effects are lower than those without tower shadow. Since, however, the region of the velocity deficit only accounts for a small proportion of the rotor swept area, the decrease in power due to tower shadow effects will not be significant. This is clearly demonstrated in Fig. 5.3, where the power coefficients calculated with and without tower shadow effects are compared for the NREL UAE Phase IV turbine.

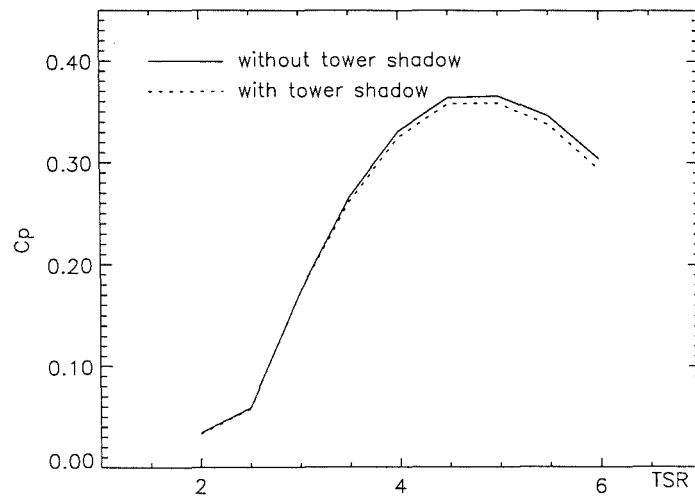


Figure 5.3: Calculated power coefficients with and without tower shadow effects for the NREL UAE Phase IV turbine in head-on flow

Whilst the tower shadow effects on the gross rotor performance are small, it may be expected that the effects on the blade local loads would be significant

when the blade passes through the tower shadow. The velocity deficit within the shadow not only influences the onset flow conditions at the blade but also substantially modifies the local wake structure. This is shown in Fig. 5.4 where the wake geometries of the NREL UAE Phase II turbine, at $\lambda = 5$ and $\gamma = 30^\circ$, for an undisturbed onset flow and with tower shadow are compared. For the sake of clarity, only six cycles of the wake structure trailed from one blade are illustrated in the figure. It should be noted here that the resultant wake structure is not produced by a single pass application of the velocity deficit but is obtained through an iterative process where the induced effect of the distorted wake influences the velocities at the blade and vice versa. Therefore, the direct effect of the velocity

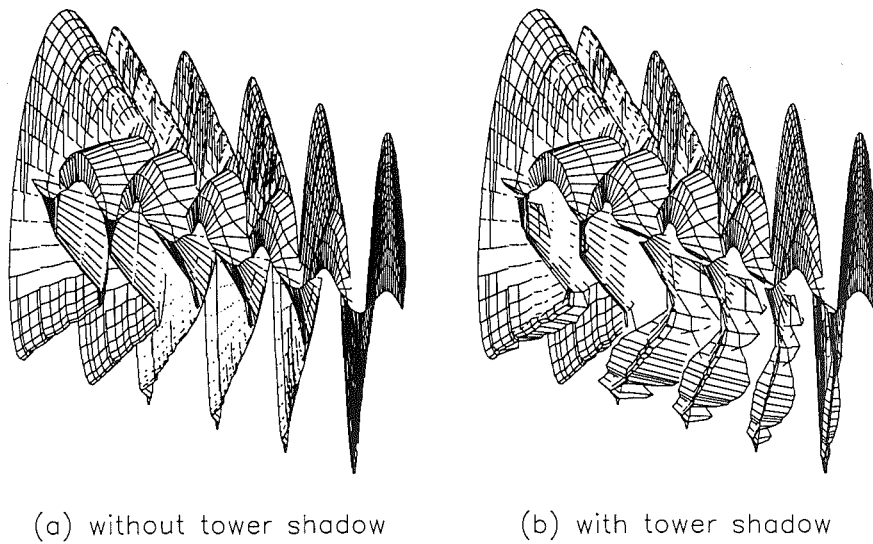


Figure 5.4: Calculated wake trailed from single blade of the NREL UAE Phase II wind turbine at $\lambda = 5$ and $\gamma = 30^\circ$

deficit and the subsequent effect of the distortion of the vortex wake significantly modify the distribution of the blade load.

In order to view the tower shadow effects, head-on flow cases should firstly be examined because, for a theoretically uniform axial flow, the tower shadow is the only source of unsteadiness and hence any variations in the blade loads are caused

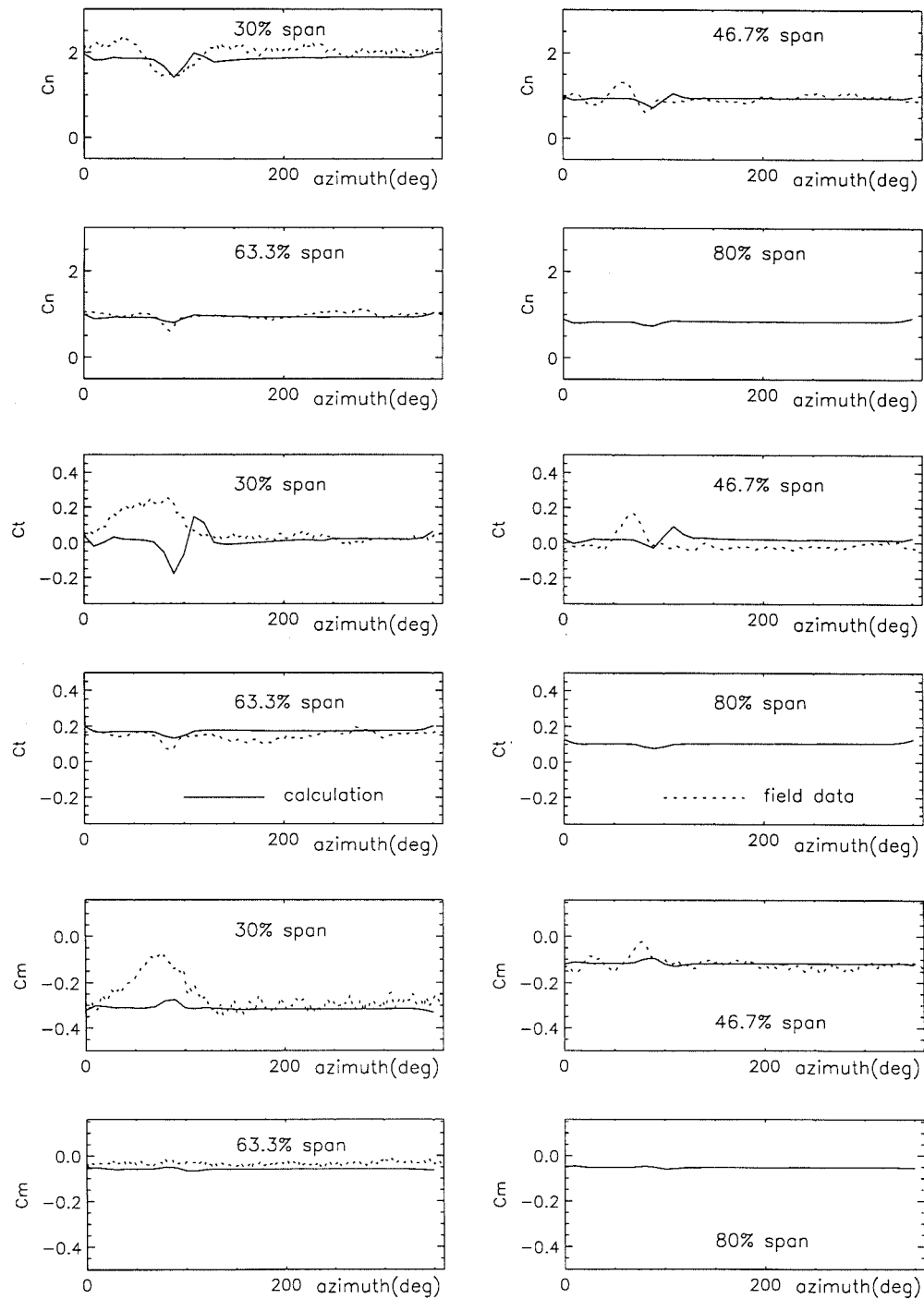


Figure 5.5: Comparison of low resolution calculation ($D_V = 0.3$, $B_t = 2.5D$) with field data of NREL UAE Phase I at $V_0 = 12.5$ m/s and $\gamma = 0.4^\circ$

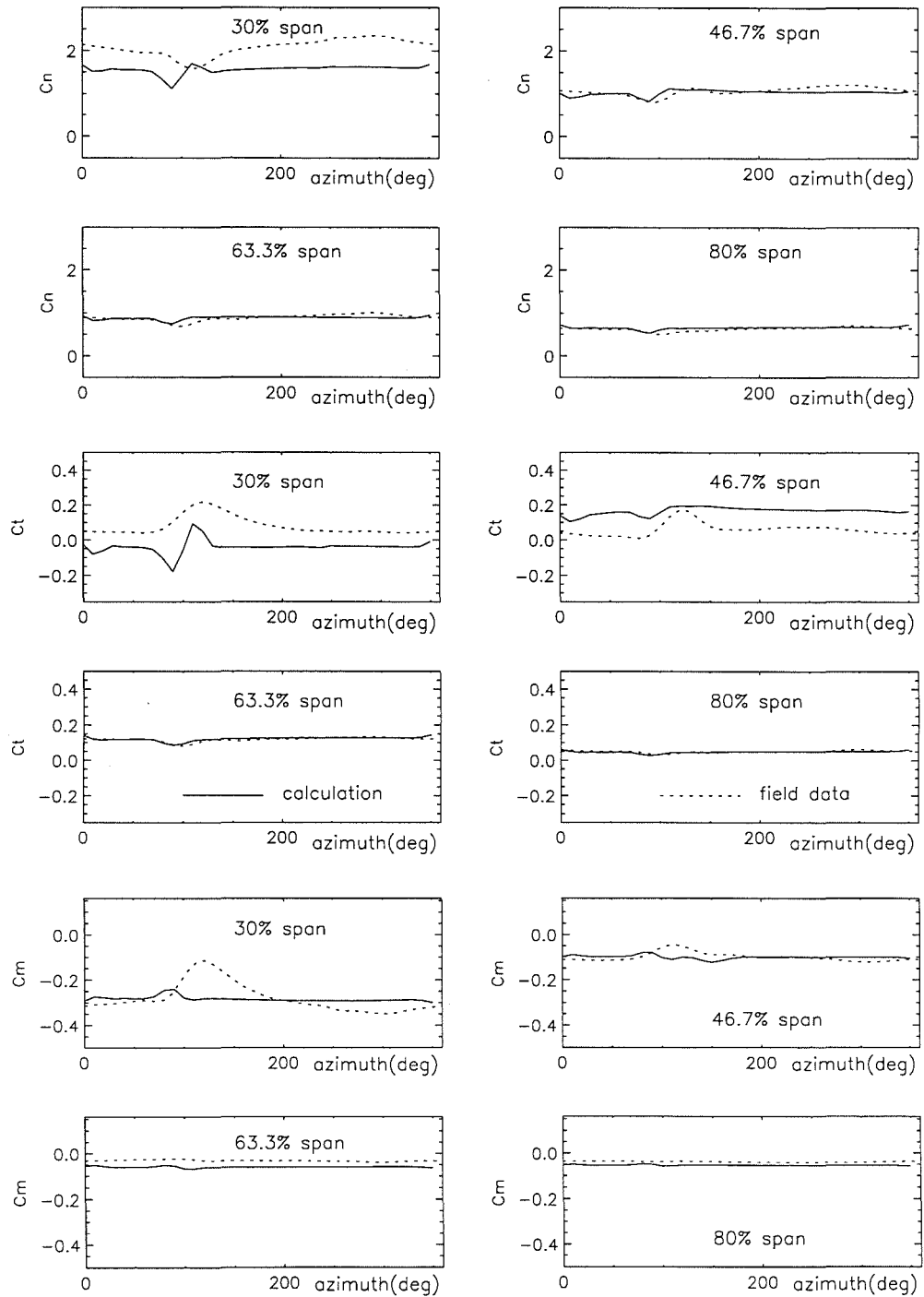


Figure 5.6: Comparison of low resolution calculation ($D_V = 0.3$, $B_t = 2.5D$) with field data of NREL UAE Phase I at $V_0 = 10.5$ m/s and $\gamma = 1.3^\circ$

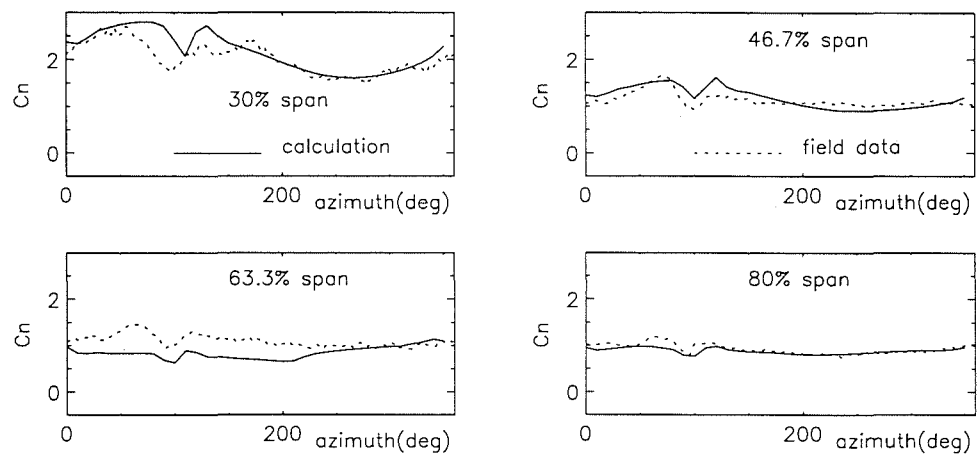


Figure 5.7: Comparison of low resolution calculation ($D_V = 0.3$, $B_t = 2.5D$) with field data of NREL UAE Phase I at $V_0 = 15.9$ m/s and $\gamma = -17.2^\circ$

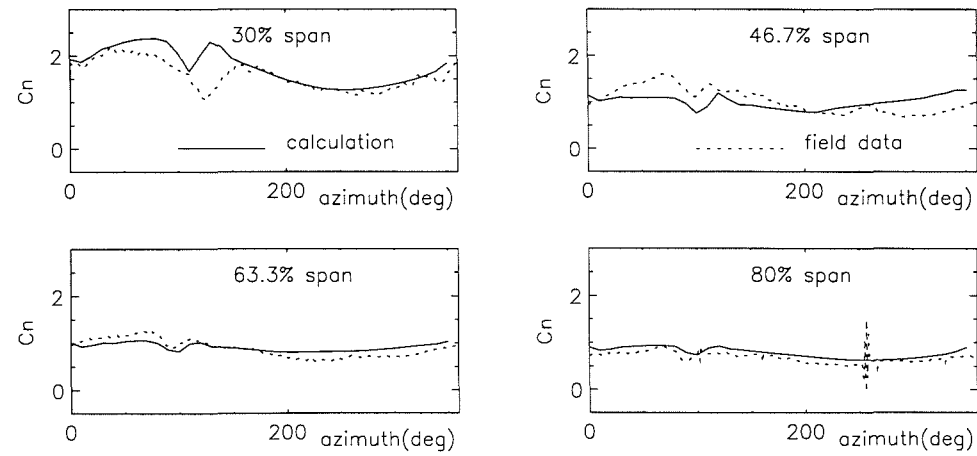


Figure 5.8: Comparison of low resolution calculation ($D_V = 0.3$, $B_t = 2.5D$) with field data of NREL UAE Phase I at $V_0 = 12.5$ m/s and $\gamma = -19.7^\circ$

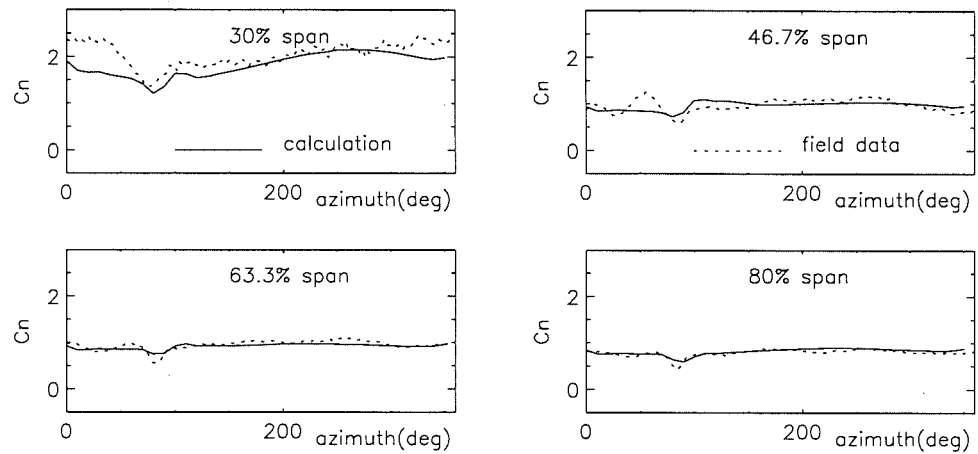


Figure 5.9: Comparison of low resolution calculation ($D_V = 0.3$, $B_t = 2.5D$) with field data of NREL UAE Phase I at $V_0 = 12.3$ m/s and $\gamma = 9.9^\circ$

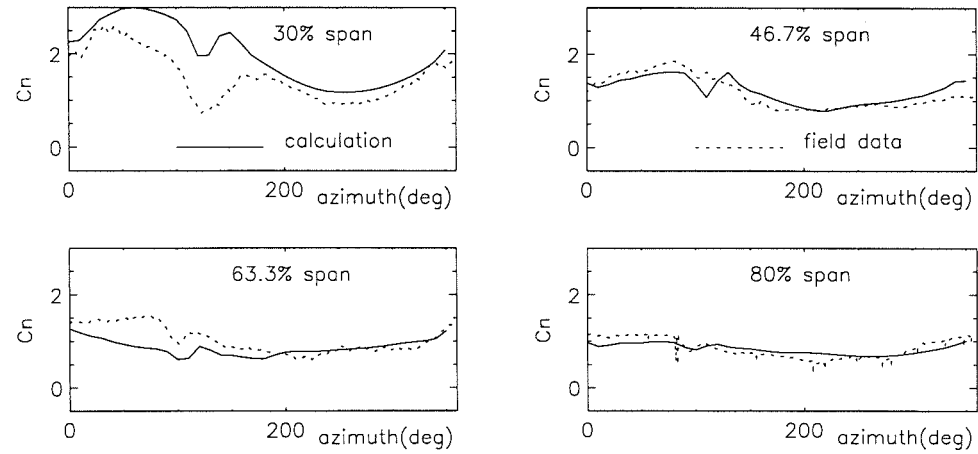


Figure 5.10: Comparison of low resolution calculation ($D_V = 0.3$, $B_t = 2.5D$) with field data of NREL UAE Phase I at $V_0 = 15.9$ m/s and $\gamma = -30.1^\circ$

by tower shadow effects. Figs. 5.5 and 5.6 give comparisons of the blade aerodynamic loads between the field data and the calculation with tower shadow effects for nominally unyawed cases. In these two calculations and those that follow, the tower shadow width is set to 2.5 times the tower diameter and the maximum velocity deficit to 30% of the freestream velocity. It can be seen from these two figures that the tower shadow effects are particularly well represented on the outboard blade sections. For the most inboard station, 30%-span, the field data appear to exhibit a wider velocity deficit in the region adjacent to the tower shadow, which is not well represented by the model. The calculated tangential force coefficient C_t at the 30% span section shows an undershoot and overshoot when the blade passes in and out of the tower shadow. This phenomenon cannot be found in the field data. Compared to the field data, the model also seems to underestimate the effect of tower shadow on the pitching moment at 30%-span.

Tower shadow effects in the yawed flow cases are illustrated in Figs. 5.7 through 5.10, where the predicted normal force coefficients are compared with the field data for various wind speeds and yaw angles. It is clear from these figures that the tower shadow effects are generally modelled quite well, particularly on outboard sections. On the other hand, there is obviously an azimuth shift in the tower shadow effects from the measurements at inboard sections in some cases (see Figs. 5.6 ~ 5.8). This may be attributed in part to the low azimuthal resolution. Further reasons will be discussed in Section 5.4.5.

5.4 High Resolution for Tower Shadow Effects

5.4.1 Introduction

Tower shadow effects have been modelled above with low azimuth resolution and some results have been presented. There are, however, practical difficulties with this approach. In particular, the azimuthal resolution of the wake calculation was

insufficient to provide a basis for convergent iterative application of the Leishman–Beddoes unsteady aerofoil model in some cases. The results presented in these cases were, therefore, generated by applying the dynamic model once and do not represent a fully converged solution. The reason for this problem lies in the sensitivity of the dynamic model to the time derivatives of velocity, blade incidence and pitch rate. Obviously, this could be overcome by repeated application of smoothing algorithms, but this is often done at the expense of accuracy. A more acceptable approach is to increase the azimuthal resolution of the prescribed wake calculation, thus increasing the resolution of the input to the unsteady aerofoil model. This would inevitably incur a high computational overhead which would be potentially unacceptable in a model which was originally developed as a design tool. For instance, the azimuthal interval for global calculations of turbine performance is normally 20° , as it is in Chapters 2 ~ 4. In the calculations which provided the results for Figs. 5.3 and 5.5 ~ 5.10, the azimuthal interval was reduced to 10° . This resulted in a six-fold increase in the required computational time. Given the fundamental frequencies associated with the tower shadow effect on outboard sections of a turbine blade, it would be necessary to reduce the azimuthal step to less than 1° , in the tower shadow region, to provide a suitable basis for repeated application of the Leishman–Beddoes model. Even if this were done over a limited azimuthal region, the increase in computational time would be severe. It was, therefore, considered necessary to develop an alternative modelling strategy.

The requirement for high temporal resolution is analogous to the case of a helicopter rotor blade undergoing dynamic stall or blade/vortex interaction. To reduce the computational effort required to solve this type of problem, Beddoes (1987) developed a novel near wake solution methodology which allowed high resolution airloads to be calculated efficiently. The near wake model itself is only used to represent the first quarter cycle of the trailed vorticity in the rotor wake and is, therefore, normally integrated with a far wake model which represents the remainder of the wake. In addition, since only trailed vorticity is represented by the

scheme, it is necessary to introduce the effects of shed vorticity in some way. This is normally achieved by coupling the scheme with the Leishman–Beddoes unsteady aerofoil model. Thus, in the fully coupled method, the locations of blade/vortex interaction are indicated by the geometry of the far wake and the resulting loading response is calculated at high temporal resolution by the fully coupled scheme (Beddoes 1989).

In the near wake model, the blade is modelled according to classical lifting line theory as a discrete series of elements from which vorticity is trailed. Unlike conventional vortex schemes, however, each trailing filament is approximated according to the flight state by either a straight line or a circular arc and the calculation of downwash from the trailing vortex system is reformulated such that the induced effect of the trailed vorticity system at a given moment in time is approximated using exponential functions. As the blade moves, these functions decay in a manner which is consistent with the downstream convection of the system. The approach is numerically efficient and allows for very high azimuthal resolution at minimal computational cost.

Although the near wake model has been successfully applied to the prediction of helicopter airloads, it exhibits some features which may limit its wider applicability. The simplifying assumptions in the method, for example, limit the accuracy that it can achieve in practical flow scenarios. In particular, for the circular arc representation, the induced effect of vorticity trailed from inboard blade sections on the outer portions of the blade is not well represented. When compared to an exact solution, obtained by application of the Biot–Savart law to a planar arc of constant vorticity strength lying inboard of the downwash evaluation point, significant errors are produced by the near wake model. For a helicopter rotor, where the loading distribution on the blade is normally dominated by the tip vortex system, this error would only have a very limited effect on performance calculation. For wind turbines, however, the root vortex often has a strength of the same order as the tip vortex (see Fig. 2.12). Therefore, it would be particularly beneficial if the effect of vortices trailed from all blade sections were appropriately represented

by the model.

In this study, the Beddoes near wake dynamic model is modified such that it is capable of providing more accurate results over a wider range of rotor flows. The modified version of the near wake model is then coupled with the prescribed wake scheme to produce high temporal resolution in the tower shadow domain whilst minimising the computational overhead for the gross calculation of the turbine performance. The manner in which the near and prescribed wake models have been coupled is described. Comparisons are made between the original low-resolution tower shadow model and the more sophisticated high-resolution scheme. The results from the latter are found to exhibit strong impulsive loading components, which may have operational implications for downwind-configured machines. The model is also compared to field data from the NREL Unsteady Aerodynamics Experiment.

5.4.2 The Near Wake Dynamic Model

Consider a vortex filament trailing from point B on the blade as shown in Fig. 5.11. For application to rotors, the trajectory of the near wake may be approximated by a circular arc. According to the Biot–Savart equation, the downwash velocity induced at Point A by a vorticity element of strength Γ and length ds at any location on the arc is given by

$$dw = \frac{\Gamma \left[1 - \left(1 - \frac{h}{r} \right) \cos \theta \right] ds}{4\pi r^2 \left[1 + \left(1 - \frac{h}{r} \right)^2 - 2 \left(1 - \frac{h}{r} \right) \cos \theta \right]^{3/2}}$$

or

$$\frac{dw}{dw_0} = \frac{\frac{h|h|}{r^2} \left[1 - \left(1 - \frac{h}{r} \right) \cos \theta \right]}{\left[1 + \left(1 - \frac{h}{r} \right)^2 - 2 \left(1 - \frac{h}{r} \right) \cos \theta \right]^{3/2}} \quad (5.9)$$

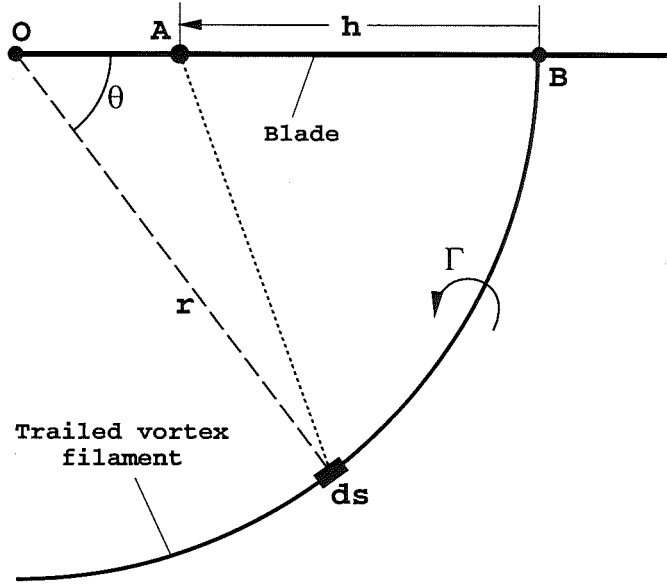


Figure 5.11: Circular arc line vortex of near wake

where r is the local radius of the blade section from which the arc line vortex trails, θ denotes the azimuthal angle of the vortex element ds in the wake, $ds = rd\theta$, dw_0 is the initial value of the downwash,

$$dw_0 = \frac{\Gamma ds}{4\pi h|h|}$$

and the parameter h is determined by $h = r - r_{cp}$, if the local radius of the blade element control point A is denoted by r_{cp} .

If only considering the first quarter cycle of the trailing filament, *i.e.* θ ranging from 0 to $\pi/2$, it is possible, as shown by Beddoes (1987), to approximate Eq. 5.9, using exponential functions, as

$$\frac{dw}{dw_0} = 1.359 \exp\left(-\frac{\theta}{\Phi}\right) - 0.359 \exp\left(-4\frac{\theta}{\Phi}\right) \quad (5.10)$$

where the decay parameter Φ is approximated by

$$\Phi = \frac{\pi}{4} \left| \left(1 + \frac{h}{2r}\right) \ln \left(1 - \frac{h}{r}\right) \right| \quad (5.11)$$

In this form, Eq. 5.10 effectively represents the time history of a vortex element of length ds as it traverses the prescribed circular arc. In practice, the integrated

downwash w due to an arc totally populated by vortex elements is required. This may be obtained by summation of the downwash calculated by successive application of Eq. 5.10 to each of the vortex elements in the arc. This allows the total downwash from the arc to be expressed, for a sampled system, as

$$w(N) = X_w(N) + Y_w(N) \quad (5.12)$$

where N denotes the current sampling, and

$$X_w(N) = X_w(N-1) \exp\left(-\frac{\Delta\theta}{\Phi}\right) + 1.359 D_w \exp\left(-\frac{\Delta\theta}{2\Phi}\right)$$

$$Y_w(N) = Y_w(N-1) \exp\left(-4\frac{\Delta\theta}{\Phi}\right) - 0.359 D_w \exp\left(-2\frac{\Delta\theta}{\Phi}\right)$$

In the above expressions, the derivations of which are given by Beddoes (1987), $X_w(N-1)$ and $Y_w(N-1)$ are the values at the previous time step and D_w represents the contribution of the closest (currently generated) element, *i.e.*

$$D_w = \frac{\Gamma \frac{\Delta s}{h}}{4\pi r \left| \frac{h}{r} \right| \sqrt{1 + \left(\frac{\Delta s}{h} \right)^2}} \quad (5.13)$$

with Γ being the strength of the currently trailed vortex element and $\Delta s = r \Delta\theta$.

Thus, in a time-stepping model, if the previous values of the two terms X_w and Y_w are known, only the current value of D_w needs to be evaluated in order to calculate the downwash from a traile vortex arc. When a large number of trailing vortices are involved and a small time interval is used, this indicial procedure, which only requires the immediate value of the vortex strength to update the prior value of the integration, consumes trivial computational cost compared to conventional numerical integration methods which effectively solve the following equation

$$w = \int_0^\theta \frac{\Gamma \left[1 - \left(1 - \frac{h}{r} \right) \cos \theta \right] d\theta}{4\pi r \left[1 + \left(1 - \frac{h}{r} \right)^2 - 2 \left(1 - \frac{h}{r} \right) \cos \theta \right]^{3/2}} \quad (5.14)$$

5.4.3 Enhancement of the Near Wake Model

Decay Rate

The value of Φ is obviously significant in obtaining a good approximation of Eq. 5.14 using Eq. 5.12. By setting θ equal to $\pi/2$ in Eq. 5.14,

$$w_E = \int_0^{\pi/2} \frac{\Gamma \left[1 - \left(1 - \frac{h}{r} \right) \cos \theta \right] d\theta}{4\pi r \left[1 + \left(1 - \frac{h}{r} \right)^2 - 2 \left(1 - \frac{h}{r} \right) \cos \theta \right]^{3/2}} \quad (5.15)$$

it is possible to calculate an exact solution for the downwash produced by a quarter-cycle circular arc of constant vortex strength for any value of h/r . By setting the total downwash in Eq. 5.12 equal to this value, *i.e.*

$$w(N) = w_E$$

it is then possible to obtain numerically the corresponding exact value of Φ . In

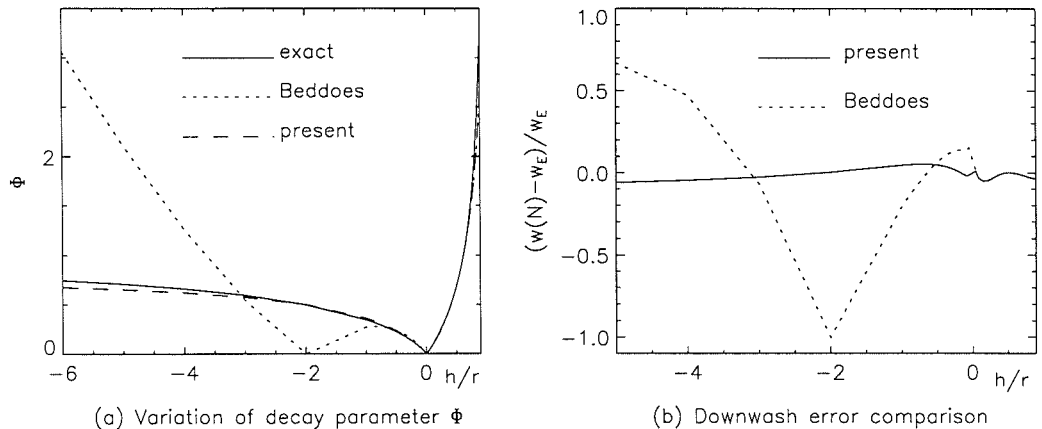


Figure 5.12: Comparison of Beddoes' original model with its modified version

Fig. 5.12(a), the variation of this exact solution for Φ with h/r is compared with Beddoes original approximation given in Eq. 5.11. It is clear that, whilst Eq. 5.11 appears to be almost identical to the exact value when $h > 0$, it bears little resemblance to the exact solution when $h < 0$. Moreover, from Eq. 5.11, Φ becomes zero when $h/r = -2$. This is clearly inappropriate and may cause numerical

difficulties in a lifting-line implementation. It is interesting to note that the loading distribution on a helicopter rotor is generally so dominated by the tip vortex system that the inappropriate nature of Beddoes Φ function for negative values of h/r , which corresponds to the influence of an inboard wake element on a point outboard, would have little effect on performance calculations. For wind turbines, however, where detailed loading distributions on the blade are significantly different from those on helicopter rotors, the errors produced by this problem can be much more significant.

On the basis of the above analysis, it was possible to develop an alternative form of the function Φ which is closer to the exact solution over a wider range of h/r . This new function has been proposed to be in the form

$$\Phi = \begin{cases} -\frac{\pi}{4} \left(1 + \frac{h}{2r}\right) \ln \left(1 - \frac{h}{r}\right) & \text{for } 0 < \frac{h}{r} < 1 \\ \frac{\ln \left(1 - \frac{h}{r}\right)}{\frac{3}{2} + \ln \left(1 - \frac{h}{2r}\right)} & \text{for } \frac{h}{r} < 0 \end{cases} \quad (5.16)$$

As may be observed in Fig. 5.12(a), this new representation is a good approximation to the exact solution over the entire range of h/r . It is identical to Eq. 5.11 over the range $0 < h/r < 1$ but differs significantly for $h/r < 0$. Fig. 5.12(b) shows the relative errors in downwash velocity, using Eqs. 5.11 and 5.16, with respect to the exact downwash from Eq. 5.15. This indicates that Eq. 5.16 should be accurate enough for general engineering use.

Tilting Angle of the Trailing Vortex Filament

As indicated above, the near wake model represents the first quarter cycle of the wake. In the original circular arc formulation, the near wake was represented by a series of arcs lying in the plane of rotation of the blade. This can provide a good approximation to a range of helicopter flight states and may also be applicable to wind turbines at high tip speed ratios. This approach becomes questionable,

however, in certain phases of helicopter flight and at low tip speed ratios on wind turbines because, in these cases, the trailing vortex filament would be expected to move well out of the rotor plane during the time period associated with a quarter revolution. In fact, even for normal wind turbine operating conditions, the inboard local speed ratio may be low enough not to ignore the out-of-plane movement of the wake. If the planar arc representation of the near wake is retained, it is convenient to consider this behaviour in terms of a tilt angle between the rotor and its near wake. This tilt angle can be particularly significant on the inboard blade sections of wind turbines where angles in excess of 45° are not uncommon.

Although the transfer velocity of the rotor wake is time-dependent, it is reasonable in most cases to adopt the planar arc assumption for the near wake. If it is assumed that the trailing filament has a constant tilt angle during the first quarter cycle and takes the value at the blade, the tilt angle is then the inflow angle at the blade element boundary point from which the wake filament trails. In the tower shadow region, the tilt angle is expressed as

$$\phi = \arctan \frac{\tilde{V} \cos \gamma + v_{z'}}{\Omega r + \tilde{V} \sin \gamma \sin \psi - v_\psi} \quad (5.17)$$

where $v_{z'}$ and v_ψ are the axial and tangential induced velocities respectively, and ψ is the blade azimuthal angle at which the current wake element trails. In this case, the current value of D_w becomes

$$D_w = \frac{\Gamma \frac{\Delta s}{h} \cos \phi}{4\pi r \left| \frac{h}{r} \right| \sqrt{1 + \left(\frac{\Delta s}{h} \right)^2}} \quad (5.18)$$

5.4.4 Application of the Near Wake Model to the Tower Shadow Problem

The manner in which the modified near wake model is incorporated within the unsteady prescribed wake calculation is best explained by consideration of the role of each element of the couple scheme.

In the present scheme, the near wake model is only applied over a quarter of the rotational cycle. This quarter cycle is chosen such that it includes the tower shadow region (see Fig. 5.13). This quarter cycle is divided into N_{ts} azimuthal intervals by $(N_{ts} + 1)$ equally-distributed points,

$$N_{ts} = \frac{\pi}{2 \Delta\theta}$$

Letting ψ_0 be the azimuthal angle of Point 0 at which the near wake model is

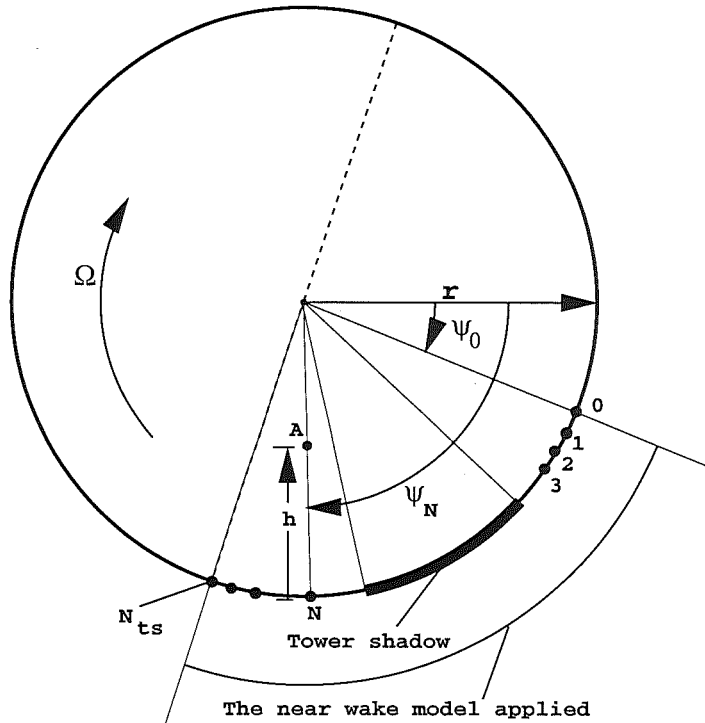


Figure 5.13: Application of the near wake model to tower shadow problem

initiated, the azimuthal angle of the current sample in the quarter cycle under consideration is

$$\psi_N = \psi_0 + N \Delta\theta$$

where $N = 1, 2, \dots, N_{ts}$. Thus, the current value of D_w is a function of the azimuth for a given vortex filament, a given evaluation point and a constant $\Delta\theta$,

$$D_w = D_w(\psi_N)$$

Then, the current downwash at the blade element control point A (see Fig. 5.13) due to the trailed vorticity in the near wake can be calculated from

$$\left\{ \begin{array}{l} w(N) = X_w(N) + Y_w(N) \\ X_w(N) = X_w(N-1) \exp\left(-\frac{\Delta\theta}{\Phi}\right) + 1.359 D_w(\psi_N) \exp\left(-\frac{\Delta\theta}{2\Phi}\right) \\ Y_w(N) = Y_w(N-1) \exp\left(-4\frac{\Delta\theta}{\Phi}\right) - 0.359 D_w(\psi_N) \exp\left(-2\frac{\Delta\theta}{\Phi}\right) \\ N = 1, 2, \dots, N_{ts} \end{array} \right. \quad (5.19)$$

In order to implement the above recursive procedure, the initial values $X_w(0)$ and $Y_w(0)$ must be determined. They may be obtained by applying the near wake model to Point 0 whose azimuthal angle is ψ_0 (as shown in Fig. 5.13). Numerically, it is important that the transition between the prescribed wake and near wake models is seamless to avoid instabilities when the Leishman–Beddoes unsteady model is applied. Therefore, the downwash $w(0)$ at Point A obtained from the near wake model must be equal to the downwash at the same point, w_{pwm} , obtained from the prescribed wake model due to the first quarter cycle of the trailed wake filament,

$$w(0) = w_{pwm}$$

It should be noted here that the downwash is opposite in direction to the induced velocity v_z calculated from the prescribed wake model. Applying the near wake model to the initial point 0 allows the ratio of the terms $Y_w(0)$ to $X_w(0)$ to be written as

$$K_w = \frac{-0.359 \exp\left(-2\frac{\Delta\theta}{\Phi}\right) \sum_{N=1}^{N_{ts}} D_w\left(\psi_N - \frac{\pi}{2}\right) \exp\left[-4(N_{ts} - N)\frac{\Delta\theta}{\Phi}\right]}{1.359 \exp\left(-\frac{\Delta\theta}{2\Phi}\right) \sum_{N=1}^{N_{ts}} D_w\left(\psi_N - \frac{\pi}{2}\right) \exp\left[-(N_{ts} - N)\frac{\Delta\theta}{\Phi}\right]}$$

This information is then used to determine the initial values $X_w(0)$ and $Y_w(0)$,

$$X_w(0) = \frac{w_{pwm}}{1 + K_w}$$

$$Y_w(0) = \frac{K_w w_{pwm}}{1 + K_w}$$

In this way, the near wake and prescribed wake models are smoothly coupled at the domain boundary.

Once $X_w(0)$ and $Y_w(0)$ are known, the near wake scheme can begin stepping around the azimuth from $N = 1$ to $N = N_{ts}$ and updating the downwash in the manner described in Eq. 5.19. It should be noted that the calculations of the near wake model are added to the induced velocity from the far wake which is provided by the prescribed wake scheme at low azimuthal resolution. The intermediate values of the far-wake induced velocity, which are small compared with those from the near wake, are obtained by linear interpolation. The near-wake value w_{pwm} from the prescribed wake scheme is also obtained by interpolation. The time step, or sampled time interval, for the near wake model is equivalent to a half degree azimuth increment in this study,

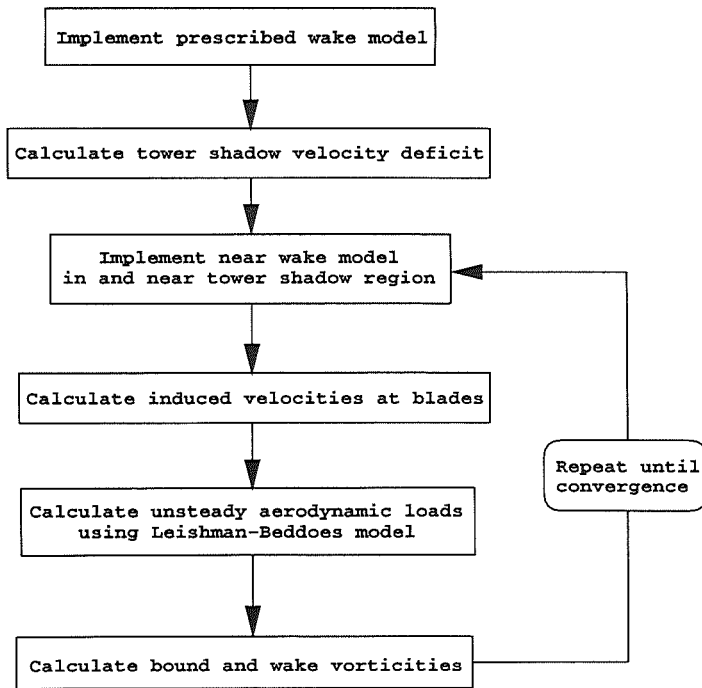


Figure 5.14: Numerical flow chart with tower shadow effects

Before the near wake model is used, a converged solution, which includes the

velocity deficit in the tower shadow region due to Eq. 5.3, is computed by the prescribed wake model using steady aerodynamic blade section data. Based on the aerodynamic information from the prescribed wake model, the near wake model is implemented to provide high resolution in and near the tower shadow region. Finally, the resulting velocity and incidence variations are input to the Leishman–Beddoes dynamic stall model which has been modified with 3-D rotational effects in Section 4.3. This enables an iteration loop to be implemented which produces converged 3-D unsteady aerodynamic results. The whole numerical procedure is illustrated in Fig. 5.14.

5.4.5 Results and Discussion

In this section, the high resolution calculations will be compared with the relative NREL UAE field data to validate the modelling of tower shadow effects. In addition, the high resolution calculations will be compared with low resolution results to illustrate the improvement of the high resolution model in the calculation of tower shadow effects.

Fig. 5.15 shows contours of C_n calculated at high resolution in the tower shadow region for the NREL UAE Phase II turbine in a head-on flow. The tower shadow effects are clearly demonstrated in this figure. It is interesting to note that the C_n distribution is not symmetrical about the central line of the tower shadow even for this steady axial freestream case. This is attributed to the unsteady effects produced by the blade passing in and out of the tower shadow. The calculated force and moment coefficient variations around a full cycle of the rotor at four spanwise locations for this unyawed case are presented in Fig. 5.16. In effect, this figure is directly comparable to Fig. 5.5 in which the same conditions, *i.e.* tower shadow width $B_t = 2.5D$ and maximum velocity deficit $D_V = 0.3$, are applied to the low resolution method. The main difference between Figs. 5.16 and 5.5 lies in the predicted tower shadow response. In general, the shape and scale of the change

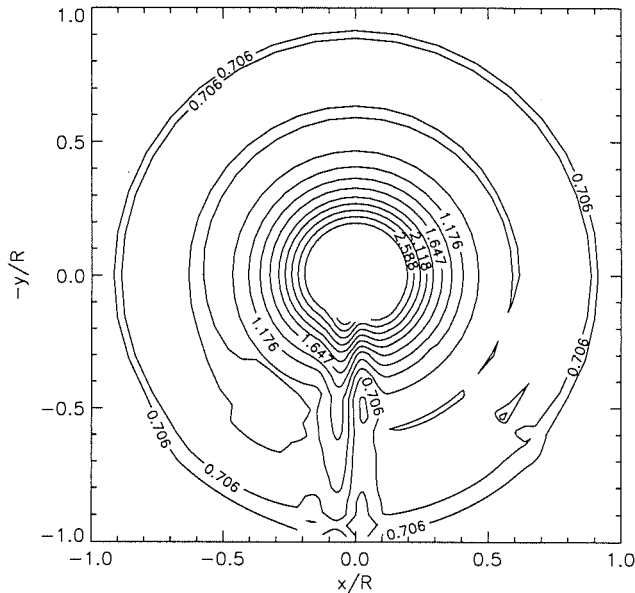


Figure 5.15: Contour of the normal force coefficient calculated with high resolution ($D_V = 0.3$, $B_t = 2.5D$) for the NREL UAE Phase I turbine at $V_0 = 12.5$ m/s and $\gamma = 0.4^\circ$

in the aerodynamic loads through the tower shadow region are better represented by the high resolution model. It does, however, exhibit an overshoot during the recovery phase which is not apparent in the field data. The results for yawed cases from the high resolution model are presented in Figs. 5.17 through 5.20, and can be compared with their low resolution counterparts in Figs. 5.7 through 5.10. These figures exhibit the same general trend as the head-on flow case.

The difference between the simple low resolution and sophisticated high resolution models can more clearly been seen in Figs. 5.21 and 5.22 where the calculated results in the tower shadow region corresponding to Figs. 5.19 and 5.9 are presented in isolation. In Fig. 5.21, the blade incidence variations through the tower shadow region predicted by the high resolution model are compared with those from the low resolution scheme at four blade span locations. The figure serves to highlight one of the major problems associated with the simple low resolution approach to tower shadow modelling. The curves of angle of attack calculated with high resolution (0.5° azimuth step) are smooth. By contrast, the results with low

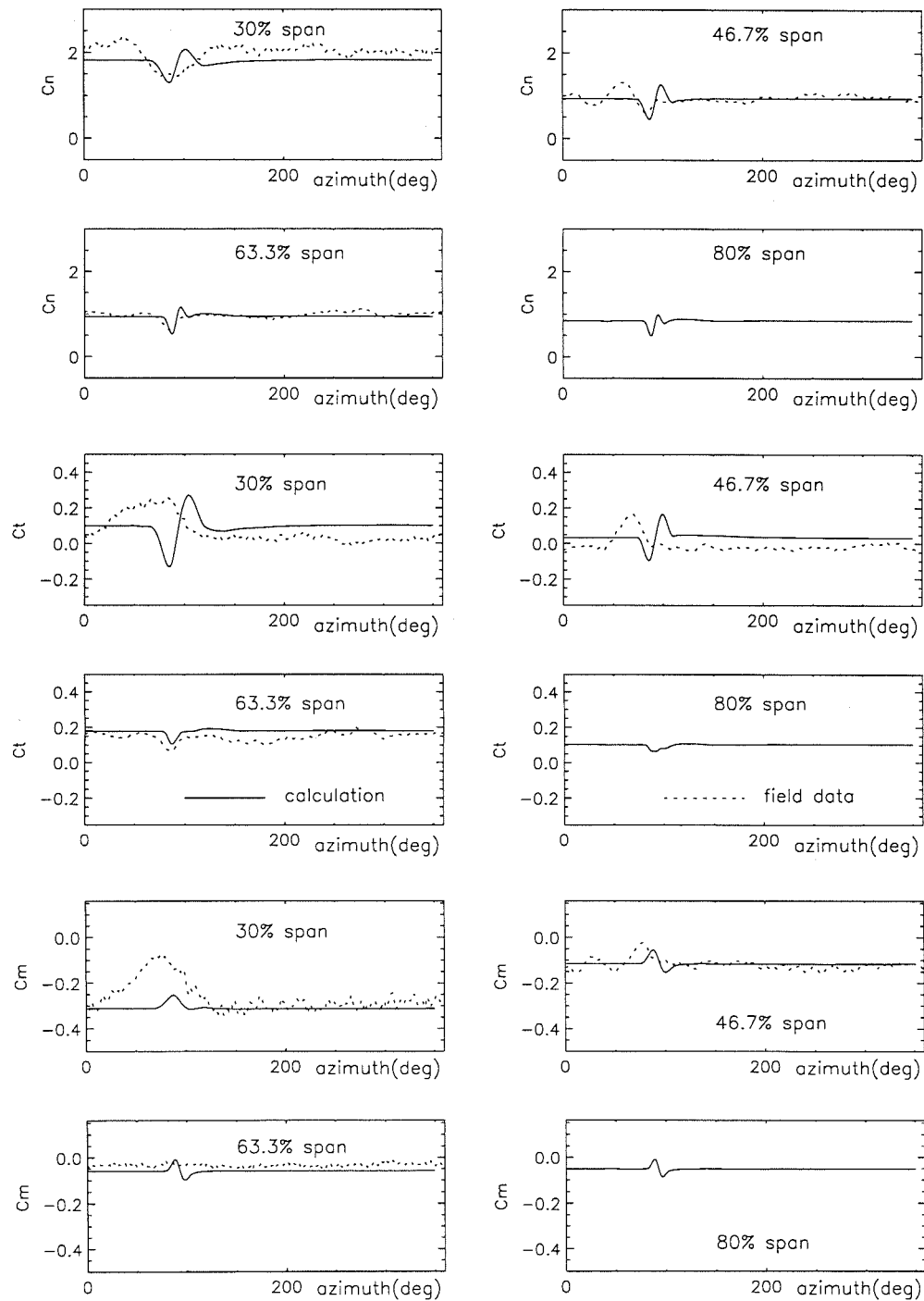


Figure 5.16: Comparison of high resolution calculation ($D_V = 0.3$, $B_t = 2.5D$) with field data of NREL UAE Phase I at $V_0 = 12.5$ m/s and $\gamma = 0.4^\circ$

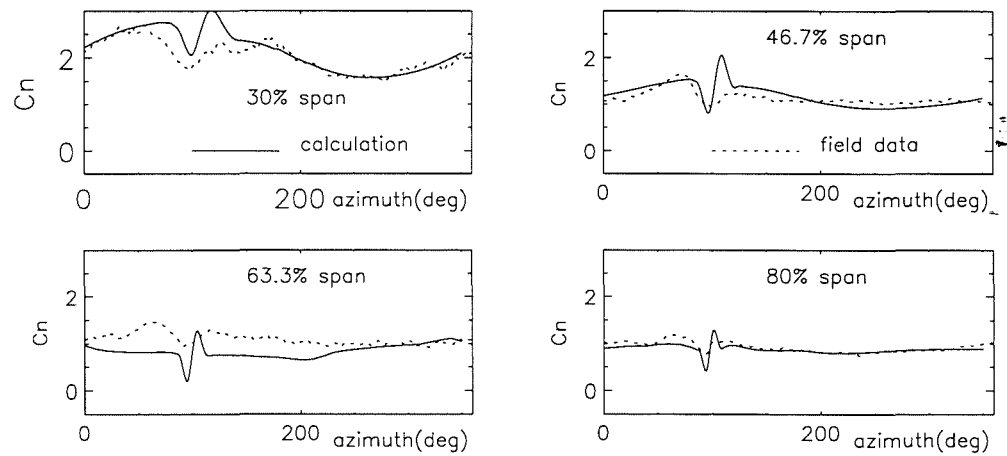


Figure 5.17: Comparison of high resolution calculation ($D_V = 0.3$, $B_t = 2.5D$) with field data of NREL UAE Phase I at $V_0 = 15.9 \text{ m/s}$ and $\gamma = -17.2^\circ$

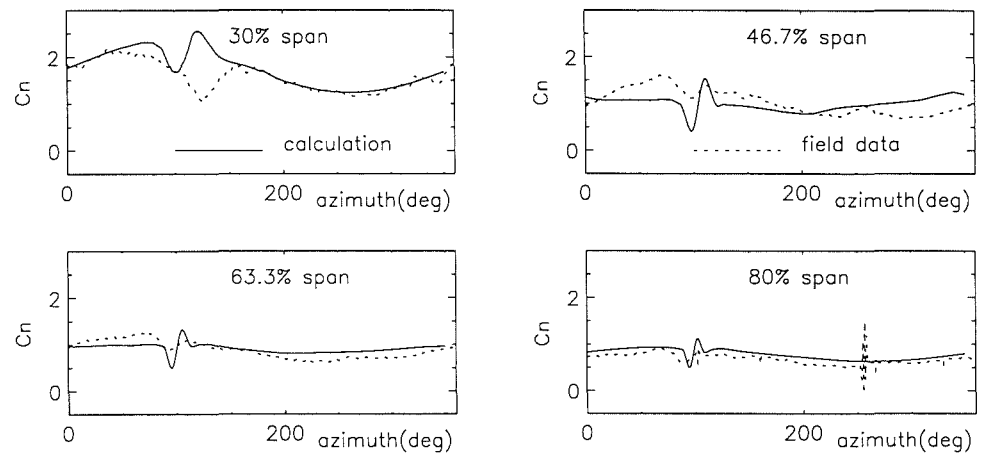


Figure 5.18: Comparison of high resolution calculation ($D_V = 0.3$, $B_t = 2.5D$) with field data of NREL UAE Phase I at $V_0 = 12.5 \text{ m/s}$ and $\gamma = -19.7^\circ$

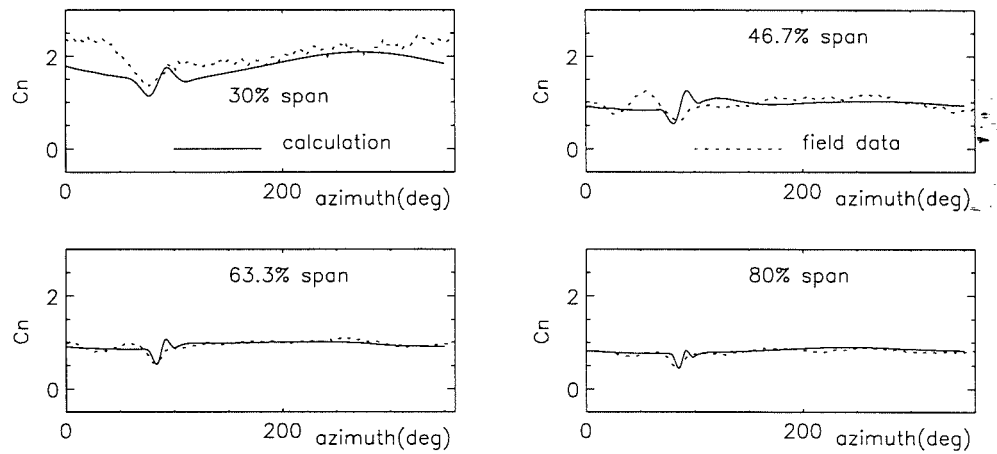


Figure 5.19: Comparison of high resolution calculation ($D_V = 0.3, B_t = 2.5D$) with field data of NREL UAE Phase I at $V_0 = 12.3$ m/s and $\gamma = 9.9^\circ$

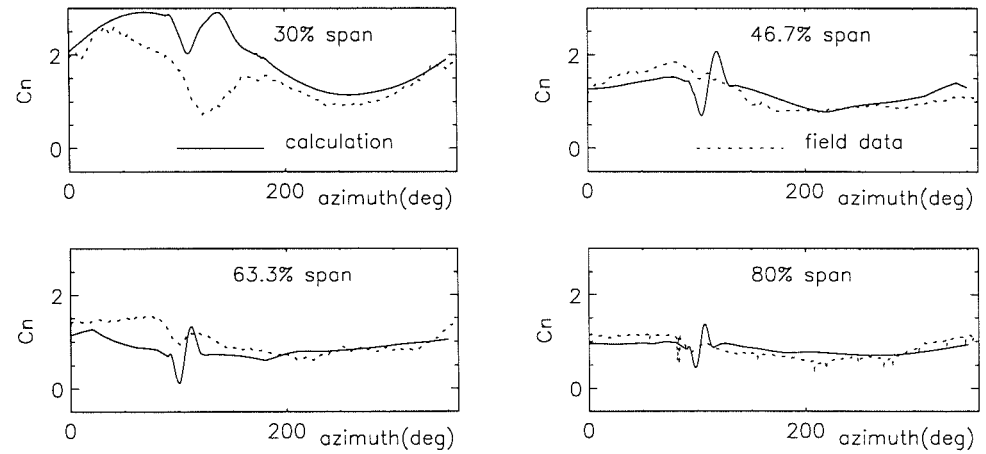


Figure 5.20: Comparison of high resolution calculation ($D_V = 0.3, B_t = 2.5D$) with field data of NREL UAE Phase I at $V_0 = 15.9$ m/s and $\gamma = -30.1^\circ$

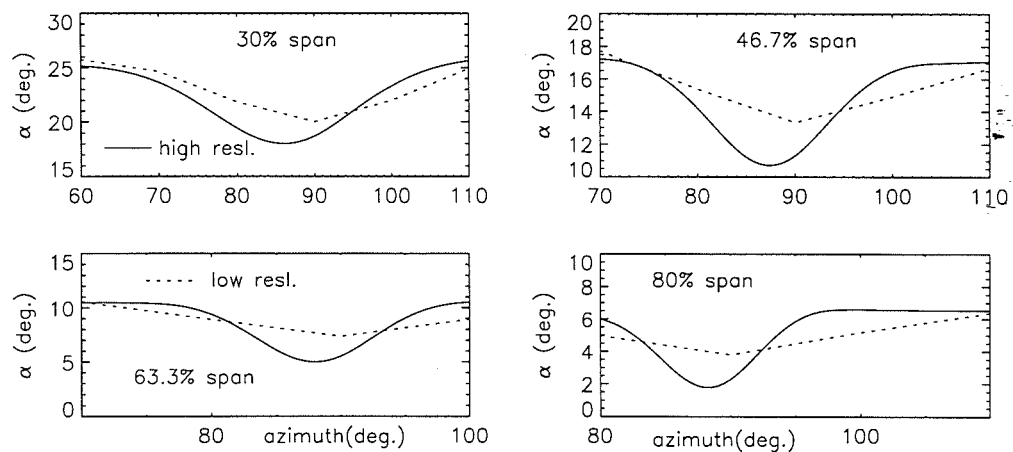


Figure 5.21: Variation of angle of attack around tower shadow region ($D_V = 0.3$, $B_t = 2.5D$) for the NREL UAE Phase I turbine at $V_0 = 12.3$ m/s and $\gamma = 9.9^\circ$

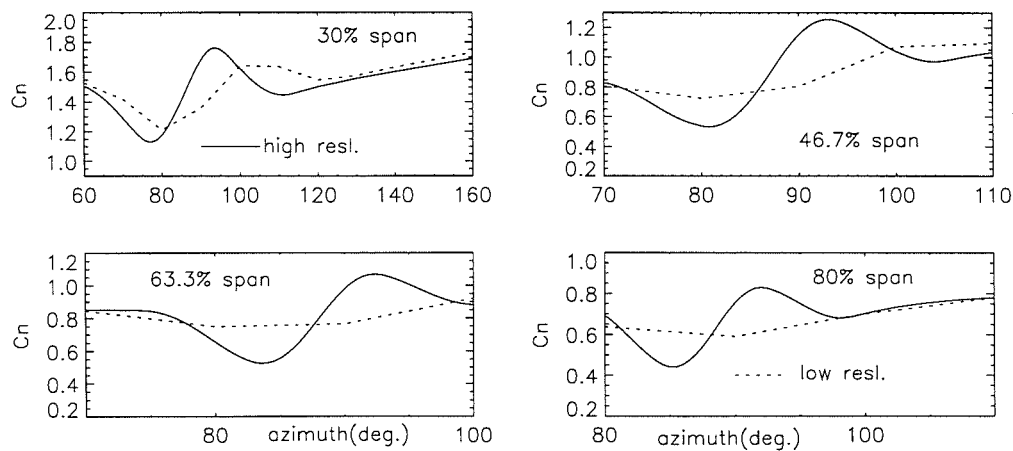


Figure 5.22: Comparison of C_n around tower shadow region with and without high resolution ($D_V = 0.3$, $B_t = 2.5D$) for the NREL UAE Phase I turbine at $V_0 = 12.3$ m/s and $\gamma = 9.9^\circ$

resolution (10° azimuth step) are rather jagged. An additional feature of the figure is the slight azimuthal offset in minimum incidence between the two sets of results which arises, primarily, from the discretisation step used in the low resolution case. It is immediately obvious that the corresponding normal force coefficients from the high resolution model in Fig. 5.22 are also smooth when compared with the simpler scheme. It is also obvious that the general shape of the curves are different. This can be attributed to strong impulsive loads which are predicted by the Leishman–Beddoes unsteady aerofoil model when applied in conjunction with the near wake model. The impulsive normal force strongly depends on the time rate of change of incidence, $\dot{\alpha} = d\alpha/dt$. In particular, it has been established that the parameter which characterises the dynamic response of an aerofoil during pitching motion is its reduced pitch rate, $\dot{\alpha}c/(2V_\infty)$. By consideration of Fig. 5.21, in which the change in incidence during tower shadow is presented, the reduced pitch rates experienced by the blades are of the order of 0.055. This is extremely high and, consequently, strong impulsive components would generally be expected in the aerodynamic response of the blade.

In the cases where the flow over the blade is predominantly separated, it has been shown that wake inertia can significantly change the aerodynamic response (Green and Galbraith 1994). At present, the Leishman–Beddoes model cannot reproduce this particular effect. This may go some way towards explaining the discrepancies between the model and the field data. However, other numerical results for tower shadow effects also show an overshoot in the aerodynamic force during the blade passing out of the tower shadow, such as the result presented in Fig. 1.11 which is reproduced from the work of Duque *et al.* (1999). The experimental results of Graham and Brown (1999) also show a strong impulsive pressure response to the tower shadow effect when the flow around the blade section is separated. This kind of strong impulsive response is not apparently viewed in the NREL UAE field data presented in this study. One of the reasons may be the manner in which the measured data were azimuth-averaged due to wide-ranging variations in wind speed and yaw angle during the collection of the data. This

might suppress, to some extent, extreme variations in the aerodynamic response. Nevertheless, more experimental and theoretical studies are needed to validate the tower shadow model.

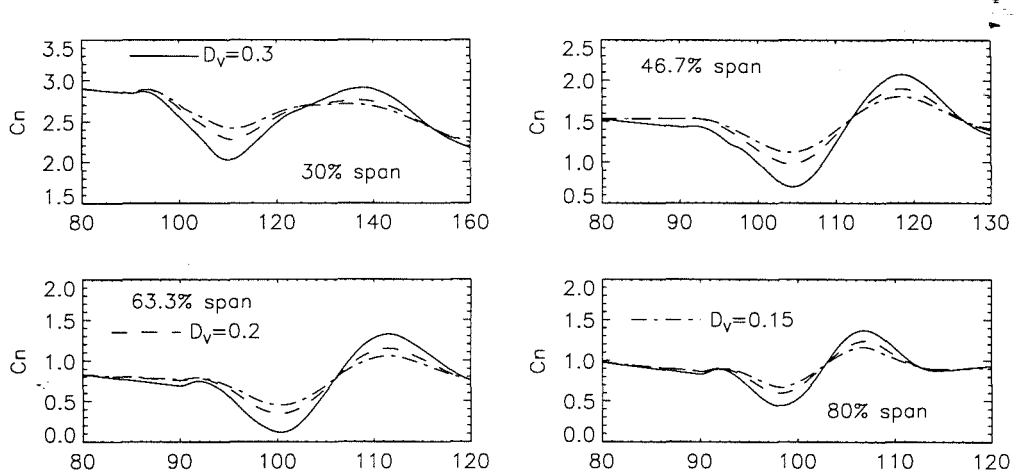


Figure 5.23: Effects of tower shadow velocity deficit ($B_t = 2.5D$) for the NREL UAE Phase I turbine at $V_0 = 15.9$ m/s and $\gamma = -30.1^\circ$

As discussed previously, the velocity profile behind the support tower depends largely on the Reynolds number based on the diameter of the tower. In general wind turbine operating conditions, the tower velocity deficit decreases with increasing Reynolds number. This deficit change will inevitably have effects on the loading response of the blade passing through the tower shadow. An attempt to study this effect is shown in Fig. 5.23 where the variations of the normal force coefficients with the maximum velocity deficit D_V in the tower shadow region, for a freestream velocity of 15.9 m/s and a yaw angle of -30.1° , are presented. Notably, the overshoots in C_n are reduced as D_V is decreased. So too, however, are the corresponding reductions in C_n as the blade passes into the tower shadow. It is unlikely, therefore, that the differences between the calculations and the field data can be explained on the basis of the magnitude of the velocity deficit alone.

Another parameter which may influence the calculations is the width of the tower shadow region which, again, depends on Reynolds number. Fig. 5.24 demon-

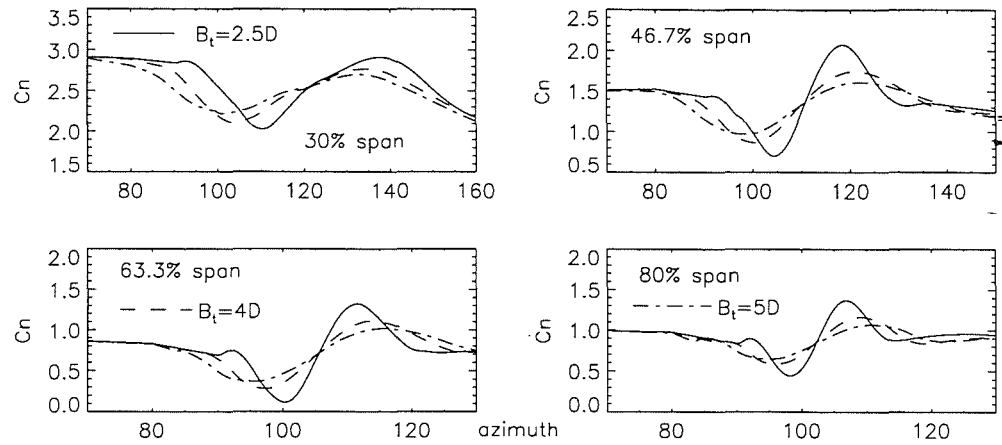


Figure 5.24: Effects of tower shadow width ($D_V = 0.3$) for the NREL UAE Phase I turbine at $V_0 = 15.9$ m/s and $\gamma = -30.1^\circ$

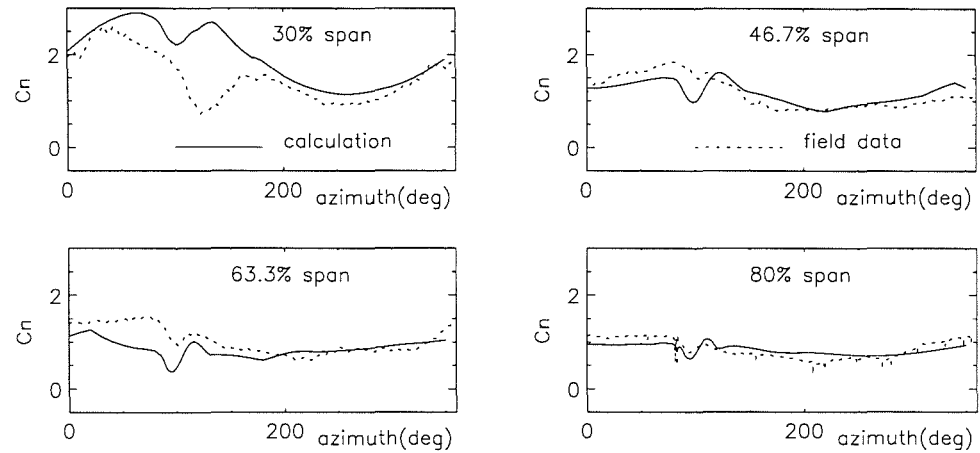


Figure 5.25: Comparison of high resolution calculation ($D_V = 0.3$, $B_t = 5D$) with field data of NREL UAE Phase I at $V_0 = 15.9$ m/s and $\gamma = -30.1^\circ$

strates the effect of the tower shadow width on the blade C_n for a maximum velocity deficit $D_V = 0.3$. According to the wind tunnel test results of Snyder and Wentz (1981), the width B_t of the shadow behind the NREL UAE tower ($D = 0.406$ m and $Z_t = 1.32$ m) should be approximately equal to $2.5D$ for a wind speed of 15.9m/s ($R_e = 4.4 \times 10^5$). The results calculated with $B_t = 2.5D$ (Fig. 5.20), however, reveal that this shadow width seems somewhat small compared to the field data. By increasing the shadow width, the general form of the calculation appears to move closer to the experiment (comparing Fig. 5.25 with Fig. 5.20). This does not cast doubt on the results from the wind tunnel test carried by Snyder and Wentz (1981), but merely emphasises the potential sensitivity of the tower wake structure to the flow environment.

It seems that the azimuth shift in the calculated tower shadow effects for low resolution cases, mentioned previously in Section 5.3.2, has been reduced by the high resolution model especially for relatively low yaw angle cases. However, the azimuth offset in the tower shadow location between the high resolution calculation and the field data becomes apparent when the yaw angle is increased (see Figs. 5.18 and 5.20). It is particularly interesting that this shift appears to vary with span position. This could be related to the different physical blockage created by the blade/tower combination in each case or to the effect of swirl on the velocity deficit region. This requires further investigation.

5.5 Conclusions

Calculations of the aerodynamic response of a wind turbine blade, due to the velocity deficit produced by a support tower, have been presented. Two different modelling strategies have adopted, both of which are based on a prescribed velocity deficit in the tower shadow region. In the first method, the velocity deficit is simply applied to the onset flow within the prescribed wake model. This significantly distorts the wake structure behind the blade and substantially modifies the blade

incidence and velocity variations through the tower shadow region. Unfortunately, this approach is compromised by the trade-off between efficient computation and the increased azimuthal resolution required to adequately represent the unsteady response of the blade; so much so that the computational overhead associated with accurate dynamic calculations in the tower shadow region is prohibitive. An alternative strategy has been developed which involves the use of an efficient near wake model of the vorticity trailed from the blade. This near wake model is integrated into the prescribed wake method to produce a hybrid scheme capable of predicting global turbine performance characteristics, together with the detailed high resolution unsteady response in the tower shadow region. The computational cost introduced by the high resolution near wake model is almost negligible.

Comparisons of the calculated results with the field data show a reasonable level of agreement. Discrepancies exist mainly when the blade experiences very high angles of attack where the aerodynamic forces are difficult to accurately predict even though 3-D effects are included. The predictions also appear to overstate the impulsive response of the blade at exit from the tower shadow region. The reason for this is not entirely clear, although some deficiencies in the unsteady aerofoil model may contribute to the problem. It is worthy of note that the Leishman-Beddoes unsteady model aerofoil model was developed as a reconstruction algorithm and, generally, requires to be tuned to specific applications. Configuration of the model to the specific characteristics of wind turbine blades will provide a focus for future work. The high turbulence in the shadow and the vortex shedding from the tower into the shadow, which are not represented in the model, should also contribute to the difference between calculation and experiment. On the other hand, the NREL UAE field data and the associated datum acquisition methods should be examined in detail because other numerical and experimental results in some cases also show a strong overshoot in the blade response to the tower shadow which is not apparent in the azimuth-averaged NREL field data.

Chapter 6

A Preliminary Study of the Numerical Simulation of HAWTs Operating in a Wind Tunnel

6.1 Introduction

As documented in Section 1.2.6, experimental studies of wind turbine aerodynamic performance are usually carried out by two means, *i.e.* operation in the field and tests in wind tunnels. Wind tunnels provide a well-controlled flow environment where a variety of tests, such as the measurement of the power output from the turbine and the aerodynamic loads on the turbine and its blades as well as determination of the turbine wake through flow visualisation, can be conducted. Model designers, usually, prefer larger, even full-scale, models so that more details can be incorporated into the model. However, as the size of wind tunnels increase, they become more expensive to build and more costly to operate. On the other hand, model size should be kept as small as possible for minimum wall interference in a given wind tunnel. Therefore, there is always a compromise necessary between requirements of the model designer and the wind tunnel operator and, in many cases, the effect of the wind tunnel walls is not negligible.

There is certainly an increasing awareness that, for many flow problems, different experimental results can sometimes be produced in different wind tunnels with the same model. This is particularly true in cases involving flow separation. This kind of problem highlights the difficulties in attempting to validate calculation models by means of comparison with experimental results. It has become almost traditional to attribute the lack of agreement between calculation and experiment, fully or partly, to the so-called *wind tunnel wall effects*. The most obvious interference between the wind tunnel walls and the test model is the solid blockage, which increases the local velocity at the test section to a higher value than it would be in an unconstrained free flow. In addition, there is a reflection effect that changes the angle of attack to lifting surfaces of the model near solid boundaries, as in the case of ground effect. Rae and Pope (1984) recommend that the maximum model frontal area should not exceed 7.5% of the test section area and list a variety of wall interference correction methods for normal tests which are mainly semi-empirical.

For wind tunnel testing of wind turbines, the tunnel wall/model interaction is even more complicated and the wall interference may be very large. The diameter of the wind turbine model is usually of the same order as the test cross section. The turbine expanding wake produces serious blockage and the vortices, trailed and shed from the rotor into the wake, interact significantly with the tunnel wall. For such cases, it seems unreasonable to expect that wind tunnel wall interference can accurately be evaluated using the classical methods due to their overly simplifying assumptions.

In recent years progress has been made in numerical methods based on the use of measurements of the flow at or near the walls (Ashill 1994). The wall pressure signature methods have been used to estimate the wind tunnel wall interference with the wind turbine (Ronsten *et al.* 1995, Ronsten 1992, Ronsten *et al.* 1989, He and Jiang 1989). However, experience with these methods remains limited and many problems with these methods need to be overcome. For wind turbine tests, the distribution of the pressure taps on the wall is particularly problematic because the wind turbine performance not only depends on the flow near the model but is

also influenced by the wake.

The boundary integral approach of panel methods offers great versatility for practical applications to complicated configurations and is considerably more efficient than finite-difference and finite-element methods in terms of computational effort. Panel methods have been used to model wind tunnel wall interference in 2-D aerofoil and 3-D wing wind tunnel tests (Lee 1981, Holt and Hunt 1982, Mokry *et al.* 1987, Cheung and Hancock 1988, Browne and Katz 1990) and in non-aeronautical tests (Mokry 1995). With panel methods it is possible to adequately model wind tunnel wall effects on wind turbine performance.

In this study, the constrained effects due to the wind tunnel walls on the HAWT flow and performance are numerically examined. The 3-D wind tunnel walls are modelled as a series of panels on which source singularities are distributed. As a preliminary study, a low order panel method is used due to its simplicity and applicability to wind tunnel wall modelling. The wind turbine and its flow are represented by the prescribed wake model that has been well established in the previous chapters. The coupling of these two schemes allows the wind tunnel walls to interact with the turbine rotor and its wake. The numerical results are presented and compared with measurements. The principal features of the combined model are discussed and possible future improvements to the method are recommended.

6.2 Panel Method

6.2.1 Introduction

The advent of powerful computers has led to the development of various numerical methods for fluid computation and analysis. One of the frequently used approaches is the so-called panel method. Panel methods are theoretically capable of providing *nominally* exact solutions for the hypothetical aerodynamic case of incompressible and inviscid flow. In practice, the method can also give very useful results for

compressible and viscous flow (Hunt 1978, Butter *et al.* 1982).

For a flow over a 3-D body, the geometry of the body is represented by a series of panels in the panel method (Fig. 6.1). These panels are usually quadrilaterals,

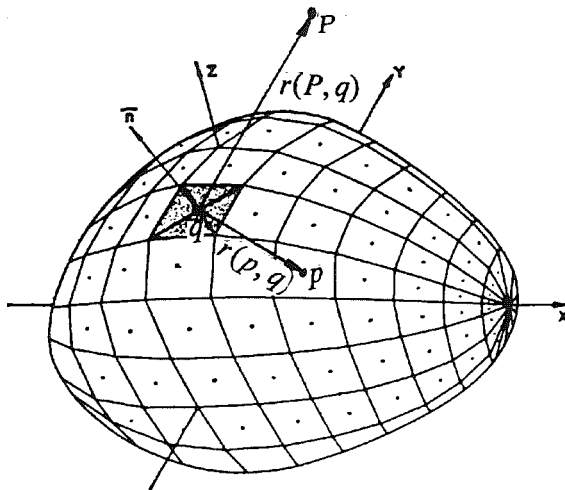


Figure 6.1: Approximation of the body surface by panel elements

although more complex geometries can be used. The flow over the body is then simulated by placing singularities at the control point or collocation point of each panel to represent the flow field around the body. Thus, the “unknowns” are situated only on the surface of the configuration rather than throughout the external space. This provides the principal advantage of the methods over alternative techniques such as finite difference, finite element, etc. The flow singularities may be sources, doublets, vortices or any combination of these. The singularity can be distributed with constant strength across a panel (a low order panel method) or with some linearly or quadratically varying strength across the panel (a high order panel method). Because only source panels are used to model the wind tunnel wall effects in this study (see Section 6.3), only aspects of the source panel method are dealt with in the following discourse.

In the case of uniform source density on each panel, the influence induced at any point by a particular panel is simply proportional to the (unknown) source density on that panel. In the case of high order scheme, the formulation of the

approach is more complex. For example, the influence of a single panel in this case involves not only terms proportional to the singularity strength of that panel but also terms proportional to the various derivatives of that strength. Therefore, high order panel methods require significantly longer computational times than low order schemes and care must be taken for high order panel methods to ensure that all the panels match up exactly because the singularity strength must be continuous across panels.

There are extensive reviews about the relative advantages and disadvantages of low and high order panel methods relating to the accuracy and required computational time (Maskew 1982, Hess 1990). In recent years, with the development of powerful computers capable of handling an ever larger number of panels, there has been a tendency towards low order methods since low order panel methods, if properly formulated, can yield accuracy levels comparable to higher order methods even for comparable panel densities (Maskew 1982).

The theory and numerical approach of panel methods have been well documented by Hess and Smith (1967), Katz and Plotkin (1991) and Hunt (1978). Only a brief introduction to the source panel method is provided here.

6.2.2 Integral Equation for a Source Distribution on the Body Surface

It is well known (Lamb 1932) that any quantity in a potential flow satisfying Laplace's equation may be expressed as an integral over the body boundary surface of a source distribution σ per unit area and a doublet distribution μ per unit area. In this case, the disturbance potential at any point P due to the body may be written as

$$\varphi(P) = \iint_{body} \left\{ \frac{-\sigma(q)}{r(P, q)} + \mu(q) \frac{\partial}{\partial n} \left[\frac{1}{r(P, q)} \right] \right\} dS + \iint_{wake} \mu(q) \frac{\partial}{\partial n} \left[\frac{1}{r(P, q)} \right] dS \quad (6.1)$$

where $r(P, q)$ is the distance from the point P where φ is evaluated to an integration point q on the surface of the body or wake shed from the body, and n denotes the

outward direction normal to the surface of the body or wake.

In Eq. 6.1, the terms related to the doublet distributions account for the lifting problem. Thus, for the model of the wind tunnel walls, only the source distribution on the surface S of the body is concerned,

$$\varphi = - \iint_S \frac{\sigma(q)}{r(P, q)} dS \quad (6.2)$$

The zero-normal velocity boundary condition on the surface S can be expressed as

$$(\mathbf{V}_0 + \nabla\varphi) \cdot \mathbf{n} = 0 \quad (6.3)$$

where \mathbf{n} is the unit outward normal vector at any point on S . Applying this boundary condition requires evaluation of the spatial derivatives of the disturbance potential on the surface S . Care must be taken here because the derivatives of $1/r(P, q)$ become singular as the point P approaches the surface. The development of a limiting process for this case has been given in many reference sources (*e.g.* Hunt 1978) and the application of this limiting process allowing the point P to approach a point p on the surface S leads the boundary condition Eq. 6.3 to

$$2\pi\sigma(p) - \iint_S \sigma(q) \frac{\partial}{\partial n} \left[\frac{1}{r(p, q)} \right] dS = -\mathbf{n}(p) \cdot \mathbf{V}_0 \quad (6.4)$$

where $\partial/\partial n$ denotes differentiation in the direction of the outward normal to the surface S at the surface point p , and the unit outward normal vector has been written as $\mathbf{n}(p)$ to show explicitly its dependence on location. Solution of Eq. 6.4 is the central task in the present source panel method.

6.2.3 Numerical Source Panel Method

One of the basic concepts in panel methods is the use of panels to represent the body in question. The distribution and total number of the surface panel elements determine the accuracy of the resulting calculations.

Once the surface is broken up into panels (see Fig. 6.1), Eq. 6.4 can be written in discretised form, breaking the whole body surface integral up into surface integrals

over each panel. If a constant strength source distribution over each panel is assumed (*i.e.* a low order panel method), the source strengths can be factored out of the integrals. The surface integrals on each panel are summed for all panels to give a set of simultaneous linear equations to be solved for the unknown source strength on each panel. This set of equations may be written as

$$\left\{ \begin{array}{l} \sum_{j=1}^N A_{ij} \sigma_j = -\mathbf{n}_i \cdot \mathbf{V}_0 \\ i = 1, 2, \dots, N \end{array} \right. \quad (6.5)$$

where N is the number of panels, σ_j the source strength on the j th panel, \mathbf{n}_i the unit vector outward normal to the i th panel, and A_{ij} the velocity influence coefficient per unit source strength for the j th panel acting on the control point of the i th panel,

$$A_{ij} = \begin{cases} 2\pi & \text{if } i = j \\ -\iint_j \frac{\partial}{\partial n_i} \left[\frac{1}{r(i,j)} \right] dS & \text{if } i \neq j \end{cases}$$

Although the formulation of the influence coefficients is complex, it is fortunately analytical for quadrilateral panels. The derivations of the influence coefficients and the formation of the influence coefficient matrix are comprehensively detailed by Hess and Smith (1967) and by Katz and Plotkin (1991).

Two approaches can be applied for the solution of the large system of equations presented by Eq. 6.5. These are a direct solution and an iterative solution. The direct solution, usually based on the Gaussian elimination method, is a reliable approach but, it becomes time-consuming as the number of panels employed is large since the computational time for a direct solution of N linear equations is approximately proportional to N^3 . Therefore, the iterative technique is usually used in the case of a large number of unknowns since the iterative approach requires much less computational overhead than the direct method. If the k th approximation of the solution σ_i in Eq. 6.5 is denoted σ_i^k , the iterative procedure may then expressed as

$$\sigma_i^{k+1} = \frac{1}{A_{ii}} \left(-\mathbf{n}_i \cdot \mathbf{V}_0 - \sum_{j=1}^{i-1} A_{ij} \sigma_i^{k+1} - \sum_{j=i+1}^N A_{ij} \sigma_i^k \right) \quad (6.6)$$

where $i = 1, 2, \dots, N$. This iterative method is commonly known as the Gauss-Seidel method. The matrix of influence coefficients A_{ij} is well conditioned for general configurations (Hess and Smith 1967) and therefore the iterative process described by Eq. 6.6 can yield a converged solution.

Once all source strengths are obtained, the disturbance velocity at a spatial point due to these panels can be calculated. This is done in exactly the same way as for the disturbance velocity at a panel control point, but the evaluation point now rests off the body surface.

6.3 Numerical Model of Wind Tunnel

In this study, the Handley Page wind tunnel at the University of Glasgow was chosen to be modelled by panels. The reason for this choice is that a series of tests have been conducted in this wind tunnel on a small wind turbine using laser sheet visualisation (LSV) and particle image velocimetry (PIV) to study the wake structure. These tests provided a basis for examination of the numerical wind tunnel wall interference model by comparing the model with the experiment. The wind tunnel is a closed circuit design and has an octagonal $2.13\text{ m} \times 1.6\text{ m}$ working section. Fig. 6.2 gives the plan view of this low speed wind tunnel.

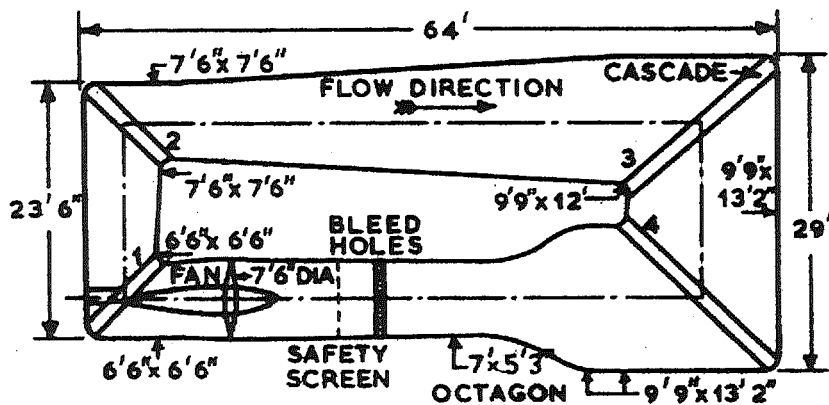


Figure 6.2: Illustration of the Glasgow University $2.13\text{ m} \times 1.6\text{ m}$ low speed wind tunnel

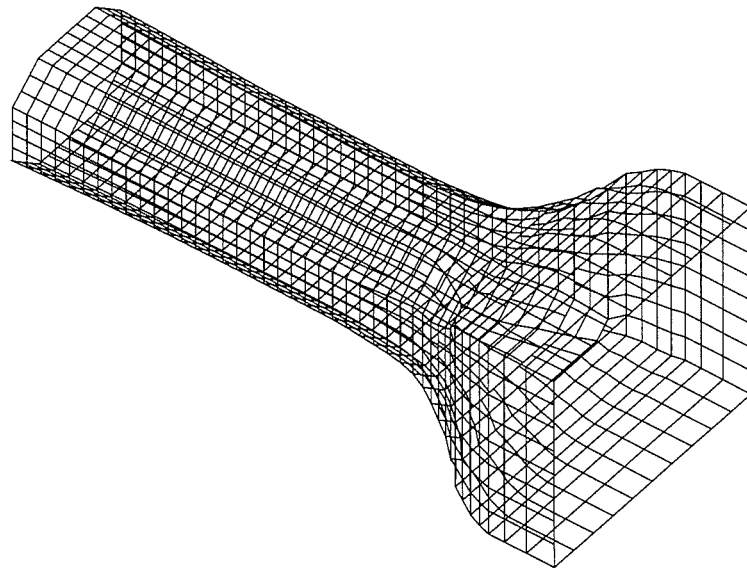


Figure 6.3: Panel discretisation of the wind tunnel settling chamber, contraction, working section and diffuser

The wind tunnel was discretised into a number of panels on which singularities could be distributed. For the purpose of this study, only the settling chamber, contraction, working section and diffuser were modelled using 1364 individual quadrilateral panel elements (Fig. 6.3). This representation gave sufficient distance upstream of the wind turbine location to ensure accurate prediction of the wall effects there, and extended far enough downstream to allow the vortex system trailed and shed from the turbine to convect out of the working section and through the diffuser, which is just prior to the fan section where the vortex system would be totally disrupted by the fan system. Due to the simple geometry of the modelled portion of the wind tunnel and the non-lifting nature of the body, plane

quadrilateral panels and a source distribution with constant strength on each panel were considered suitable and sufficient for this case.

The panels do not have to be of the same size or to form a uniform geometry. However, the panel distribution along the longitudinal direction of the wind tunnel must be carefully arranged in order to achieve optimal modelling accuracy. A non-uniform distribution of the panels was used. In particular, panels were concentrated in the region of the contraction (area of high curvature), where flow leakage would be large, and the working section, where the turbine model would be situated. Each panel consists of four corner points which have 3-D coordinates. From these points the centroid, which is chosen as the panel control point or collocation point, is calculated by simply determining the intersection of the two diagonals of the quadrilateral. A transformation is used to transform from the wind tunnel coordinate system into a panel-based coordinate system, thus enabling the influence coefficients due to the source panels to be determined.

6.4 Combination of the Prescribed Wake Model and Panel Method

Having modelled the wind tunnel walls as a series of source panels, the wall effects on the flow around the wind turbine tested in the tunnel may be examined by combination of the panel method and the prescribed wake method. The source strength on each panel depends on the boundary condition imposed on the tunnel walls. This boundary condition is greatly influenced by the turbine flow. In this study, the wind turbine aerodynamic performance in the constrained flow is still calculated by the prescribed wake model but the wall interference is taken into account. The associated numerical procedure is described below.

6.4.1 The Wind Tunnel Wall Boundary Condition

Now consider a HAWT situated in the wind tunnel working section. The wind coordinate system (x, y, z) depicted in Fig. 3.1 is used here. In the prescribed wake model, the blade is discretised into N_E blade elements, whose coordinates are determined by Eq. 3.4, and the positions of the wake elements trailed from the blade are prescribed by Eq. 3.11. The induced velocity \mathbf{v}_p^w at a panel control point p due to the turbine wake vortex system (trailed and shed vorticities) can be calculated by Eq. 3.16. In addition, the bound vorticities on the blades also induce a velocity \mathbf{v}_p^b at the point p whose coordinates (normalised by the rotor diameter R) are denoted \bar{x}_p , \bar{y}_p and \bar{z}_p . This induced velocity can be calculated directly by applying the Biot-Savart law,

$$\bar{\mathbf{v}}_p^b = \frac{\mathbf{v}_p^b}{V_0} = \sum_{k=1}^B \sum_{i=1}^{N_E} (\bar{\Gamma}_b)_{i,m} \frac{\mathbf{r}_A \times \mathbf{r}_B}{|\mathbf{r}_A \times \mathbf{r}_B|^2} \left(\frac{\mathbf{r}_A \cdot \mathbf{r}_{AB}}{|\mathbf{r}_A|} - \frac{\mathbf{r}_B \cdot \mathbf{r}_{AB}}{|\mathbf{r}_B|} \right) \quad (6.7)$$

where

$$\mathbf{r}_A = [\bar{x}_p - (\bar{x}_{bp})_{i,m}] \mathbf{i} + [\bar{y}_p - (\bar{y}_{bp})_{i,m}] \mathbf{j} + [\bar{z}_p - (\bar{z}_{bp})_{i,m}] \mathbf{k}$$

$$\mathbf{r}_B = [\bar{x}_p - (\bar{x}_{bp})_{i+1,m}] \mathbf{i} + [\bar{y}_p - (\bar{y}_{bp})_{i+1,m}] \mathbf{j} + [\bar{z}_p - (\bar{z}_{bp})_{i+1,m}] \mathbf{k}$$

$$\begin{aligned} \mathbf{r}_{AB} = & [(\bar{x}_{bp})_{i+1,m} - (\bar{x}_{bp})_{i,m}] \mathbf{i} + [(\bar{y}_{bp})_{i+1,m} - (\bar{y}_{bp})_{i,m}] \mathbf{j} + \\ & + [(\bar{z}_{bp})_{i+1,m} - (\bar{z}_{bp})_{i,m}] \mathbf{k} \end{aligned}$$

In the above calculations, the bound vorticity $\bar{\Gamma}_b$ and the coordinates of the blade element boundary point (\bar{x}_{bp} , \bar{y}_{bp} and \bar{z}_{bp}) are obtained from Eqs. 2.28 and 3.4, respectively; the azimuth index m , which is different from blade to blade, is determined as previously by Eqs. 2.33 and 2.34.

When considering the boundary condition that there is no flow through the surface of the body, the total induced velocity due to the turbine vortex system

$$\mathbf{v}_p^\Gamma = \mathbf{v}_p^b + \mathbf{v}_p^w \quad (6.8)$$

must be taken into account. In this way, Eq. 6.5 becomes

$$\left\{ \begin{array}{l} \sum_{j=1}^N A_{ij} \sigma_j = -\mathbf{n}_i \cdot (\mathbf{V}_0 + \mathbf{v}_p^\Gamma) \\ i = 1, 2, \dots, N \end{array} \right. \quad (6.9)$$

From this equation, all distributed source strengths can be obtained.

6.4.2 Wind Tunnel Wall Effects on the Turbine Wake

Once the source strength distribution is known, the velocity due to this distribution at any point in the modelled tunnel can be calculated,

$$\mathbf{v} = \nabla \varphi$$

The formulation of the disturbance velocity due to the sources at any point off the body surface has been well documented by Hess and Smith (1967) and by Katz and Plotkin (1991).

For a wind turbine operating in a wind tunnel, the disturbance velocities at the blade consist not only of the induction of the wake vortex system but also of the induction of the source panels. Let \mathbf{V}_i^p be the induced velocity at a spatial point $(\bar{x}, \bar{y}, \bar{z})$ due to a *unit* strength of the source on the panel i . The induced velocity due to the source distribution is then

$$\mathbf{v}^p(\bar{x}, \bar{y}, \bar{z}) = \sum_{i=1}^N \sigma_i \mathbf{V}_i^p \quad (6.10)$$

Substitution of $(\bar{x}_{bp})_{i,j}$, $(\bar{y}_{bp})_{i,j}$ and $(\bar{z}_{bp})_{i,j}$ into Eq. 6.10 yields the three disturbance velocity components, $(\bar{v}_x^p)_{i,j}^{bp}$, $(\bar{v}_y^p)_{i,j}^{bp}$ and $(\bar{v}_z^p)_{i,j}^{bp}$, at the blade element boundary point due to the panels,

$$\left\{ \begin{array}{l} (\bar{v}_x^p)_{i,j}^{bp} \mathbf{i} + (\bar{v}_y^p)_{i,j}^{bp} \mathbf{j} + (\bar{v}_z^p)_{i,j}^{bp} \mathbf{k} = \frac{\mathbf{v}^p((\bar{x}_{bp})_{i,j}, (\bar{y}_{bp})_{i,j}, (\bar{z}_{bp})_{i,j})}{V_0} \\ i = 1, 2, \dots, N_E + 1 \\ j = 1, 2, \dots, N_T \end{array} \right. \quad (6.11)$$

Thus, the axial induced velocity factor and non-dimensional radial induced velocity at the blade are

$$a = -(\bar{v}_z^\Gamma)_{i,j}^{bp} - (\bar{v}_z^p)_{i,j}^{bp} \quad (6.12)$$

$$\bar{v}_r = \left[(\bar{v}_x^\Gamma)_{i,j}^{bp} + (\bar{v}_x^p)_{i,j}^{bp} \right] \cos \psi_j + \left[(\bar{v}_y^\Gamma)_{i,j}^{bp} + (\bar{v}_y^p)_{i,j}^{bp} \right] \sin \psi_j \quad (6.13)$$

where $(\bar{v}_x^\Gamma)_{i,j}^{bp}$, $(\bar{v}_y^\Gamma)_{i,j}^{bp}$ and $(\bar{v}_z^\Gamma)_{i,j}^{bp}$ are the non-dimensional velocity components induced by the turbine wake vortex system and are determined by Eq. 3.18. Substitution of these total values of a and \bar{v}_r due to the vortex and source systems into Eqs. 3.10 and 2.11 produces the axial and radial positions of the turbine wake node, $(\bar{z}_w)_{i,j,k,n}$ and $(\bar{r}_w)_{i,j,k,n}$, trailed from the i th blade element boundary at the j th azimuthal position of the k th blade for the n th wake cycle. The position of the wake element node (i, j, k, n) can be expressed in the cartesian coordinate system,

$$\left\{ \begin{array}{l} (\bar{x}_w)_{i,j,k,n} = (\bar{r}_w)_{i,j,k,n} \cos \psi_{j,k} \\ (\bar{y}_w)_{i,j,k,n} = (\bar{r}_w)_{i,j,k,n} \sin \psi_{j,k} \\ (\bar{z}_w)_{i,j,k,n} = (\bar{z}_w)_{i,j,k,n} \\ i = 1, 2, \dots, N_E + 1 \\ j = 1, 2, \dots, N_T \\ k = 1, 2, \dots, B \\ n = 1, 2, \dots, N_C \end{array} \right. \quad (6.14)$$

Similarly, substitution of $(\bar{x}_w)_{i,j,k,n}$, $(\bar{y}_w)_{i,j,k,n}$ and $(\bar{z}_w)_{i,j,k,n}$ into Eq. 6.10 yields the three disturbance velocity components at the wake node due to the sources,

$$\left\{ \begin{array}{l} (\bar{v}_x^p)_{i,j,k,n}^{wn} = \frac{\mathbf{i} \cdot \mathbf{v}^p ((\bar{x}_w)_{i,j,k,n}, (\bar{y}_w)_{i,j,k,n}, (\bar{z}_w)_{i,j,k,n})}{V_0} \\ (\bar{v}_y^p)_{i,j,k,n}^{wn} = \frac{\mathbf{j} \cdot \mathbf{v}^p ((\bar{x}_w)_{i,j,k,n}, (\bar{y}_w)_{i,j,k,n}, (\bar{z}_w)_{i,j,k,n})}{V_0} \\ (\bar{v}_z^p)_{i,j,k,n}^{wn} = \frac{\mathbf{k} \cdot \mathbf{v}^p ((\bar{x}_w)_{i,j,k,n}, (\bar{y}_w)_{i,j,k,n}, (\bar{z}_w)_{i,j,k,n})}{V_0} \end{array} \right. \quad (6.15)$$

In the prescribed wake model, the wake geometry is prescribed by Eqs. 3.10 and 2.11. In the flow now constrained by the wind tunnel walls, the influence of the

source panels must be taken into account in the determination of the turbine wake. The position of the wake nodes may simply be expressed as

$$\left\{ \begin{array}{l} \bar{x}_w(i, j, k, n) = (\bar{x}_w)_{i,j,k,n} \cos \gamma + \frac{7}{4}\pi (\bar{v}_x^p)_{i,j,k,n}^{wn} \Delta \bar{t} \\ \bar{y}_w(i, j, k, n) = (\bar{y}_w)_{i,j,k,n} + \frac{7}{4}\pi (\bar{v}_y^p)_{i,j,k,n}^{wn} \Delta \bar{t} \\ \bar{z}_w(i, j, k, n) = (\bar{r}_{bp})_i \sin \gamma \cos \psi_{j,k} + (\bar{z}_w)_{i,j,k,n} + \frac{7}{4}\pi (\bar{v}_z^p)_{i,j,k,n}^{wn} \Delta \bar{t} \end{array} \right. \quad (6.16)$$

where the non-dimensional time step interval $\Delta \bar{t}$ is determined by Eq. 2.16.

6.4.3 Numerical Procedure

Having described the basic formulation of the effects of the distributed sources, the panel method may now be combined with the prescribed wake model to examine the wind tunnel wall interference on the turbine flow. The whole calculation procedure is illustrated in Fig. 6.4 and briefly stated below.

1. System Parameters The required inputs to the model are those associated with wind turbine and wind tunnel. The wind turbine data include turbine position in the wind tunnel, blade geometric parameters, blade aerofoil data, tip speed ratio, and discretisation parameters for the prescribed wake model (N_E , N_T , B and N_C), etc. The wind tunnel input data define the discretised geometries of the settling chamber, contraction, working section and diffuser. The order in which the points defining the wall surface are input is also provided. The order of input determines which direction is considered the outward normal direction.

2. Generation of Panels The input points for the wind tunnel are converted into the corner points of panels, thus creating N quadrilateral panels to represent the wind tunnel walls.

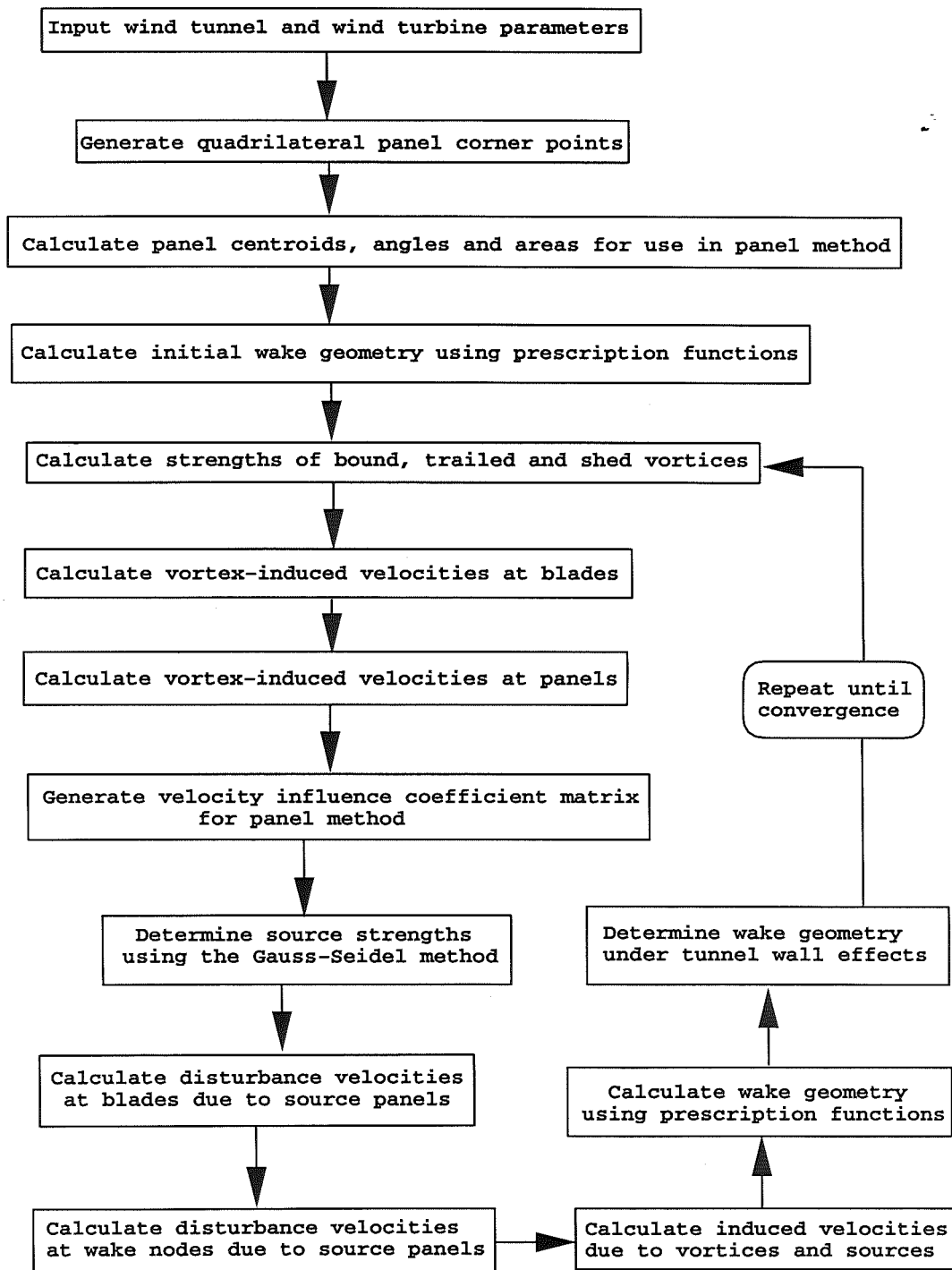


Figure 6.4: Numerical procedure for the wind tunnel wall interference calculation

3. Panel Parameters The centroid of each panel is calculated and the normal direction is determined. The centroid is chosen as the panel control point. The normal direction of the panel is defined by the angles between the unit normal vector and the axes of the wind coordinate system. These angles will also be used to transform data between the panel-based coordinate system, in which the panel-induced velocities are calculated, and the wind coordinate system, in which the global flow over the turbine is calculated.

4. Initial Wake Based on BEM theory, the initial wake structure is generated in this step using the prescription functions.

5. Vortex System The blade conditions are produced and the bound vorticity $\bar{\Gamma}_b$ on each blade element is calculated. Based on these bound vorticities, the trailed vorticity $\bar{\Gamma}_t$ and shed vorticity $\bar{\Gamma}_s$ are generated and distributed onto the turbine wake.

6. Vortex-Induced Velocity The velocities induced by the turbine vortex system can be calculated by application of the Biot-Savart law. For the induced velocities at the blade element control point, only the wake vortex induction is considered (Eq. 3.17). Similarly, the induced velocities $(\bar{v}_x^\Gamma)_{i,j}^{bp}$, $(\bar{v}_y^\Gamma)_{i,j}^{bp}$ and $(\bar{v}_z^\Gamma)_{i,j}^{bp}$ at the (i,j) th blade element boundary point due to the trailed and shed vorticities can be obtained (Eq. 3.18).

The induced velocities at the panel control points due to the wake vortex system and due to the blade-bound vortex system, \bar{v}_p^w and \bar{v}_p^b , can also be calculated using the Biot-Savart law (Eqs. 3.16 and 6.7). The total vortex induced velocity \bar{v}_p^Γ (Eq. 6.8) together with the onset flow velocity provides a basis for the boundary condition at the panel.

7. Influence Coefficient Matrix The matrix of the influence coefficients due to the source panels contains the normal components of velocity induced at

the control point of a specific panel by itself (diagonal entry A_{ii}) or by another panel (A_{ij} , $i \neq j$) with a unit value of source strength. The induced velocity is evaluated, for the sake of convenience, in a coordinate system based on the panel quadrilateral that produces the disturbance. This velocity is then transformed into a component normal to the panel whose control point is the current evaluation point. Repeating for each panel control point gives all entries of the influence coefficient matrix A_{ij} .

8. Source Strength Once the boundary conditions and the matrix of influence coefficients are known, the strengths of the distributed sources on the wind tunnel walls can be determined using the Gauss–Seidel method (Eq. 6.6).

9. Off-Body Velocity After evaluation of the source strengths, the disturbance velocities at the blades $\left[(\bar{v}_x^p)_{i,j}^{bp}, (\bar{v}_y^p)_{i,j}^{bp}, (\bar{v}_z^p)_{i,j}^{bp} \right]$, and the disturbance velocities in the wake $\left[(\bar{v}_x^p)_{i,j}^{wn}, (\bar{v}_y^p)_{i,j}^{wn}, (\bar{v}_z^p)_{i,j}^{wn} \right]$, due to the source panels can be obtained from Eqs. 6.11 and 6.15. These off-body induced velocities are calculated in the panel-based coordinates in the panel method and therefore must be transformed into the global wind coordinate system.

10. New Wake Geometry Based on the above off-body disturbance velocities, the turbine wake geometry can be updated. Firstly, the wake element position can be given using the prescription functions based on the new values of the axial and radial induced velocity factors a and \bar{v}_r (Eqs. 6.12 and 6.13). The new wake geometry is then obtained by superposing the direct effect of the source panels on the wake movement upon the result from the prescribed wake model (Eq. 6.16).

Usually, the turbine wake geometry in the constrained flow obtained in Step 10 above does not compare well in the first few iterations with the previous iterative results. Therefore, the calculation goes back to Step 5 above and repeats until global convergence of the wake shape is achieved.

6.5 Results and Discussion

Results and Comparisons

Comparison of calculation with wind tunnel tests is handicapped by the fact that either appropriate measured data or details of wind tunnel geometries are not available for most published wind tunnel tests on wind turbines. In this section, comparisons of the calculated results are only made with experimental data obtained in the University of Glasgow 2.13 m \times 1.6 m wind tunnel. In these tests, the turbine model was a two-bladed upwind design and had a rotor diameter of 1 m. The NACA 4415 section blades had a constant chord length of 0.1 m. PIV and LSV techniques were used to capture the vortices trailing from the blade tips. A detailed description of the experiment together with a selection of the experimental results have been presented by Grant *et al.* (1998).

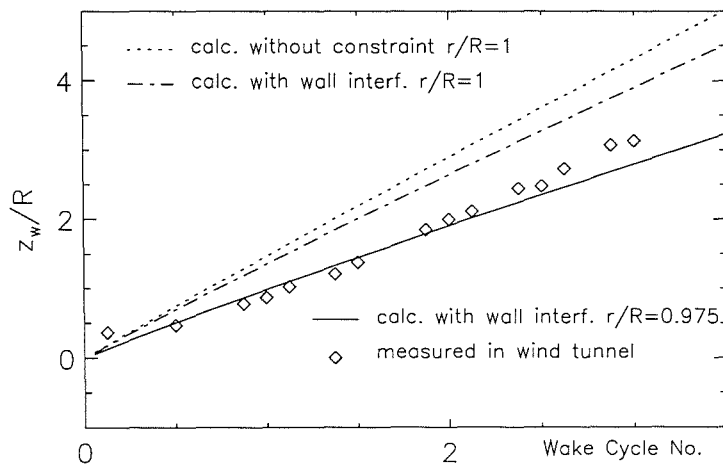
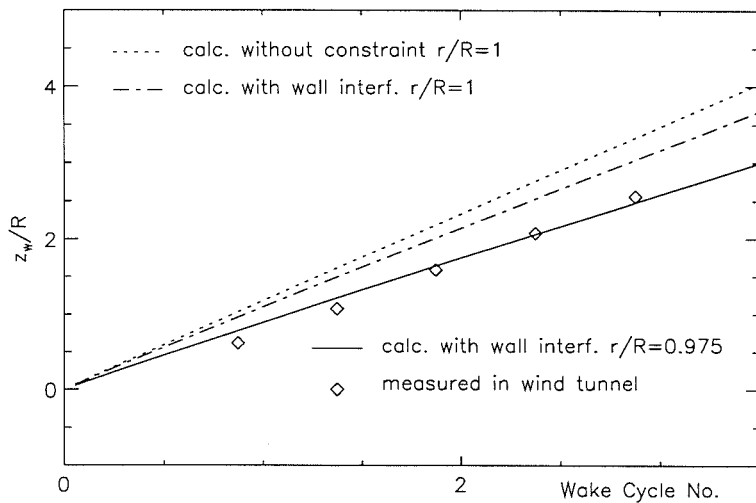
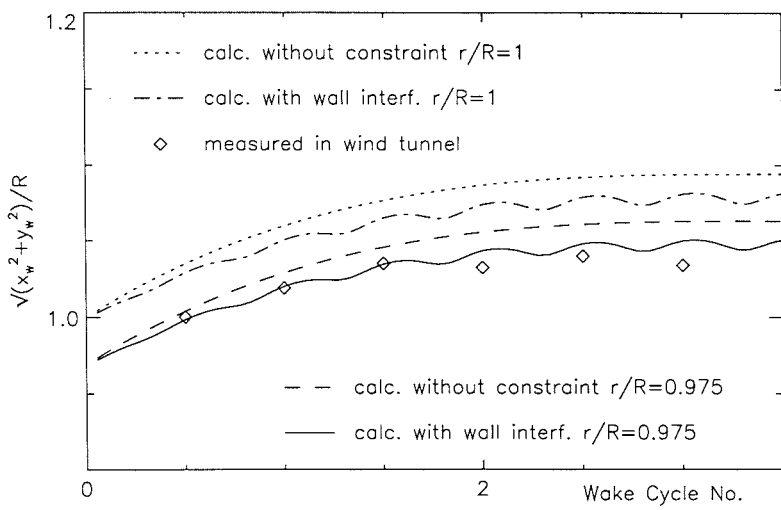


Figure 6.5: Downstream convection of wind turbine wake at $\lambda = 4$ in head-on flow

Figs. 6.5 through 6.8 show the predicted and measured turbine wake development in two head-on flow cases. In these figures, the constraint effect of the tunnel wall is clearly demonstrated by comparison of the downstream convection and ra-

Figure 6.6: Downstream convection of wind turbine wake at $\lambda = 5$ in head-on flowFigure 6.7: Radial expansion of wind turbine wake at $\lambda = 4$ in head-on flow

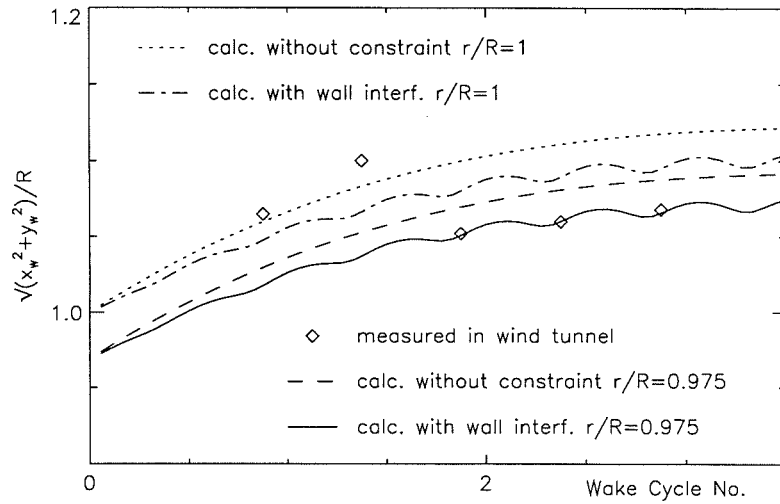


Figure 6.8: Radial expansion of wind turbine wake at $\lambda = 5$ in head-on flow

dial expansion of the wake filament trailed from the blade tip ($\bar{r} = 1$) between the calculations with and without wind tunnel wall effects. At both tip speed ratios, $\lambda = 4$ and $\lambda = 5$, the downstream movement of the tip filament under tunnel wall interference is slower than that in the unconstrained flow. It is understandable that, compared to the free expansion case, the wake expansion is small due to the wall interference, as shown by the calculated results presented in these figures. Obviously, when the wind tunnel wall effects are taken into account, the calculated results for $\bar{r} = 1$ are closer to the measurements, but there still exist large discrepancies. The measured data in the figures are the trajectories of the tip vortex.

In reality, vortices trailed from different blade sections interact mutually. Due to the great variation in aerodynamic loading in the tip region, the vortices trailed from the tip area usually roll up to form a strong tip vortex. Obviously, this tip vortex rolls up at a location near the tip instead of exactly at the tip. According to Miller (1982), the rolled-up tip vortex is located at approximately 97.5% of the span. The predicted downstream distance of the wake filament at $\bar{r} = 0.975$ with wind tunnel wall interference is compared with the measured downstream

convection of the tip vortex convection in Figs. 6.5 and 6.6. The calculated results at $\bar{r} = 0.975$ coincide very well with the measured data. The predicted radial development of the wake for $\bar{r} = 0.975$ is also compared with the wind tunnel test for tip speed ratios of 4 and 5 in Figs. 6.7 and 6.8. The calculated wake expansion for $\bar{r} = 0.975$ under the constraint of the wind tunnel walls agrees well with the measurement for the tip vortex except at the first two datum points of the wind tunnel test for $\lambda = 5$. In contrast, the calculated freely-expanding wake radial position for the same span location diverges significantly from the measured data.

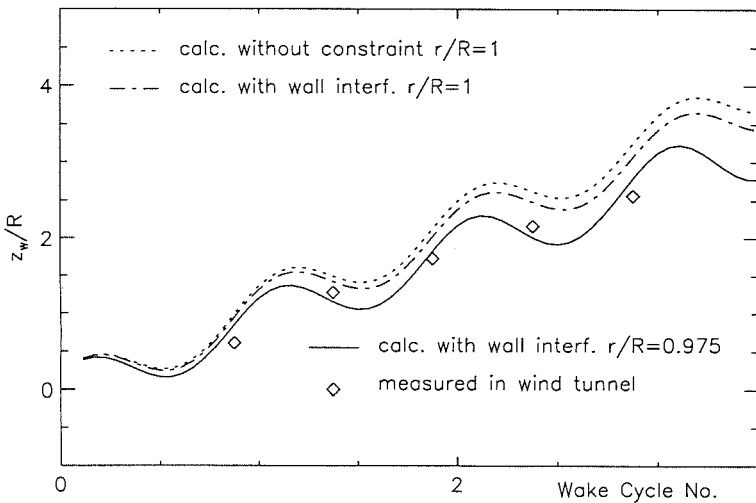


Figure 6.9: Downstream convection of wind turbine wake at $\lambda = 5$ and $\gamma = 20^\circ$

Figs. 6.9 and 6.10 give comparisons of the wake development at $\lambda = 5$ for a yaw angle of 20° . The calculated non-dimensional downstream distance \bar{z}_w for $\bar{r} = 0.975$ compare well with the measured tip vortex movement. Considering that the wake positions in the wind coordinate system vary with the azimuth ψ (see Eq. 6.16), the results from this numerical modelling strategy is very encouraging.

As just mentioned, the downstream and radial positions of the wake are a function of the azimuthal angle as described by Eqs. 6.14 and 6.16. Thus, the variations of $\sqrt{\bar{x}_w^2 + \bar{y}_w^2}$ and \bar{z}_w with azimuth are represented by their oscillations with the wake cycle number. It should be noted here that the oscillations calculated

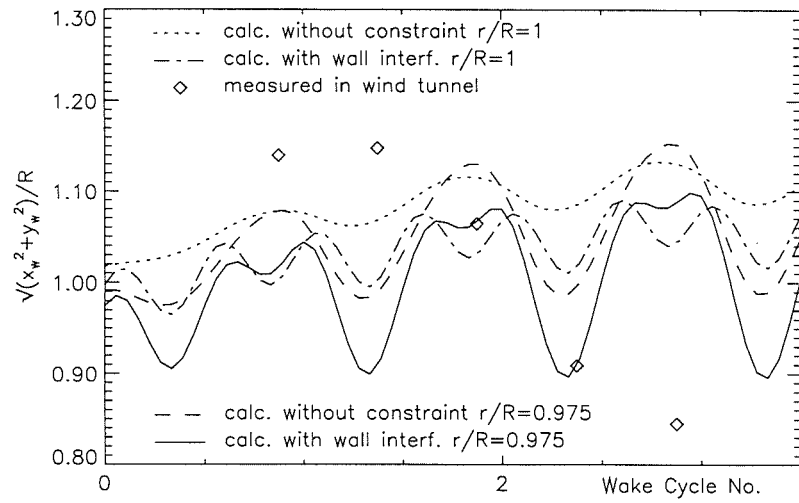


Figure 6.10: Radial expansion of wind turbine wake at $\lambda = 5$ and $\gamma = 20^\circ$

with the wind tunnel wall constraint in Fig. 6.10 are not only due to the azimuth variation but also due to the wall interference variation at different positions. This oscillating variation in wake radial position due to the wall effects can clearly be seen from Figs. 6.7 and 6.8 for the head-on flow cases where the wind coordinate system (x, y, z) is identical to the turbine-fixed coordinate system (x', y', z') . The cross-section of the wind tunnel is octagonal instead of circular. Therefore, the constraint effect varies along the cross-section circumference.

For $\lambda = 5$ in both the head-on flow and the yawed flow cases, relatively large wake expansions were measured in the wind tunnel tests at the first two points (wake cycle numbers were approximately 0.875 and 1.375, respectively). This phenomenon is not well represented by the model. The reasons for this are not clear but the solid and wake blockages of the nacelle and rotor, which are not modelled in the present study, may contribute to the disagreement. This requires further investigation in future work.

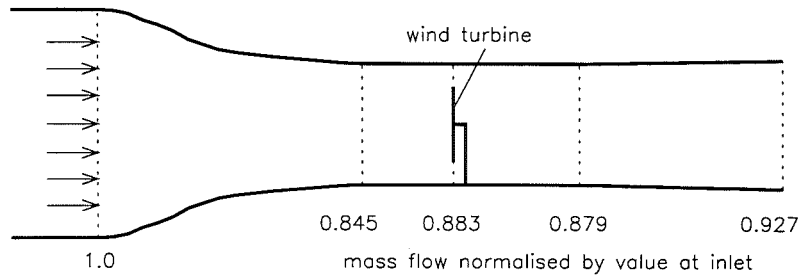


Figure 6.11: Calculated mass flows in the modelled wind tunnel with the turbine model at $\lambda = 4$ and $\gamma = 0$

Leakage Error

The combined model of the prescribed wake and panel methods has shown promising results for the modelling the effect of the wind tunnel interference on a wind turbine flow. However, there are problems associated with applying the Neumann boundary condition to internal flows (Ashby and Sandlin 1985). The primary problem is the so-called *leakage* that manifests itself as a non-constant mass flux down the length of the tunnel. Fig. 6.11 shows the variation in mass flux at different sections due to the panel method for the nonyawed wind turbine case. The mass fluxes have been normalised by the value at the inlet section of the contraction. It can be seen from this figure that the maximum leakage occurs in the contraction portion. This can be as high as 15.5%. Even in the working section where the flow is of most interest, leakage is apparent; from the inlet of the working section to the wind turbine location, the leakage is nearly 4%. This problem inevitably affects the modelling accuracy, since, to accurately resolve flows in a duct, it is essential that the mass flow leaving the downstream station is the same as that entering the upstream one.

Most of the panel methods that have been developed for aeronautical applications have concentrated on external aerodynamics, where for a low order method,

the effects of leakage errors tend to be small and are reduced by being of opposite sign to the errors in representing a curved geometry by plane panels (Butter *et al.* 1982). However, most low order panel methods suffer severely from leakage when applied to internal flows. Leakage occurs because the boundary conditions are applied only at the control point of each panel and the flow is free to “leak” everywhere else. Holt and Hunt (1982) examined the case of a duct with straight parallel walls which is the simplest internal flow problem. They modelled such a duct, using a piecewise constant source distribution on the wall panels, as a long open tube in a uniform external flow field to predict wall interference corrections for a wing in a tunnel. Even for this very simple case, low levels of leakage were observed through the tunnel walls, leading to an apparently varying mass flux down the tunnel. Cheung and Hancock (1988), Browne and Katz (1990) and Mokry (1995) also modelled the wind tunnel walls as an open box with parallel sides to calculate wind tunnel wall interference. Leakage errors are not reported in the three articles but the leakage errors should influence the interference calculations.

The leakage problem becomes more pronounced when a wind tunnel with a full 3-D contraction, working section and diffuser is modelled, as the case in this study. This problem is much more difficult to solve using low order source-distributed panel methods, because the tunnel walls typically have to turn the flow a great deal and the contraction and diffuser impart large changes in velocity down the length of the wind tunnel. For example, Hess (1973) has examined the severe case of leakage through an axisymmetric duct with a contraction ratio of 16 using a low order panel method. For this case the maximum leakage is 32%, much higher than that presented in Fig. 6.11. Therefore, consideration of how to reduce the leakage error in panel methods is very important for internal flows.

Tunnel wall/vortex interaction

For the case of tunnel/turbine interaction examined in this study, in addition to the leakage caused in the contraction, the interactions between the tunnel walls and

the turbine vortex system may be very large. These interactions greatly influence the boundary condition. Fig. 6.12 shows the normal velocities, V_n due to the freestream and the turbine vortex system, at the panel control points closest to the central line of the top wall, where $V_n = -\mathbf{n}_i \cdot (\mathbf{V}_0 + \mathbf{v}_p^\Gamma)$ (see Eq. 6.9). This kind of rapid change in V_n along the length of the wind tunnel has been identified by Hunt (1978) as the main primary reason for leakage and loss of accuracy in most existing panel methods. The calculation of the vortex/surface interaction and the influence of this interaction on the singularity distribution on the panels have been investigated by Maskew (1982, 1980). Appropriate modelling of the close wall/vortex interaction would reduce the leakage error.

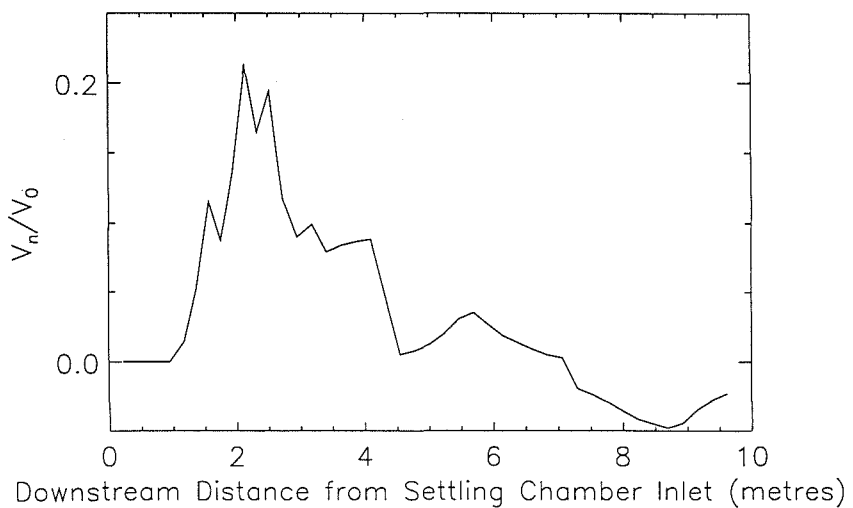


Figure 6.12: Velocity normal to the modelled wind tunnel wall due to freestream and turbine vortices at $\lambda = 4$ and $\gamma = 0$

High Order panel Method

Experience and a variety of published results have shown that low order panel methods are perfectly satisfactory for the vast majority of flows, including practically all external flows. It appears that only in two situations might a high order analysis require to be used; one is the internal flow case, where a channel or duct

of decreasing cross-section greatly accelerates the fluid, and the other is the strong lift interaction case (Hess 1990). High order panel methods tend to be more accurate than low order methods because they better model a continuous singularity distribution over the body. Hess (1973) has formulated an axisymmetric high order method for internal flow and his results show that the leakage errors presented in the low order method for the axisymmetric duct with the contraction ratio of 16, mentioned above, can be almost eliminated by the high order method. The maximum leakage is reduced to 0.6% for the high order method from 32% for the low order formulation.

It was argued that, compared with the low order methods, the more continuous representation of the surface singularity distribution in the high order panel methods should allow a reduction in panel density for a given solution accuracy, and hence should lead to lower computing costs. However, no such benefits have appeared so far for the general 3-D case. In fact, high order methods require significantly longer computational times and care must be taken to ensure that all the panels exactly match up due to the requirement that the singularity strength be continuous across panels. This makes the model more complicated. In particular, for the case of tunnel wall interference on the wind turbine flow, the panel density must be increased in order to exactly account for the interaction between the walls and the turbine vortex system even if a high order technique is used (Maskew 1982). The long computation times required for the high order panel methods can, thus, be a limiting factor for 3-D geometries which require high panel densities. Therefore, there is considerable interest in improving the accuracy of low order panel methods without sacrificing their shorter computation times.

Mixed Singularity Distribution

The potential flow over a body can be represented by a source distribution and a doublet distribution on the closed body surface and its wake (Eq. 6.1). This kind of mixed source–doublet distribution has been used in low order panel meth-

ods for both external and internal flows (Lee 1981, Maskew 1982, Ashby and Sandlin 1985, Ashby *et al.* 1991, Sudhakar and Shevare 1991). The body in the method must be modelled as a closed surface which divides all space into an inner and an outer region. The outer region contains the flow field of interest (flow within the duct for wind tunnel tests) whilst the inner region contains a fictitious flow. The boundary conditions used in the source–doublet panel methods are an external Neumann boundary condition which implies a known normal velocity at the control point of each panel and an internal Dirichlet boundary condition of zero perturbation potential inside the body surface (fictitious flow field outside the duct for wind tunnel tests). Applying such a mixed singularity panel method to the wind tunnel wall interference problem, the freestream in the tunnel is produced by the sources distributed on the inlet and exit faces of the wind tunnel which must be modelled as a closed box. The fictitious flow outside the tunnel has no effects on the generation of the freestream in the tunnel and, therefore, the onset velocity of the fictitious flow can be adjusted to obtain minimal leakage errors. It has been demonstrated that, for comparable density of panels, the low order mixed singularity panel method gives comparable accuracy to the high order methods (Maskew 1982, Miranda 1984, Sudhakar and Shevare 1991).

Ashby and Sandlin (1985) applied the source–doublet panel method to the wind tunnel interference problem by modelling the NFAC 40 feet \times 80 feet wind tunnel at NASA Ames Research Center by a closed box. Only the portion of the tunnel which contained the contraction, with a contraction ratio of 7.9, the test section, and the diffuser with a diffusion ratio of 2.6 and diffusion half angle of approximately 2.75° was modelled. In total 2450 panels were used in the model. By appropriately choosing the fictitious onset flow, the leakage was almost completely eliminated. There was a 0.57% decrease in mass flux between the inlet face of the contraction and the test section and a 0.32% decrease in mass flux between the test section and the exit of the diffuser.

A source panel method combined with the prescribed wake model, presented in this chapter, has given encouraging results but, the leakage errors in the method

remain to be resolved. From the discussion above, the mixed source–doublet technique may be a good alternative for eliminating the leakage problem in the panel method.

Errors from the Prescribed Wake Model

It should be noted that the modelling errors in this study are produced not purely by the panel method but also by the prescribed wake model.

The prescription functions for the wake structure are based on the momentum and continuity theories. Whilst continuity is satisfied in the turbine wake, this does not mean that the flow fluxes induced by the turbine vortex system, which are calculated *via* the Biot–Savart law, satisfy the equation of continuity at different stations ahead of the turbine and elsewhere outside the turbine wake. This may contribute to the apparent leakage through the tunnel walls.

The model wind turbine had untwisted blades with constant chord and the blade pitch angle was set to a constant value of 12° . For such a turbine design, $\lambda = 5$ is already a high tip speed ratio, at which the wake may not be appropriately represented by the prescribed wake model (see Section 2.4). It is possible that the large discrepancies between the model and measurement in Figs. 6.8 and 6.10 could be mainly due to the basic modelling of the turbine wake.

In this combined model, the turbine nacelle and support tower, both of which produced solid and wake blockages in the wind tunnel test, are not modelled. In addition, the blade is represented by a bound vortex in the model. The interaction of this vortex with tunnel walls has been modelled. However, the turbine rotor also produces a solid blockage, which should be proportional to the turbine solidity. This solidity effect together with the nacelle effect on the blockage could, in the future, be modelled by distributing source singularities on the blade and nacelle.

6.6 Conclusions

A low order panel method and prescribed wake model have been combined to investigate the constraint effects of wind tunnel walls on HAWT flow and performance. The wind tunnel walls are modelled as a series of quadrilateral panels on which source singularities are distributed. The wind turbine and its flow in the wind tunnel are represented by the prescribed wake model. The interaction between the tunnel walls and the vortices on the turbine blades and in the wake greatly influences the strengths of the sources on the panels. The velocity induced at the control point of each panel by the vortex system is calculated using the Biot-Svart law. These induced velocities together with the freestream velocity determine the source strengths through satisfaction of the external Neumann boundary conditions on the panel control points. The off-surface disturbance velocities due to the panels are superposed on the prescribed velocities in the wake, thus obtaining a new wake structure with the effect of the wall interference. This new wake geometry modifies the wind turbine aerodynamic performance.

The numerical results from the model have been presented and have shown strong effects of the wind tunnel walls on the turbine wake structure. The inclusion of wall interference has significantly improved the level of correlation of the calculations with the measurements and, in general, the calculated results with the wall effects compare well with the wind tunnel test data. It has also been noted that there is a leakage problem for the low order panel method in the modelling of internal flows. Several possible reasons for the leakage errors have been discussed and several ways to improve the modelling accuracy have been suggested for the combined panel/prescribed wake model. A possibly practical method is the mixed source/doublet panel analysis in which the wind tunnel of interest is modelled as a closed box. Source singularities may also be distributed on the turbine blades and nacelle to simulate the solid blockage associated with them.

Chapter 7

Conclusions and Recommendations

The work presents an investigation of unsteady aerodynamic modelling for HAWT performance prediction. The basic method used in this study is an unsteady prescribed wake model. The unsteady aspects addressed in the study include yawed flow, the atmospheric boundary layer and tower shadow. The wind tunnel wall effects on the wind turbine flow are also numerically examined based on a source panel method and the prescribed wake model.

7.1 The Prescribed Wake Model

A prescribed wake model for the prediction of the aerodynamic performance of HAWTs operating in steady axial and yawed flows has been presented. This method can be used not only to estimate the gross rotor performance but also to calculate the detailed aerodynamic characteristics such as blade loading, incidence information, and wake structure, etc.

In the prescribed wake model, the turbine blade is modelled as a series of bound vortex elements, from which vortex filaments corresponding to the spanwise vorticity distribution are trailed. In unsteady cases, shed vorticity is also introduced into the wake to account for the temporal changes in bound circulation. The tur-

bine wake is divided into a near wake and far wake. The latter represents the far field equilibrium condition of the flow and is modelled as a semi-infinite cylinder. The geometry of the near wake is prescribed by simple prescription functions based on momentum theory. In this way, the detailed wake structure is defined beforehand, avoiding the calculation of wake self-induction as is done in free wake analysis.

For unsteady cases, an unsteady aerofoil model has been coupled into the prescribed wake model to give the unsteady aerodynamic and dynamic stall loads on the blades.

The coupled model gives good estimates of gross rotor performance when compared to measurements and other numerical simulations. In general, the predicted aerodynamic loads on the blades compare well with field data, particularly on outboard blade sections. The large differences in the aerodynamic loads at blade inboard stations are attributed mainly to 3-D effects on the rotating blade, which must be modelled in order to provide accurate blade loading distributions.

In its present form, the prescribed wake model is not designed to deal with large-scale reversed flow regions in the wake. As a result, unrepresentative wake shapes at high tip speed ratios may produce artificially high induced velocities at the blades; this is a common problem in vortex wake methods. Overcoming this problem provides a focus for future work. Firstly, there is strong evidence that vortices traile from the blade tend to roll up into a strong tip vortex and root vortex. It is expected that modelling of the tip and root roll-ups may improve the level of accuracy of the model at high tip speed ratios (Miller 1982). Secondly, at high tip speed ratios, the HAWT blade may induce a turbulent wake state at a certain downstream distance, where the dissipation of the wake vorticity is particularly significant and the breakdown of the vortex structure takes place. Appropriate accounting of vortex diffusion may eliminate the divergence problem in the vortex wake model at high tip speed ratios and make calculated results more reliable.

In the unsteady prescribed wake model, the Leishman–Beddoes semi-empirical dynamic stall model is used to obtain the aerodynamic loads on the blades. Given that the Leishman–Beddoes model was developed as a performance estimation tool for helicopter rotors, other aspects of it may be inappropriate for calculations on wind turbine rotors where the freestream speed and rotation rates are normally much lower than for a helicopter. Therefore, the unsteady model requires some specific modifications to become directly applicable to low speed flows on the type of aerofoils used on wind turbines.

In the unsteady model, the Kirchhoff flow theory is used to represent the movement of the separation point. The Kirchhoff theory is an idealised flow model for a 2-D flat plate based on the assumption of zero pressure in the wake of the separated flow region. A more appropriate representation of the non-linear response of the separation point to the unsteady forcing is required for accurate unsteady aerodynamic calculations.

7.2 Three-Dimensional Rotational Effects

The unsteady prescribed wake model has been extended to include 3-D effects on rotating blades *via* a series of correction factors based on the semi-empirical stall delay model of Du and Selig, which is based on the analysis of laminar boundary layers developing under the influence of rotational effects. For unsteady calculations, the Leishman–Beddoes unsteady model has been modified to represent 3-D rotational effects and then coupled with the prescribed wake model to provide the 3-D aerodynamic performance of HAWTs. The basis for the 3-D modification is the delay in the forward movement of the separation point due to the centrifugal and Coriolis forces in a rotating frame. This delay modifies the predicted normal force and, together with consideration of the likely chordwise loading distribution, provides the basis for corrections to the tangential force and pitching moment.

It has been demonstrated that application of the proposed 3-D modifications can significantly improve the prediction of the detailed aerodynamic loads on the

blades. In general, the method is shown to give accurate predictions over a wide range of operating conditions and inflow angles. The substantial improvement in the prediction of aerodynamic force and moment coefficients is, however, confined mainly to inboard blade sections and depends on inflow conditions on the blades. For a typical case, the 3-D calculated normal force and pitching moment at 30% of span are as high as twice their 2-D counterparts and the normal force at 46.7% of span is increased by 45% by the 3-D correction. The 3-D correction also improves the gross performance prediction, particularly at high wind speeds where separated flows and hence 3-D effects are significant.

In order to improve the 3-D calculation, a better understanding is needed of the flow mechanisms associated with the rotational effects and therefore it is necessary to conduct more experimental and theoretical studies of 3-D flows on rotating blades.

The present 3-D correction scheme is based on the analysis of laminar boundary layer behaviour. Most flows around wind turbine blades are, however, turbulent in natural conditions. Further studies of rotational effects on turbulent boundary layer separation should help to improve 3-D correction strategies.

The radial flow in the boundary layer of a rotating blade is influenced by a number of factors, such as the chordwise and spanwise pressure distributions, the centrifugal and Coriolis force fields, and the freestream velocity field. For a HAWT in yaw, the oblique flow to local blade sections varies with azimuthal position. This results in a periodic radial flow which may affect the development of the blade boundary layer. The influence of the radial flow directly arising from the yawed flow on flow separation should be taken into account in future 3-D models.

In the stall delay model used in this study, the empirical constants are all set to unity. In fact, they should vary with rotor and flow conditions to reproduce the solution of the boundary layer equations. A clear and explicit empirical relationship between these empirical constants and the dependent factors is worthy of refinement in future work.

7.3 Tower Shadow Effects

Two different modelling strategies for downwind-configured HAWTs have been developed to calculate the aerodynamic response of the blade due to the velocity deficit produced by the support tower. Both methods are based on a prescribed velocity deficit in the tower shadow region.

In the first method, the velocity deficit is simply applied to the onset flow within the prescribed wake model. This significantly distorts the wake structure behind the blade and substantially modifies the blade incidence and velocity variations through the tower shadow region. The results from the model are encouraging and clearly show tower shadow effects on the turbine aerodynamic performance. Unfortunately, the increased azimuthal resolution required to adequately represent the unsteady response of the blade is such that the computational overhead associated with accurate dynamic calculations in the tower shadow region becomes prohibitive.

An alternative strategy for tower shadow effects has been developed which involves the use of an efficient near wake model of the vorticity trailed from the blade. The near wake model has been enhanced with appropriate modifications and integrated into the prescribed wake scheme to produce a hybrid method capable of predicting the detailed high resolution unsteady response in the tower shadow region. The azimuth interval used within the shadow region has been reduced to 0.5° . The computational cost introduced by the high resolution near wake model is almost negligible. Comparisons of the results of the high resolution scheme with measurement show a reasonable level of agreement. Discrepancies exist mainly at very high blade incidences where the aerodynamic forces are difficult to accurately predict even though 3-D effects are included.

The high resolution model for tower shadow effects requires further validation. Compared to the NREL UAE field data, the model appears to overstate the impulsive response of the blade when the blade is passing out of the tower shadow.

However, some other CFD analyses and wind tunnel tests do show this type of strong impulsive response. The reason for this phenomenon is not entirely clear. More experimental studies should be helpful to explain the difference and provide a sound basis for the model validation.

The Leishman–Beddoes semi-empirical dynamic stall model, which is used to produce blade unsteady response, is sensitive to the time derivatives of inflow velocity, blade incidence and pitch rate. In this unsteady aerofoil model, the unsteady response to the aerodynamic forcing is related to the first time derivative and second differential of the resultant velocity and first two derivatives and third differential of the blade incidence. In order to improve the accuracy of the high azimuthal resolution model, it will be necessary to obtain smooth representations of these high order derivatives and differentials in the tower shadow region, especially around the shadow boundaries.

In addition to the velocity deficit produced by the support tower, vortices are also shed from the tower into its wake, which will influence the blade loads when the blade passes through the tower wake. Modelling the effect of the shed vortices from the tower provides a focus for future work.

7.4 Wind Tunnel Wall Interference

A low order panel method and the prescribed wake model have been combined into a coupled model capable of estimating the interference of the solid wind tunnel walls with the wind turbine flow. The wind tunnel walls are discretised into a series of panels and sources distributed on these panels simulate the constraint effect of the wind tunnel walls. The wind turbine and its wake are represented by the prescribed wake model. The source strengths are related to the induced velocities at the panel control points due to the turbine vortex system by satisfying the boundary condition of zero normal velocity on the solid tunnel wall. The vortex-induced and source-induced velocities at the blade are summed to determine an interim turbine wake using the prescription functions. The effect of the

disturbance velocities due to the source panels are then superposed upon the prescribed wake, to obtain the final wake geometry under the influence of wind tunnel wall interference. This new wake structure modifies the wind turbine aerodynamic performance. Either an unyawed or a yawed HAWT test in a wind tunnel can be numerically simulated using this method.

In this preliminary study, the numerical results from the combined model have been encouraging and shown strong wind tunnel wall effects on the wind turbine structure. With the numerical representation of wind tunnel walls, it appears that the calculated wake trailed from 97.5% of span compares well with the wind tunnel data associated with the tip vortex but, this can only be fully validated if the tip vortex roll-up is modelled within the prescribed wake scheme. In addition, a severe leakage problem has been detected in the study. This leakage error is associated with the application of low order source panel methods to internal flows. This problem must be addressed in future work.

Having examined the reasons for the leakage and reviewed several panel methods, it seems that a low order source–doublet analysis would be the most practical technique to eliminate the leakage errors for the internal flow problem. In such a mixed singularity panel method, the wind tunnel must be modelled as a closed box. The source strengths on the inlet and exit faces can be easily determined directly from the required (known) mass flow. Thus, only the doublet strengths on the tunnel walls remain to be calculated by solving the associated simultaneous linear equations. This technique can greatly reduce the leakage errors while retaining the advantage of low computational costs.

The solid blockages due to the turbine nacelle and rotor is not modelled in the present study. These blockage effects could be simulated by distributing source singularities on the nacelle and blades. Moreover, close interactions between the turbine vortex system and the tunnel walls should be further examined in future work.

Appendix A

Velocity Induced by a Straight-line Vortex

The fundamental relation required for the determination of the induced velocity due to a vortex is given by the Biot–Savart law. Consider a directed infinitesimal vortex filament \mathbf{dl} of strength Γ , whose direction abides by the “right-hand rule” and is as same as \mathbf{dl} , as shown in Fig. A.1. The radius vector from the element \mathbf{dl} to the point P in space is \mathbf{r} . The velocity field induced by the vortex element is expressed by the Biot–Savart law as

$$\mathbf{dv} = \frac{\Gamma}{4\pi} \frac{\mathbf{dl} \times \mathbf{r}}{|\mathbf{r}|^3}$$

For a spatial straight-line vortex of constant strength Γ from point $A(x_1, y_1, z_1)$ to $B(x_2, y_2, z_2)$, the induced velocity at point $P(x, y, z)$ due to this line vortex is

$$\mathbf{v} = \frac{\Gamma}{4\pi} \int_A^B \frac{\mathbf{dl} \times \mathbf{r}}{|\mathbf{r}|^3}$$

From Fig. A.1, the perpendicular distance from the point P to the vortex line is

$$h = |\mathbf{r}| \sin \theta$$

and

$$|\mathbf{dl}| = h \csc^2 \theta d\theta$$

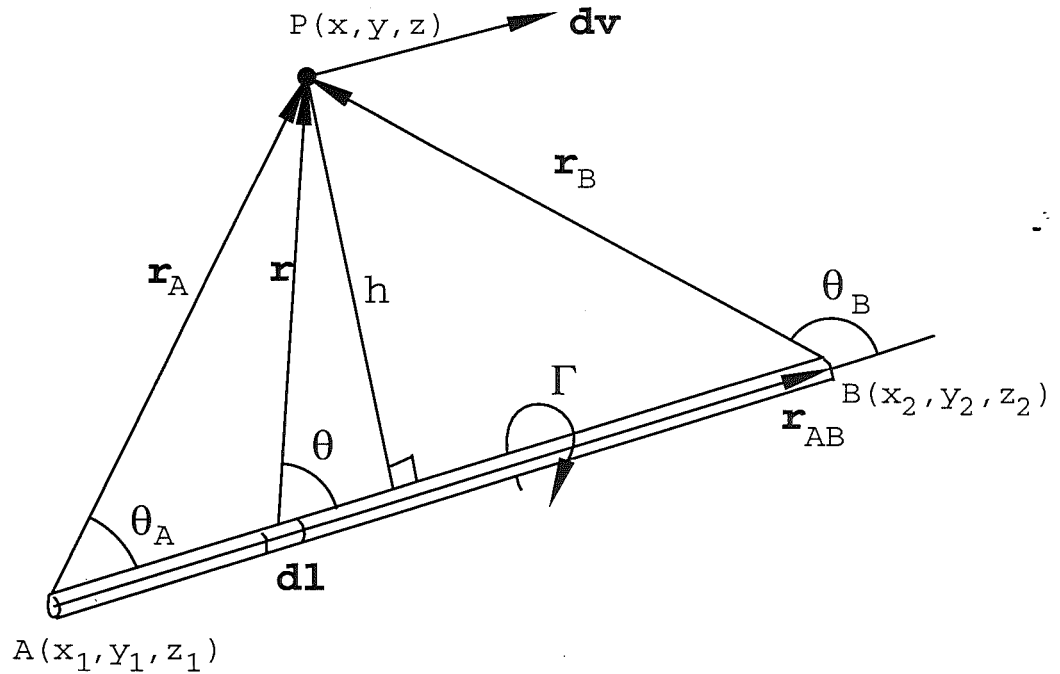


Figure A.1: Illustration of velocity induced by a straight-line vortex

Thus, the magnitude of the induced velocity is

$$v = \frac{\Gamma}{4\pi} \int_A^B \frac{|\mathbf{dl} \times \mathbf{r}|}{|\mathbf{r}|^3} = \frac{\Gamma}{4\pi} \int_A^B \frac{|\mathbf{dl}| \sin \theta}{|\mathbf{r}|^2} = \frac{\Gamma}{4\pi h} \int_{\theta_A}^{\theta_B} \sin \theta d\theta$$

or

$$v = \frac{\Gamma}{4\pi h} (\cos \theta_A - \cos \theta_B) \quad (\text{A.1})$$

Let

$$\mathbf{r}_A = (x - x_1) \mathbf{i} + (y - y_1) \mathbf{j} + (z - z_1) \mathbf{k}$$

$$\mathbf{r}_B = (x - x_2) \mathbf{i} + (y - y_2) \mathbf{j} + (z - z_2) \mathbf{k}$$

$$\mathbf{r}_{AB} = (x_2 - x_1) \mathbf{i} + (y_2 - y_1) \mathbf{j} + (z_2 - z_1) \mathbf{k}$$

Then

$$\cos \theta_A = \frac{\mathbf{r}_A \cdot \mathbf{r}_{AB}}{|\mathbf{r}_A| |\mathbf{r}_{AB}|} \quad (\text{A.2})$$

$$\cos \theta_B = \frac{\mathbf{r}_B \cdot \mathbf{r}_{AB}}{|\mathbf{r}_B| |\mathbf{r}_{AB}|} \quad (\text{A.3})$$

and

$$h = \frac{|\mathbf{r}_A \times \mathbf{r}_B|}{|\mathbf{r}_{AB}|} \quad (\text{A.4})$$

Substitution of Eqs. A.2, A.3 and A.4 into Eq. A.1 obtains

$$v = \frac{\Gamma}{4\pi} \frac{\mathbf{r}_A \times \mathbf{r}_B}{|\mathbf{r}_A \times \mathbf{r}_B|} \left(\frac{\mathbf{r}_A \cdot \mathbf{r}_{AB}}{|\mathbf{r}_A|} - \frac{\mathbf{r}_B \cdot \mathbf{r}_{AB}}{|\mathbf{r}_B|} \right) \quad (\text{A.5})$$

The direction of the induced velocity is determined by the cross product of \mathbf{r}_A and \mathbf{r}_B . Thus, in vector notation Eq. A.5 becomes

$$\mathbf{v} = \frac{\Gamma}{4\pi} \frac{\mathbf{r}_A \times \mathbf{r}_B}{|\mathbf{r}_A \times \mathbf{r}_B|^2} \left(\frac{\mathbf{r}_A \cdot \mathbf{r}_{AB}}{|\mathbf{r}_A|} - \frac{\mathbf{r}_B \cdot \mathbf{r}_{AB}}{|\mathbf{r}_B|} \right) \quad (\text{A.6})$$

where the cross product term can be expanded to

$$\begin{aligned} \mathbf{r}_A \times \mathbf{r}_B = & [(y - y_1)(z - z_2) - (y - y_2)(z - z_1)] \mathbf{i} + \\ & + [(z - z_1)(x - x_2) - (z - z_2)(x - x_1)] \mathbf{j} + \\ & + [(x - x_1)(y - y_2) - (x - x_2)(y - y_1)] \mathbf{k} \end{aligned}$$

and therefore

$$\begin{aligned} |\mathbf{r}_A \times \mathbf{r}_B|^2 = & [(y - y_1)(z - z_2) - (y - y_2)(z - z_1)]^2 + \\ & + [(z - z_1)(x - x_2) - (z - z_2)(x - x_1)]^2 + \\ & + [(x - x_1)(y - y_2) - (x - x_2)(y - y_1)]^2 \end{aligned}$$

The dot product terms in Eq. A.6 are

$$\mathbf{r}_A \cdot \mathbf{r}_{AB} = (x - x_1)(x_2 - x_1) + (y - y_1)(y_2 - y_1) + (z - z_1)(z_2 - z_1)$$

$$\mathbf{r}_B \cdot \mathbf{r}_{AB} = (x - x_2)(x_2 - x_1) + (y - y_2)(y_2 - y_1) + (z - z_2)(z_2 - z_1)$$

and the magnitudes of the vectors \mathbf{r}_A and \mathbf{r}_B are

$$|\mathbf{r}_A| = \sqrt{(x - x_1)^2 + (y - y_1)^2 + (z - z_1)^2}$$

$$|\mathbf{r}_B| = \sqrt{(x - x_2)^2 + (y - y_2)^2 + (z - z_2)^2}$$

Appendix B

Description of NREL Wind Turbine

Basic Machine Parameters

1. Number of blades: 3
2. Rotor diameter: 10.06 m
3. Hub height: 17.03 m
4. Rotational speed: 72 rpm synchronous speed
5. Location of rotor: downwind
6. Rotational direction: clockwise (viewed from downwind)
7. Rotor overhang: 1.32 m
8. Tower diameter: 0.4064 m
9. Power regulation: stall

Rotor

1. Root extension: 0.723 m

2. Blade set angle:
 - Phase II: 12 degrees
 - Phases III and IV: 3 degrees
3. Blade pitch: fixed along the blade
4. Blade aerofoil: NREL S809
5. Blade chord: 0.4572 m at all span stations
6. Blade twist:
 - Phase II: None
 - Phases III and IV: see Fig. B.1
7. Aerofoil coordinates: see Table B.1
8. Aerofoil aerodynamics: see Fig. B.2

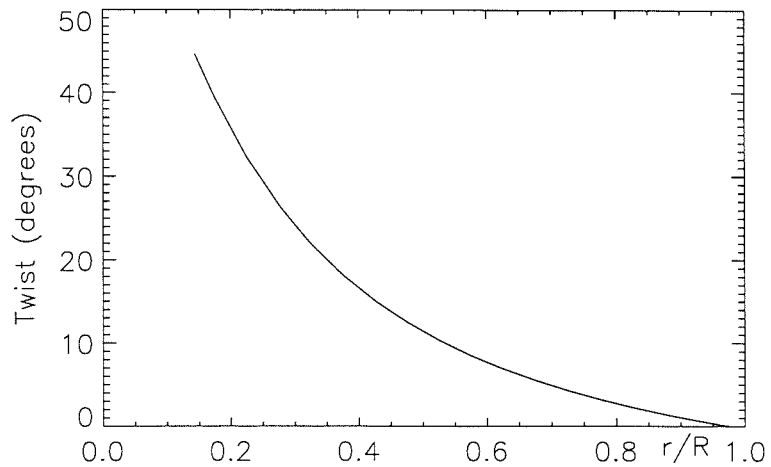


Figure B.1: Phases III and IV blade twist

Table B.1: NREL S809 aerofoil

x/c	y/c	x/c	y/c	x/c	y/c	x/c	y/c
0.00037	0.00275	0.52005	0.09237	0.00140	-0.00498	0.52837	-0.08697
0.00575	0.01166	0.56801	0.08356	0.00933	-0.01272	0.57663	-0.07442
0.01626	0.02133	0.61747	0.07379	0.02321	-0.02162	0.62649	-0.06112
0.03158	0.03136	0.66718	0.06403	0.04223	-0.03144	0.67710	-0.04792
0.05147	0.04143	0.71606	0.05462	0.06579	-0.04199	0.72752	-0.03558
0.07568	0.05132	0.76314	0.04578	0.09325	-0.05301	0.77668	-0.02466
0.10390	0.06082	0.80756	0.03761	0.12397	-0.06408	0.82348	-0.01559
0.13580	0.06972	0.84854	0.03017	0.15752	-0.07467	0.86677	-0.00859
0.17103	0.07786	0.88537	0.02335	0.19362	-0.08447	0.90545	-0.00370
0.20920	0.08505	0.91763	0.01694	0.23175	-0.09326	0.93852	-0.00075
0.24987	0.09113	0.94523	0.01101	0.27129	-0.10060	0.96509	0.00054
0.29259	0.09594	0.96799	0.00600	0.31188	-0.10589	0.98446	0.00065
0.33689	0.09933	0.98528	0.00245	0.35328	-0.10866	0.99612	0.00024
0.38223	0.10109	0.99623	0.00054	0.39541	-0.10842	1.00000	0.00000
0.42809	0.10101	1.00000	0.00000	0.43832	-0.10484	0.00000	0.00000
0.47384	0.09843	-	-	0.48234	-0.09756	-	-

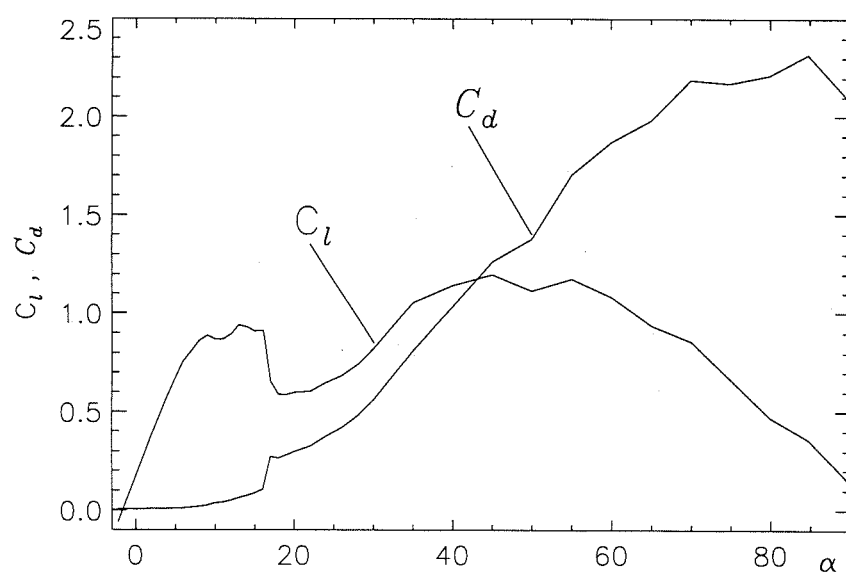


Figure B.2: NREL S809 aerofoil aerodynamic data

Appendix C

Nomenclature

Principal Notation

bar ($\bar{\cdot}$)	denoting non-dimensional quantity quantities of length are normalised by R except where otherwise stated; quantities of time are normalised by T_{nw} except where otherwise stated; quantities of velocity are normalised by V_0 except where otherwise stated
A_{ij}	normal component of velocity induced at the control point of the i th panel by a unit value of source strength on the j th panel
A_1, A_2, A_3, A_4	constants used in indicial response functions
a	axial induced velocity factor at blade
a'	tangential induced velocity factor at blade
B	number of blades
B_t	width of tower shadow
b_1, b_2, b_3, b_4, b_5	constants used in indicial response functions

$(CP)_v$	vortex-induced centre of pressure
C_d	drag coefficient
C_l	lift coefficient
$C_{l\alpha}$	lift curve slope
C_m	pitching moment coefficient
C_{m_0}	zero-lift pitching moment coefficient
C_n	normal force coefficient
C'_n	force coefficient normal to the rotor disc
$C_{n\alpha}$	normal force (lift) curve slope
C_P	power coefficient
C_Q	torque coefficient
C_T	thrust coefficient
C_t	tangential (chordwise) force coefficient
C'_t	force coefficient circumferential to the rotor disc
C_1, C_2, C_3	correction factors in stall delay model
c	chord
c_p	pressure coefficient
D	resultant change rate; deficiency function; tower diameter
D_V	maximum velocity deficit
D_w	contribution of currently trailed vortex element to downwash
$\mathbf{e}_r, \mathbf{e}_\psi, \mathbf{e}_{z'}$	unit vectors in cylindrical coordinate system
F	far wake velocity parameter
F_t	Prandtl tip loss factor
f	parameter for tip loss correction (Eq. 1.29); separation point
f_a	see Eq. 2.61
f_d, f_l	drag and lift 3-D correction factors

f_t	see Eq. 2.62
H	hub height
h	height above the ground (Chapter 3); distance from vortex trailing point to evaluation point on blade; perpendicular distance from a point in space to a vortex line
h_0	reference height
I	influence coefficient due to vortex
i, j, k	unit vectors in cartesian coordinate system
K_f	constant representing dynamic stall effect on chordwise force
K_w	downwash component ratio
k	constant representing velocity gradient
k_t	chordwise force efficiency
k_0, k_1, k_2	coefficients representing pitching moment curve fit
L	lift
l	azimuth index (Eq. 2.33)
M	Mach number
m	azimuth index (Eq. 2.34)
N	sample index; number of panels
N_C	number of wake cycles
N_E	number of blade elements
N_T	number of time steps per revolution
N_{ts}	number of azimuthal intervals within a quarter cycle used in high resolution model
n	unit normal vector
P	rotor power; evaluation point in space
p	pressure; evaluation point on boundary surface (Chapter 6)

Q	rotor torque
q	pitch rate; point where singularity is located
R	rotor radius
R_c	vortex core radius
R_e	Reynolds number
R_t	root radius or extension
R_1	wake radius
r	radial distance; distance between two points; polar coordinate
r_c	distance from vortex core centre
\bar{r}_c	$= r_c/R_c$
r_1	local radius of wake far downstream
S	non-dimensional distance travelled by aerofoil in semi-chords; boundary surface
$S_q^m, S_q^n, S_\alpha^m, S_\alpha^n$	constants used in indicial response functions
S_f, S_p	empirical constants used in modelling lags in unsteady responses
S_v	non-dimensional vortex decay time constant
S_1, S_2	coefficients representing separation point curve fit
s	laminar separation point; arc length of vortex filament
T	rotor thrust
T_{nw}	time period from blade to near wake cut-off point
t	time
u	velocity induced by a two-dimensional vortex
V	velocity; axial velocity through the rotor disc

V_0	uniform wind velocity;
	wind velocity at hub height
V_1	axial velocity in the wake far downstream
V_∞	freestream velocity
\tilde{V}	flow velocity within tower shadow
V_i^p	velocity induced at a point in space by a unit value of source strength
W	resultant inflow velocity
w	wash flow velocity
w_E	exact value of downwash
w_{pwn}	downwash obtained from the prescribed wake model due to first quarter cycle of trailed vortex element
w_0	initial value of downwash
X_w, Y_w	components of downwash
X_1, X_2, X_3, X_4	deficiency functions
Y_1, Y_2, Y_3	deficiency functions
x, y, z	cartesian coordinates in wind system
x', y', z'	cartesian coordinates in turbine-based system
y_f	vertical coordinate of separation point
Z_t	distance from yawing axis to rotor rotation plane
α	angle of attack
α_0	zero-lift angle of attack
α_1	angle of attack at break point of separation point fit curve
β	$= \sqrt{1 - M^2}$, compressibility correction parameter
Γ	vorticity
γ	yaw angle
Δ	denoting increment or decrement

η	shear exponent
η_t	see Eq. 3.51
θ	blade pitch angle; polar coordinate (Chapter 4)
	azimuthal angle of wake vortex element (Chapter 5)
Λ	modified tip speed ratio
λ	tip speed ratio
λ_r	local tip speed ratio
μ	exponent used in pitching moment curve fit; doublet strength (Chapter 6)
ϱ	air density
σ	local solidity of rotor; time variable (Section 3.3.2)
	source strength (Chapter 6)
τ_v	non-dimensional vortex time
τ_{vl}	non-dimensional time period during which vortex reaches trailing edge
v	induced velocity
Φ	decay parameter used in the near wake dynamic model
ϕ	inflow angle; indicial response function (Section 3.3.2)
φ	perturbation potential
ψ	azimuth
ψ_t	azimuthal angle of tower shadow
ψ_0	half angle of tower shadow; azimuth at which the near wake model is initiated
ψ_1	azimuthal angle at which blade enters tower shadow
ψ_2	azimuthal angle at which blade leaves tower shadow
Ω	angular velocity of rotor
ω	angular velocity of the wake just behind the rotor disc

Superscript

prime (')	denoting lag in unsteady leading edge pressure response
double prime (")	denoting lag in unsteady boundary layer response
<i>b</i>	denoting velocity induced by blade-bound vortex system
<i>bp</i>	denoting velocity at blade element boundary point
<i>C</i>	denoting circulatory response
<i>cp</i>	denoting velocity at blade element control point
<i>f</i>	denoting aerodynamic load associated with trailing edge separation
<i>I</i>	denoting impulsive response
<i>k</i>	denoting <i>k</i> th iteration
<i>p</i>	denoting induced velocity due to source panels
<i>q</i>	denoting unsteady response due to change in pitch rate
<i>s</i>	denoting contribution of shed vorticity
<i>t</i>	denoting contribution of trailed vorticity
<i>v</i>	denoting unsteady response due to dynamic stall vortex
<i>w</i>	denoting velocity induced by turbine wake vortex system
<i>wn</i>	denoting disturbance velocity at wake node
α	denoting unsteady response due to change in angle of attack
Γ	denoting velocity induced by turbine vortex system

Subscript

- ac denoting aerodynamic centre
- b denoting bound vorticity
- bp denoting quantity at blade element boundary point
- cp denoting quantity at blade element control point
- e denoting effective value
- f denoting quantity associated with trailing edge separation
- i blade element index;
 - blade element boundary index;
 - panel index
- j azimuth index;
 - panel index
- k blade index
- l azimuth index (see Eq. 2.33)
- m azimuth index (see Eq. 2.34);
 - denoting quantity associated with pitching moment (Section 3.3.2)
- n wake cycle index;
 - denoting normal direction;
 - denoting quantity associated with normal force
- p denoting quantity associated with pressure (Section 3.3.3);
 - denoting quantity at panel control point (Chapter 6)
- q denoting quantity associated with pitch rate (Section 3.3.2)
- r denoting radial component
- s denoting shed vorticity;
 - denoting quantity associated with separation
- t denoting trailed vorticity;
 - denoting quantity associated with tangential force;
 - denoting quantity associated with tower shadow

v	denoting quantity associated with dynamic stall vortex
W	denoting quantity associated with resultant velocity (Section 3.3.2)
w	denoting quantity in wake; denoting quantity associated with downwash (Chapter 5)
x, y, z, z'	denoting components in the coordinate axis directions
α	denoting quantity associated with angle of attack
θ, ψ	denoting tangential or circumferential component
$2D$	denoting two-dimensional quantity
$3D$	denoting three-dimensional quantity

Bibliography

- Abbott, I. H. and A. E. von Doenhoff (1959). *Theory of wing sections*. Dover Publications, Inc.. New York.
- Acker, T. L. and M. M. Hand (1999). Aerodynamic performance of the NREL Unsteady Aerodynamics Experiment (Phase IV) twisted rotor. In: *A Coll. 1999 ASME Wind Energy Symp. Tech. Papers Presented 37th AIAA Aerospace Sci. Meeting and Exh., Reno, USA, AIAA-99-0045*.
- Ackerman, M. C. (1992). Yaw modelling of small wind turbines. *J. Wind Eng. and Ind. Aerodyn* **39**(1–3), 1–9.
- Afjeh, A. A. and T. G. Jr. Keith (1986a). A simplified free wake method for horizontal axis wind turbine performance prediction. *ASME J. Fluids Eng.* **108**(4), 400–406.
- Afjeh, A. A. and T. G. Jr. Keith (1986b). A vortex lifting line method for the analysis of horizontal axis wind turbines. *ASME J. Solar Energy Eng.* **108**(4), 303–309.
- Afjeh, A. A. and T. G. Jr. Keith (1989). Simple computational method for performance prediction of tip-controlled horizontal axis wind turbines. *J. Wind Eng. and Ind. Aerodyn.* **32**(3), 231–245.
- Ahmad, J. and E. P. N. Duque (1996). Helicopter rotor blade computation in unsteady flows using moving embedded grids. *J. Aircraft* **33**(1), 54–60.
- Anderson, M. B., D. J. Milborrow and J. N. Ross (1982). Performance and wake measurements on a 3 m diameter horizontal axis wind turbine rotor. In: *Proc. 4th Int. Symp. on Wind Energy Systems, Stockholm*.
- Arsuffi, G., G. Guj and L. Morino (1993). Boundary element analysis of unsteady aerodynamics of windmill rotors in the presence of yaw. *J. Wind Eng. and Ind. Aerodyn.* **45**(2), 153–173.
- Ashby, D. L. and D. R. Sandlin (1985). Application of a low order panel method to complex three-dimensional internal flow problems. NASA CR-179656.

- Ashby, D. L., M. R. Dudley, S. K. Iguchi, L. Browne and J. Katz (1991). Potential flow theory and operation guide for the panel code PMARC. NASA TM-102851.
- Ashill, P. R. (1994). Boundary-flow measurements for wall interference assessment and correction. *AGARD-CP - 5351* pp. 12.1–12.2.
- Aspliden, C., T. Healy, E. Johanson, T. Kornreich, R. Kottler, W. Robins, R. Thomas, I. Vas, L. Wendell and R. Williams (1981). The wind energy program in the united states of america. In: *Alternative Energy Sources* (J.T. Manassah, Ed.). pp. 405–517. Academic Press.
- AWEA (1997). *Wind energy and climate change*. American Wind Energy Association. Available through <http://www.econet.org/aewa>.
- Banks, W. H. H. and G. E. Gadd (1963). Delaying effect of rotation on laminar separation. *AIAA J.* **1**(4), 941–942.
- Barnsley, M. J. and J. F. Wellicome (1992). Wind tunnel investigation of stall aerodynamics for a 1.0 m horizontal axis rotor. *J. Wind Eng. and Ind. Aerodyn.* **39**(1–3), 11–21.
- Basuno, B. (1992). A prescribed wake model for vertical axis wind turbines. PhD thesis. Univ. of Glasgow.
- Beans, E. W. (1983). Approximate aerodynamic analysis for horizontal axis wind turbines. *J. Energy* **7**(3), 243–249.
- Beddoes, T. S. (1978). Onset of leading edge separation effects under dynamic conditions and low Mach number. In: *Proc. 34nd Ann. Forum – Am. Helicopter Soc.*
- Beddoes, T. S. (1983). Representation of airfoil behaviour. *Vertica* **7**(2), 183–197.
- Beddoes, T. S. (1984). Practical computation of unsteady lift. *Vertica* **8**(1), 55–71.
- Beddoes, T. S. (1987). A near wake dynamic model. In: *Proc. Am. Helicopter Soc. Nat. Specialists Meeting on Aerodyn. and Acoustics, Feb. 1987.*
- Beddoes, T. S. (1989). Two and three dimensional indicial methods for rotor dynamic airloads. In: *Proc. Am. Helicopter Soc. Nat. Specialists Meeting on Rotorcraft Dynamics, Arlington, Texas, 1989.*
- Betz, A. (1926). *Wind energy and its exploitation by windmills*. Gottingen.
- Bierbooms, W. A. A. M. (1992). A comparison between unsteady aerodynamic models. *J. Wind Eng. and Ind. Aerodyn.* **39**(1–3), 23–33.
- Bisplinghoff, R. L., H. Ashley and R. L. Halfman (1996). *Aeroelasticity*. Dover Publications, Inc.. New York.

- Bliss, D. B., M. E. Teske and T. R. Quackenbush (1987). A new methodology for free wake analysis using curved vortex elements. NASA CR-3958.
- Bloy, A. W. and D. G. Robert (1993). Aerodynamic characteristics of the NACA 63₂-215 aerofoil for use in wind turbines. *Wind Eng.* **17**(2), 67–75.
- Bourillon, C. (1999). Wind energy – clean power for generations. *Renewable Energy* **16**(1–4), 78–82.
- Breglio, V. (1995). *Sustainable energy budget coalition survey*. Washington.
- Browne, L. and J. Katz (1990). Application of panel methods to wind-tunnel wall interference corrections. AIAA-90-0007.
- Bruining, A. and W. A. Timmer (1992). Airfoil characteristics of rotating wind turbine blades. *J. Wind Eng. and Ind. Aerodyn.* **39**(1–3), 35–39.
- Burgers, J. M. (1948). A mathematical model illustrating the theory of turbulence. *Adv. Appl. Mech.* **1**, 171–199.
- Butter, D. J., B. Hunt and G. R. Hargreaves (1982). A survey on boundary integral method. In: *Numerical Method in Aeronautical Fluid Dynamics* (P. L. Roe, Ed.). pp. 469–515. Academic Press.
- Butterfield, C. P. (1989a). Aerodynamic pressure and flow-visualization measurement from a rotating wind turbine blade. In: *8th ASME Wind Energy Symp. Houston, TX, USA*.
- Butterfield, C. P. (1989b). Three-dimensional airfoil performance measurements on a rotating wind turbine wing. In: *Proc. Eur. Wind Energy Conf. '89, Glasgow, Scotland*.
- Butterfield, C. P., G. Scott and W. Musial (1992a). Comparison of wind tunnel airfoil performance data with wind turbine blade data. *ASME J. Solar Energy Eng.* **114**(2), 119–124.
- Butterfield, C. P., W. P. Musial and D. A. Simms (1992b). Combined Experiment Phase I – final report. NREL/TP-257-4655. Nat. Renewable Energy Lab.
- Butterfield, C. P., W. P. Musial, G. N. Scott and D. A. Simms (1992c). NREL Combined Experiment final report – Phase II: draft. NREL/TP-442-4807. Nat. Renewable Energy Lab.
- Cardona, J. L. (1984). Flow curvature and dynamic stall simulated with an aerodynamic free-vortex model for VAWT. *Wind Eng.* **18**(3), 135–143.
- Carr, L. W. (1988). Progress in analysis and prediction of dynamic stall. *J. Aircraft* **25**(1), 6–17.
- Carr, L. W. and M. S. Chandrasekhara (1996). Compressibility effects on dynamic stall. *Prog. Aerospace Sci.* **32**, 523–573.

- Carr, L. W., K. W. McAlister and W. J. McCroskey (1977). Analysis of the development of dynamic stall based on oscillating airfoil experiments. NASA TN D-8382.
- Cavallo, A. J., S. M. Hock and D. R. Smith (1993). Wind energy: technology and economics. In: *Renewable Energy: Sources for Fuels and Electricity* (T.B. Johansson, H. Kelly, A.K.N. Reddy and R.H. Williams, Eds.). pp. 121–156. Island Press.
- Chaviaropoulos, P. K. (1996). Development of a state-of-the-art aeroelastic simulator for horizontal axis wind turbines. Part 1. Structural aspects. *Wind Eng.* **20**(6), 405–421.
- Cheung, C. W. and G. J. Hancock (1988). Wind tunnel interference on unsteady two-dimensional aerofoil motions in flow speed flows. *Aeronaut. J.* **92**(913), 115–121.
- Chiou, Y. D. and D. A. Peters (1988). Numerical solutions of induced velocities by semi-infinite tip vortex lines. *J. Aircraft* **25**(8), 684–694.
- Clark, R. N. and R. G. Davis (1991). Performance changes caused by rotor blade surface debris. In: *Windpower '91*. pp. 470–474. American Wind Energy Association.
- Clausen, P. D. and D. H. Wood (1988). An experimental investigation of blade element theory for wind turbines. part2. phase-locked averaged results. *J. Wind Eng. and Ind. Aerodyn.* **31**(2–3), 305–322.
- Clausen, P. D., D. M. Piddington and D. H. Wood (1987). An experimental investigation of blade element theory for wind turbines. part1. mean flow results. *J. Wind Eng. and Ind. Aerodyn.* **25**(2), 189–206.
- Clayton, B. R. and P. Filby (1984). Improved performance analysis from tests on model wind turbines. In: *Proc. Eur. Wind Energy Conf., EWEC '84, Hamburg*. pp. 487–492.
- Conlisk, A. T. (1997). Modern helicopter aerodynamics. *Ann. Rev. Fluid Mech.* **29**, 515–567.
- Corrigan, J. J. and J. J. Schillings (1994). Empirical model for stall delay due to rotation. In: *Proc. Am. Helicopter Soc. Aerodyn. Specialists Conf., San Francisco, CA, Jan. 1994*. pp. 1–16 (8.4).
- Corsiglia, V. R., R. G. Schwind and N. A. Chigier (1973). Rapid scanning, three-dimensional hot-wire anemometer surveys of wing-tip vortices. *J. Aircraft* **10**(12), 752–757.
- Coton, F. N., D. Jiang and R. A. McD. Galbraith (1994). Unsteady prescribed wake model for vertical axis wind turbines. *Proc. I.Mech.E., Part A: J. Power and Energy* **208**(1), 13–16.
- Crouse, G. L. Jr. and J. G. Leishman (1993). A new method for improved rotor free-wake convergence. AIAA-93-9872.

- David, S., P. Sandra, L. Simon and L. Brian (1997). Blyth harbour wind farms and birds. In: *Proc. Eur. Wind Energy Conf. '97, Dublin, Ireland.*
- Dawn, T. (1994). Sonar helps windpower tackle tonal noise. *Noise and Vibration Worldwide* **25**(7), 13–17.
- de Vries, O. (1979a). Fluid dynamic aspects of wind energy conversion. *AGARDograph – 243.*
- de Vries, O. (1979b). Wind tunnel tests on a model of a two bladed horizontal axis wind turbine. NLR-TR-79071L. Nat. Aerospace Lab., Amsterdam.
- de Vries, O. and M. den Blanken (1981). Second series of wind tunnel tests on a model of a two-bladed horizontal axis wind turbine. NLR-TR-81069. Nat. Aerospace Lab., Amsterdam.
- Dini, P., M. D. Selig and M. D. Maughmer (1991). A simplified method for separated boundary layers. AIAA-91-3285.
- Dress, J. (1976). The art and science of rotary wing data correction. *J. Am. Helicopter Soc.*
- Du, Z. and M. S. Selig (1998). A 3-D stall-delay model for horizontal axis wind turbine performance prediction. In: *A Coll. 1998 ASME Wind Energy Symp. Tech. Papers Presented 36th AIAA Aerospace Sci. Meeting and Exh., Reno, USA, AIAA-98-0021.*
- Duque, E. P. N., C. P. van Dam and S. C. Hughes (1999). Navier-Stokes simulations of the NREL Combined Experiment Phase II rotor. In: *A Coll. 1999 ASME Wind Energy Symp. Tech. Papers Presented 37th AIAA Aerospace Sci. Meeting and Exh., Reno, USA, AIAA-99-0037.*
- Dwyer, H. and W. J. McCroskey (1970). Crossflow and unsteady boundary layer effects on rotating blades. AIAA-70-50.
- Eggers, A. J. Jr. and R. V. Digumarthi (1992). Approximate scaling of rotational effects of mean aerodynamic moments and power generated by the Combined Experiment rotor blades operating in deep-stalled flow. In: *11th ASME Wind Energy Symp.* pp. 33–43. ASME Solar Eng. Div., Vol.12.
- Eggleson, D. M. (1991). Wind turbine bug roughness sampling and power degradation. In: *Windpower '91.* American Wind Energy Association.
- Egolf, T. A. (1988). Helicopter free-wake prediction of complex wake structures under blade-vortex interaction operating conditions. In: *Proc. 44th Ann. Forum – Am. Helicopter Soc..* pp. 819–832.
- Egolf, T. A. and S. P. Sparks (1986). A full potential rotor analysis with wake influence using an inner-outer domain technique. In: *Proc. 42nd Ann. Forum – Am. Helicopter Soc..* pp. 997–1011.

- Ekaterinaris, J. A. and M. F. Platzer (1997). Computational prediction of airfoil dynamic stall. *Prog. Aerospace Sci.* **33**(11–12), 759–846.
- Ekaterinaris, J. A., N. N. Sorensen and F. Rasmussen (1998). Numerical investigation of airfoil dynamic stall in simultaneous harmonic oscillatory and translatory motion. *ASME J. Solar Energy Eng.* **120**(1), 75–83.
- Eldridge, F. R. (1980). *Wind Machines*. 2nd ed.. Van Nostrand Reinhold Company. New York.
- Eppler, R. (1990). *Airfoil design and data*. Springer-Verlag. Berlin/New York.
- Ericsson, L. E. and J. P. Reding (1972). Dynamic stall of helicopter blades. *J. Am. Helicopter Soc.* **17**(1), 11–19.
- Ericsson, L. E. and J. P. Reding (1987). Fluid dynamics of unsteady separated flow. *Prog. Aerospace Sci.* **24**, 249–356.
- European Commission Directorate-General for Energy (1998). *Wind Energy – the Facts*. European Wind Energy Association. Available through <http://www.ewea.org>.
- Fingersh, L. J., D. A. Simms, C. P. Butterfield and M. D. Jenks (1995). Overview of the Unsteady Aerodynamics Experiment Phase III data acquisition system and instrumentation. In: *Wind Energy 1995 – Proc. Energy-Source Technology Conf. and Exh., Houston, TX, USA* (W. D. Musial, S. M. Hock and D. E. Berg, Eds.). pp. 277–280. ASME Solar Eng. Div., Vol.16.
- Flavin, C. and S. Dunn (1998). Climate of opportunity: Renewable energy after Kyoto. In: *World Renewable Energy Policy Project*. Washington, DC. Available through <http://www.repp.org>.
- Fogarty, L. E. (1951). The laminar boundary layer on a rotating blade. *J. Aeronaut. Sci.* **18**(4), 247–252.
- Fogarty, L. E. and W. R. Sears (1950). Potential flow around a rotating, advancing cylindrical blade. *J. Aeronaut. Sci.* **17**(9), 599.
- Froude, R. E. (1889). On the part played in propulsion by differences of fluid pressure. *Trans. Inst. Naval Arch.* **30**, p. 390.
- Fuglsang, P. and H. A. Madsen (1998). Wind turbine design with numerical optimization and a semi-empirical noise prediction model. *Wind Eng.* **22**(1), 31–41.
- Fulton, R., K. Koch and C. Moffat (1984). *Wind energy study, Anelos National Forest*. Calif. State Polytech. Univ.. Pomona, CA.
- Galbraith, R. A. McD., A. J. Niven and F. N. Coton (1990). Aspects of unsteady aerodynamics in wind turbines. *Wind Eng.* **14**(5), 286–299.

- Gangwani, S. T. (1982). Prediction of dynamic stall and unsteady airloads for rotor blades. *J. Am. Helicopter Soc.* **27**(4), 57–64.
- Gaudiosi, G. (1999). Offshore wind energy prospects. *Renewable Energy* **16**(1–4), 828–834.
- Giannakidis, G. and J. M. R. Graham (1997). Prediction of loading on a HAWT rotor including effects of stall. In: *Proc. Eur. Wind Energy Conf. '97, Dublin, Ireland*.
- Giguere, P. and M. S. Selig (1997). Low Reynolds number airfoils for small horizontal axis wind turbines. *Wind Eng.* **21**(6), 367–380.
- Gipe, P. (1995). *Wind energy comes of age*. John Wiley & Sons, Inc.
- Gipe, P. (1998). Overview of worldwide wind generation. *Renewable Energy* **15**(1–4), 78–82.
- Glauert, H. (1935). Airplane propellers. In: *Aerodynamic Theory* (W. F. Durand, Ed.). Vol. IV, Div.L. Springer. Berlin.
- Glauert, H. (1948). *The Elements of Aero Foil and Airscrew Theory*. Cambridge Univ. Press. Cambridge.
- Gohard, J. (1978). Free wake analysis of wind turbine aerodynamics. In: *Wind Energy Conversion*. Vol. VIII. U. S. Dept of Energy, COO 3141-T1/MIT, ASRL TR-184-14.
- Gormont, R. E. (1973). A mathematical model of unsteady aerodynamics and radial flow for application to helicopter rotors. US Army AMRDL Eustis Directorate Report TR-72-67. US Army Air Mobility Res. Dev. Lab.
- Gould, J. and S. P. Fiddes (1992). Computational methods for the performance of hawts. *J. Wind Eng. and Ind. Aerodyn.* **39**(1–3), 61–72.
- Graber, A. and A. Rosen (1987). Velocities induced by semi-infinite helical vortex filaments. *J. Aircraft* **24**(5), 289–290.
- Graham, J. M. R. and C. J. Brown (1999). Aerodynamics of horizontal axis rotor interacting with the tower. In: *Proc. Eur. Wind Energy Conf. '99, Nice, France*.
- Grant, I., M. Mo, X. Pan, P. Parkin, J. Powell, H. Reineche, K. Shuang, F. Coton and D. Lee (1998). Optical evaluation of the wake characteristics of a wind turbine and a prescribed wake model. In: *8th Int. Symp. on Flow Visualization*.
- Green, R. B. and R. A. McD. Galbraith (1994). Phenomena observed during aerofoil ramp-down motions from the fully separated states. *Aeronaut. J.* **98**(979), 349–356.
- Griffiths, R. T. (1977). Effect of aerofoil characteristics on windmill performance. *Aeronaut. J.* **81**(799), 322–326.

- Griffiths, R. T. and M. G. Woollard (1978). Performance of the optimal wind turbine. *Applied Energy* **4**(4), 261–272.
- Grubb, M.J. and N.I. Meyer (1993). Wind energy: Resources, systems and regional strategies. In: *Renewable Energy: Sources for Fuels and Electricity* (T.B. Johansson, H. Kelly, A.K.N. Reddy and R.H. Williams, Eds.). pp. 157–212. Island Press.
- Guilmineau, E. and P. Queutey (1999). Numerical study of dynamic stall on several airfoil sections. *AIAA J.* **37**(1), 128–130.
- Hackett, J. E., D. J. Wilsden and W. A. Stevens (1981). Review of the “wall pressure signature” and other tunnel constraint correction methods for high angle-of-attack tests. *AGARD R – 692*.
- Hales, R. L. (1991). Dynamic stall on horizontal-axis wind turbines. In: *Wind Energy Technology and Implementation – Proc. Eur. Wind Energy Conf. '91* (F. J. L. van Hulle, P. T. Smulders and J. B. Dragt, Eds.). pp. 34–39. Elsevier Science Publishers B. V.
- Hammarlund, K. (1997). The social impacts of wind power. In: *Proc. Eur. Wind Energy Conf. '97, Dublin, Ireland*.
- Han, Y. (1999). Wind energy development in China— reality and market forces. *Renewable Energy* **16**(1–4), 965–969.
- Hansen, A. C. (1995). Aerodynamic damping of blade flap motions at high angles of attack. *ASME J. Solar Energy Eng.* **117**(3), 194–199.
- Hansen, A. C. and C. P. Butterfield (1993). Aerodynamics of horizontal-axis wind turbines. *Ann. Rev. Fluid Mech.* **25**, 115–149.
- Hansen, A. C., C. P. Butterfield and X. Cui (1990). Yaw loads and motions of a horizontal axis wind turbine. *ASME J. Solar Energy Eng.* **112**(4), 310–314.
- Harris, F. D. (1966). Preliminary study of radial flow effects on rotor blades. *J. Am. Helicopter Soc.* **11**(3), 1–21.
- Harris, F. D., F. J. Tarzanin and R. K. Jr. Fisher (1970). Rotor high-speed performance; theory vs. test. *J. Am. Helicopter Soc.* **15**(3), 35–44.
- Hartin, J. R. (1990). Evaluation of prediction methodology for blade loads on a horizontal axis wind turbine. *ASME J. Solar Energy Eng.* **112**(4), 315–319.
- He, D. and G. Jiang (1989). An investigation of blockage correction for a wind turbine in CARDC low speed wind tunnel. In: *Proc. Eur. Wind Energy Conf. '86, Rome, Italy*.

- Hemon, P., D. Olivari and M. Wurmser (1992). Experimental investigation of horizontal axis wind turbine dynamic stall in a wind tunnel. *J. Wind Eng. and Ind. Aerodyn.* **39**(1–3), 73–82.
- Henderson, A. and M. Petel (1998). Rigid-body motion of a floating offshore wind farm. *Int. J. Ambient Energy* **19**(3), 127–134.
- Hernandez, J. and A. Crespo (1987). Aerodynamic calculation of the performance of horizontal axis wind turbines and comparison with experimental results. *Wind Eng.* **11**(4), 177–187.
- Hess, J. L (1973). High-order numerical solution of the integral equation for the two-dimensional Neumann problem. *Comput. Methods Appl. Mech. Eng.* **2**, 1–15.
- Hess, J. L (1990). Panel methods in computational fluid dynamics. *Ann. Rev. Fluid Mech.* **22**, 255–274.
- Hess, J. L and A. M. O. Smith (1967). Calculation of potential flow about arbitrary bodies. *Prog. Aerospace Sci.* **8**, 1–138.
- Holt, D. R. and B. Hunt (1982). The use of panel methods for the evaluation of subsonic wall interference. *AGARD-CP – 335* pp. 2.1–2.16.
- Hoskins, P. S., N. Bose and J. Rong (1992). Experimental characteristics of a NASA LS(1)-0417 aerofoil with simulated icing. *Wind Eng.* **16**(4), 236–246.
- Hunt, B. (1978). The panel method for subsonic aerodynamic flows: a survey of mathematical formulations and numerical models and an outline of the new British Aerospace scheme. Lecture Series 1978 – 4: Computational Fluid Dynamics. Von Karman Institute for Fluid Dynamics.
- Hunt, V. D. (1981). *Wind power: a handbook on wind energy conversion systems*. van Nostrand Reinhold Company. New York.
- Hurst, D., R. A. McD. Gaibraith, F. N. Coton and I. Grant (1998). Facility for simultaneous particle image velocimetry and high resolution unsteady pressure measurement. *Aeronaut. J.* **102**(1014), 201–209.
- Huyer, S. A., D. Simms and M. C. Robinson (1996). Unsteady aerodynamics associated with a horizontal-axis wind turbine. *AIAA J.* **34**(7), 1410–1419.
- Huyer, S. A., M. A. Reavis and M. W. Luttges (1988). A comparative study of differing vortex structures arising in unsteady separated flows. In: *Proc. 6th AIAA Applied Aerodyn. Conf., Williamsburg, USA, AIAA-88-2582*.
- Jamieson, P. (1998). Small wind turbines – the market. *Wind Directions* **17**(April), 16–17.

- Jasinski, W. J., S. C. Noe, M. S. Selig and M. B. Bragg (1998). Wind turbine performance under icing conditions. *ASME J. Solar Energy Eng.* **120**(1), 60–65.
- Johnson, W. (1995). General free wake geometry calculation for wings and rotors. In: *Proc. 51st Ann. Forum – Am. Helicopter Soc.*. Vol. 1. pp. 137–153.
- Jones, C. N. (1983). Blade element performance in horizontal-axis wind-turbine rotors. *Wind Eng.* **7**(3), 129–137.
- Katz, J. and A. Plotkin (1991). *Low speed aerodynamics: from wing theory to panel methods*. McGraw-Hill.
- Kelley, N. D. and H. E. McKenna (1985). Acoustic noise associated with the MOD-1 wind turbine: its source, impact and control. SERI/TP-635-116. Sol. Energy Res. Inst.
- Kirchhoff, R. H., F. C. Kaminsky and P. Soikkeli (1990). Downwind wake behavior of a wind turbine superimposed above an operating wind farm: wind tunnel experiments. In: *9th ASME Wind Energy Symp. New Orleans, USA*. pp. 39–46. ASME Solar Eng. Div., Vol.9.
- Kocurek, D. (1987). Lifting surface performance analysis for horizontal axis wind turbines. SERI/STR-217-3163. Sol. Energy Res. Inst.
- Koh, S. G. and D. H. Wood (1991a). Formulation of a vortex wake model for horizontal-axis wind turbines. *Wind Eng.* **15**(4), 196–210.
- Koh, S. G. and D. H. Wood (1991b). Implementation of a vortex wake model for horizontal-axis wind turbines. *Wind Eng.* **15**(5), 262–274.
- Kotb, M. A. and J. A. Schetz (1984). Windmill flowfield with non-uniform approach flow. In: *Proc. Eur. Wind Energy Conf., EWEC '84, Hamburg*. pp. 500–505.
- Kotb, M. A. and M. M. AbdelHaq (1992). Rigid wake model for a horizontal axis wind turbine. *Wind Eng.* **16**(2), 95–108.
- Krohn, S. and S. Damborg (1999). On public attitudes towards wind power. *Renewable Energy* **16**(1–4), 954–960.
- Kumar, S. (1999). Wind energy – India overview. *Renewable Energy* **16**(1–4), 961–964.
- Lain, S., J. A. Garcia and R. Aliod (1995). Development of a lifting surface-2D panel method to compute the three-dimensional pressure distribution over the blade of a horizontal-axis wind turbine. *Wind Eng.* **19**(1), 21–40.
- Lakshminarayana, B. and T. R. Govindan (1981). Analysis of turbulent boundary layer on cascade and rotor blades of turbomachinery. *AIAA J.* **19**(10), 1333–1341.

- Lamb, H. (1932). *Hydrodynamics*. Cambridge University Press.
- Landahl, M. T. (1981). Roll-up model for rotor wake vortices. ASRL-TR-194-4. MIT.
- Larrabee, E. E. and S. E. French (1983). Minimum induced loss windmills and propellers. *J. Wind Eng. and Ind. Aerodyn.* **15**(1-3), 317-327.
- Lee, K. D. (1981). Numerical simulation of the wind tunnel environment by a panel method. *AIAA J.* **19**(4), 470-475.
- Leishman, J. G. (1987a). Practical modeling of unsteady airfoil behaviour in nominally attached two-dimensional compressible flow. UM-AERO-87-6. University of Maryland.
- Leishman, J. G. (1987b). A semi-empirical model for dynamic stall. UM-AERO-87-24. University of Maryland.
- Leishman, J. G. (1988). Validation of approximate indicial aerodynamic functions for two-dimensional subsonic flow. *J. Aircraft* **25**(10), 914-922.
- Leishman, J. G. and T. S. Beddoes (1989). A semi-empirical model for dynamic stall. *J. Am. Helicopter Soc.* **34**(3), 3-17.
- Li, J. and L. Zhu (1999). Wind power commercialization development in China. *Renewable Energy* **16**(1-4), 817-821.
- Loeffler, A. L. Jr. and J. S. Steinhoff (1985). Computation of wind tunnel wall effects in ducted rotor experiments. *J. Aircraft* **22**(3), 188-192.
- Lowson, M. V. (1992). Applications of aero-acoustic analysis to wind turbine noise control. *Wind Eng.* **16**(3), 126-140.
- Lowson, M. V. (1994). New prediction model for wind turbine noise. *Wind Eng.* **18**(2), 51-61.
- Mager, A. (1954). Three-dimensional laminar boundary layer with small cross-flow. *J. Aeronaut. Sci.* **21**(12), 835-845.
- Manwell, J. F., W. Q. Jeffries and J. G. McGowan (1991). Power fluctuations from a horizontal axis wind turbine. In: *Proc. 14th Ann. Energy-Sources Tech. Conf. and Exh., Houston, TX, USA*. pp. 63-69. ASME Solar Energy Div., Vol.11.
- Marini, M., A. Massardo and A. Satta (1992). Performances of vertical axis wind turbines with different shapes. *J. Wind Eng. and Ind. Aerodyn.* **39**(1-3), 83-93.
- Martinez, A. and P. Prats (1999). Wind technology issues. *Renewable Energy* **16**(1-4), 835-839.
- Maskew, B. (1980). Calculation of two-dimensional vortex/surface interference using panel methods. NASA CR-159334.

- Maskew, B. (1982). Prediction of subsonic aerodynamic characteristics: A case for low-order panel methods. *J. Aircraft* **19**(2), 157–163.
- McCroskey, W. J. (1981). The phenomenon of dynamic stall. NASA TM-81264.
- McCroskey, W. J. (1995). Vortex wakes of rotorcraft. AIAA-95-0530.
- McCroskey, W. J. and P. F. Yaggy (1968). Laminar boundary layers on helicopter rotors in forward flight. *AIAA J.* **6**(10), 1919–1926.
- McCroskey, W. J., L. W. Carr and K. W. McAlister (1975). Dynamic stall experiments on oscillating airfoils. AIAA-75-125.
- McGhee, R. J., W. D. Beasley and R. T. Whitcomb (1979). NASA low- and medium-speed airfoil development. NASA TM-78709.
- Milborrow, D. J. (1985). Changes in aerofoil characteristics due to radial flow on rotating blades. In: *Proc. 7th BWEA Wind Energy Conf., Oxford, England*.
- Miller, R. H. (1982). Free wake techniques for rotor aerodynamic analysis; Volume No. I – Summary of results and background theory. NASA CR-166434.
- Miller, R. H. (1983a). The aerodynamics and dynamic analysis of horizontal axis wind turbines. *J. Wind Eng. and Ind. Aerodyn.* **15**, 329–340.
- Miller, R. H. (1983b). Rotor hovering performance using the method of fast free wake analysis. *J. Aircraft* **20**(3), 257–261.
- Miller, R. H. (1984). Application of fast free wake analysis techniques to rotors. *Vertica* **8**(3), 255–261.
- Miller, R. H. (1985). Methods for rotor aerodynamic and dynamic analysis. *Prog. Aerospace Sci.* **22**(2), 113–160.
- Miller, R. H., J. Dugundji, M. Martinez-Sanchez, J. Gohard, S. Y. Chung and T. Humes (1978). Aerodynamics of horizontal axis wind turbines. In: *Wind Energy Conversion*. Vol. II. U. S. Dept of Energy, COO 3141-T1/MIT, ASRL TR-184-8.
- Miranda, L. R. (1984). Application of computational aerodynamics to airplane design. *J. Aircraft* **21**(6), 355–370.
- Mokry, M. (1995). Wall interference correction to drag measurements in automotive wind tunnels. *J. Wind Eng. and Ind. Aerodyn.* **56**(2–3), 107–122.
- Mokry, M., J. R. Digney and R. J. D. Poole (1987). Doublet-panel method for half-model wind-tunnel corrections. *J. Aircraft* **24**, 322–327.

- Munduate, X. and F. N. Coton (1999). An aerodynamic method for the preliminary design of horizontal axis wind turbines. In: *Proc. 1st Int. Conf. Advanced Eng. Design, Prague, Czech R.*
- Musial, W. D., C. P. Butterfield and M. D. Jenks (1990). A comparison of two- and three-dimensional S809 airfoil property for rough and smooth HAWT rotor operation. In: *9th ASME Wind Energy Symp. New Orleans, USA*. pp. 63–70. ASME Solar Eng. Div., Vol.9.
- Musters, C. J. M., M.A.W. Noordervliet and W. J. ter Keurs (1996). Bird casualties caused by a wind energy project in an estuary. *Bird Study* **43**, 124–126.
- Narramore, J. C. and R. Vermeland (1992). Navier–Stokes calculations of inboard stall delay due to rotation. *J. Aircraft* **29**(1), 73–78.
- Nathan, G. K. and M. H. T. Yin (1990). Theoretical and experimental study of off-peak performance of horizontal axis wind turbines. *Wind Eng.* **14**(6), 347–361.
- Neogi, S. (1995). Modified flexible iterative model for the performance of slow speed wind turbines for water pumping. *Wind Eng.* **19**(5), 249–264.
- Niven, A. J. and R. A. McD. Galbraith (1997). Modelling dynamic stall vortex inception at low Mach numbers. *Aeronaut. J.* **101**(1002), 67–76.
- Niven, A. J., R. A. McD. Galbraith and D. G. F. Herring (1989). Analysis of reattachment during ramp-down tests. *Vertica* **13**(2), 187–196.
- Omnibus Report (1995). *Public Attitudes towards wind energy*. Canadian Wind Energy Association and Environment Monitor. Toronto.
- Owen, P. R. (1970). The decay of a turbulent trailing vortex. *Aeronaut. Quarterly* **21**, 69–78.
- Parkinson, G. V. and T. Jandali (1970). A wake source model for bluff body potential flow. *J. Fluid Mech.* **40**(3), 577–594.
- Percival, S. (1999). Birds and wind turbines: can they live together?. *Wind Directions* **18**(4), 18–20.
- Petot, D. (1983). Progress in the semi-empirical prediction of the aerodynamic forces due to large amplitude oscillations of an airfoil in attached or separated flow. In: *Proc. 9th Eur. Rotorcraft Forum, Stresa, Italy*.
- Pierce, K. and A. C. Hansen (1995). Prediction of wind turbine rotor loads using the Beddoes–Leishman model for dynamic stall. *ASME J. Solar Energy Eng.* **117**(3), 200–204.
- Powles, S. J. R. (1983). Effects of tower shadow on the dynamics of a horizontal-axis wind turbine. *Wind Eng.* **7**(1), 26–42.

- Powles, S. J. R. and M. B. Anderson (1984). Relative effect of stochastic and deterministic processes on fatigue damage in a large horizontal-axis wind turbine using numerical simulation. In: *Proc. 6th BWEA Wind Energy Conf., Reading, England.*
- Preuss, R. D., E. O. Suci and L. Morino (1980). Unsteady potential aerodynamics of rotors with applications to horizontal-axis windmills. *AIAA J.* **18**(4), 385–393.
- Quarton, D. C. (1997). Calculation of design loads for offshore wind turbines. *Wind Eng.* **21**(4), 267–279.
- Rae, W. H. Jr. and A. Pope (1984). *Low-speed wind tunnel testing*. 2nd ed.. John Wiley & Sons, Inc.. New York.
- Raghunathan, S., J. R. Harrison and B. D. Hawkins (1988). Thick airfoil at low Reynolds number and high incidence. *J. Aircraft* **25**(7), 669–671.
- Ramachandran, K., S. Schlechtriem, F. X. Caradonna and J. Steinhoff (1993). The application of vorticity embedding to the computation of advancing rotor flows. In: *Proc. 49th Ann. Forum – Am. Helicopter Soc.*.. pp. 571–584.
- Rand, O. and A. Rosen (1984). Efficient method of calculating the axial velocities induced along rotating blades by trailing helical vortices. *J. Aircraft* **21**(6), 433–435.
- Rankine, W. J. (1865). On the mechanical principles of the action of ship propellers. *Trans. Inst. Naval Arch.* **6**, 13–39.
- Rawlinson-Smith, R. I. and R. L. Hales (1990). Computational study of stalled rotor performance. In: *Proc. British Wind Energy Conf. '1990.*
- Rijs, R. P. P., P. Jacobs and P. T. Smulders (1992). Parameter study of the performance of slow running rotors. *J. Wind Eng. and Ind. Aerodyn.* **39**(1–3), 95–103.
- Riziotis, V. A., P. K. Chavariopoulos and S. G. Voutsinas (1996). Development of a state-of-the-art aeroelastic simulator for horizontal axis wind turbines. Part 2. Aerodynamic aspects and application. *Wind Eng.* **20**(6), 423–440.
- Robinson, M. C., R. A. McD. Galbraith, D. E. Shipley and M. S. Miller (1995). Unsteady aerodynamics of wind turbines. In: *33rd AIAA Aerospace Sci. Meeting and Exh., Reno, USA, AIAA-95-0526.*
- Robison, D. J., F. N. Coton, R. A. McD. Galbraith and M. Vezza (1994). The development of a prescribed wake model for the prediction of the aerodynamic performance of horizontal axis wind turbines in steady axial flow. GU AERO Reort-9403. University of Glasgow.

- Robison, D. J., F. N. Coton, R. A. McD. Galbraith and M. Vezza (1995). Application of a prescribed wake aerodynamic prediction scheme to horizontal axis wind turbines in axial flow. *Wind Eng.* **19**(1), 41–51.
- Ronsten, G. (1992). Static pressure measurements on a rotating and a non-rotating 2.375m wind turbine blade – comparison with 2D calculations. *J. Wind Eng. and Ind. Aerodyn.* **39**(1–3), 105–118.
- Ronsten, G., J. A. Dahlberg, G. Jiang and D. He (1995). An experimental investigation of the performance and wind tunnel wall interference for a wind turbine operating in yaw. FFA TN-1994-13. Aeronaut. Research Inst. of Sweden.
- Ronsten, G., J. A. Dahlberg, S. Meijer, D. He and M. Chen (1989). Pressure measurements on a 5.35m HAWT in CARDC 12 × 16m wind tunnel compared to theoretical pressure distributions. In: *Proc. Eur. Wind Energy Conf. '89, Glasgow, Scotland*.
- Rosen, A., I. Lavie and A. Seginer (1990). A general free-wake efficient analysis of horizontal-axis wind turbines. *Wind Eng.* **14**(6), 362–373.
- Rott, N. and W. E. Smith (1956). Some examples of laminar boundary-layer flow on rotating blades. *J. Aeronaut. Sci.* **23**(11), 991–996, 1006.
- Rule, J. A. and D. B. Bliss (1998). Prediction of viscous trailing vortex structure from basic loading parameters. *AIAA J.* **36**(2), 208–218.
- Saffman, P. G. (1973). Structure of turbulent line vortices. *Phys. Fluids* **16**(3), 1181–1188.
- Savino, J. M. and T. W. Nyland (1983). Wind turbine flow visualization studies: tip and root vortices and wind stream pattern at low power. Wind Energy Project Office PIR-241. NASA Lewis Research Center.
- Sayers, A. T. and D. R. Ball (1983). Blockage corrections for rectangular flat plates mounted in an open jet wind tunnel. *Proc. I.Mech.E., Part C: J. Mech. Eng. Sci.* **197**, 259–263.
- Schepers, J. G., A. J. Brand, A. Bruining, J. M. R. Graham, M. M. Hand, D. G. Infield, H. A. Madsen, R. J. H. Paynter and D. A. Simms (1997). Final report of IEA Annex XIV: Field Rotor Aerodynamics. ECN-C-97-027. Netherlands Energy Research Foundation ECN.
- Scherer, R. (1999). Blade design aspects. *Renewable Energy* **16**(1–4), 1272–1277.
- Schetz, J. A. and R. L. Figard (1982). Numerical solution of the flow near the rotor of a wind turbine. *J. Energy* **6**(2), 65–70.
- Schlichting, H. (1979). *Boundary-layer theory*. McGraw-Hill. New York.

- Scully, M. P. (1975). Computation of helicopter rotor wake geometry and its influence on rotor harmonic loads. ASRL-TR-178-1. MIT.
- Sears, W. R. (1950). Potential flow around a rotating cylindrical blade. *J. Aeronaut. Sci.* **17**(3), 183–184.
- Sesto, E. (1999). Wind energy in the world: reality and prospects. *Renewable Energy* **16**(1–4), 888–893.
- Sforza, P. M., P. Sheerin and M Smorto (1981). Three-dimensional wakes of simulated wind turbines. *AIAA J.* **19**(9), 1101–1107.
- Shipley, D. E., M. S. Miller and M. C. Robinson (1995a). Dynamic stall occurrence on a horizontal axis wind turbine. In: *Wind Energy 1995 – Proc. Energy-Source Technology Conf. and Exh., Houston, TX, USA* (W. D. Musial, S. M. Hock and D. E. Berg, Eds.). pp. 167–173. ASME Solar Eng. Div., Vol.16.
- Shipley, D. E., M. S. Miller, M. C. Robinson, M. W. Luttges and D. A. Simms (1995b). Techniques for the determination of local dynamic pressure and angle of attack on a horizontal axis wind turbine. NREL/TP-442-7393. Nat. Renewable Energy Lab.
- Simms, D. A., L. J. Fingersh and C. P. Butterfield (1995). NREL Unsteady Aerodynamics Experiment Phase III test objectives and preliminary results. In: *Wind Energy 1995 – Proc. Energy-Source Technology Conf. and Exh., Houston, TX, USA* (W. D. Musial, S. M. Hock and D. E. Berg, Eds.). pp. 273–275. ASME Solar Eng. Div., Vol.16.
- Simoes, F. J. and J. M. R. Graham (1992). Application of a free vortex wake model to a horizontal axis wind turbine. *J. Wind Eng. and Ind. Aerodyn.* **39**(1–3), 61–72.
- Simon, A. M. (1996). *A summary of research conducted into Attitudes to wind power from 1990 – 1996*. Planning and Research for British Wind Energy Association. London.
- Sipcic, S. R. and L. Morino (1985). Wake dynamics for incompressible and compressible flows. In: *Computational Methods in Potential Aerodynamics*. pp. 679–699. Springer-Verlag.
- Snel, H., R. Houwink and J. Bosschers (1994). Sectional prediction of lift coefficients on rotating wind turbine blades in stall. ECN-C-93-052. Netherlands Energy Research Foundation ECN.
- Snel, H., R. Houwink, J. Bosschers, W. J. Piers, G. J. W. van Bussel and A. Bruining (1993). Sectional prediction of 3-D effects for stalled flow on rotating blades and comparison with measurements. In: *Proc. Eur. Community Wind Energy Conf., Germany*. pp. 395–399.
- Snyder, M. H. and W. H. Jr. Wentz (1981). Dynamics of wakes downstream of wind turbine towers. NASA-CP-2185.

- Sorensen, J. N. and A. Myken (1992). Unsteady actuator disc model for horizontal axis wind turbines. *J. Wind Eng. and Ind. Aerodyn.* **39**(1–3), 139–149.
- Sorensen, J. N., J. A. Michelsen, M. O. L. Hansen, P. J. Nygreen and D. N. Sorensen (1997). Incompressible Navier-Stokes models for aerodynamic flows. *Advances Fluid Mech.* **11**, 185–224.
- Spalart, P. R. (1998). Airplane trailing vortices. *Ann. Rev. Fluid Mech.* **30**, 107–138.
- Spera, D. A. and D. C. Janetzke (1981). Performance and load data from MOD-OA and MOD-1 wind turbines. In: *Proc. Workshop on Large Horizontal-Axis Wind Turbines*. pp. 447–468. NASA CP-2230.
- Squire, H. B. (1965). The growth of a vortex in turbulent flow. *Aeronaut. Quarterly* **16**, 302–306.
- Steinhoff, J. and K. Ramachandran (1990). Free wake analysis of compressible rotor flows. *AIAA J.* **28**(3), 426–431.
- Stewart, H. J. (1976). Dual optimum aerodynamic design for a conventional windmill. *AIAA J.* **14**(11), 1524–1527.
- Stork, C. and G. Solmi (1991). Theoretical and experimental investigation on a one-bladed medium size WT to improve the design criteria – progress report. In: *Wind Energy Technology and Implementation – Pro. Eur. Wind Energy Conf. '91* (F. J. L. van Hulle, P. T. Smulders and J. B. Dragt, Eds.). pp. 452–455. Elsevier Science Publishers B. V.
- Strawn, R. C. and F. X. Caradonna (1987). Conservative full potential method for unsteady transonic rotor flows. *AIAA J.* **25**(2), 193–198.
- Sudhakar, K. and G. R. Shevare (1991). Low-order panel method for internal flows. *J. Aircraft* **28**(4), 286–288.
- Sutton-Vane, V. (1988). A new form of straight bladed vawt: a preliminary report. *Wind Eng.* **12**(1), 27–46.
- Swisher, R. (1998). Windpower: a US perspective. *Wind Eng.* **22**(4), 185–188.
- Tan, H. S. (1953). On laminar boundary layer over a rotating blade. *J. Aeronaut. Sci.* **20**(11), 780–781.
- Tangler, J. L. (1982). Comparison of wind turbine performance prediction and measurement. *ASME J. Solar Energy Eng.* **104**(2), 84–88.
- Tangler, J. L. (1983). Assessment of blade -element/momentum analysis for horizontal axis wind turbines. In: *Proc. 6th Biennial Wind Energy Conf. and Workshop, Minneapolis and St. Paul, MN, USA*.

- Tangler, J. L. and D. M. Somers (1995). NREL airfoil families for HAWTS. NREL/TP-442-7109. Nat. Renewable Energy Lab.
- Tangler, J. L. and M. S. Selig (1997). An evaluation of an empirical model for stall delay due to rotation for HAWTS. In: *Proc. Windpoer'97, Austin, Texas, USA*.
- Thresher, R. W., A. D. Wright and E. L. Hershberg (1986). A computer analysis of wind turbine blade dynamic loads. *ASME J. Solar Energy Eng.* **108**(1), 17–25.
- Thwaites, B. (1960). *Incompressible aerodynamics*. Oxford University Press.
- Touryan, K. J., J. H. Strickland and D. Berg (1987). Electric power from vertical-axis wind turbines. *J. Propulsion* **3**(6), 481–493.
- Tran, C. T. and D. Petot (1981). Semi-empirical model for the dynamic stall of airfoils in view of the application to the calculation of responses of a helicopter blade in forward flight. *Vertica* **5**, 35–53.
- Tucker, V. A. (1996). A mathematical model of bird collisions with wind turbine rotors. *ASME J. Solar Energy Eng.* **118**(4), 253–262.
- Twidell, J. (1998). Editorial. *Wind Eng.* **22**(4), 183.
- van der Borg, N. J. C. M. and W. J. Stam (1989). Acoustic noise measurements of wind turbines. In: *Proc. Eur. Wind Energy Conf. '89, Glasgow, Scotland*.
- van Kuik, G. A. M. (1997). 25 years of wind turbine technology development. In: *Proc. Eur. Wind Energy Conf. '97, Dublin, Ireland*.
- van Wijk, A.J.M and J.P. Coelingh (1993). *Wind Potential in the OECD Countries*. Univ. of Utrecht.
- Vatistas, G. H., V.Kozel and W. C. Mih (1991). A simpler model for concentrated vortices. *Exp. Fluids* **11**, 73–76.
- Veers, P. S. and S. R. Winterstein (1998). Application of measured loads to wind turbine fatigue and reliability analysis. *ASME J. Solar Energy Eng.* **120**(4), 233–239.
- Vick, B. D., W. Wrigglesworth, L. B. Scott and K. M. Ragsdell (1988). Optimal design of wind turbines using BIAS, a method of multipliers code. In: *Advances in Design Automation – 1988, Proc. 1988 ASME Design Automation Conf., Kissimmee, FL, USA*. pp. 201–210. ASME Design Eng. Div., Vol.14.
- Viterna, L. A. and D. C. Janetzke (1982). Theoretical and experimental power from large horizontal-axis wind turbines. NASA TM-82944.

- Voutsinas, S. G. and V. A. Riziotis (1996). Vortex particle modelling of stall on rotors. Application to wind turbines. *Proc. 1996 ASME Fluids Eng. Div. Summer Meeting, San Diego, CA, USA, ASME Fluids Eng. Div.* **238**(3), 25–32.
- Wei, J., D. Shen and J. Ma (1990). Comparative wind tunnel tests on multi-blade rotors with parallel and tapered blades. *Wind Eng.* **14**(5), 312–318.
- Wilmshurst, S., A. J. F. Metherell, D. M. A. Wilson, D. J. Milborrow and J. N. Ross (1984). Wind turbine performance in the high thrust region. In: *Proc. 6th BWEA Wind Energy Conf., Reading, England*.
- Wilmshurst, S. M. B., S. J. R. Powles and D. M. A. Wilson (1985). The problem of tower shadow. In: *Proc. 7th BWEA Wind Energy Conf., Oxford, England*.
- Wilson, R. E. (1981). Aerodynamic potpourri. In: *Proc. Wind Turbine Dynamics Conf., Cleveland, Ohio, NASA Conf-2185*.
- Wilson, R. E. and C. R. Harman (1995). Tangential induction and its effect on wind turbine performance and loads. *ASME J. Solar Energy Eng.* **117**(2), 157–158.
- Wilson, R. E. and P. B. S. Lissaman (1974). Applied aerodynamics of wind power machines. Oregon State Univ. Report NSF/RA/N-7413. NTIS PB 238594.
- Wood, D. H. (1991). Three-dimensional analysis of stall-delay on a horizontal-axis wind turbine. *J. Wind Eng. and Ind. Aerodyn.* **37**(1), 1–14.
- Woods, L. C. (1961). *The theory of subsonic plane flow*. Cambridge University Press.
- Xu, G. and L. N. Sanka (1999). Computational study of horizontal axis wind turbines. In: *A Coll. 1999 ASME Wind Energy Symp. Tech. Papers Presented 37th AIAA Aerospace Sci. Meeting and Exh., Reno, USA, AIAA-99-0042*.
- Yekutieli, O. and R. N. Clark (1987). Influence of blade surface roughness on the performance of wind turbines. In: *Proc. 6th ASME Wind Energy Symp.*
- Yeznasi, A., R. Derdelinckx and C. Hirsch (1992). Influence of dynamic stall in the aerodynamic study of HAWTs. *J. Wind Eng. and Ind. Aerodyn.* **39**(1–3), 187–198.
- Young, W. H. and J. C. Williams (1972). Boundary-layer separation on rotating blades in forward flight. *AIAA J.* **10**(12), 1613–1619.